

The origin of the Lupus I molecular cloud Formation between colliding shells?



Dissertation der Fakultät für Physik
der Ludwig-Maximilians-Universität München

vorgelegt von
Benjamin Gaczkowski

30.11.2015

Erstgutachter: Prof. Dr. Thomas Preibisch
Zweitgutachter: Prof. Dr. Andreas Burkert
Datum der mündlichen Prüfung: 25.01.2016

Contents

Contents	vii
Zusammenfassung	ix
1 Introduction	1
1.1 Interstellar medium	3
1.1.1 The gaseous ISM	3
1.1.2 Interstellar dust	5
1.2 Molecular cloud formation	7
1.3 Structure of molecular clouds	9
1.4 Observing molecular clouds	12
1.5 Star formation	13
1.6 Feedback from massive stars	15
1.7 The Scorpius-Centaurus region	17
1.8 The Lupus I molecular cloud	19
2 Far-infrared to millimeter astronomy	23
2.1 Radio telescopes	23
2.1.1 Observing methods	25
2.1.2 Antenna properties	26
2.2 Radiative transfer	26
2.2.1 Blackbody radiation	27
2.2.2 Local Thermodynamical Equilibrium conditions	29
2.2.3 Brightness and antenna temperature	30
2.2.4 Continuum emission	31
2.3 Molecular spectroscopy	32
2.3.1 Molecular excitation	33
2.3.2 Molecular line profiles and broadening	34
2.3.3 Molecular column density	36
3 Observations and data reduction	39
3.1 LABOCA continuum	39
3.2 APEX CO emission	41

3.3	Herschel archival data	42
3.4	Planck archival data	43
4	Constraining the physical properties of Lupus I using dust emission	45
4.1	Column density and temperature maps of Lupus I	45
4.1.1	Column density and temperature map from <i>Herschel</i> SED fit with all SPIRE bands	45
4.1.2	How the choice of a dust model influences the column density and temperature map	47
4.1.3	How the inclusion of the PACS bands influences the SED fit	48
4.1.4	Column density map from <i>Herschel</i> SPIRE 250 μm map	50
4.1.5	The influence of convolution on the <i>Herschel</i> column density maps	50
4.1.6	Column density map from the LABOCA data	51
4.1.7	Column density and temperature map from the <i>Planck</i> data	52
4.1.8	Results of the column density and temperature maps	55
4.2	Column density PDFs of Lupus I	56
4.2.1	Results of the column density PDFs	58
4.2.2	Robustness of the PDF fit with respect to the bin size	62
4.2.3	An alternative approach to fitting column density PDFs	62
4.3	Distribution of cores in Lupus I from LABOCA	66
4.4	Total mass estimates of Lupus I	69
4.5	Summary of the dust emission results	70
5	Describing the gas kinematics in Lupus I using molecule emission	71
5.1	Spectra	71
5.2	Velocity channel maps	73
5.3	PV diagrams	77
5.4	Moment maps	81
5.5	LTE analysis	85
5.5.1	Optical depth	85
5.5.2	Excitation temperature	87
5.5.3	Column density and PDFs	88
5.5.4	Errors of the LTE analysis	94
5.6	Determination of different velocity components	96
5.6.1	Non-thermal motions	103
5.6.2	Comparison to other molecular observations of Lupus I	103
5.7	Summary of the kinematic results	111
5.8	Comparison to the HI data	112
6	Lupus I in context of the star formation history of Sco-Cen	115
6.1	Surroundings of Lupus I	115
6.2	Geometrical model for the interaction zone	118

7 Summary and outlook	125
A CO spectra of cut A, B, and C	131
A.1 cut A	132
A.2 cut B	144
A.3 cut C	154
List of figures	165
List of tables	167
List of Abbreviations	169
Bibliography	171

Zusammenfassung

Aus heutiger Sicht scheinen sich Molekülwolken im dynamischen und turbulenten interstellarem Medium (ISM) durch die Kollision von großräumigen Strömungen zu bilden, welche durch Feedbackprozesse massereicher Sterne - wie z.B. UV-Strahlung, Winde und Supernovae - angetrieben werden. Ein mögliches Beispiel eines solchen Entstehungsprozesses bildet die Lupus I Molekülwolke. Sie befindet sich zwischen den beiden Untergruppen Upper-Scorpius (USco) und Upper-Centaurus-Lupus (UCL) der Scorpius-Centaurus OB Assoziation (Sco-Cen). Ihre Position liegt zwischen einer expandierenden HI Schale um USco, welche mit einer windgetriebenen Blase verbliebener B-Sterne in UCL zu interagieren scheint. Da Lupus I mit etwa 150 pc Abstand sehr nah ist, stellt sie ein gutes Studienobjekt dar, um zu untersuchen, auf welche Weise Kollisionsprozesse neue Molekülwolken entstehen lassen und neue, dichte Wolken beeinflussen könnten.

Für diese Arbeit habe ich neue Sub-mm und Millimeter Beobachtungen von Lupus I mit dem APEX 12 m Teleskop in Chile durchgeführt, sowohl vom Kontinuum bei $870 \mu\text{m}$, als auch vom $J = 2 \rightarrow 1$ Linienübergang des ^{13}CO und C^{18}O Moleküls. Diese Daten habe ich um Multi-Wellenlängen Archivdaten erweitert, um sowohl die physikalischen Eigenschaften der Wolke, als auch deren Umgebung charakterisieren zu können und mögliche Hinweise auf eine Interaktion mit der expandierenden Schale oder Windblase zu finden.

Aus meinen LABOCA Sub-mm Kontinuumsbeobachtungen, sowie *Herschel*- und *Planck*-Archivdaten der Staubemission, habe ich eine Säulendichte- und Temperaturkarte von Lupus I erstellt. Diese haben gezeigt, dass sich Lupus I in zwei unterschiedliche Regionen unterteilen lässt. Der nördliche Teil hat im Durchschnitt niedrigere Säulendichten und höhere Temperaturen und zeigt keine aktive Sternentstehung. Der zentral-südliche Teil der Wolke beherbergt dagegen dutzende prä- und protostellare Kerne und in ihm haben Säulendichte und Temperatur ihr Maximum bzw. Minimum.

Die Säulendichte-Wahrscheinlichkeitsdichtefunktionen (PDFs) aus den *Herschel*-Daten zeigen Doppelpeaks für alle Teile der Wolke, was ich auf eine externe Kompression zurückführe. In den Teilen von Lupus I, in welchen aktive Sternentstehung sichtbar ist, verhält sich die PDF bei hohen Säulendichten gemäß eines Potenzgesetzes.

Mit LABOCA habe ich 15 Kerne mit Massen zwischen 0.07 und $1.71 M_{\odot}$ sowie einer Gesamtmasse von etwa $8 M_{\odot}$ gefunden. Deren Verteilung bestätigt, dass nur im zentral-südlichen Teil der Wolke aktive Sternentstehung stattfindet. Die gesamte Staub- und Gasmasse von Lupus I aus den LABOCA-Daten beläuft sich auf etwa $164 M_{\odot}$, womit sich etwa 5% der Gesamtmasse in Kernen wiederfindet. Aus den *Herschel*- und *Planck*-Daten habe ich für die Wolke eine Gesamtmasse von $171 M_{\odot}$ bzw. $174 M_{\odot}$ bestimmt.

Die Analyse meiner CO Beobachtungen für drei ausgewählte Teilbereiche von Lupus I hat gezeigt, dass die Gasgeschwindigkeiten innerhalb der Wolke hauptsächlich im Bereich von $v_{\text{LSR}} = 3\text{--}6\text{ km s}^{-1}$ liegen. Der nördliche Teil der Wolke zeigt dabei im Schnitt $0.5\text{--}1\text{ km s}^{-1}$ höhere Geschwindigkeiten als der zentrale und südliche Teil. Alle drei Teile der Wolke scheinen aus sich überlagernden Teilfilamenten zu bestehen, welche verschiedene Geschwindigkeitskomponenten entlang der Sichtlinie aufweisen. Die nicht-thermische Komponente der C^{18}O Linienbreiten liegt in allen drei Teilen der Wolke im transsonischen Bereich, was auf ein signifikantes Niveau an Turbulenz innerhalb der Wolke hinweist. Diese könnte durch eine externe Kompression aufgrund der expandierenden USco Schale oder UCL Windblase in die Wolke injiziert worden sein.

Die Geschwindigkeiten der CO-Moleküle in Lupus I liegen im selben Bereich wie die des atomaren Wasserstoffes. Zudem geht innerhalb der Wolke eine höhere C^{18}O Emission im zentralen und südlichen Teil mit einem dortigen Defizit in der HI Emission einher. Der umgekehrte Fall liegt dagegen im Norden vor. Dies könnte darauf hindeuten, dass sich im nördlichen Teil der Wolke noch nicht genügend atomares in molekulares Material umgewandelt hat, wodurch keine Sternentstehung und niedrigere C^{18}O Emission zu sehen sind. Dieses Bild wird auch durch die Staub-Säulendichtekarten von Lupus I unterstützt, da Staub einen Katalysator für die Bildung von molekularem Wasserstoff bildet.

Großräumige Beobachtungen der Staub-, und Molekülemission, des atomaren Wasserstoffes und des Röntgengases zeigen, dass Lupus I wahrscheinlich Teil der ca. 6 pc breiten USco HI Schale ist. Dies wird auch durch die ähnlichen Gasgeschwindigkeiten von Wolke und Schale gestützt. Innerhalb der Schale scheint das Material vorzugsweise derart angeordnet zu sein, dass sich am äußeren Rand das atomare und weiter innen das molekulare befindet, was im Einklang mit der möglichen Entstehung von Lupus I in der Schale ist. Westlich und östlich dieses Schalenbereichs sind weder Staub noch atomares Gas oder molekulares Material vorhanden. Jedoch sind diese Bereiche mit heißem Röntngas gefüllt, welches im Falle von USco durch die vor ca. 5 Myr begonnene Ausbreitung der Schale und im Falle von UCL durch Sternwinde verbliebener B-Sterne zu erklären sein könnte.

Meine Ergebnisse deuten darauf hin, dass Lupus I stark von externen, großräumigen Kompressionen seitens der USco Schale und der UCL Windblase beeinflusst wurde und wird. Die Wolke hat sich wahrscheinlich aus dem atomaren Material gebildet, welches die USco Schale durch ihre Expansion aufgestaut hat und bewegt sich nun mit der Schale. Die Zeitskala für die Umwandlung atomar-molekular ist konsistent mit dem Alter der Schale und der jungen Kerne in Lupus I. Die Kollision mit der UCL Windblase könnte ein Faktor gewesen sein, der dazu geführt hat, dass eine lokale Inhomogenität in der USco Schale an einer Position verstärkt wurden, die die Bildung der Lupus I Wolke favorisiert hat. Ein von mir aufgestelltes geometrisches Modell hat gezeigt, dass die Beobachtungsdaten ein derartiges Szenario nicht ausschließen und dass sich Lupus I sehr wahrscheinlich am Innenrand der USco Schale befindet. Dieses Szenario könnte auch Position, Orientierung, und Elongation der Wolke, die Doppelpeaks in den PDFs und die sehr junge Generation von prä- und protostellaren Kernen erklären.

Chapter 1

Introduction

Star formation is one of the most important processes in the universe. Many would consider it even the most important process because we came into existence through it; planetary systems usually form in protoplanetary discs surrounding new born stars. Hence, it is also related to the ever fascinating question if there is other life than us in the Universe? However, star formation is still a big puzzle that cannot be put together easily, because of the amount of physics that has to be considered. Almost every discipline of physics plays its part in the whole process: mechanics, gravitation, magneto-hydrodynamics, thermodynamics, nuclear physics, and a lot of chemistry as to mention just a few of them. Therefore, not only has each single process to be understood, but also the complex picture that arises from the interaction of those processes. Moreover, these processes act on scales that span several orders of magnitude: from Galactic kiloparsec scales to microscopic dust particles.

Giving answers to these questions is challenging for observers, theoreticians, and simulators as it requires the most precise observational instruments available and continuous improvements in computing power and theoretical models. There are some answers that we seem to know quite well, e.g. low-mass star formation (see Section 1.5), others concerning for example the origin of the environment in which stars can form are far from being understood.

Without the advance of radio astronomy in the middle of the 20th century and the rapid development of the related observational equipment (e.g. receivers and antennas) we would not be able to observe anything that is directly related to star formation (see Section 2). To actually probe the conditions that are necessary for star formation to occur, observations outside the optical wavelength regime are needed. Thus, it was the upswing of radio astronomy that first allowed the detection of the 21 cm line of atomic hydrogen and the detection of molecules in space and established dense and cold molecular clouds (MCs) as the primary sites of star formation. Especially the first detection of the $^{12}\text{CO}(1-0)$ line by Wilson et al. (1970)¹ subsequently gave rise to systematic CO surveys that revealed the distribution of molecular clouds in our Galaxy and allowed to obtain their sizes, masses, and other physical properties (e.g. Scoville & Solomon 1975; Kutner et al. 1977; Blitz &

¹The full abstract is: "We have found intense 2.6-mm line radiation from nine galactic sources which we attribute to carbon monoxide."

Thaddeus 1980; Dame et al. 1987). They also showed that MCs contribute significantly to the total mass budget of the interstellar medium (ISM) in which they reside and out of which they are formed (see Section 1.1). A more recent, and the most cited, CO survey of the entire Milky Way was done by Dame et al. (2001) and a part of their resulting map is shown in Figure 1.1. Most of the molecular clouds are found in or near the Galactic plane, but there are also several complexes at latitudes higher than $b = \pm 10^\circ$. ρ Ophiuchus and the Lupus cloud complex are two examples that both are part of the Scorpius-Centaurus region discussed in this work (see Section 1.7).

How molecular clouds are formed is a highly debated topic, in particular for the last two decades. New far-infrared and sub-mm ground-, air-, and space-based telescopes like APEX, ALMA, SOFIA, and *Herschel* allowed observations with unprecedented angular and spatial resolution, and sensitivity of our Galaxy and other nearby galaxies like the Large Magellanic Cloud (LMC). Rapid computational development allowed sophisticated numerical simulations of molecular cloud formation that greatly advanced our knowledge of the process and could be tested against observational data. Turbulence was found to be a much more important ingredient in the formation and evolution of MCs, and its behavior on large and small scales was studied in more detail. This led to a new view of the ISM as a dynamic and turbulent medium in which molecular clouds form from turbulent, colliding flows (see e.g. Ballesteros-Paredes et al. 1999; Koyama & Inutsuka 2000, and Section 1.2). These flows consist mainly of warm atomic hydrogen (several thousand Kelvin) that is first converted into cold atomic hydrogen ($T < 100$ K) through collisions and subsequently into molecular hydrogen the main constituent of molecular clouds.

In many cases, however, these flows have the form of expanding shells or bubbles with radii from several ten parsecs in the Milky Way to even several hundred parsecs as has been observed in other galaxies. Those shells may be driven by either Galactic scale density waves due to the rotation of the spiral arms or feedback from massive stars that disperse their natal molecular cloud and accumulate material into an expanding shell (see Section 1.6). During the collision of such shells new molecular clouds can be formed in the interaction zone. A mechanism that has not yet been studied in detail numerically and so far just a few examples have been found observationally.

One of those few examples is the Lupus I cloud that is analyzed in this work. Lupus I is one of the closest molecular clouds to us. This is very favorable because it enables high resolution observations that can resolve structures as small as 0.01 pc. This corresponds to the size of cores, the smallest sub-structure in a MC, in which finally new stars are formed (see Sections 1.3 and 1.5). Furthermore, the cloud sits at a position that is very likely linked to the expansion of an atomic hydrogen shell and its interaction with a bubble driven by winds of several massive stars. Lupus I location seems to be in between those two shells and thus represents a rare example where the possible formation of a new molecular cloud through flow collisions in the ISM can be studied in great detail.

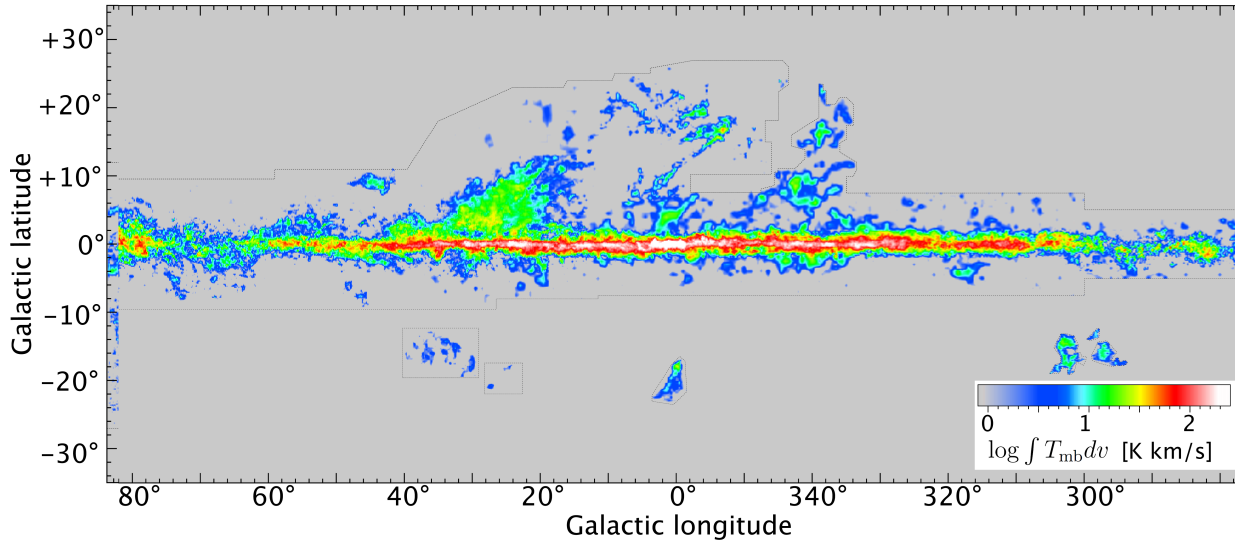


Figure 1.1: Velocity-integrated CO emission of the central Milky Way region. The Lupus I cloud is located at $l = 339^\circ$ and $b = +17^\circ$; ρ Ophiuchus at $l = 353^\circ$, $b = +18^\circ$. Adapted from Dame et al. (2001).

1.1 Interstellar medium

In the beginning of the 20th century first observational evidence has been found that the space between stars in our Galaxy is not just empty (Hartmann 1904; Hubble 1922). Today we know that this space is filled by the ISM which accounts for about 10–15% of our Galaxy’s total mass. It is mostly a remainder of the Big Bang, i.e. from the time when the universe had cooled down enough to allow atoms to form (Schulz 2005). As hydrogen and helium were predominant at that time, the composition of today’s ISM is basically still the same. About 70% is found in hydrogen, 28% in helium and the remaining 2% of the ISM constituents are all the other heavier elements, called metals in Astronomy, that were created after the Big Bang by nucleosynthesis in the stars. Furthermore, 99% of the ISM consists of gas and only 1% of dust.

1.1.1 The gaseous ISM

The gaseous content of the ISM is divided into several components that occupy different volumes of the Milky Way and contribute differently to the mass budget of our Galaxy (Field et al. 1969; McKee & Ostriker 1977). Table 1.1 summarizes those components and lists their properties. In principle these different components are distinguished by the chemical phase of hydrogen which can either be ionized H II (H^+), neutral H I (H), or molecular H_2 . The hot ionized medium (HIM) is mainly created by supernova explosions that create large bubbles filled with million degrees hot and ionized gas (McKee & Ostriker 1977). It fills about half of our Galaxy’s volume, but contributes almost no mass because of its very low density ($< 10^{-2} \text{ cm}^{-3}$). However, 90% of the ionized gas is found as the warm ionized medium (WIM) with temperatures around 8000 K and densities of about

Table 1.1: Phases and components of the gaseous ISM. Columns give the phase, the number density, the temperature, the volume filling factor, and the total mass of each component, respectively. *Adapted from Klessen & Glover (2014), Brinks (1990), and Ferrière (2001).*

Phase	n [cm^{-3}]	T [K]	Vol	M_{tot} [$10^9 M_{\odot}$]
Hot ionized medium (HIM)	$\sim 10^{-2}$	$\sim 10^6$	$\sim 50\%$	–
Warm ionized medium (WIM)	0.2–0.5	~ 8000	15%	1.0
Warm neutral medium (WNM)	0.2–0.5	6000–10 000	30%	1.4
Cold neutral medium (CNM)	20–50	50–100	4%	2.5
Molecular clouds (MCs)	> 100	10–30	1%	2.5

0.5 cm^{-3} and thus comparable to the warm neutral medium (Reynolds 1991; Gaensler et al. 2008; Haffner et al. 2009). It is ionized by X-rays and cosmic rays, has a scale height of about 1 kpc and its volume filling factor increases significantly with Galactic latitude. Usually, classical H II regions around OB-stars are not counted as part of the WIM (Klessen & Glover 2014). The neutral or atomic phase of the ISM has two components: the warm and the cold component. Both were found to be thermally stable conditions (Field et al. 1969). The cold neutral medium (CNM) has temperatures around 100 K and densities of about 50 cm^{-3} , the warm neutral medium (WNM) instead, has temperatures around 10^4 K , but densities of just 0.5 cm^{-3} . Thus, both phases have a similar pressure $P = n \times T = 5000 \text{ K cm}^{-3}$ and may co-exist. The CNM is associated with diffuse HI clouds surrounding molecular clouds. The neutral medium plays an important role in the formation of molecular clouds which will be described in Section 1.2. Finally, there is the molecular phase of the ISM which consists of very dense ($> 10^2$ – 10^5 cm^{-3}) and cold (10–30 K) molecular clouds that occupy a small volume, but due to their high densities contribute significantly to the total mass of the ISM (see e.g. Blitz et al. 2007). Molecular clouds are the sites of star formation and are very important in the context of this work. Their structure will be described in Section 1.3.

The picture of the ISM described above might, however, be too simplistic. Observations performed over the last years and a number of numerical simulations have shown that the gas in the ISM cannot always be assigned to one of those phases, but rather is subject to turbulent mixing. There exist also intermediate stages of the neutral medium that are neither in equilibrium nor can be assigned unambiguously to either CNM or WNM (Heiles & Troland 2003; Roy et al. 2013; Klessen & Glover 2014). Large-scale turbulence driven by different mechanisms like thermal instabilities, supernovae and massive star feedback, and galactic disc inflow motions (see reviews by Elmegreen & Scalo 2004; Scalo & Elmegreen 2004), mixes different phases of the ISM making them hard to distinguish (Klessen & Glover 2014).

1.1.2 Interstellar dust

Although it constitutes only 1% of the ISM mass and has a volume density on the order of 10^{-9} cm^{-3} , interstellar dust is of great importance as a cooling and heating agent (Burke & Hollenbach 1983; Xilouris et al. 2012), and for the creation and shielding of molecules and thus molecular clouds. Dust grains mainly consist of graphites (Mathis et al. 1977), amorphous silicates (Draine & Li 2007) or water ice (Sirono 2013). They have typical sizes of $0.01\text{--}1 \mu\text{m}$ and their size distribution is described by a power-law (Mathis et al. 1977)

$$N(a)da \propto a^{-3.5}da \quad (1.1)$$

where a is the size of the grain. Therefore, there are more small than large grains. The nature of dust can be studied through its extinction of the interstellar light. The so-called dust extinction curve indicates at which wavelengths interstellar radiation is absorbed or scattered by the dust grains (see left panel in Figure 1.2). In the optical these effects show up as dark patches against the background illumination as is illustrated in the right panel of Figure 1.2.

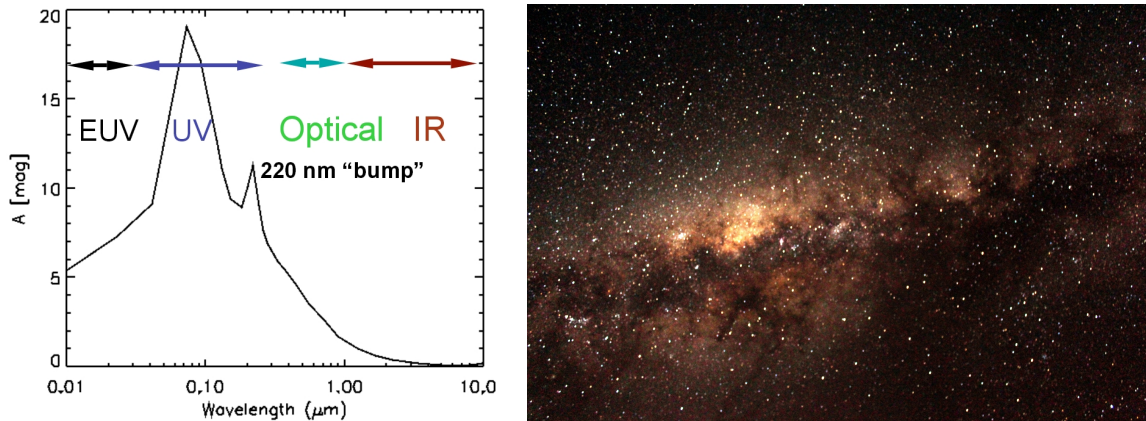


Figure 1.2: *Left:* Optical image of the Southern sky I have taken in Chile during the observing run with APEX. Dark areas are due to dust extinction. *Right:* Schematic view of the dust extinction curve. *Adapted from lecture notes on the ISM of A. Glassgold (<http://w.astro.berkeley.edu/ay216/08/NOTES/Lecture05-08.pdf>)*

From the amount of extinction at a given wavelength one can then deduce the size distribution of the dust grains under the assumption that grains pre-dominantly absorb or scatter light of wavelengths smaller than their own size. Different types of grains also produce different characteristic "bumps" in the extinction curve (e.g. UV bump at $0.2 \mu\text{m}$ is typically attributed to graphite). From those, the chemical structure of different dust grains could be deduced by comparison to laboratory spectra. Since dust grains have first been described by Mathis et al. (1977) models of dust properties have been continuously improved (see e.g. discussion by Draine 2011). The formation of dust is not yet completely understood. So far it is known that dust is either formed in the atmospheres of red giants

and planetary nebulae (Woolf & Ney 1969; Salpeter 1976), in supernovae, and in the ISM itself (see reviews by Ferrière 2001; Draine 2003, and references within). The dust mass usually is taken as 1% of the gas mass in the ISM, i.e. the gas-to-dust mass ratio $R = 100$, but it may significantly vary depending on the environment (e.g. Frisch & Slavin 2003; Krüger et al. 2015). The typical temperature of dust in molecular clouds has been found to be around 10–30 K (Planck Collaboration et al. 2011; Galametz et al. 2012).

Dust is an important catalyst in the formation of molecules, i.e. molecular hydrogen. The rate coefficient for a direct formation of H_2 from two hydrogen atoms in the gas phase is extremely small and thus this reaction can be ignored in astro-chemistry (Draine 2011). Therefore, dust is needed as a catalyst to absorb the excess binding energy (Hollenbach & Salpeter 1971; Cazaux & Tielens 2004; Charnley & Rodgers 2009). Further, dust provides effective shielding against the interstellar UV radiation field which would otherwise photo-dissociate the newly formed hydrogen molecules in just a few hundred or thousand years (Shull & Beckwith 1982). Typically, the dust extinction in a molecular cloud must exceed a value of $A_v = 1$ mag to provide sufficient shielding for H_2 to survive. It is thus not surprising that molecules and dust are very often observed together.

Dust grains are effective UV absorbers and therefore constitute an important cooling agent in dense and cold environments like molecular clouds. The UV radiation is re-radiated in the far-infrared and can freely escape the molecular cloud. Dust emission is a powerful tracer of molecular clouds and helps to constrain the physical conditions in the clouds. Especially, since the launch of the *Herschel* space observatory (Pilbratt et al. 2010) this method has become very popular. *Herschel* provided for the first time a sensitivity and resolution in the far-infrared that made it possible to study molecular clouds at sub-parsec resolution. The analysis of the dust emission from Lupus I is a great part of this work. The physical nature of it will be described in more detail in Section 2.2.4 and its analysis presented in Chapter 4.

Finally, the destruction of dust by shocks can release its atoms and molecules back into the ISM (Seab 1987; Van Loo et al. 2013). This provides new heavy elements in the gaseous ISM that can be used to restart the life cycle of the ISM which is illustrated in Figure 1.3. Dense molecular clouds form out of the diffuse ISM through condensation. From those new stars are born. During their lifetime stars may produce dust in their atmospheres and mix it into the ISM via winds. At the end of their lifetime they either lock all metals produced via nucleosynthesis because they end as compact dwarfs or they mix those elements back into the ISM via supernova explosions. Depending on the position of the supernova explosions in the Galaxy, the material is either expelled into the Galactic halo or the diffuse ISM is replenished again. Then the newly unlocked metals can be used for cooling, molecule production and shielding. In this way the life cycle can restart.

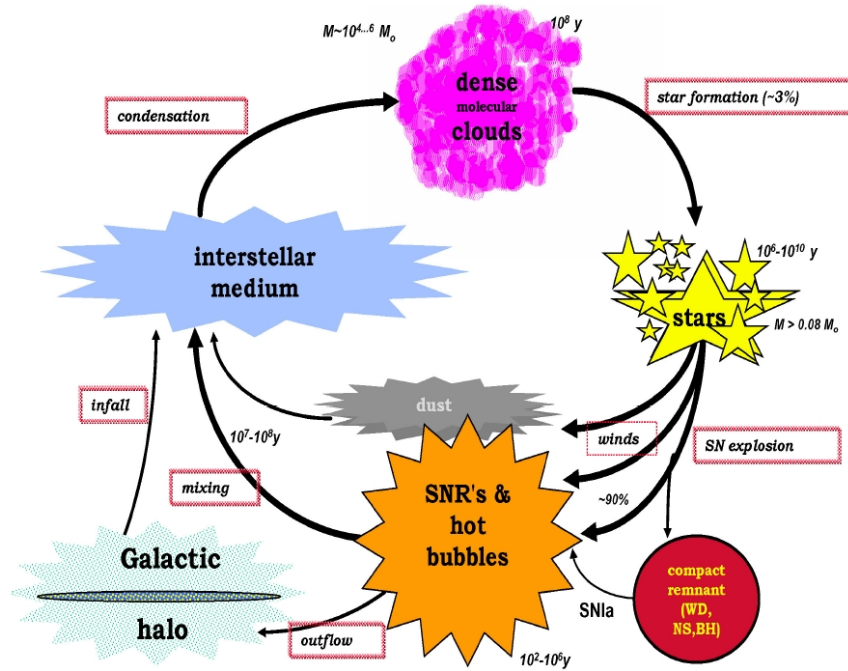


Figure 1.3: Life cycle of the ISM. Adapted from lecture notes on the ISM by A. Burkert.

1.2 Molecular cloud formation

Molecular clouds by definition are regions in which most of the gas is in its molecular form. From a chemical perspective a cloud could be called molecular when the majority of the hydrogen is in form of H_2 . However, H_2 cannot be easily observed at typical molecular cloud temperatures (see also Sections 1.4 and 2.3.1). Therefore, another observationally motivated definition of a molecular cloud has become common: the point at which the cloud becomes visible in CO (Klessen & Glover 2014). Newly formed molecules are subject to the interstellar radiation field (ISRF). It is the ambient radiation field that penetrates the ISM. It consists of several components that have different energy densities and thus contribute with a different strength to it. Details about the ISRF can be found in Draine (2011). In the context of this work the most important contributors are the optical and UV starlight and the far-infrared emission of dust grains heated by starlight. Both H_2 and CO are photodissociated through the absorption of UV photons. This puts the molecule into an excited state. The transition back into the ground state may then happen under dissociation (van Dishoeck 1987). This means that newly formed molecules must be shielded from the ISRF in order to survive. Otherwise they are destroyed on timescales of several hundred or thousand years in the diffuse ISM with a mean galactic ISRF strength. The shielding can be provided by either dust or self-shielding. When the H_2 gas column density becomes high enough ($> 10^{21} \text{ cm}^{-2}$), almost all UV radiation is absorbed by the outer layer of the cloud and the radiation cannot penetrate further into the cloud. In this way it shields itself from the ISRF (Klessen & Glover 2014).

For typical Milky Way conditions the H_2 formation timescale t_{f,H_2} is (Jura 1975)

$$t_{f,\text{H}_2} \approx 10^9 \left(\frac{n}{\text{cm}^{-3}} \right)^{-1} \text{ yr} \quad (1.2)$$

where n is the total number density of the gas. For typical molecular cloud densities of $n = 100 \text{ cm}^{-3}$ the formation timescale is several ten Myr. Sufficient shielding of the CO molecule requires even ten times higher column densities. Regarding this Klessen & Glover (2014) point out that the question of how molecular clouds form is fairly simple to answer: whenever gas in the ISM is gathered in one place in a form such that the column density exceeds the threshold for self-shielding and the gas stays in this place for longer than t_{f,H_2} , the transition from atomic to molecular gas can occur sufficiently often and the molecules can survive. What still remains unclear is how the gas is actually gathered out of the diffuse and atomic ISM to form a dense molecular cloud.

In the current picture of the dynamic ISM, molecular cloud formation is attributed to collisions of large-scale flows in the ISM (see review by Dobbs et al. 2014, and references within). A basic sketch of this model is presented in Figure 1.4. Initially, these flows are warm and atomic (1). Supersonic shocks and turbulent dissipation trigger a cooling instability in the collision zone that allows a rapid formation of a cold neutral medium cloud (2) (see e.g. Audit & Hennebelle 2005; Vázquez-Semadeni et al. 2007; Banerjee et al. 2009). This CNM cloud has densities of order 100 cm^{-3} and provides enough shielding for H_2 formation on timescales shorter than the duration of the collision (Clark et al. 2012). In some areas of the post-shock region the gas will become sub-sonic and exceed the critical mass for gravitational collapse allowing the formation of CO in a molecular cloud (3) (Heitsch & Hartmann 2008; Clark et al. 2012).

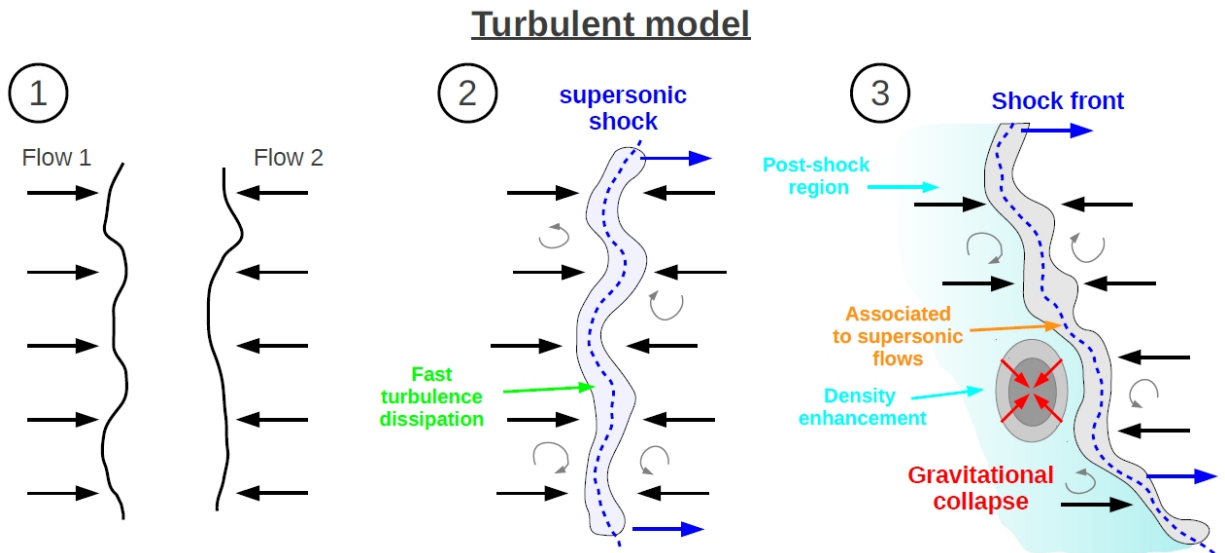


Figure 1.4: Molecular cloud formation in the colliding flow model. A description of the model can be found in the text. *Adapted from Hacar (2013).*

In this context cooling, i.e. removal of kinetic energy via collisions and radiation, is mainly provided by atoms like [C II] ($158\ \mu\text{m}$) or [O I] ($63\ \mu\text{m}$) via their fine structure lines. With decreasing temperature and increasing density of the cloud, the cooling is more and more dominated by dust (see Section 1.1.2) and molecules like CO (see Section 2.3), because their far-infrared and (sub-)mm radiation can still freely escape from the cloud.

Such turbulent flows can be driven by stellar feedback processes, i.e. UV-radiation, winds, and supernovae. Compression, cooling, and fragmentation of the diffuse atomic medium produces cold sheets and filaments at the interface of the colliding flows that may later become molecular and self-gravitating and dominate the appearance of the ISM as observed today (see review by André et al. 2014). In this picture the fast formation (and dispersion) of molecular clouds and the often simultaneous onset of star formation within appears plausible (see Hartmann et al. 2001; Vázquez-Semadeni et al. 2007; Banerjee et al. 2009; Gómez & Vázquez-Semadeni 2014).

One example of such a large-scale flow is an expanding shell or supershell around, for example, an OB association or in general driven by multiple stellar feedback of a star cluster or association (see review by Dawson 2013). Molecular clouds may then either form inside the wall of such a shell (Dawson et al. 2011a) or at the interface region when two such shells collide with each other. The latter case has recently been investigated by Dawson et al. (2015) for a young giant molecular cloud (GMC) at the interface of two colliding supershells. From the comparison of CO observations with high-resolution 3D hydrodynamical simulations they found that the GMC assembled into its current form by the action of the shells. Inutsuka et al. (2015) even suggest that the expanding-bubble picture of molecular cloud formation dominates in our Galaxy. They argue that molecular clouds are formed through multiple compressions by colliding dense shells driven by massive stellar feedback. In this work, I will discuss whether one of the above mentioned mechanisms, i.e. shell interactions, is likely to have formed the Lupus I molecular cloud.

1.3 Structure of molecular clouds

Molecular clouds span a wide range of sizes and masses in our Galaxy. At the low mass end there are clouds like the here analyzed Lupus I cloud with masses around $100\text{--}200\ M_{\odot}$. Such clouds are mainly found at high Galactic latitudes (Magnani et al. 1985) or in the outer disk of our Galaxy (Heyer et al. 2001). On the other hand, giant molecular clouds (GMCs) in the central molecular zone of the Milky Way can have masses of up to $10^7\ M_{\odot}$ (Oka et al. 2001). A recent discussion of cloud size and mass relations in the Milky Way can be found in Heyer & Dame (2015). The internal structure of molecular clouds is very inhomogeneous, filamentary, clumpy, and fractal. Over the past years the *Herschel* mission in particular has revealed that the appearance of molecular clouds is dominated by filaments (see reviews by André et al. 2014; Molinari et al. 2014). Aligned along such filaments or inside large and dense clumps, there reside the cores that represent the densest parts of molecular clouds. In those cores new stars can form through gravitational collapse (see Section 1.5). Figure 1.5 illustrates the different sub-structures found in a molecular cloud and their typical length scales.

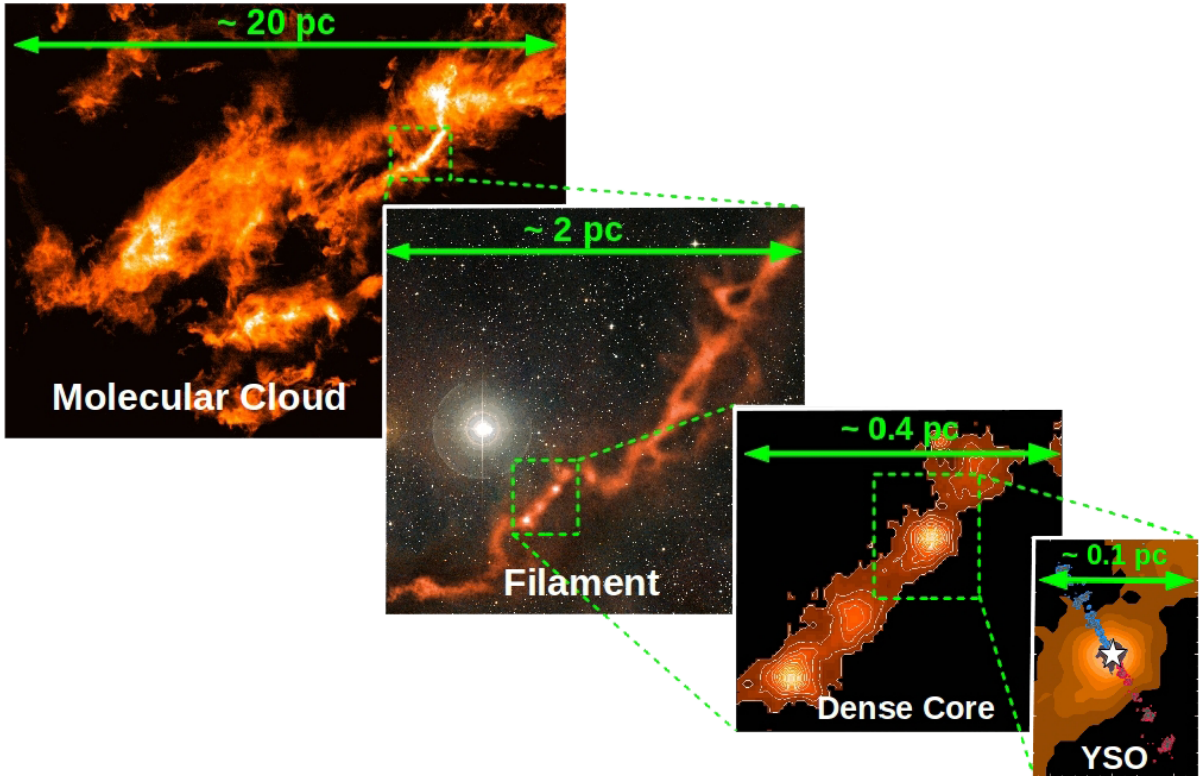


Figure 1.5: Illustration of the (sub-)structure of molecular clouds: a) Formation of the cloud [Image: Integrated $^{13}\text{CO}(1-0)$ emission in Taurus (Goldsmith et al. 2008)]. b) Formation of a filament [Image: APEX/LABOCA continuum emission at $850\ \mu\text{m}$ of B213 (ESO/APEX/Hacar et al. 2012 photo release eso1209a)]. c) Fragmentation and formation of a dense core [Image: Zoom into marked region of b) (Hacar et al. 2013)]. d) Formation of a YSO through gravitational collapse of the core [Image: APEX/LABOCA ($850\ \mu\text{m}$, orange) and APEX/SABOCA ($350\ \mu\text{m}$, red) continuum emission around IRAS 04166+2906 (Hacar et al. 2013). Overlaid is the bipolar molecular outflow emission (Santiago-García et al. 2009)]. Adapted from Hacar (2013).

The origin of these (sub-)structures is not yet completely understood. However, the main formation mechanisms are thought to be the before mentioned colliding flows, supersonic turbulence (Padoan et al. 2001), magnetic fields (e.g. Nakamura & Li 2008), and gravitational collapse (e.g. Burkert & Hartmann 2004). Typical physical properties of molecular clouds, clumps, and cores are summarized in Table 1.2.

The stability of a cloud is determined by the Jeans criterion

$$M_J = 5.46 \left(\frac{k_B T}{G \mu m_H} \right)^{3/2} \rho^{-1/2} \approx 1 M_\odot \left[\frac{T}{10 \text{ K}} \right]^{3/2} \left[\frac{n_{\text{H}_2}}{10^4 \text{ cm}^{-3}} \right]^{-1/2} \quad (1.3)$$

with T the temperature of the cloud, ρ its density (n_{H_2} its mean H_2 number density), μ the mean molecular mass, m_H the hydrogen atom mass, G the gravitational constant, and k_B the Boltzmann constant. It describes the mass a spherical and isothermal cloud must have to maintain equilibrium between its gas pressure and its self-gravity. If the mass of

Table 1.2: Properties of molecular clouds and their sub-structures. Columns give temperature, mean H₂ number density, size, total mass, free-fall, and crossing time. *Adapted from Klessen (2011).*

	T [K]	n_{H_2} [cm ⁻³]	R [pc]	M [M _⊙]	τ_{ff} [Myr]	τ_{cross} [Myr]
Molecular clouds	10–30	10 ² –10 ³	2–20	10 ² –10 ⁶	0.3–3	2–10
Clumps	10–20	10 ³ –10 ⁵	0.1–2	10–10 ³	0.1–1	≤ 1
Cores	7–12	> 10 ⁵	≤ 0.1	0.1–10	≤ 0.1	0.1–0.5

the cloud is smaller/larger than its Jeans mass, it will collapse/expand. This means that a molecular cloud of given mass M will become gravitationally unstable once it is dense and cold enough such that $M > M_{\text{J}}$. For instance the Jeans mass of a cloud like Lupus I, with a total mass of about 170 M_⊙, would be $M_{\text{J}} \approx 30 \text{ M}_{\odot}$ for $T = 20 \text{ K}$ and $n_{\text{H}_2} = 100 \text{ cm}^{-3}$. The same applies also for a typical GMC which instead has a total mass of $\approx 10^4 \text{ M}_{\odot}$. This means that molecular clouds should be highly gravitationally unstable and collapse. The important timescale for the collapse of an isothermal sphere is the free-fall time

$$\tau_{\text{ff}} = \sqrt{\frac{3\pi}{32G\rho}} \approx 3.4 \text{ Myr} \sqrt{\frac{n_{\text{H}_2}}{100 \text{ cm}^{-3}}} \quad (1.4)$$

which for a GMC is about 3.4 Myr. Clumps and cores will collapse even faster. Hence, one should expect a Galactic star formation rate of about 1000 M_⊙ yr⁻¹ when the total molecular cloud mass is $\sim 10^9 \text{ M}_{\odot}$ and clouds would collapse within τ_{ff} . But the observed star formation rate is only 2 M_⊙ yr⁻¹ (see recent review by Krumholz 2014). Therefore, there must be something else besides gas pressure that stabilizes molecular clouds and prevents fast collapse. This driving force was found to be supersonic turbulence. On large scales it provides sufficient counter-pressure to prevent a collapse of the whole cloud by significantly increasing the Jeans mass, while at the same time it helps to enhance the density on small scales by creating supersonic shocks, triggering cooling instabilities, and amplifying self-gravity (Klessen 2011). Then the cloud can fragment into filaments, clumps, cores and finally form stars (see Section 1.5).

In this context I would like to introduce another important and often used timescale of molecular clouds: the crossing or dynamical timescale. It is defined by

$$\tau_{\text{cross}} = \frac{R}{c_{\text{s}}} \quad (1.5)$$

with R the size of the cloud and c_{s} the sound speed in the cloud. The sound speed is defined by

$$c_{\text{s}} = \sqrt{\frac{\gamma \partial P}{\partial \rho}} \approx \alpha \sqrt{\frac{T}{10^4 \text{ K}}} \text{ km s}^{-1} \quad (1.6)$$

where γ is the adiabatic exponent, P is the pressure and ρ the density of the medium.

The factor α is either 9 or 12 in the isothermal ($\gamma = 1$, $P \propto \rho$) or adiabatic ($\gamma = 5/3$, $P \propto \rho^{5/3}$) case, respectively. This means that for typical molecular cloud temperatures of 10–30 K the sound speed is about 0.5 km s^{-1} . Both the crossing and the free-fall time are given in Table 1.2. Notably, the crossing timescale is longer than the free-fall time for molecular clouds.

The overall lifetime of molecular clouds is still under much debate (see Dobbs et al. 2014, for a discussion). Solar neighborhood GMCs have estimated lifetimes of $10 \pm 3 \text{ Myr}$ (see e.g. Ballesteros-Paredes & Hartmann 2007; Jeffries et al. 2011) whereas extra-galactic GMCs have lifetimes of even $> 10^8 \text{ yr}$ (see e.g. Koda et al. 2009). However, molecular clouds are in general disrupted again by their internal massive stellar feedback before they can turn a significant fraction of their mass into stars (Dobbs et al. 2014). Therefore, an upper limit of $\approx 20\text{--}30 \text{ Myr}$ for the lifetime of molecular clouds seems consistent for our Galaxy. But there are also cases like the Upper-Scorpius (USco) progenitor cloud that are dispersed in less than 5 Myr (see Section 1.7). Hence, the cloud lifetime depends on the mass distribution of the stars formed within and their level of destructive feedback.

1.4 Observing molecular clouds

Molecular clouds are the densest and coldest part of the ISM. This means that most of the short wavelength radiation ($< 10 \mu\text{m}$) is not able to escape from the inside of the cloud. Therefore, molecular clouds appear dark in optical images and near-infrared observations reveal only the clouds' surface. The important wavelength regime at which molecular clouds are observed is the far-infrared to radio regime. Molecular clouds are optically thin to this radiation and it can freely escape from the inner regions. The cause of this radiation are cooling processes by dust and molecules (see Sections 1.1.2 and 2.3). Molecular hydrogen is basically not observable at temperatures as low as in molecular clouds and thus dust and CO emission are the commonly used tracers. The thermal dust emission and the rotational CO lines both peak in this observable wavelength window. In the end, however, observers express the observed or inferred quantities in terms of molecular hydrogen for which conversion factors are used that relate dust and CO to H_2 . For dust, this factor is called the gas-to-dust mass ratio R which is normally assumed to be 100. But it may significantly vary depending on the environment (e.g. Frisch & Slavin 2003; Krüger et al. 2015). For CO the so-called X_{CO} or CO-to- H_2 conversion factor is applied (Dame et al. 2001)

$$X_{\text{CO}} = N(\text{H}_2)/W_{\text{CO}} = 2 \times 10^{20} \frac{\text{cm}^{-2}}{\text{K km s}^{-1}} \quad (1.7)$$

where $N(\text{H}_2)$ is the H_2 column density and W_{CO} the integrated CO line intensity. This factor depends on the Galactic environment (see e.g. Wilson & Rood 1994) and thus is always a source of error in the analysis because an exact determination is not possible. CO needs a higher cloud column density to be sufficiently shielded from the ISRF and thus survive within the cloud. Hence, there is a significant fraction of so-called CO-dark H_2 gas at the surface of molecular clouds that cannot be accounted for with CO. This

fraction could even be as high as 50%–100% of the molecular mass (Grenier et al. 2005). It must be inferred from observations of C II, C I or γ -rays that trace the interaction of molecular hydrogen with high energetic cosmic rays. Cosmic rays consist mostly of high-energy protons or He nuclei with energies ranging from several 100 MeV to 1 TeV (see Blasi 2014, for a recent review).

Molecular line observations are helpful to obtain information on the kinematics of a molecular cloud (see also Section 2.3). The linewidth is a common measure of turbulence in a cloud. Observations have shown that molecular clouds have much larger linewidths than just the thermal one and are highly turbulent and supersonic (see e.g. review by Mac Low & Klessen 2004, and Section 2.3.2).

The atomic HI as a tracer for the neutral medium can be observed in the radio regime. The forbidden hyperfine-structure line at 21 cm arises from the electron spin flip within the atom. The orientation of the spins of proton and electron changes from parallel to anti-parallel under the emission of a photon. In this work I will also analyze HI data as the origin of Lupus I is related to the expansion of an HI shell (see Chapter 5).

Observations of molecular clouds and atomic hydrogen are performed either with sub-mm and radio telescopes from earth or with space telescopes on-board of satellites. Both telescopes and observation techniques will be described in Chapter 2.

1.5 Star formation

As has been outlined above, stars generally form in cores of molecular clouds. Today star formation is still not fully understood, but the formation of low-mass stars is thought to be reasonably well known (see e.g. Shu et al. 1987; McKee & Ostriker 2007). The formation of high-mass stars ($M > 8 M_{\odot}$) follows a different mechanism which is of less importance for this work and thus I refer the reader to the reviews of Zinnecker & Yorke (2007) and Tan et al. (2014). The established dynamic picture of low-mass star formation is based on the process of gravo-turbulent fragmentation (see e.g. Padoan & Nordlund 2002; Mac Low & Klessen 2004). Supersonic turbulence injected into a molecular cloud acts, on the one hand, as a source of extra pressure and stabilizes clouds on large scales against gravitational collapse. On the other hand, it creates strong local density fluctuations which are amplified by self-gravity and cooling, leading to fragmentation of the cloud and quick core collapse (birth of a protostar) on smaller scales. Driver of interstellar turbulence is the feedback of massive stars. As soon as a part of the molecular cloud exceeds its Jeans mass it starts to collapse. Therefore, small initial inhomogeneities in the cloud lead to fragmentation because parts with higher density collapse faster. But the smaller the fragments become in size, the higher their density. Thus, at some point the density increases such, that the fragments become optically thick to their own radiation. Then the collapse is not isothermal anymore because radiative cooling that almost instantaneously removed the energy of the gravitational collapse, is no longer possible. As a consequence, the temperature in the fragments rises and the Jeans mass does not decrease any more. This stops the fragmentation process and cores existing at this point quickly, i.e. within τ_{ff} , collapse to protostars.

As cores are the coldest and densest parts of a molecular cloud their thermal emission can only be observed in the far-infrared and (sub-)mm wavelengths. Data obtained in several of those wavelengths allow the construction of a spectral energy distribution (SED) and from that one can infer the evolutionary status of the core (Lada 1987; Andre & Montmerle 1994), i.e. if it is still pre-stellar or already contains a protostellar object. For this work I observed several cores at $870 \mu\text{m}$ and found that probably just one of them already contains a protostar (see Section 4.3).

The fragmentation of a molecular cloud into cores gives rise to the core mass function (CMF)

$$\frac{dN}{dm} \propto m^{-\alpha} \quad (1.8)$$

with m the mass of a core. Observations have shown that the power-law holds for masses above $1 M_{\odot}$ and has a slope of $2 < \alpha < 2.5$ (Offner et al. 2014). Below one solar mass there are several observed shapes of the CMF depending on the cloud. It can be another power-law with a flatter slope or even a log-normal distribution (André et al. 2010). The CMF is thought to be closely related to the initial mass function (IMF) of stars, but seems to be shifted towards higher masses by a factor of ~ 3 . The IMF was first proposed by Salpeter (1955) and later refined by Kroupa (2001) and Chabrier (2003). For masses above $1 M_{\odot}$ it follows a power-law of slope -2.35 . Below it has again different representations depending on the conditions. The fact that CMF and IMF might be similar, is a currently debated topic and might imply that the final stellar mass is determined by the mass of the core in which it forms. The shift of the IMF towards lower masses, however, suggests that probably just a fraction of the core mass is actually turned into a star. For an extensive discussion on this topic see the review of Offner et al. (2014). The star formation efficiency is thus mainly determined by the cloud mass and surface density (see e.g. Burkert & Hartmann 2013; Evans et al. 2014). For an entire galaxy the star formation rate (SFR) is given by the Kennicutt-Schmidt-law (Schmidt 1959; Kennicutt 1998)

$$\Sigma_{\text{SFR}} = (2.5 \pm 0.7) \times 10^{-4} M_{\odot} \text{ yr}^{-1} \text{ kpc}^{-2} \left(\frac{\Sigma_{\text{gas}}}{M_{\odot} \text{ pc}^{-2}} \right)^{1.4 \pm 0.15} \quad (1.9)$$

with Σ_{gas} the surface density of the available gas. The Kennicutt-Schmidt-law provides good SFR estimates on galactic scales, but fails on the level of individual molecular clouds. For our Galaxy the star formation rate was found to be between $\approx 3\%$ - 5% (see e.g. Evans et al. 2009; Molinari et al. 2014).

1.6 Feedback from massive stars

Massive OB-stars (spectral type B3 or earlier) with masses above $\approx 8 M_{\odot}$ are the main and most important drivers of stellar feedback. They profoundly influence their natal environment, drive large-scale turbulence, and as most stars are born in clusters their combined feedback ultimately causes the dispersal of the surrounding molecular cloud. In context of this work, massive stellar feedback is of importance as the driver of shell and wind bubble expansion. There are three different stellar feedback mechanisms:

- UV radiation:** The UV radiation of massive stars can either photodissociate molecules of the cloud in which the stars are embedded in, photoevaporate dust, or ionize the surrounding atomic hydrogen creating and driving so-called H II regions. The size of such an H II region is determined by the equilibrium of ionization and recombination that happens behind the ionization front. The radius at which this equilibrium is established - in the time-independent case and an expansion into a homogenous solely atomic hydrogen medium - is called the Stromgren radius. In reality the time-dependent evolution of an H II region is not that simple. For the first few hundred years the ionization front of an H II region expands very fast with $v_{\text{exp}} \approx 6000 \text{ km s}^{-1}$. The temperature in the ionized gas rises to $\sim 10^4 \text{ K}$ and the pressure inside the region up to a thousand times the pressure of the surrounding cold cloud. In this phase, no motions of material are induced because the ionization front propagates much faster than the sound speed $c_s \approx 1 \text{ km s}^{-1}$. In the second phase the thermal expansion of the H II region begins because of the pressure difference between inside and outside. This expansion will be supersonic and thus a shock front will precede the ionization front once the velocity of the ionization front drops below c_s . This phase lasts for several Myr and efficiently sweeps up surrounding material into a shell. Once the H II region reaches the edge of the molecular cloud it will quickly expand into the low density medium. Typical UV fluxes of early OB-stars are on the order of $\sim 10^{48-53} \text{ photons/s}$ depending on the spectral type. With such an UV flux an O5 star can disperse about $0.01 M_{\odot} \text{ yr}^{-1}$ of cloud material. This means that during its lifetime of $\sim 3 \text{ Myr}$ it might destroy a $3 \times 10^4 M_{\odot}$ cloud. A more in-depth introduction into this type of feedback can be found in Osterbrock & Ferland (2006).
- Winds:** Stellar winds are basically mass ejecta expelled from the atmosphere of the star. They are driven through radiation pressure. Stellar photons are absorbed by metals in the atmosphere of the star transferring parts of their momentum onto the ion and thus accelerating it. These metals then transfer their momentum onto hydrogen and helium by collisions. However, the fraction of non-ionized hydrogen and helium is small because of the large temperatures of the OB-stars ($\sim 10^4 \text{ K}$). The mass loss rates of OB stars reach about $\dot{M} = 10^5 M_{\odot} \text{ yr}^{-1}$ with wind velocities of up to $\sim 3000 \text{ km s}^{-1}$ (Maeder & Meynet 2012). Such mass loss rates are a billion times higher than for the Sun, showing the power of the driven winds which scales with $P_w \propto M^{4.5}$. This power can be even $\sim 1\%$ of the bolometric luminosity of the star. Winds create strong shocks in the surrounding cloud. These shocks can heat the gas

to temperatures of up to $\sim 10^8$ K and cause strong X-ray emission. Close to the end of the star's main-sequence lifetime the mass loss rate can increase by even one order of magnitude. This is due to the sudden, large enrichment of the atmosphere with metals produced in the final stages of the fusion processes and mixed into the outer layers of the star. For the first Myr the wind expands inside the H II region because of the slower expansion velocity. While expanding it sweeps up the previously shocked material into a shell. When the shell has accumulated enough material the fast wind expansion is halted. Then the thermal expansion of the material inside the wind shell starts with typical velocities of $\sim 10 \text{ km s}^{-1}$. After a few Myr the expansion of the wind shell will overtake that of the H II region. Therefore, the entire system will become a wind-driven bubble. Further reading about stellar winds can be found e.g. in Conti et al. (2008).

- **Supernovae:** Stars above $\sim 8 M_{\odot}$ may explode as a Type-II supernova (SN). Such an explosion injects an energy of $\sim 10^{51}$ erg into the surrounding ISM. This is approximately the same amount of energy that the star produces through UV radiation and winds during its entire lifetime. At the beginning during the very short (~ 100 yr) free-expansion phase the SN ejecta move with velocities of several thousand km s^{-1} sweeping up material by colliding with the slower wind ejecta. In this phase the SN shock wave travels roughly 1 pc. When the mass of the swept-up material becomes comparable to the ejecta mass, the shock wave is slowed down and the adiabatic expansion phase starts. This phase is called the Sedov-Taylor phase and lasts for several $\sim 10^4$ yr. After that the longest expansion phase starts. It is the so-called snow-plow phase which is mainly momentum driven and lasts for about 1 Myr. The cooling timescale of the shocked gas inside the shell becomes smaller than the expansion timescale and the adiabaticity is broken. Radiation losses become substantial and the expansion velocity is further decreased. The SN now plows through the ambient ISM. Finally, the shell breaks up into individual pieces and the expansion velocity becomes subsonic. A review on blastwaves can be found in Ostriker & McKee (1988).

The above mentioned feedback effects are described for a single star only. However, almost all stars form in clusters. Thus, the feedback effects of the massive stars will combine and affect each other which is in detail not yet well understood. But this combined feedback is capable of driving very large supershells with radii of several ten to hundred parsecs. As a consequence these shells effectively destroy the natal molecular cloud of the cluster and stop further star formation. On the other hand, they can also trigger the formation of new molecular clouds and star formation within. The newly swept-up material is compressed, can cool, becomes molecular, and starts to form stars as has been described in Section 1.2. A prototype region to study such effects is the Scorpius-Centaurus region which will be introduced in the following section.

1.7 The Scorpius-Centaurus region

The Scorpius-Centaurus OB association (Sco-Cen Blaauw 1964; Preibisch et al. 1998; de Zeeuw et al. 1999; Preibisch et al. 2002) is the closest site of recent massive star formation to us and it consists of three subgroups with different ages and well-known stellar populations down to $2 M_{\odot}$ (de Bruijne 1999). An overview can be found in Preibisch & Mamajek (2008). The oldest one is the Upper Centaurus-Lupus (UCL) subgroup with an age of ~ 17 Myr harboring 66 B-stars. With an age of ~ 15 Myr the Lower Centaurus Crux (LCC) subgroup is somewhat younger and contains 42 B-stars. The youngest subgroup is Upper-Scorpius (USco) with an age of ~ 5 Myr and consisting of 49 B-stars. An optical and sub-mm image of the Sco-Cen region is shown in Figure 1.6.

The feedback of the numerous massive stars in Sco-Cen probably cleared the inner region of the association from diffuse matter creating expanding loop-like HI shells around each of the subgroups of the association (de Geus 1992). At the edge of the USco shell several dense molecular clouds with very young ($\leq 1-2$ Myr) stellar populations are found. Of those the most prominent ones are the Lupus I cloud (near the Galactic western edge of the shell) and the ρ Oph cloud (near the Galactic eastern edge). The formation of the subgroups as well as that of Lupus I and ρ Ophiuchus are closely related to each other. Preibisch & Zinnecker (2007) proposed a sequential formation scenario which will be discussed in Chapter 6.1 in context of Lupus I.

The scope of the project "Deciphering the ISM around the Sco-Cen OB-association" (Krause et al. 2016, in preparation), of which this work is part of, is to characterize the ISM in Sco-Cen, shed light on its formation history, and analyze the effects of combined stellar feedback. For this purpose, multi-wavelength observations are compared to numerical simulations. Numerous observational data are available, i.e. on large scales that cover the entire complex. Each wavelength regime gives the opportunity to study different physical processes at work. The atomic medium can be traced with HI radio observations of the GASS survey (McClure-Griffiths et al. 2009; Kalberla et al. 2010). The dust emission was observed by the *Planck* satellite that scanned the entire sky in nine different wavelengths between $350 \mu\text{m}$ – 10 mm . From those *Planck* surveys, all-sky CO distribution maps were inferred that revealed the large-scale distribution of molecular material in Sco-Cen. From optical and near-infrared images (see e.g. Figure 1.6) the stellar population was determined. The massive stellar feedback can be traced by X-ray observations performed with ROSAT (traces shocked and ionized gas inside USco shell and shocks of wind-blown bubble from UCL; Trümper et al. 1991), $\text{H}\alpha$ emission of the SHASS survey (traces the hydrogen gas of e.g. USco; Gaustad et al. 2001), and γ -ray data from the INTEGRAL satellite (traces e.g. the radioactive ejecta of the SN that exploded in USco; Winkler et al. 2003). This allows a determination of physical properties like density, temperature or ionization degree, for the different components of the ISM interacting with each other in a complex manner. These observational results can then be used to set up hydrodynamical simulations that will help to distinguish and narrow down possible formation scenarios of the Sco-Cen subgroups.

In this work, however, I focus on observations of the immediate surroundings of the Lupus I cloud and analyze the distribution of dust, atomic hydrogen, and molecular CO (see Chapter 6.1).

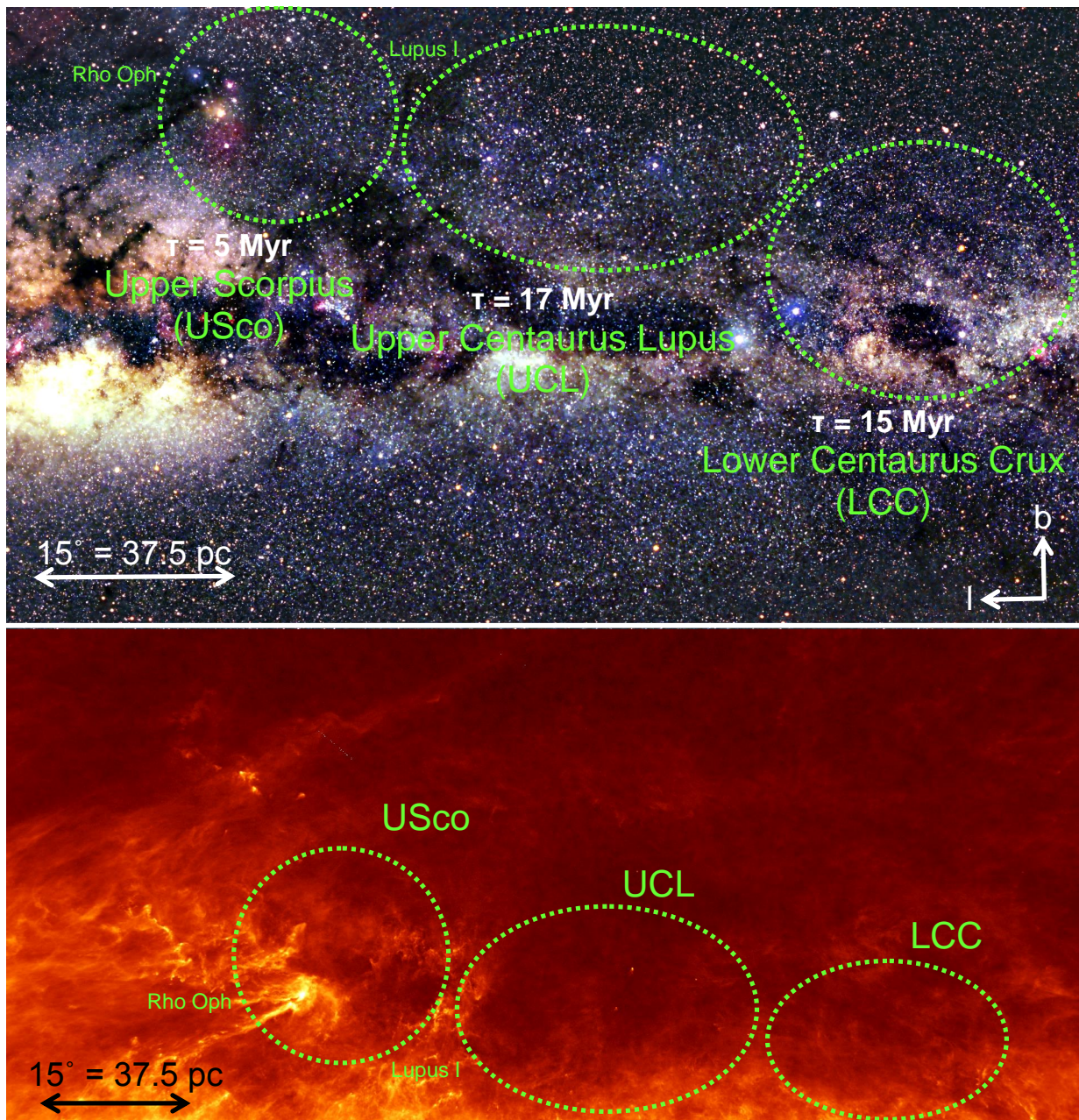


Figure 1.6: *Top*: Optical image of the Sco-Cen region. The approximate positions of the three stellar subgroups are marked with green ellipses. Below each ellipse the name and age of the corresponding subgroup is given. *Credit: Axel Mellinger (image adapted from Mellinger (2008))*. *Bottom*: The Sco-Cen region seen in dust emission by *Planck* at $850\ \mu\text{m}$.

1.8 The Lupus I molecular cloud

The Lupus I molecular cloud complex (for an overview see Comerón 2008) is found at a distance of 150 pc and consists of a $\approx 2.6^\circ \times 0.6^\circ$ (corresponds to a physical size of $\approx 6.8 \times 1.6$ pc) main filament extending in a north to south direction (Galactic coordinates) and a ring-like structure of $\sim 0.6^\circ$ in diameter west of the main filament (towards UCL; see Tothill et al. 2009, and overview in Figure 1.7). Recently Matthews et al. (2014) also noted two smaller secondary filaments one of which is about half a degree long and runs perpendicular to the main filament and seems to connect with it in the south. The other is about a degree long and lies southwest of the main filament extending from the southern end of the main filament to the ring-like structure. In this work, I concentrate my analysis on the main filament commonly seen in all analyzed observations of Lupus I. I refer to it as Lupus I or the Lupus I filament. An overview of the cloud where the before mentioned regions are marked is shown in Figure 1.7. The cloud is found between the USco and the UCL subgroups at a location where the expanding USco shell appears to interact with a bubble currently powered by the winds of the remaining B-stars of UCL. Because it is close, Lupus I is a good candidate to study how such a collision process may form and influence new dense clouds in the ISM.

Lupus I has been mapped as part of several large surveys like the *Herschel* Gould-belt survey (André et al. 2010; Rygl et al. 2013; Benedettini et al. 2015) and the *Spitzer* Legacy Program ‘From molecular clouds to planet-forming disks’ (c2d; Chapman et al. 2007; Merín et al. 2008). These near-infrared to far-infrared surveys revealed the population of YSOs within the cloud showing that it is dominated by pre-stellar and protostellar cores indicating an on-going star formation event. Rygl et al. (2013) found that the SFR has been increasing over the past 0.5–1.5 Myr and Merín et al. (2008) estimated a SFR of $4.3 M_\odot \text{ Myr}^{-1}$ for Lupus I from their *Spitzer* data. Benedettini et al. (2015) have studied the filamentary sub-structure of Lupus I. They identified sub-filaments from their *Herschel* column density maps and CS(2–1) observations. They found that most of the sub-filaments are gravitationally unbound although they harbor a large population of pre- and protostellar cores.

Extinction maps of Lupus I have been created by various authors using different methods. Cambrésy (1999) created an extinction map based on optical star counts with a resolution of a few arc-minutes. Using 2MASS data Chapman et al. (2007) created a visual extinction map with a $2'$ resolution. Lombardi et al. (2008a) also used 2MASS data for a wide-field extinction map of Lupus I. It allowed extinction measurements down to $A_K = 0.05$ mag, but had a resolution of $3'$. Merín et al. (2008) created extinction maps from their *Spitzer* data by estimating the visual extinction towards each source classified as a background star, based on their SED from 1.25 to $24 \mu\text{m}$. Their maps had a resolution of $2'–5'$. Rygl et al. (2013) and Benedettini et al. (2015) created a column density map of dust emission in Lupus I from the *Herschel* data by making a modified blackbody fit for each pixel in the four bands from 160– $500 \mu\text{m}$. The resulting resolution was $36''$ in both cases.

Molecular line observations with different CO isotopes and other high-density tracers have been performed by several groups over the past two decades. Most of them have spatial resolutions of only several arcminutes. Tachihara et al. (1996) observed the entire Lupus I cloud in the $^{13}\text{CO}(1-0)$ line with the 4 m telescope at Nagoya University. Their observations have a HPBW of $2.7'$ and they chose a grid spacing of $8'$. They estimated the cloud mass to be $\sim 1200 M_{\odot}$ and discovered the molecular outflow of IRAS source 15398–3359. Hara et al. (1999) have studied twelve cores in Lupus I in the $\text{C}^{18}\text{O}(1-0)$ line. The HPBW of the NANTEN telescope is $2.7'$ and their grid spacing was $2'$. They derive column densities, temperatures, and sizes for the cores and estimate their total mass to be $152 M_{\odot}$ which represents 46% of their total $\text{C}^{18}\text{O}(1-0)$ emitting gas mass. Vilas-Boas et al. (2000) found 15/14 condensations in $\text{C}^{18}\text{O}(1-0)/^{13}\text{CO}(1-0)$ with the 15 m Swedish-ESO Submillimeter telescope (SEST). Their angular resolution was $48''$. They conclude recent star formation activity in the cloud. A large-scale $^{12}\text{CO}(1-0)$ survey of Lupus I has been performed by Tachihara et al. (2001). They mapped the cloud with a grid-spacing of $8'$ and a HPBW of $2.7'$ with NANTEN. They report a velocity gradient along the long axis of Lupus I from 4 km s^{-1} in the south to 6 km s^{-1} in the north. Tothill et al. (2009) analyzed Lupus I in both $\text{CO}(4-3)$ and $^{13}\text{CO}(2-1)$. They used the Antarctic Submillimeter Telescope and Remote Observatory (AST/RO) that allowed an angular resolution of $1.7'$ (CO) and $3.3'$ (^{13}CO), respectively. They found several possible signs of interaction between Lupus I and the USco HI shell. Benedettini et al. (2012) found eight dense cores in Lupus I using high-density molecular tracers at 3 and 12 mm with the Mopra telescope. They report the presence of velocity gradients in the cloud and several velocity components along the line-of-sight. Finally, Benedettini et al. (2015) have observed the southern part of the main filament in $\text{CS}(2-1)$ and found several sub-filaments in velocity space that correspond to sub-filaments they have identified in their *Herschel* column density maps.

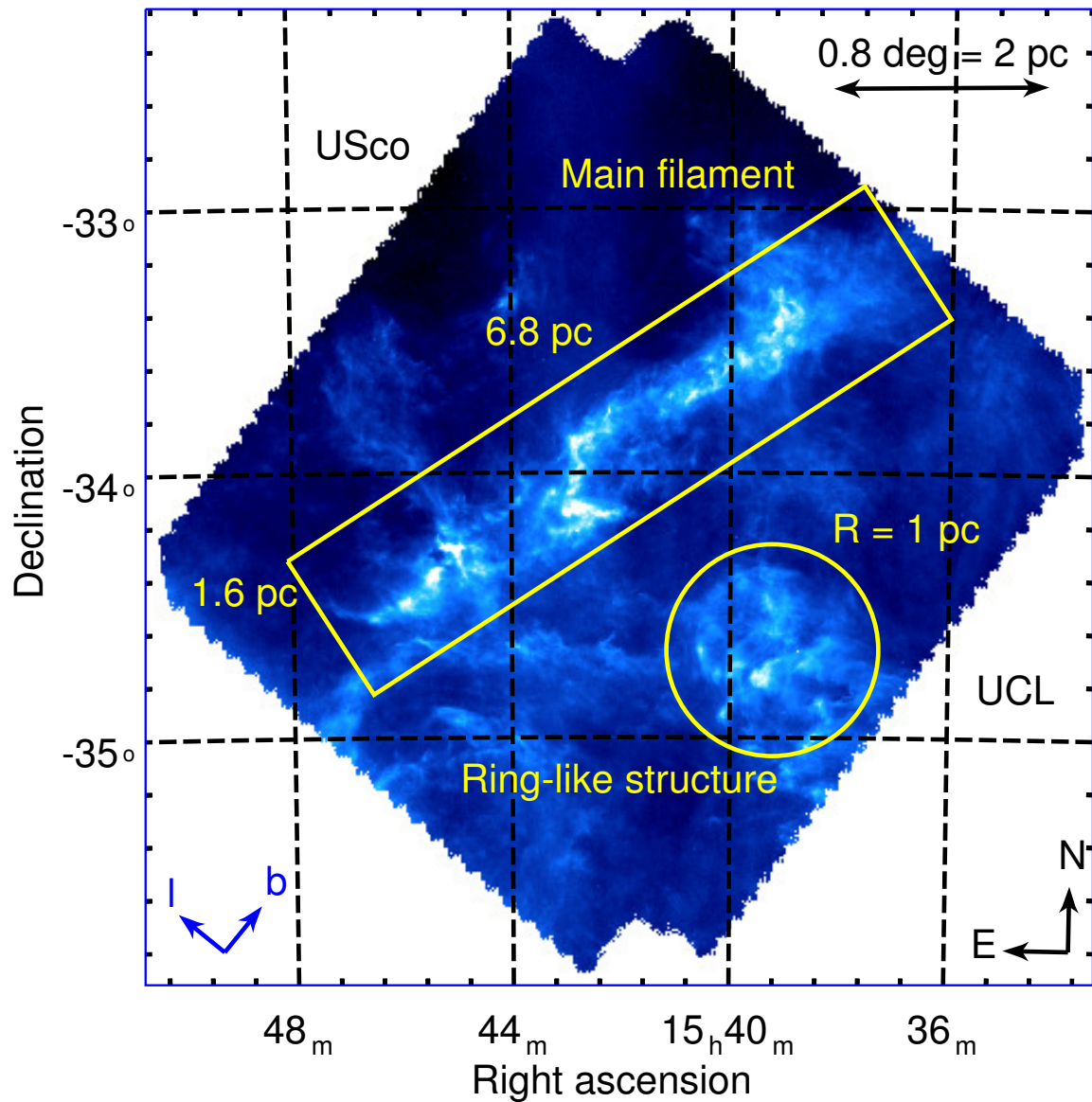


Figure 1.7: Overview of the Lupus I cloud. The black compass in the lower right corner is in Celestial coordinates (J2000), the blue one in the lower left corner in Galactic coordinates. The yellow box marks the main filament of Lupus I and its approximate size; the ring-like structure to the south-west and its radius is marked by the yellow circle. The direction towards USco and UCL is indicated by the black labels in the top left and bottom right corner of the map, respectively. The Background image is the *Herschel* 250 μm map.

Chapter 2

Far-infrared to millimeter astronomy

The far-infrared to radio part of the electromagnetic spectrum is of great importance for observations of the ISM, molecular clouds, and star formation. Many of the involved processes happen in dense and cold environments opaque to radiation of shorter wavelengths. Moreover, typical temperatures in the ISM and molecular clouds are on the order of 10–100 K and thus the corresponding black body radiation peaks between $\approx 300\text{--}30\ \mu\text{m}$. In addition, emission lines of typical tracer molecules for molecular clouds like CO are in the millimeter and sub-mm wavelength regime. Observations from Earth are mostly limited by the Earth's atmosphere which only has a few windows where it is transparent to the incoming radiation (see Figure 2.1). This is mainly due to the water vapor in the atmosphere. Hence, radio telescopes observing below the centimeter window are found on very high sites, like the Atacama desert in Chile (see left panel of Figure 2.2) which is more than 5000 m above sea level (telescopes found there are the Atacama Pathfinder Experiment APEX, the Atacama Large Millimeter Array ALMA, and NANTEN2) or Mount Mauna Kea on Hawaii which is more than 4000 m above sea level (James Clerk Maxwell Telescope JCMT, Caltech Submillimeter Observatory CSO). To further reduce influences of the atmosphere one can either use an aircraft (Stratospheric Observatory for Infrared Astronomy SOFIA) or balloons (Stratospheric TeraHertz Observatory STO). Finally, all atmospheric disturbances can be eliminated by observing with satellites like the *Herschel* or *Planck* space observatories. Both were launched in 2009 and their missions ended in 2013 when the amount of cooling helium was exhausted. Especially *Herschel* had and still has substantial influence on our knowledge about the ISM, and molecular and star formation.

2.1 Radio telescopes

The most common type of telescopes used in radio astronomy is the single-dish telescope. The one used to for this work is the APEX telescope in the Atacama desert in Chile (Güsten et al. 2006). The technical background of radio telescopes is very complex and an extensive description can be found in (Wilson et al. 2009). Here, I only point out the most important aspects.

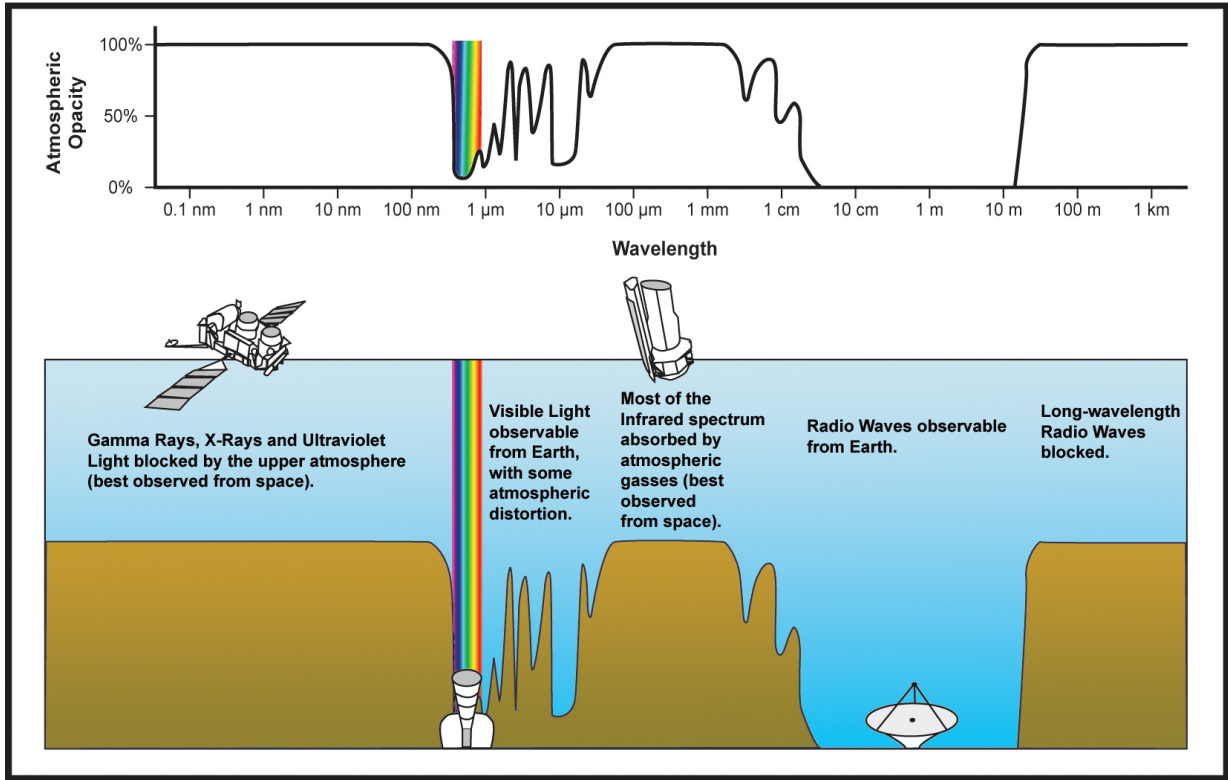


Figure 2.1: Transmission of Earth's atmosphere in dependence on the wavelength of the incoming radiation. *Credit: NASA/IPAC*

A single-dish telescope usually consists of a large antenna (parabolic dish or mirror) which collects the incoming radiation and focuses it into the secondary mirror which then reflects the radiation into the receiver. APEX has a parabolic primary reflector of 12 m in diameter which is composed of 264 single aluminum panels (see right panel of Figure 2.2). The secondary reflector has a diameter of 75 cm and is mounted in the focal point of the primary. For this work two types of receivers have been used:

- **Bolometer:** This receiver type is typically used for continuum observations over a large wavelength range. It basically consists of an absorber coupled to a heat sink of fixed temperature. Incoming photons will be absorbed causing the absorber to heat up. This change in temperature is measured and used to calculate the energy of the absorbed photon. Bolometers are very sensitive to the total power of incoming radiation but do not provide any spectral or polarization information. For this work I used the LARge APEX BOLometer CAMERA (LABOCA, Siringo et al. 2009) to measure the $870\ \mu\text{m}$ dust continuum radiation of Lupus I. Also the two imaging cameras of *Herschel*, PACS and SPIRE, are bolometers operating in the far-infrared. I used their continuum measurements between $70\text{--}500\ \mu\text{m}$ to construct a dust column density map of Lupus I. Details about those observations will be described in the following chapters.

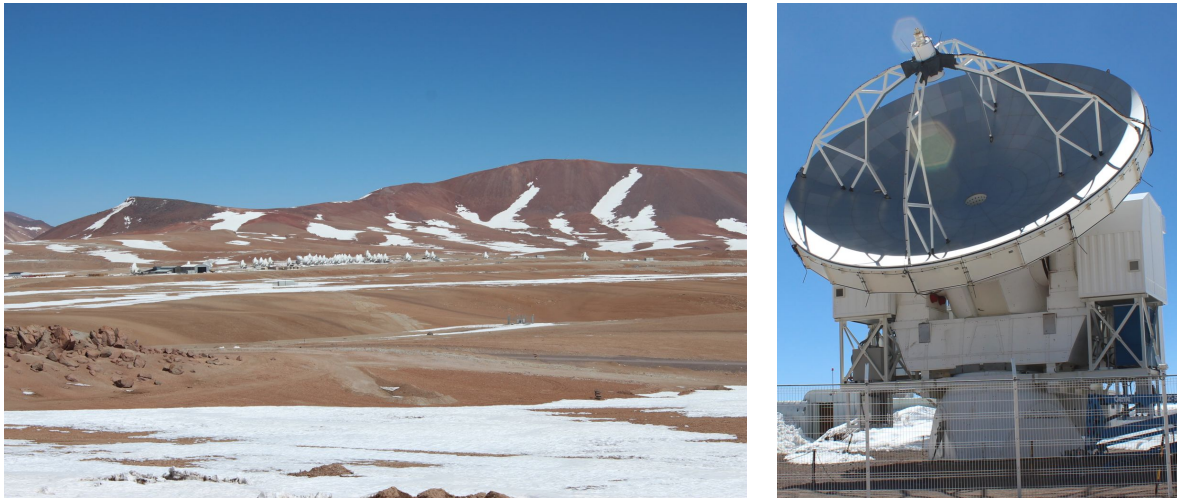


Figure 2.2: *Left:* The Llano de Chajnantor plateau in the Atacama desert about 50 km east of San Pedro de Atacama in northern Chile. The telescopes are part of ALMA. *Right:* The APEX telescope at 5105 m in the Chilean desert. The primary reflector is composed of 264 aluminum panels and the small (75 cm) secondary reflector is mounted in the focal point of the primary. The whole construction weighs about 125 t.

- Heterodyne receiver:** This type of receiver is used to obtain high resolution spectra. It usually consists of a frontend and a backend. The frontend is a mixer that first amplifies and then shifts the incoming high-frequency sky signal (a few hundred GHz) to a lower frequency signal by mixing it with a sine-wave of a local oscillator (LO). This conserves all astronomical information of the original signal but makes it easier to further amplify and filter the signal. On the contrary, homodyne receivers that do not mix the sky signal are prone to leakage of the amplified signal back into the original one. Mixers are typically Superconductor-Insulator-Superconductor (SIS) compositions. The converted signal then goes into the backend which is a spectrometer. Usually, it is a Fourier-transform spectrometer (FTS) that transforms the time-dependent input signal into a spectrum through a Fourier transformation. For this work I used the APEX-1 receiver of the Swedish Heterodyne Facility Instrument (SHeFI; Vassilev et al. 2008) that operates in the 230 GHz band.

2.1.1 Observing methods

The sensitivity of observations with radio telescopes is determined by the total observing time (for spectroscopic observations also by the desired spectral resolution) and both the telescope itself and atmospheric factors (measured as the perceptible water vapor (PWV) in the atmosphere). The influence of all radiation emitting sources that are not the observed source but rather the telescope and its components, is expressed by the system's noise temperature T_{sys} . As observing times might even be as long as a few hours the whole system should be kept as stable as possible throughout that time. However, in reality the

thermal emission of the telescope and the surroundings as well as atmospheric changes happen on timescales of several minutes. Therefore, observations must be divided into individual parts to assure the best stability of the system. In between those parts, focus and calibration measurements on well known and bright calibrators (usually planets) are carried out. During the observations, switching methods are used to account for the instabilities. After measuring the desired source on the sky (On-position), the telescope switches to an Off-position which is supposed to be free of emission. Then those two measurements are subtracted to minimize instabilities. There are two important observing modes:

- **On-Off observations:** Hereby, just one single position on the sky is observed. First, the source is observed at the On-position and then only the telescope beam is switched to the Off-position by moving the secondary mirror. This method is suitable if On- and Off-position have a small angular distance to each other.
- **On-the-fly (OTF) observations:** Here, the telescope scans the sky at a constant speed according to a chosen pattern (e.g. spiral or linear). Each scan consists of several legs. After one or two legs the whole telescope moves to an Off-position before beginning the next leg. Thus, several legs typically share one Off-position. To achieve a better coverage and reduce noise as well as striping effects, the scans may be performed perpendicular to each other. This method is efficient for observing large sources and was used in this work to obtain both the continuum and the spectral line observations of Lupus I.

2.1.2 Antenna properties

The beam or power pattern of a telescope is the Fourier transform of the telescope's aperture. It depends on the geometry of telescope. For APEX which has a parabolic primary, the beam pattern is mostly a Gaussian convolved with the primary's disk. The resulting function has one main, strong, and Gaussian shaped maximum and several significantly lower side maxima or side lobes. This main maximum is called main beam. In radio astronomy it is common to define the half power beam width (HPBW) or full width to half power (FWHP) as

$$\Theta_{\text{HPBW}} = 1.03 \frac{\lambda}{D} \quad (2.1)$$

with λ the wavelength of the measured radiation and D the diameter of the primary. It is the angle (in radians) between points of the main beam where the beam pattern equals half of the maximum. In analogy to optical telescopes this also is the angular resolution of the telescope as long as $\lambda \ll D$.

2.2 Radiative transfer

All observations are based on the detection of radiation. Hence, it is important to understand what happens to the radiation during its way from the emitting source to us

observers. The fundamental equation that describes this behavior is called the equation of transfer

$$dI_\nu = \epsilon_\nu ds - I_\nu \kappa_\nu ds \quad (2.2)$$

In empty space the specific intensity I_ν would be constant along the line-of-sight. However, there is a medium between the observer and the emitting source and thus the specific intensity changes along its path ds . This can either be due to absorption - described by the absorption coefficient κ_ν - or due to emission - described by the emission coefficient ϵ_ν - of the medium. For this work two emission mechanisms are relevant: continuum emission and molecular line emission. By defining the optical depth $d\tau_\nu = \kappa_\nu ds$ and the source function $S_\nu = \epsilon_\nu/\kappa_\nu$ one can rewrite the equation of transfer to

$$\frac{dI_\nu}{d\tau_\nu} = -I_\nu + S_\nu \quad (2.3)$$

A medium is called optically thin if $\tau_\nu \ll 1$. Then one is able to completely look through it. If, on the other hand, a medium is optically thick, then $\tau_\nu \gg 1$ and the emitted radiation is absorbed again within the medium. In this case, only the outermost layer is observed. The equation of transfer is in general very complicated to solve because both I_ν and S_ν have to be known and usually depend on each other. However, under the assumption of a constant source function, i.e. a homogeneous medium with constant emission and absorption coefficient, there exists the analytic solution

$$I_\nu = I_0 \exp(-\tau_\nu) + S[1 - \exp(-\tau_\nu)] \quad (2.4)$$

where I_0 is the incoming external intensity that is attenuated inside the medium. The second term describes the emission of the medium itself. The most important example for a constant source function is a homogenous blackbody. In this case the source function can be replaced by Planck's law $S = B_\nu(T)$.

2.2.1 Blackbody radiation

The spectral distribution of the radiation of a blackbody of temperature T is given by the Planck law

$$B_\nu(T) = \frac{2h\nu^3}{c^2} \left[\exp\left(\frac{h\nu}{k_B T}\right) - 1 \right]^{-1} \quad (2.5)$$

where ν is the considered frequency, h the Planck constant, c the speed of light, and k_B the Boltzmann constant. This can be converted into the wavelength scale through the relation

$$B_\nu(T) d\nu = -B_\lambda(T) d\lambda \quad (2.6)$$

and $d\nu = -(c/\lambda^2)d\lambda$. The total brightness of the blackbody is obtained by integrating over all frequencies

$$B(T) = \int_0^\infty B_\nu(T) d\nu = \sigma T^4 \quad (2.7)$$

with σ the Stefan-Boltzmann constant. The wavelength of the peak intensity is given by Wien's displacement law

$$\lambda_{\max} = \frac{2897.8 \mu\text{m K}}{T} \quad (2.8)$$

For a set of relevant temperatures for this work Table 2.1 lists the wavelengths of the corresponding blackbody peaks. There are two important approximations of the Planck

Table 2.1: Peak of the blackbody spectrum for different temperatures.

T [K]	λ_{\max} μm
10	290
12	241
15	193
18	161
20	145
25	116

law. For $h\nu \gg k_B T$ the Planck function turns into Wien's law which is useful for stellar measurements in the optical and UV, but plays no role in radio astronomy (Wilson et al. 2009). The second approximation plays a crucial role in radio astronomy and is called the Rayleigh-Jeans law

$$B_{\nu,\text{RJ}}(T) = \frac{2\nu^2 k_B T}{c^2} \leftrightarrow B_{\lambda,\text{RJ}}(T) = \frac{2c k_B T}{\lambda^4} \quad (2.9)$$

It is valid for $h\nu \ll k_B T$ and holds for frequencies or wavelengths

$$\frac{\nu}{\text{GHz}} \ll 21 \left(\frac{T}{\text{K}} \right) \leftrightarrow \frac{\lambda}{\text{cm}} \gg 0.7 \left(\frac{T}{\text{K}} \right) \quad (2.10)$$

Using the Rayleigh-Jeans law one can introduce the very common concept in radio astronomy of brightness temperature as a measure for observed intensities (see Section 2.2.3).

2.2.2 Local Thermodynamical Equilibrium conditions

A gas or radiation field in thermodynamical equilibrium can be described by the following characteristic physical quantities:

1. The velocities of the particles are given by the Maxwell-Boltzmann distribution:

$$f(v) \propto v^2 \exp[-v^2/(k_B T_{\text{kin}})] (k_B T_{\text{kin}})^{-3/2} \quad (2.11)$$

where T_{kin} is the kinetic temperature.

2. The population F_i of an energy level i is given by the Boltzmann distribution:

$$F_i \propto \exp(-E_i/k_B T_{\text{ex}}) \quad (2.12)$$

where E_i is the level's energy and T_{ex} is the excitation temperature. For a two-level system with an upper level u and a lower level l the population of the two levels is given by the ratio

$$\frac{n_u}{n_l} = \frac{g_u}{g_l} \exp\left(-\frac{h\Delta E_{ul}}{k_B T_{\text{ex}}}\right) \quad (2.13)$$

with n_i the number density and g_i the statistical weight of level i .

3. The spectral energy distribution of the emitted radiation follows Planck's law:

$$B_\nu(T_{\text{rad}}) \propto \nu^3 \{\exp[-\nu/(k_B T_{\text{rad}})] - 1\}^{-1} \quad (2.14)$$

where T_{rad} is the temperature of the radiation.

In thermodynamical equilibrium all three above mentioned temperatures are equal and the gas can be described by one single thermodynamical temperature $T = T_{\text{kin}} = T_{\text{ex}} = T_{\text{rad}}$. In general, the assumption of (global) thermodynamical equilibrium for a system will not hold. But it can often be applied for small enough volumes where temperatures and densities are near constant. This is then called local thermodynamical equilibrium (LTE). In this work LTE conditions will be used in the analysis of molecular line emission from a molecular cloud (see Chapter 5).

In LTE conditions Kirchhoff's law states that the source function follows Planck's law $S_\nu = \epsilon_\nu/\kappa_\nu = B_\nu(T)$ (see Wilson et al. 2009). Then Equation 2.4 can be written as

$$I_\nu = B_\nu(T_{\text{ex}})[1 - \exp(-\tau_\nu)] + I_\nu^{\text{bg}} \exp(-\tau_\nu) \quad (2.15)$$

where I_ν^{bg} is the intensity of the background radiation. Usually, molecular line emission observations are done by measuring first the intensity I_{on} on the target and then the intensity I_{off} at a position off the target where no molecule emission is expected. Then those two intensities are subtracted from each other what yields with Equation 2.15

$$\Delta I_\nu = I_{\text{on}} - I_{\text{off}} = I_\nu - I_\nu^{\text{bg}} = [B_\nu(T_{\text{ex}}) - I_\nu^{\text{bg}}][1 - \exp(-\tau_\nu)] \quad (2.16)$$

2.2.3 Brightness and antenna temperature

In the Rayleigh-Jeans approximation for long wavelengths ($h\nu \ll k_B T$) the blackbody radiation becomes directly proportional to the temperature and Planck's law becomes the Rayleigh-Jeans law (Equation 2.9). For the millimeter and sub-millimeter range one defines an effective source radiation temperature $J(\nu, T_{\text{rad}})$ by

$$J(T) \equiv \frac{c^2}{2k_B\nu^2} B_\nu(T) = \frac{h\nu}{k_B} [\exp(h\nu/k_B T) - 1]^{-1} \quad (2.17)$$

assuming the source is a blackbody of temperature T_{rad} . In the literature $J(\nu, T_{\text{rad}})$ is also called the radiation temperature T_R for the source (Kutner & Ulich 1981). This is not to be confused with the temperature of the radiation T_{rad} emitted by a blackbody.

Even if the emitting source is not a blackbody, i.e. $I_\nu \neq B_\nu$, it is common in radio astronomy to express the intensity I_ν of a source as the so-called brightness temperature T_B which can be obtained using Equation 2.9

$$T_B = \frac{c^2}{2k_B\nu^2} I_\nu = \frac{\lambda^2}{2k_B} I_\nu \quad (2.18)$$

It is the temperature that would yield the measured intensity if inserted into the Rayleigh-Jeans law (see Wilson et al. 2009). The brightness temperature is in general dependent on the frequency ν . Only if the emitting source is a blackbody and then only in the Rayleigh-Jeans limit T_B will be independent of ν and equal to the thermodynamical temperature of the source. Introducing the concept of brightness temperature into Equation 2.16 yields

$$T_B = [J(T_{\text{ex}}) - J(T_{\text{bg}})][1 - \exp(-\tau_\nu)] \quad (2.19)$$

The antenna temperature T_A is defined through the temperature of a resistor in the antenna's receiver. This temperature is proportional to the received spectral power P_ν from the source

$$P_\nu = k_B T_A \quad (2.20)$$

The antenna temperature can be converted into a main-beam temperature T_{mb} dividing by the main-beam efficiency η_{mb} of the telescope

$$T_{\text{mb}} = T_A / \eta_{\text{mb}} \quad (2.21)$$

The main-beam temperature can then be related to the brightness temperature T_B of the observed source via the beam-filling factor f_{beam}

$$T_{\text{mb}} = f_{\text{beam}} T_B \quad (2.22)$$

The beam-filling factor corrects for the geometry of the telescope's beam and the brightness distribution of the source. An extended cloud that fills the entire telescope beam has $f_{\text{beam}} = 1$ and thus $T_{\text{mb}} = T_B$. The spectra analyzed in this work have an intensity scale given in main-beam temperature T_{mb} . The assumption of $f_{\text{beam}} = 1$ will be made for the LTE analysis of the CO spectra presented in this work (see Chapter 5) such that T_{mb} is equal to the brightness temperature of the source. However, it is a simplification that in general is not accurate for molecular clouds since they are structured on small scales. Therefore, a beam filling factor of less than one might be more accurate.

2.2.4 Continuum emission

For this work, the important source of continuum emission is interstellar dust. Dust grains preferentially absorb UV photons, e.g. coming from a protostar which is embedded in a dust cloud, causing them to heat up. Then the hot grain re-emits the absorbed energy as thermal continuum radiation in the far-infrared and sub-mm regime. Dust is optically thin to its own thermal radiation and hence equation 2.15 simplifies to

$$I_\nu = B_\nu(T) \tau_\nu \quad (2.23)$$

However, dust grains are actually not perfect blackbodies and have strongly frequency dependent emission. Instead, they are often modeled as a modified blackbody (or greybody)

$$I_\nu = B_\nu(T) \Sigma \kappa_0 \left(\frac{\nu}{\nu_0} \right)^\beta \quad (2.24)$$

where Σ is the surface density and $\kappa_\nu = \kappa_0(\nu/\nu_0)^\beta$ is the specific absorption coefficient (per mass) or dust opacity. It is related to the optical depth via

$$\tau_\nu = \int \kappa_\nu \rho \, ds \quad (2.25)$$

with ρ the density of the gas. In general the dust opacity depends on the geometry of the dust grains, e.g. their size and surface. As one observes not just single dust grains, a certain average dust opacity determined by the dust composition has to be assumed. Hence, there are many different theoretical dust models found in the literature for which dust opacities are tabulated for a variety of conditions and grain properties. In this work, I use the models of Ossenkopf & Henning (1994).

Modeling the dust emission as a modified blackbody allows to determine the dust temperature and mass from far-infrared and sub-mm observations. Knowing the emitted intensity I_ν in several bands (e.g. the five *Herschel* bands), one can fit the modified blackbody curve to those data points and determine the dust temperature and mass from the fit. This procedure will be described in more detail in Section 4.1.1.

2.3 Molecular spectroscopy

Molecules are the main constituent of molecular clouds and therefore play an important role in the context of cloud and star formation. Their emission often dominates the cooling of molecular clouds and is a key diagnostic tool for the observations of molecular clouds because it allows an insight view of the physical conditions in the cloud.

The total energy of a molecule is given by

$$E_{\text{tot}} = E_{\text{el}} + E_{\text{rot}} + E_{\text{vib}} \quad (2.26)$$

with E_{el} the energy of the electronic states, E_{rot} its rotational, and E_{vib} its vibrational energy. Transitions in the molecule between electronic, rotational, and vibrational states occur at three different wavelength regimes (Wilson et al. 2009):

- Electronic transitions have the highest energies of a few eV corresponding to optical or UV wavelengths and thus temperatures $T = E/k_B$ of $> 10^4$ K.
- Vibrational transitions have energies of $\approx 0.1\text{--}0.01$ eV corresponding to IR wavelengths or temperatures of a few hundred Kelvin.
- Rotational transitions have the lowest energies of $\approx 10^{-3}$ eV corresponding to sub-mm and radio wavelengths or temperatures of $\approx 10\text{--}20$ K.

In cold molecular clouds, like the here analyzed Lupus I, with typical temperatures of 10–100 K most molecules will only be rotationally excited. To excite rotational dipole transitions the molecule cannot be symmetric. If it is, then the center of mass coincides with the center of electric charge and thus the molecule has no permanent dipole moment μ and will not emit dipole radiation (Schulz 2005). However, rotational quadrupole emission is still possible, but requires higher excitation temperatures. Molecular hydrogen H_2 is the most prominent example. It is the by far most abundant molecule in the Galaxy, but hardly to observe at typical molecular cloud temperatures. Hence, the important molecule for observations is carbon-monoxide $^{12}\text{C}^{16}\text{O}$ or just CO and its isotopologues. It is asymmetric, the second most abundant molecule in the ISM with an abundance of $N_{\text{CO}} = 10^{-4} N_{\text{H}_2}$, and easily excited at low temperatures. CO can be described as a rigid di-atomic rotator with rotational energy levels given by

$$E_{\text{rot}} = \frac{h^2}{8\pi^2 I} J(J+1) = hB_{\text{rot}} J(J+1) \quad (2.27)$$

where $B_{\text{rot}} = h/(8\pi^2 I)$ is the rotational constant, I the moment of inertia with respect to the rotation axis, and $J = 0, 1, 2, \dots$ the rotational quantum number. Rigid rotator means that both atoms have a fixed distance to each other. This is in general not the case because the distance increases with rotational frequency due to centrifugal forces. Therefore, the observed transition frequencies are actually lower than those from the rigid rotator model. However, this difference is negligible for the $J = 2 \rightarrow 1$ transition considered in this work and for low- J transitions in general.

The rotational energy levels depend on the moment of inertia and I depends on the mass of the two atoms involved. This fact is very profitable for observations because it means that the rotational energy levels of different isotopologues of the same molecule are distinct from each other. Hence, they will show different transition frequencies for the same transition ΔJ and the observer is able to distinguish between the isotopologues. In my work I make use of the $^{13}\text{CO}(2-1)$ and $\text{C}^{18}\text{O}(2-1)$ molecule. Their $J = 2 \rightarrow 1$ transition rest frequencies differ by 0.838320 GHz.

The selection rules for electrical dipole radiation generally imply $\Delta J = 0, \pm 1$ (Schulz 2005). Thus, the difference of neighboring rotational energy levels is given by

$$\Delta E_{\text{rot}} = h\Delta\nu = 2hB_{\text{rot}} J \quad (2.28)$$

for $\Delta J = \pm 1$ and with $\Delta\nu$ the observed transition frequency.

There exist several spectral line catalogs, as well as molecule databases where one can find transition frequencies, constants, and spectra. Here, I would like to mention those I used for my work. Foremost, there is the "Cologne Database for Molecular Spectroscopy"¹ (Müller et al. 2001, 2005) and the "Jet Propulsion Laboratory catalog"² (JPL catalog; Pickett et al. 1998). Both are part of the "Virtual Atomic and Molecular Data Centre"³ (Walton et al. 2011) which is a very large and useful database of various atomic and molecular catalogs.

2.3.1 Molecular excitation

Molecules can be excited either through the absorption of photons or collisions with other molecules. The de-excitation of a molecule will then proceed either through a collision or the molecule will spontaneously (or induced) emit a photon of frequency $\Delta\nu = \Delta E/h$ which corresponds to the energy difference between the two states. The latter mechanism is the one producing the observable spectral line. The intensity or strength of this line will depend on the gas density, i.e. the balance of excitation and de-excitation rates. In a two-level system with an upper level u and a lower level l and under LTE conditions these rates are related through the principle of detailed balance

$$n_l n \gamma_{lu} = n_u n \gamma_{ul} + n_u A_{ul} \quad (2.29)$$

with n_u and n_l the number density of the upper and lower level, $n = n_u + n_l$, A_{ul} the Einstein coefficient for spontaneous emission, and γ_{ij} the collision rate coefficients. LTE conditions apply if collisions among the molecules entirely dominate the distribution of states and thus other radiative (de-)excitation processes than spontaneous emission may be neglected. This only holds if the ambient radiation field is not too strong. The populations n_u and n_l of the upper and the lower level are given by the Boltzmann distribution (Equation 2.13).

¹www.cdms.de

²<http://spec.jpl.nasa.gov/>

³http://portal.vamdc.org/vamdc_portal/nodes.seam

The critical density of the gas is defined by

$$n_{\text{crit}} = \frac{A_{ul}}{\gamma_{ul}} \quad (2.30)$$

which is the density at which the probability of collisional and radiative de-excitation is equal and in general depends weakly on temperature. For gas densities $n \ll n_{\text{crit}}$, the rate of collisional excitation will increase with increasing gas density and de-excitation will occur mainly radiatively. Thus, the intensity of the observed line will increase until the critical density is reached. Above the critical density collisional de-excitation will dominate and the intensity of the line will decrease again. Therefore, molecular emission lines are best observed for densities near the critical density. The critical density of $\text{C}^{18}\text{O}(2-1)$ is $n_{\text{cr}}^{18} = 2 \times 10^4 \text{ cm}^{-3}$, that of $^{12}\text{CO}(2-1)$ is $n_{\text{cr}}^{12} = 7 \times 10^3 \text{ cm}^{-3}$. The critical density of $^{13}\text{CO}(2-1)$ is found in between those two. This again shows how useful the dependence of E_{rot} on the moment of inertia is. In conditions where the density of one isotopologue is already above critical and the line becomes optically thick, another (rarer) one might still be below and thus allow to look more deeply into the cloud.

The excitation temperature T_{ex} of the gas describes the expected number density of a level for the given temperature (Boltzmann distribution). For high gas densities, i.e. collisions dominate, $T_{\text{ex}} \rightarrow T_{\text{kin}}$ the kinetic temperature of the gas. If, on the contrary, densities are low and radiative excitation dominates then $T_{\text{ex}} \rightarrow T_{\text{R}}$ the radiation temperature. This means that $T_{\text{R}} < T_{\text{ex}} < T_{\text{kin}}$. However, T_{ex} obtains a physical meaning, i.e. the actual temperature of the gas/molecular cloud, only if LTE conditions apply and all temperatures can be described by a single thermodynamical temperature T of the gas.

2.3.2 Molecular line profiles and broadening

Molecular emission lines are described by a certain line profile function $\Phi(\nu)$ which is normalized to

$$\int_0^\infty \Phi(\nu) d\nu = 1 \quad (2.31)$$

Ideally, the profile should be a sharply peaked Delta function. In reality, there are several factors that contribute to a broadening of the line. The most important are:

- **Natural broadening:** The frequency of a transition $E = h\nu$ is not exactly fixed, but obeys the Heisenberg's uncertainty principle $\Delta E \Delta t \geq \hbar/2$ with Δt the finite lifetime of the excited state. This means that molecules absorb and emit photons in a range around the theoretically predicted frequency of a transition. The resulting line profile is called a damping or Lorentzian profile.

$$\Phi(\nu) \propto \frac{\gamma}{\gamma^2 + \nu^2} \quad (2.32)$$

with γ the damping constant. Additional damping may occur if molecules are de-excited collisionally before they have emitted a photon. This is then called pressure broadening.

- **Thermal or Doppler broadening:** The thermal motion of the molecules also causes a line broadening through the Doppler effect. If the emitting molecule has a radial velocity v_r relative to the observer, its emitted photon of frequency ν_0 will be received with a Doppler shifted frequency ν such that

$$\frac{\nu - \nu_0}{\nu_0} = \frac{v_r}{c} \quad (2.33)$$

with c the speed of light. In radio astronomy the commonly measured radial velocity v_{LSR} (LSR = local standard of rest) is a velocity given relative to the barycenter of the solar system, i.e. accounting for the standard solar motion ($v_{\text{sun}} = 20 \text{ km s}^{-1}$; Wilson et al. 2009). If LTE conditions apply the velocity distribution of the molecules is described by the Maxwell-Boltzmann distribution (Equation 2.11)

$$f(v_r) \propto \exp\left(\frac{-v_r^2}{2\sigma^2}\right) \quad (2.34)$$

with v_r the radial velocity of the molecules, $\sigma = \sqrt{k_B T / m_{\text{mol}}}$ the thermal velocity dispersion of the gas and m_{mol} the mass of the molecule under consideration. Therefore, the resulting line profile has a Gaussian shape

$$\Phi(v_{\text{LSR}}) = \sqrt{\frac{4 \ln 2}{\pi \Delta v^2}} \exp\left(-\frac{4 \ln 2 v_{\text{LSR}}^2}{\Delta v^2}\right) \quad (2.35)$$

with Δv the full width at half maximum (FWHM) of the observed profile. It is related to the thermal velocity dispersion of the gas via

$$\sigma = \sqrt{8 \ln 2} \Delta v \quad (2.36)$$

and typically measured in km s^{-1} . For the two considered CO isotopologues in this work the thermal velocity dispersion for 10 K is $\approx 0.05 \text{ km s}^{-1}$. If the molecular gas can be treated as an ideal gas, then the thermal velocity dispersion is equal to the (isothermal) sound speed c_s .

The final resulting line profile is the convolution of the Lorentzian with the Gaussian profile which leads to the so-called Voigt profile. However, in radio astronomy natural broadening can be neglected as it contributes very little to the line broadening. Thus, most line profiles can be approximated by a Gaussian under the condition that only the thermal motion of the molecules contributes.

Observations have shown that in most cases line profiles are much broader than could be explained solely through thermal broadening. The major contribution to the linewidth are in fact the non-thermal motions of the gas along the line-of-sight of which interstellar turbulence is the most important. If the turbulence is independent of the thermal motion, it can be modeled by a Gaussian profile and the resulting convolution with the thermally broadened one will be another Gaussian where the observed velocity dispersion is given by

$$\sigma_{\text{obs}} = \sqrt{\sigma_{\text{thermal}}^2 + \sigma_{\text{non-thermal}}^2} \leftrightarrow \Delta v_{\text{obs}} = \sqrt{\Delta v_{\text{th}}^2 + \Delta v_{\text{non-th}}^2} \quad (2.37)$$

which can be equivalently expressed through the linewidths Δv . In this way there is a simple tool to obtain information about gas kinematics directly from the measured linewidth. In practice one fits a Gaussian to the observed line profile and obtains the relevant parameters, like FWHM, peak and integrated intensity, v_{LSR} velocity of the peak, from the fit.

Besides turbulence there are also other processes that can change the line profile significantly. Non-random large-scale gas motions, such as infall, expansion or rotation, may shift the line or parts of it causing an asymmetry. An optically thick medium will cause the line to flatten and ultimately become a top-hat. This effect must be taken into account especially when calculating column densities for ^{12}CO lines that become optically thick very easily. Self-absorption may occur when warmer gas is surrounded by a colder envelope. Then, emission from the inner part can be absorbed by the outer envelope and the line profile will show a characteristic dip at the velocity of the peak. Finally, line profiles of different objects along the LOS may overlay each other causing very complex and blended line profiles that are difficult to disentangle.

2.3.3 Molecular column density

In LTE conditions the level population is described by the Boltzmann distribution. In a two-level system the number density n_u of the upper level can also be expressed by a column density which is the integrated number density over the path ds , $N_u = \int n_u ds$. Thus, the population of the upper level is given by

$$N_u = N \frac{g_J}{Q} \exp\left(\frac{-E_i}{k_B T_{\text{ex}}}\right) \quad (2.38)$$

where N is the total column density, g_J the statistical weight of level J ($g_J = 2J + 1$ for rotational states), and $Q = \sum_i g_i \exp[-E_i/(k_B T_{\text{ex}})]$ the partition function.

Observers usually derive the total column density of a molecule along the LOS from the observed molecular line. The observed line profile, the optical depth, and the column density of the upper level are related to each other by

$$\tau_\nu = \frac{c^2}{8\pi\nu^2} \left[\exp\left(\frac{h\nu}{k_B T_{\text{ex}}}\right) - 1 \right] A_{ul} \Phi(\nu) N_u \quad (2.39)$$

This follows from the definition of the optical depth $d\tau_\nu = \kappa_\nu ds$ and using the Boltzmann distribution for a two-level system (Equation 2.13). A detailed derivation is given in Mangum & Shirley (2015). Integrating Equation 2.39 and using Equation 2.38 one obtains for the total column density

$$N = \frac{3h}{8\pi^3\mu^2} \frac{Q}{g_u} \exp\left(\frac{E_u}{k_B T_{\text{ex}}}\right) \left[\exp\left(\frac{h\nu}{k_B T_{\text{ex}}}\right) - 1 \right]^{-1} \int \tau_\nu d\nu \quad (2.40)$$

where μ is the electrical dipole moment of the molecule. It enters in the equation by inserting the Einstein coefficient $A_{J,J-1}$ for a rotational transition $J \rightarrow J - 1$ in a linear

molecule

$$A_{J,J-1} = \frac{64\pi^4\nu^3\mu^2}{3hc^3} \frac{J}{2J+1} \quad (2.41)$$

In this work, I calculate the total column density of the C¹⁸O(2–1) line. Thus, $J = J_l = 1 \Rightarrow J_u = J + 1 = 2$ and $g_u = 2J_u + 1 = 5$. In LTE conditions and the optically thin limit, which should hold for the C¹⁸O line, one can substitute the integral over the optical depth by one over the observed brightness temperature T_B (Wilson et al. 2009). By assuming that the cloud completely fills the beam, i.e. $f_{\text{beam}} = 1$, one can rewrite Equation 2.40 using the main-beam temperature and Equation 2.19 (Carlhoff et al. 2013):

$$N(\text{C}^{18}\text{O}) = \frac{\tau_{18}}{1 - \exp(-\tau_{18})} f(T_{\text{ex}}) \int T_{\text{mb}}^{18} d\nu \quad (2.42)$$

where the functions $f(T_{\text{ex}})$ and Q are defined as

$$f(T_{\text{ex}}) = \frac{3h}{8\pi^3\mu^2} Q(T_{\text{ex}}) \left\{ [(J(T_{\text{ex}}) - J(T_{\text{bg}}))] \left[1 - \exp\left(-\frac{T_{\nu}^{18}}{T_{\text{ex}}}\right) \right] \right\}^{-1} \quad (2.43)$$

$$Q(T_{\text{ex}}) = \frac{k_B T_{\text{ex}}}{J_u B_{\text{rot}} h} \exp\left(\frac{B_{\text{rot}} J_u (J_u + 1) h}{k_B T_{\text{ex}}}\right) \quad (2.44)$$

and $T_{\nu} = h\nu/k_B$. The partition function $Q(T_{\text{ex}})$ is approximated for a linear molecule (Mangum & Shirley 2015). The factor $\tau_{18}/(1 - \exp(-\tau_{18}))$ corrects the integrated intensity for possible opacity broadening of the line (see Goldsmith & Langer 1999).

Hence, the total column density of a molecular species can be calculated from the integrated intensity of the observed line, knowing the optical depth and the excitation temperature.

Chapter 3

Observations and data reduction

3.1 LABOCA continuum

The reduction of the LABOCA data was done by myself using adapted scripts provided by my collaborator Thomas Stanke from ESO.

The sub-mm continuum observations of Lupus I were performed with the APEX 12 m telescope located in the Chilean Atacama desert (Güsten et al. 2006). I used the LArge APEX BOlometer CAmera (LABOCA, Siringo et al. 2009) which operates in the atmospheric window at $870\ \mu\text{m}$ (345 GHz). The angular resolution is $19.2''$ (HPBW), and the total field of view is $11.4'$. At the distance of Lupus I (150 pc) the angular resolution corresponds to a spatial scale of $\sim 2800\ \text{AU}$ ($\sim 0.01\ \text{pc}$). This is sufficient to resolve the structure of molecular cores.

The LABOCA observations of Lupus I were obtained in Max-Planck and ESO Periods 91 and 92, on 24th March, 31st August, 12th, 13th September 2013, and 31st March 2014 (PI: B. Gaczkowski). The observational setup is shown in the left panel of Figure 3.1. The filament's major axis (shown in red) is rotated by an angle of 42° with respect to the east direction in the Celestial coordinate frame (cyan compass). The observations were performed in the on-the-fly (OTF) mode, scanning perpendicularly and along the filament's major axis with a random position angle between -7° (yellow box) and $+7^\circ$ (green box) with respect to the major axis for each scan to reduce striping effects and improve the sampling. The total observing time was 11.3 hours and the weather conditions were good to average.

Data reduction included standard steps for sub-millimeter bolometer data, using the BoA software package (Schuller 2012). First, data were converted from instrumental count values to a Jansky scale using a standard conversion factor, then a flatfield correction (derived from scans of bright, compact sources) was applied. Corrections for atmospheric opacity were derived from skydips taken every 1–2 hours, and finally residual correction factors were determined from observations of planets and secondary calibrator sources. Data at the turning points of the map were flagged, as were spikes. The data from the individ-

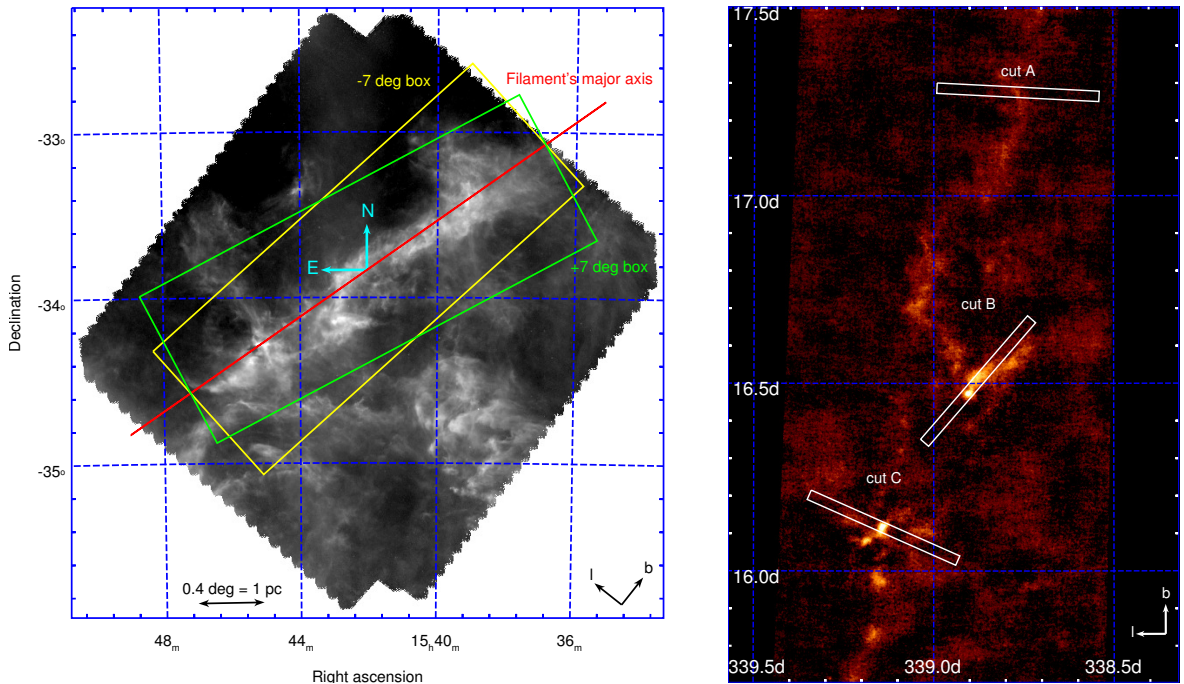


Figure 3.1: *Left:* Setup of the LABOCA observations of Lupus I. The background image is the *Herschel* $250 \mu\text{m}$ map. The red line marks the filament's major axis which is rotated by 42° with respect to the east direction of the J2000 coordinate frame (cyan compass). The yellow and green box mark the minimum and maximum possible position angle (with respect to the major axis). From this range a random angle is chosen for each scan. In this way striping is reduced and sampling improved. *Right:* Setup of the APEX-1 $^{13}\text{CO}(2-1)$ and $\text{C}^{18}\text{O}(2-1)$ observations of Lupus I. Along each of the three cuts A, B, and C an on-the-fly map was obtained simultaneously in both lines. The size of each map is marked with a white box. The background image is the final LABOCA continuum map. Both coordinates and the white compass are Galactic.

ual bolometers were then corrected for slow amplitude drifts due to instrumental effects and atmosphere by subtracting low-order polynomials from the time-stream data. Short timescale sky brightness variations (sky-noise) was corrected by removing the correlated signal (over a large number of bolometers) in an iterative fashion. Then the time-stream data were converted into sky-brightness maps for each scan, and finally all scans combined into one map.

The removal of the correlated sky variations is also known to filter out astronomical emission from extended sources, usually leading to negative artifacts surrounding bright emission structures. In order to recover some of the extended emission, an iterative source modeling procedure was applied, using the result from the previous iteration to construct an input model for the following iteration. To construct the model, the previous map was smoothed, all pixels below a pixel value of 0 set to 0, and the map smoothed again. In the following iteration, the model is subtracted from the time-stream data before de-spiking, baseline subtraction, and sky-noise removal, and then added back to the data stream, before the new map is created. This procedure effectively injects artificial flux into the

mapped area and is prone to creating runaway high surface brightness areas especially in regions without significant astronomical signal and low signal-to-noise. For that reason, the model image was set entirely to 0 in areas of the map with poor coverage, below a certain threshold in rms (basically the map edges), and the procedure was stopped after 25 iterations. This process is illustrated in the top panel of Figure 3.2: the resulting map is shown after the first iteration, after eight, after 16, and after 25 iterations. Extended structures are more and more recovered after each iteration. Typically, structures on scales on the order of 3–4' can be recovered, while larger scales get more and more filtered out (see simulations done by Belloche et al. 2011). The gridding was done with a cell size of 6.1'' and the map was smoothed with a Gaussian kernel of size 9'' (FWHM). The angular resolution of the final map is 21.2'' (HPBW) and the rms noise level is 23 mJy/21.2''-beam (hereafter the notation per beam in context of LABOCA will mean per 21.2''-beam). The final resulting map is shown in the bottom panel of Figure 3.2.

In order to determine the total sub-mm flux of the entire LABOCA map, I integrated all pixel values above the 3σ noise level of 69 mJy/beam. This yielded a total flux value of 476 Jy. The peak intensity in the map is $I_{\nu}^{\max} = 1.37$ Jy/beam.

3.2 APEX CO emission

The reduction of the APEX CO data was done by myself adapting scripts provided by the APEX telescope team.

The molecular observations of Lupus I were performed with the APEX telescope using the APEX-1 receiver of the Swedish Heterodyne Facility Instrument (SHeFI; Vassilev et al. 2008) was used. The observations were obtained in Swedish time period 93 on 18th and 20th August 2014 (PI: B. Gaczkowski). Lupus I was observed simultaneously in the $^{13}\text{CO}(2-1)$ (rest frequency $\nu_0^{13} = 220.398677$ GHz) and $\text{C}^{18}\text{O}(2-1)$ ($\nu_0^{18} = 219.560357$ GHz) line at three different cuts across the cloud. The observational setup is shown in the right panel of Figure 3.1. The observing mode was on-the-fly and the maps for each cut have slightly different sizes that are listed in Table 3.1. The scanning direction was along the long side of a cut. The velocity resolution of the spectra is $\Delta v = 0.1$ km s $^{-1}$ and the rms noise ranges between ≈ 0.05 – 0.1 K for both lines. The perceptible water vapor (PWV) during the observations was between 1.5 and 2 mm. Each map contains about 620 spectra.

The data reduction was done using the CLASS package of the IRAM GILDAS software¹. The antenna temperature T_A was converted into a main-beam temperature $T_{\text{mb}} = T_A/\eta$ adopting a main-beam efficiency of $\eta = 0.75$ for APEX-1². All spectra were baseline subtracted. First, with a 0th order baseline and were needed also with one of high polynomial order. Finally, for each line and cut a map (or 1mv cube) was produced with the XY_MAP task which convolves the data with a Gaussian of one third of the beam. The final angular

¹<http://www.iram.fr/IRAMFR/GILDAS>

²<http://www.apex-telescope.org/telescope/efficiency>

resolution is $30.1''$ and the pixel size is $14.3''$. With the task `GILDAS_FITS` the `lmv` cube can easily be converted into a FITS file for further analysis in IDL or inspection with `ds9`.

Table 3.1: Details of the molecular line maps obtained for Lupus I with APEX-1. The first column gives the name of the cut, the second and third column give the x and y size of the whole map. Column four gives the length of the cut, columns five and six the position of the center of the map (Celestial coordinates), and the last column gives the number of pixels that contain a spectrum. These parameters are valid for both the ^{13}CO and C^{18}O maps of one cut. The angular resolution of the maps is $30.1''$ and the pixel size $14.3''$.

Cut	Map size X	Map size Y	Length	Center Ra	Center Dec	No. of spectra
A	21'	18'	26'	15:40:05.35	-33:36:44.4	617
B	26'	6'	24'	15:42:49.80	-34:08:37.8	618
C	13'	24'	26'	15:44:57.60	-34:17:13.3	620

3.3 Herschel archival data

The Lupus I cloud complex was observed by the *Herschel* far-infrared observatory (Pilbratt et al. 2010) in January 2011 as part of the Gould-belt survey (obsIDs: 1342213182 and 1342213183; see André et al. 2010; Rygl et al. 2013). The Photodetector Array Camera and Spectrometer (PACS, Poglitsch et al. 2010) and the Spectral and Photometric Imaging Receiver (SPIRE, Griffin et al. 2010) were used to map an area of $\approx 2^\circ \times 2.3^\circ$. I retrieved these data from the *Herschel* science archive and reduced them using HIPE v12.1 (Ott 2010) for the calibration and the deglitching of the Level 0 PACS and SPIRE data. The Level 1 data of both instruments were then used to produce the final maps with the Scanamorphos package v24 (Roussel 2013, `/parallel` and `/galactic` options were switched on in both cases to preserve extended structures in complex, bright Galactic fields). The pixel-sizes for the five maps at 70, 160, 250, 350 and $500\ \mu\text{m}$ were chosen as $3.2''$, $4.5''$, $6''$, $8''$, and $11.5''$, respectively.

The absolute calibration of the *Herschel* data was done following the approach described in Bernard et al. (2010). Using the *Planck* and the IRAS data of the same field as the *Herschel* data the expected fluxes to be observed by *Herschel* are calculated at each band and from that the zero-level offsets are computed (see Table 3.2). These are then added to the *Herschel* maps to create the final mosaics.

For the dust properties and temperatures considered in my analysis the color corrections for both PACS and SPIRE are on the order of 1-2% and so are negligible.

Table 3.2: Zero-level offsets for the *Herschel* maps obtained from the cross-correlation with Planck and IRAS.

Band [μm]	Offset MJy sr $^{-1}$
70	5.68954
160	14.3011
250	8.11490
350	4.06405
500	1.68754

3.4 Planck archival data

I retrieved the all-sky maps of the High-Frequency-Instrument (HFI) in the 353, 545, and 857 GHz bands (corresponding to the FIR and sub-mm wavelengths of 850, 550, and 350 μm) from the *Planck* legacy archive³ (release PR1 21.03.2013). From these data cubes in HEALPix⁴ format I extracted the area covering the Lupus I region separately for each wavelength and created gnomonic projected maps. The resolution in each of the three bands is 5' and the pixel size was chosen as 1.7'.

From the *Planck* archive I also retrieved the all-sky thermal dust model map⁵. From that I extracted the dust emissivity index β and the dust opacity $\tau_{353\text{ GHz}}$ map for the region covering Lupus I. Those maps have a resolution of 30' and 5', respectively. The pixel size was again chosen as 1.7' in both cases.

³<http://pla.esac.esa.int/pla/>

⁴<http://healpix.jpl.nasa.gov/html/intro.htm>

⁵HFI_CompMap_ThermalDustModel_2048_R1.20.fits



Figure 3.2: *Top*: Lupus I LABOCA 870 μm map shown after four different numbers of iterations during the reduction process. In each step more of the extended emission is recovered. All four maps have the same logarithmic intensity scaling in units of Jy/beam . *Bottom*: Final LABOCA 870 μm map with square-root intensity scaling in units of $\text{Jy}/21.2''\text{-beam}$. Galactic compass is given in the lower left corner of the map, the Celestial compass in the lower right corner.

Chapter 4

Constraining the physical properties of Lupus I using dust emission

This chapter is based on the article entitled "*Squeezed between shells? The origin of the Lupus I molecular cloud. APEX/LABOCA, Herschel, and Planck observations*" published in *Astronomy & Astrophysics* (Gaczkowski et al. 2015). The whole analysis presented here was done by myself.

4.1 Column density and temperature maps of Lupus I

As outlined in Section 1.1.2, dust emission is an important tracer of molecular clouds. As dust and molecular hydrogen are closely coupled, one can infer hydrogen column densities from dust column density maps. An estimate of the dust temperature can be determined when observations in several far-infrared wavelengths are available. The procedure is described in this chapter. I concentrate my analysis only on the main filament commonly seen in all three observational data sets of LABOCA, *Herschel*, and *Planck*. I will refer to it as Lupus I or the Lupus I filament (see Figure 1.7). All calculated quantities like e.g. a mean column density will refer to this area, if not explicitly stated otherwise. From my three data sets, I calculated column density maps to characterize the cloud in a multi-wavelength approach. Additionally, I constructed a temperature map from the *Herschel* data.

4.1.1 Column density and temperature map from *Herschel* SED fit with all SPIRE bands

The standard and often practiced way to derive column density and temperature maps from the *Herschel* data is to fit an SED to the observed fluxes of the *Herschel* bands for each pixel of the maps (see e.g. Alves de Oliveira et al. 2014; Lombardi et al. 2014; Battersby et al. 2014). Here, I fit the SED to the three SPIRE bands at 250, 350, and 500 μm . I did not include the two PACS 70 and 160 μm bands because mainly these observations were

corrupted by stray moonlight which manifests itself in a bright stripe across the entire map. Hence those observations are less reliable for an analysis of large-scale structures. However, I did the fits also with all five bands and excluding only the PACS 70 μm band. These results are discussed in Section 4.1.3. The contaminating stray light in the SPIRE bands is confined to the central region of the filament and contributes significantly only in regions of low cloud emission. The possible overestimation of the fluxes even in such regions is covered by the overall error of the flux calibration ($\approx 20\%$).

Lupus I is optically thin to the dust emission at the considered densities and wavelengths and thus I can model its emission as a modified blackbody. I assume that the long wavelength emission ($\lambda \geq 250 \mu\text{m}$) of a pixel $[i, j]$ comes from a unique species of grains being all at the same equilibrium temperature, and having a power-law wavelength dependent opacity. If $L_\nu^{i,j}(\lambda)$ is the monochromatic luminosity of pixel $[i, j]$ at wavelength λ , then it can be expressed as

$$L_\nu^{i,j}(\lambda) = M_d^{i,j} \times \kappa(\lambda_0) \left(\frac{\lambda_0}{\lambda} \right)^\beta \times 4\pi B_\nu(\lambda, T_d^{i,j}) \quad (4.1)$$

where κ is the dust opacity, β the emissivity index, and $B_\nu(\lambda, T_d)$ the blackbody spectral flux density for a dust temperature T_d . The two free parameters $M_d^{i,j}$ and $T_d^{i,j}$ are the dust mass and temperature per pixel of the material along the line-of-sight. Here, I adopt a typical $\kappa(\lambda_0) = 5.91 \text{ cm}^2 \text{ g}^{-1}$ with $\lambda_0 = 350 \mu\text{m}$ for dust grains with thin ice mantels and gas densities $< 10^5 \text{ cm}^{-3}$ (Ossenkopf & Henning 1994). Using the available information about β from the *Planck* data, I found that the emissivity index within the Lupus I cloud lies between ~ 1.6 and ~ 1.7 . Therefore, I fixed its value to $\beta = 1.65$ as an average value within the cloud. Considering the low resolution of the β map of $30'$ this is a reasonable approximation. In this way, I also limit the number of free parameters in the fit making it more stable.

After convolving the 250 and 350 μm maps to the resolution of the 500 μm band using the kernels from Aniano et al. (2011), the modified black body fit was performed pixel-by-pixel. From the dust mass $M_d^{i,j}$ in each pixel the total column density for both dust and gas was then calculated as

$$N_{\text{H}_2}^{\text{HSED}} = \frac{M_{i,j} R}{\mu_{\text{H}_2} m_{\text{H}}} \quad (4.2)$$

where $R = 100$ is the gas-to-dust mass ratio, $\mu_{\text{H}_2} = 2.8$ the molecular weight per hydrogen molecule, and m_{H} the hydrogen atom mass. The resulting dust temperature values $T_d^{i,j}$ from the fit at each pixel give the temperature map of Lupus I (shown in left panel of Figure 4.1) at the resolution of the 500 μm band, i.e. $\text{FWHM}_{500} = 36''$. The obtained column density map from the SED fit is shown in the middle panel of Figure 4.2. The statistical error on both the final column density map and the temperature map consists of errors in the calibration, the photometry, and the SED fitting process. I conservatively estimated the sum of these uncertainties to be $\sim 20\%$ for both maps.

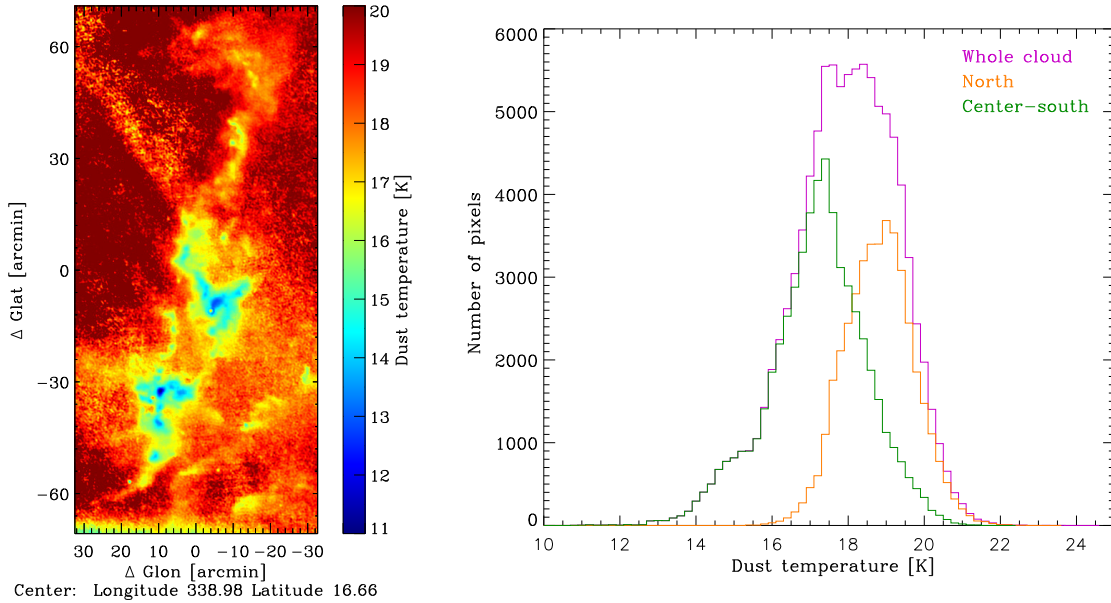


Figure 4.1: *Left*: Temperature map of Lupus I from the *Herschel* SPIRE SED fit. *Right*: Histogram of the dust temperature for the whole cloud (purple), the north part (orange), and in the center-south (green).

4.1.2 How the choice of a dust model influences the column density and temperature map

Since the composition of the dust grains and their density is unknown, the choice of a particular dust model, i.e. a specific opacity law, introduces an uncertainty of the dust opacity and thus of the resulting column density. In order to estimate it, I looked at different $\kappa(\lambda_0)$ values at $\lambda_0 = 350 \mu\text{m}$ for grains with and without ice mantles and the three initial gas densities of $< 10^5$, 10^5 , and 10^6 cm^{-3} in the online table of Ossenkopf & Henning (1994). They vary between $3.64 \text{ cm}^2 \text{ g}^{-1}$ (MRN¹ without ice mantles and $\rho < 10^5 \text{ cm}^{-3}$) and $11.3 \text{ cm}^2 \text{ g}^{-1}$ (MRN with thin ice mantles and $\rho = 10^6 \text{ cm}^{-3}$). Hence, my chosen value of $\kappa(\lambda_0) = 5.91 \text{ cm}^2 \text{ g}^{-1}$ might still vary by a factor of about 2. To explore how the choice of a certain dust model influences the resulting column density map, I did the SED fit also for the minimum and maximum value of $\kappa(\lambda_0)$. The two resulting maps, as well as the one for the chosen value of $5.91 \text{ cm}^2 \text{ g}^{-1}$ are shown in Figure 4.2. All three maps have the same intensity scaling. Table 4.1 shows the maximum and minimum value, the mean, and the median of the column density for all three resulting maps. As expected, the minimum, maximum, mean, and median value of the column density decreases by the same factor of ≈ 3.1 by which the dust opacity increases from 3.62 to $11.3 \text{ cm}^2 \text{ g}^{-1}$. However, the mass of the cloud decreases by a factor of about 6 which is not surprising as with decreasing column density the number of pixels that fall below the chosen threshold of 10^{21} cm^{-2} for

¹Mathis-Rumpl-Nordsieck size distribution of interstellar grains (Mathis et al. 1977)

the mass calculation increases. This is well visualized in Figure 4.2. The area of the cloud enclosed by the $1.1 \times 10^{21} \text{ cm}^{-2}$ contour (lowest one) becomes smaller with increasing dust opacity.

Changes of the dust opacity in Equation 4.1 cause a shift of the Planck function towards lower or higher intensities, but do not change its shape. To compensate this shift, the free parameter of the dust mass in each pixel has to be adjusted. Therefore, the temperature remains unaffected by the choice of a dust model and the resulting temperature maps from the SED fits will be identical. Physically speaking a higher/lower dust opacity will require a lower/higher dust mass to generate the same luminosity at a given temperature.

Table 4.1: Parameters of the column density maps created from the *Herschel* SED fit using a dust model based on three different $\kappa(\lambda_0)$ values. First column gives the chosen dust opacity, the following columns give the minimum, maximum, mean, and median value of each resulting column density map, respectively. The last column gives the total mass of the Lupus I above a threshold of $N_{\text{H}_2} > 10^{21} \text{ cm}^{-2}$.

$\kappa(\lambda_0)$ [$\text{cm}^2 \text{ g}^{-1}$]	min	max	$\langle N_{\text{H}_2} \rangle$ [$\times 10^{21} \text{ cm}^{-2}$]	median(N_{H_2})	$M_{\text{tot}}(N_{\text{H}_2} > 10^{21} \text{ cm}^{-2})$ [M_{\odot}]
3.62	0.311	56.4	2.34	1.67	341
5.92	0.194	34.8	1.44	1.03	174
11.3	0.100	18.2	0.75	0.54	56

4.1.3 How the inclusion of the PACS bands influences the SED fit

In the paper, on which this chapter is based on, I presented the column density and temperature maps resulting from the SED fit to the three SPIRE bands at 250, 350, and 500 μm (Section 4.1.1). The contamination by stray moonlight, which occurred during the observations, is wavelength dependent and thus higher for the shorter wavelengths (PACS 70 and 160 μm bands) but contributes less at the SPIRE bands. Therefore, the two PACS bands were excluded from the SED fit. For this work, however, I also investigated how the SED fit is influenced by the inclusion of the PACS bands. Using the same dust model with $\kappa(\lambda_0) = 5.91 \text{ cm}^2 \text{ g}^{-1}$, I additionally calculated a column density and temperature map from the SED fit to all five *Herschel* bands, as well as to just the PACS 160 μm and the three SPIRE bands. The resulting column density and temperature maps are shown in Figure 4.3. The PACS 70 μm band introduces a lot of artifacts to both resulting maps (4.3 c+f). Thus, they are not reliable for a further analysis. The column density map produced from the fit to the PACS 160 μm band together with the SPIRE bands (4.3 b) does not show these artifacts anymore. Compared to the fit with just the SPIRE bands the mean and median of the column density map remains unchanged with values of $\langle N_{\text{H}_2} \rangle = 1.44 \times 10^{21} \text{ cm}^{-2}$ and a median of $1.03 \times 10^{21} \text{ cm}^{-2}$. A similar behavior is found in the two temperature maps. The mean temperature within the filament rises only by 0.3 K ($\approx 2\%$) from 18.0 to 18.3 K when the PACS 160 μm is taken into account, whereas

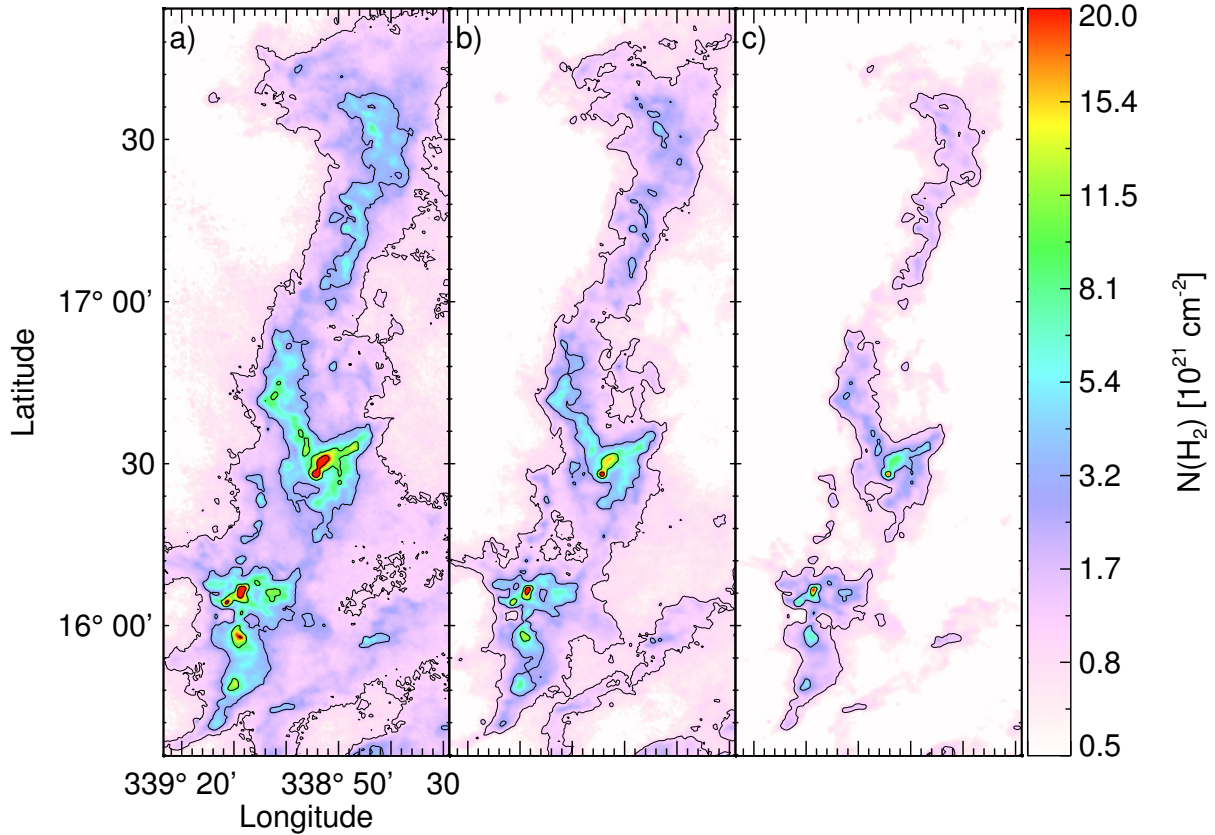


Figure 4.2: Comparison of the column density maps resulting from the *Herschel* SED fit using the three different dust models (opacities): (a) $\kappa(\lambda_0) = 3.64 \text{ cm}^2 \text{ g}^{-1}$, (b) $\kappa(\lambda_0) = 5.91 \text{ cm}^2 \text{ g}^{-1}$ which represents the dust model used for further analysis, and (c) $\kappa(\lambda_0) = 11.3 \text{ cm}^2 \text{ g}^{-1}$. All three maps have the same intensity scaling and contour levels of 1.1, 4.9, 8.7, 12, 16, and $20 \times 10^{21} \text{ cm}^{-2}$.

the median stays the same (18.1 K). The total mass of the cloud (for $N_{\text{H}_2} > 10^{21} \text{ cm}^{-2}$) changes by $\approx 2\%$ from $174 M_{\odot}$ to $177 M_{\odot}$ from the three band to the four band fit. These results show that the SED fit for Lupus I is robust even if only the three SPIRE bands are taken into account. Leaving out the $160 \mu\text{m}$ band introduces changes to the results that are within the overall uncertainties of the fit.

Figure 4.4 exemplary illustrates the behavior of the fit, with respect to the number of bands, for four selected pixels. Their positions are marked with black crosses in Figure 4.3 b. The solid line marks the fit using the three SPIRE bands, the dashed line the fit to the PACS $160 \mu\text{m}$ together with the SPIRE bands. The resulting dust temperature $T_{\text{d},3/4}$ and column density $N_{\text{H}_2,3/4}$ for a given pixel are shown next to the corresponding curve. Hereby, the index three or four denotes the number of bands used in the fit. For very high density regions ($N_{\text{H}_2} > 1.5 \times 10^{22} \text{ cm}^{-2}$) the three band fit tends to underestimate the temperature and hence overestimate the column density (red curves). In this example the solid red curve of the three band fit does not intersect the error bars of the $160 \mu\text{m}$ flux. The resulting temperature difference is about 6%, whereas the difference in dust mass about 20%.

In a density regime of $10^{21} < N_{\text{H}_2} \leq 1.5 \times 10^{22} \text{ cm}^{-2}$ the two fits agree with each other within the error bars of the fluxes (green and blue curves). This is the regime in which most of the cloud material is located. For the green and blue fits the temperatures $T_{\text{d},3/4}$ agree within about 4% and 1%, respectively. The column densities $N_{\text{H}_2,3/4}$ agree within $\approx 9\%$ and $\approx 1\%$, respectively.

In regions with column densities $< 10^{21} \text{ cm}^{-2}$ both fits become unreliable since the contribution of actual cloud material is too low and other material along the line-of-sight will dominate those pixels (yellow curves). Although the two fits do not agree with each other in this case, the difference in temperature and column density is only $\approx 7\%$ and $\approx 16\%$, respectively. Nevertheless, pixels with such a low column density are not counted as part of the cloud and hence do not play a role in the further analysis.

4.1.4 Column density map from *Herschel* SPIRE 250 μm map

To obtain a column density map with the resolution of the SPIRE 250 μm band (i.e. $\text{FWHM}_{250} = 18''$), I followed the technique described in Juvela et al. (2013). Using the intensity map of the SPIRE 250 μm band and the previously calculated temperature map (at the lower resolution) to compute the Planck function $B_\nu(T_{\text{d}})$, it is possible to gain an additional factor of two in resolution compared to the SED fitting (to all three SPIRE bands) case. In this way the column density is simply

$$N_{\text{H}_2}^{\text{H}_{250}} = \frac{I_{250 \mu\text{m}}^{i,j} R}{B_\nu(250 \mu\text{m}, T_{\text{d}}^{i,j}) \kappa_{250 \mu\text{m}} \mu_{\text{H}_2} m_{\text{H}}} \quad (4.3)$$

with $I_{250 \mu\text{m}}^{i,j}$ the intensity of the SPIRE 250 μm band. I used this higher resolution *Herschel* column density map for my further analysis of Lupus I.

4.1.5 The influence of convolution on the *Herschel* column density maps

Often observational data and inferred results of molecular clouds have to be compared to each other. These data might either be taken with different telescopes and instruments or if with the same one, the clouds will hardly ever be at the same distance. Therefore, the data sets will have different angular and spatial resolutions. How such effects have to be taken into account is briefly discussed in this section.

I convolved the column density map created from the *Herschel* 250 μm map with a set of Gaussians with different FWHM to decrease the resolution by a factor of two to 16. Hence, the angular resolution of the resulting maps was in the range between $36''$ and $5'$, i.e. the resolution of the *Planck* data. This simulates how *Herschel* observations of Lupus I would look like if the cloud was at further distance. The maximum column density decreases and the minimum increases with decreasing resolution because convolving leads to a local averaging of map values among neighboring pixels. The maximum column density of the original map decreased from 1.44×10^{23} to $7.07 \times 10^{21} \text{ cm}^{-2}$ in the map with the

worst resolution. Similarly, the minimum increased from 0.177 to $0.303 \times 10^{20} \text{ cm}^{-2}$. The mean changed by less than 1%, whereas the median increased by about 10%. The total mass of the cloud remained constant and was unaffected by the convolution. However, small fluctuations did occur because pixels were shifted above or below the chosen column density threshold of 10^{21} cm^{-2} for the mass calculation (cf. Section 4.4). In this case, the total mass increased by $\approx 3\%$ from 174 to 179 M_{\odot} . From these findings, I conclude that in general a comparison of different data sets of molecular clouds at different distances and possibly observed with different telescopes, is meaningful for quantities like the average column density or the total mass that do not depend on the particular local distribution of map values.

4.1.6 Column density map from the LABOCA data

Lupus I is sufficiently far away from ionizing UV sources to exclude significant amounts of free-free emission. I may therefore assume the sub-mm fluxes to be entirely due to thermal dust emission. To determine whether the cloud is optically thin in this wavelength regime one can look at the peak intensity in the LABOCA map, which is $I_{\nu}^{\text{max}} = 1.37 \text{ Jy/beam}$. The corresponding optical depth can be calculated via Equation (3) in Schuller et al. (2009).

$$\tau_{870 \mu\text{m}} = -\ln \left[1 - \frac{I_{\nu}}{\Omega B_{\nu}(T_{\text{d}})} \right] \quad (4.4)$$

where Ω is the beam solid angle. In the case of Lupus I this yields values of $\tau_{870 \mu\text{m}} \leq 0.01$ for temperatures $T_{\text{d}} \geq 10 \text{ K}$ and therefore the cloud is clearly optically thin in this wavelength regime. Hence, the $870 \mu\text{m}$ intensities are directly proportional to the column densities of the interstellar dust and the line-of-sight extinction. They can be converted to the beam-averaged hydrogen molecule column density via equation (4.3).

I again assume a gas-to-dust mass ratio of $R = 100$ and for consistency extrapolate the dust model used for the *Herschel* analysis to the LABOCA wavelength, which yields a value of $\kappa_{870 \mu\text{m}} = 1.32 \text{ cm}^2 \text{ g}^{-1}$. The assumption of a constant dust temperature throughout the cloud is not valid; I used the temperature map from the *Herschel* analysis to calculate the blackbody function at each pixel of the map. In this way a column density map is obtained at the original resolution of the LABOCA map (i.e. $\text{FWHM}_{870} = 21.2''$).

4.1.7 Column density and temperature map from the *Planck* data

The thermal emission of interstellar dust over the whole sky was captured by the HFI-instrument of *Planck* at its six available wavelengths between $350\ \mu\text{m}$ and $3\ \text{mm}$. Together with the IRAS $100\ \mu\text{m}$ data the emission can be modeled well by a modified blackbody. The details of the model and the fitting procedure are described in Planck Collaboration et al. (2014). The resulting maps of temperature and optical depth (at $850\ \mu\text{m}$) can be downloaded from the *Planck* archive². I extracted the part covering Lupus I from both maps to get gnomonic projected maps. The column density map was then computed from the optical depth map using the relation

$$N_{\text{H}_2} = \frac{5.8 \times 10^{21} \text{ cm}^{-2}}{2} \times 0.497 \times 10^4 \tau_{353 \text{ GHz}} \quad (4.5)$$

suggested in Planck Collaboration et al. (2014) for regions with higher column density than the diffuse ISM, i.e. molecular clouds.

²http://irsa.ipac.caltech.edu/data/Planck/release_1/all-sky-maps/maps/HFI_CompMap_ThermalDustModel_2048_R1.20.fits

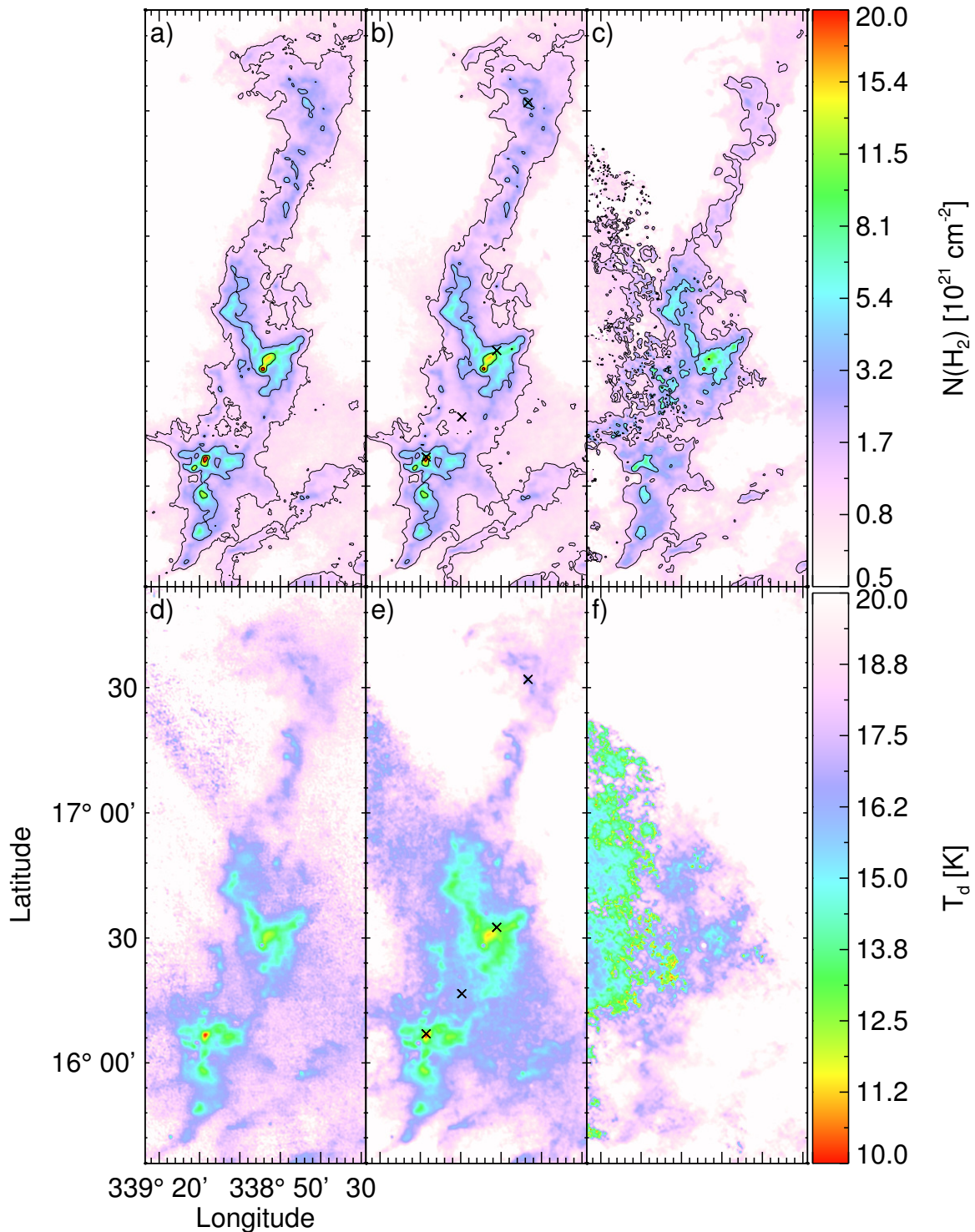


Figure 4.3: Comparison of column density and temperature maps calculated with the *Herschel* SED fit method using only the three SPIRE bands (a+d), the PACS 160 μm and the three SPIRE bands (b+e), and all five *Herschel* bands (c+f), respectively. All column density maps have the same intensity scaling and contour levels of 1, 3, 9, and $20 \times 10^{21} \text{ cm}^{-2}$. The three temperature maps also have the same intensity scaling. Black crosses in panels b) and e) mark the four selected pixels at which the modified blackbody fit to either three or four *Herschel* bands was inspected (see Figure 4.4).

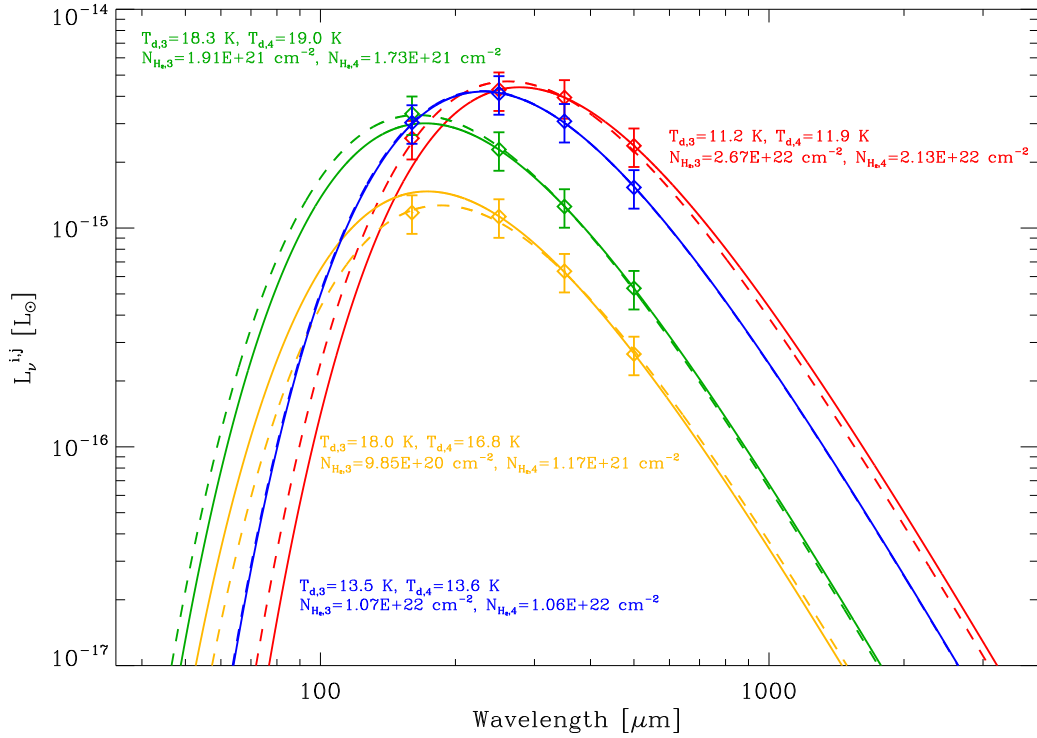


Figure 4.4: Comparison of SED fits performed with three and with four *Herschel* bands for four selected pixels in the column density map. The diamonds mark the four data points with 20% error bars. The solid line marks the fit using the three SPIRE bands, the dashed line the fit to the PACS 160 μm together with the SPIRE bands. The resulting dust temperature $T_{d,3/4}$ and mass $M_{d,3/4}$ for a given pixel are shown next to the corresponding curve. Hereby, the index three or four denotes the number of bands used in the fit. The four pixels are located: one in a cold dense core in the southern part ($l = 339.14454^\circ$, $b = +16.121623^\circ$; red), one in the lower density region between the center and the southern part (338.99580° , $+16.28046^\circ$; yellow), one in the central part of Lupus I (338.89019° , $+16.487218^\circ$; blue), and the last one in the northern part (338.75041° , $+17.504414^\circ$; green), respectively. Their positions are marked with black crosses in Figure 4.3 b+e.

4.1.8 Results of the column density and temperature maps

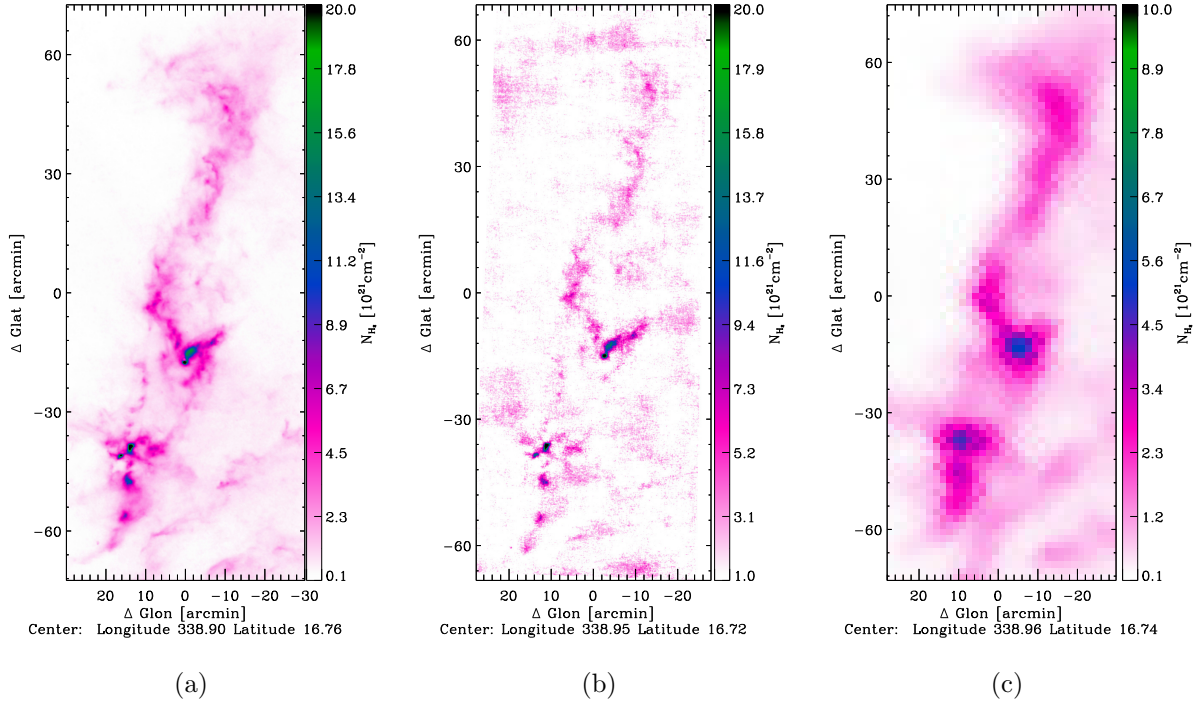


Figure 4.5: Column density maps of Lupus I from (a) the *Herschel* 250 μm map, (b) LABOCA, and (c) *Planck*.

The *Herschel* column density map of Lupus I is shown in Figure 4.5(a). The average column density is $\langle N_{\text{H}_2} \rangle = 1.44 \times 10^{21} \text{ cm}^{-2}$. The map reveals two distinct regions within the filament (see also Figure 4.6), the north where the column densities are lowest ($\langle N_{\text{H}_2} \rangle = 1.10 \times 10^{21} \text{ cm}^{-2}$) and just one dense core can be seen (Rygl et al. 2013) and the center-south where several cores with high column densities above 10^{22} cm^{-2} are found and the average column density ($\langle N_{\text{H}_2} \rangle = 1.72 \times 10^{21} \text{ cm}^{-2}$) is about 60% higher than in the north.

Comparing my map to the one derived by Rygl et al. (2013), I note that my values are lower by a factor of about 2–2.5. This can be explained by the use of a different dust model (opacity law and dust spectral index) and the inclusion of the PACS 160 μm band in their work. However, my map shows similar values compared to the column density map presented in the recent work by Benedettini et al. (2015). They did the same analysis as Rygl et al. (2013), but reduced the raw data with a different pipeline and used newer calibration files. They confirmed that the different data reduction and additionally the choice of a different opacity law are the reasons for the discrepancy to the results of Rygl et al. (2013). The extinction maps created from 2MASS and *Spitzer* data (see Chapman et al. 2007; Lombardi et al. 2008a; Merín et al. 2008) have a resolution that is lower by a factor of about 7–30. Nevertheless, there is a clear resemblance between those maps and my column density map.

The column density map of Lupus I obtained from LABOCA (see Figure 4.5(b)) is dominated by the dozen cores in the center-south and the denser dust in the central part of the filament. The average column density is $\langle N_{\text{H}_2} \rangle = 1.47 \times 10^{21} \text{ cm}^{-2}$.

The *Planck* column density map of Lupus I, with a resolution of $5'$, reveals the basic structure of the cloud that agrees well with the column density maps from LABOCA and *Herschel* (see Figure 4.5(c)). This is consistent with what is shown by the other two maps when convolved to the resolution of *Planck* and thus averaging out the highest column density peaks.

The temperature map obtained from the *Herschel* SED fit (see left panel of Figure 4.1) shows an anti-correlation of the temperature with the column density. The densest parts are the coldest and the less dense the material the warmer it becomes. In addition, a difference between the northern and the center-south part of the cloud can be seen again. In the north, dust temperatures between $\approx 15\text{--}23 \text{ K}$ with a mean and median of $\approx 19 \text{ K}$ are found, but only in the dense pre-stellar core and slightly north of it does the temperature decrease to $\approx 15 \text{ K}$. The maximum temperature in the center-south is $\approx 22 \text{ K}$ at the edges of the filament. The inner part of the filament has an average temperature of $\approx 17 \text{ K}$, but it decreases to even 11 K in the densest cores. The histogram of the dust temperatures (see right panel of Figure 4.1) shows that most of the dust in the north (orange histogram) ranges between $\approx 18\text{--}20 \text{ K}$ whereas in the center-south (green) it is between $\approx 16\text{--}18 \text{ K}$. This means that the dust in the center-south is on average 2 K colder than in the north.

4.2 Column density PDFs of Lupus I

Probability distribution functions (PDFs) of the column density are a widely used way to characterize the evolution and state of molecular clouds. Both simulators (see e.g. Federrath & Klessen 2012; Ward et al. 2014; Girichidis et al. 2014) and observers (see e.g. Kainulainen et al. 2009, 2011; Palmeirim et al. 2013; Tremblin et al. 2014; Schneider et al. 2015; Roccatagliata et al. 2015) use them in their studies and they are a good tool for comparing both simulations and observations with each other.

As Lupus I is close to us and lies at a high Galactic latitude - far away from the Galactic plane, I expect the contamination of the map by overlaying foreground or background emission to be small. I normalize the PDFs to the dimensionless $\eta = \ln(N_{\text{H}_2}/\langle N_{\text{H}_2} \rangle)$, which gives the opportunity of comparing different regions of different column density, as well as the same cloud, but observed with different instruments. For similar observations of the Orion clouds Schneider et al. (2013) showed that the effect of varying the resolution of the maps within $18''$ and $36''$ did not significantly affect the main features of the PDFs (shape, width, etc.). The Lupus I cloud is much closer, yielding a much finer physical resolution and the tests I performed on my maps convolving them with a grid of Gaussians with different FWHM confirmed their findings (see Section 4.1.5). If the difference, however, is as big as the one, for example, in angular resolution between *Herschel* and *Planck*, it is no longer possible to maintain the features of the PDF unchanged when degrading the resolution of the *Herschel* map by a factor of ≈ 8 (from $500 \mu\text{m}$) to ≈ 17 (from $250 \mu\text{m}$). In

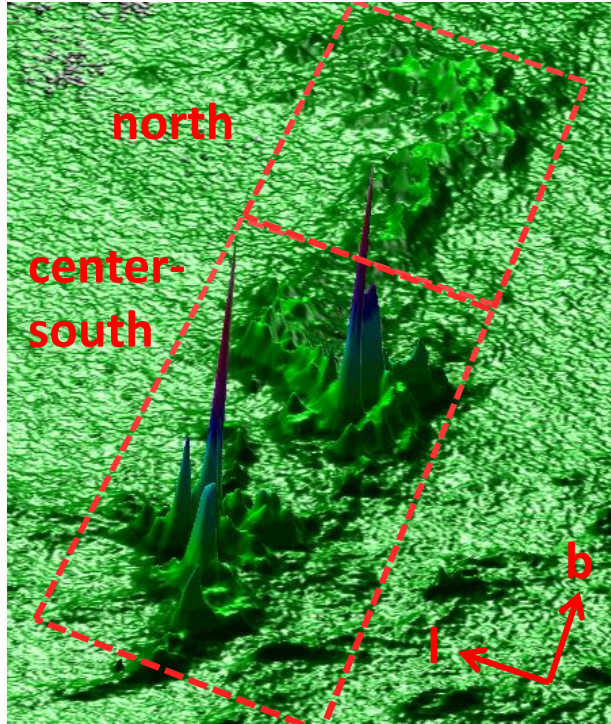


Figure 4.6: 3D-surface plot of the *Herschel* 250 μm column density map. One can clearly identify the cores in the center-south of Lupus I and see the on average lower column density in the northern part of the cloud. The red dashed boxes mark the two regions I distinguish in this work. The compass is Galactic.

this work, both the angular resolution and the pixel size of the *Herschel* and the LABOCA column density map are almost the same. Therefore, both maps have sufficiently large numbers of pixels to have a high statistic.

The basic shape of the PDF in the low column density regime is still a matter of debate but often can be described by a lognormal distribution. In more complicated cases the PDF might also be the combination of two lognormals:

$$p(\eta) = \frac{\epsilon_1}{\sqrt{2\pi\sigma_1^2}} \exp\left(-\frac{(\eta - \mu_1)^2}{2\sigma_1^2}\right) + \frac{\epsilon_2}{\sqrt{2\pi\sigma_2^2}} \exp\left(-\frac{(\eta - \mu_2)^2}{2\sigma_2^2}\right) \quad (4.6)$$

where ϵ_i is the norm, and μ_i and σ_i are the mean logarithmic column density and dispersion of each lognormal. In the high column density regime one often finds a deviation from the lognormal. This can be modeled with a power-law of slope s which is equivalent to the slope of a spherical density profile $\rho(r) \propto r^{-\alpha}$ with $\alpha = -2/s + 1$ (see Federrath & Klessen 2013; Schneider et al. 2013).

Using a least-squares method (Levenberg Marquardt algorithm; Poisson weighting),³ I derived the characteristic values of the distributions by fitting the PDFs with either one lognormal to the distribution around the single peak and where applicable a power-law

³MPCURVEFIT routine for IDL

to the high density tail, or with two lognormals to the distributions around the first and second peak, respectively, and a possible power-law tail. I checked the robustness of the fits by performing it on four different bin sizes for the histograms of 0.05, 0.1, 0.15, and 0.2 (see Section 4.2.2). The variation of the resulting fit parameters was on the order of 2%–8%. I took the final parameters from the fits for a binsize of 0.1 (see Schneider et al. 2015) and conservatively adopted an error of 10% for all fit parameters. The results are summarized in Table 4.2.

Table 4.2: Results of the fits to the *Herschel* PDFs of Figure 4.7.

Region	σ_1	σ_2	$N_{\text{H}_2,\text{peak}2}$	$N_{\text{H}_2,\text{peak}1}$ [$\times 10^{21} \text{ cm}^{-2}$]	$\langle N_{\text{H}_2} \rangle$	$N_{\text{H}_2,\text{dev}}$	s	α
Whole cloud	0.56	0.26	0.866	2.57	1.44	3.60	-2.55	1.78
Center-south	0.46	0.35	0.934	2.71	1.72	4.50	-2.43	1.82
North	0.55	0.18	0.794	2.23	1.10	–	–	–

4.2.1 Results of the column density PDFs

I derived PDFs of the Lupus I cloud from the *Herschel* and LABOCA column density maps for the two distinct parts of the cloud (north and center-south; see Figure 4.6), and for the whole cloud. They are shown in Figure 4.7. For a correct interpretation of the PDFs the completeness limit of the underlying column density map must be considered; here I adopted the lowest closed contour, which is 1.1×10^{21} and $2 \times 10^{21} \text{ cm}^{-2}$ for the *Herschel* and LABOCA map, respectively. It is marked by the vertical dashed line in the plots in Figure 4.7.

Looking at the entire cloud the *Herschel* PDF is very complex with clear deviations from a simple lognormal distribution which would be expected for a cloud that is dominated by isothermal, hydrodynamic turbulence (e.g. Klessen et al. 2000). The distribution shows two peaks in the low column density regime and a power-law tail in the high density end. The first peak at $N_{\text{H}_2,\text{peak}1} = 8.66 \times 10^{20} \text{ cm}^{-2}$ falls below the completeness limit, so it might just be reflecting the drop of observational sensitivity and will not be used for interpretation. However, the distribution above the limit can be represented well by a fit of two lognormals around the first and second peak which is at $N_{\text{H}_2,\text{peak}2} = 2.57 \times 10^{21} \text{ cm}^{-2}$. The width of the first component is $\sigma_1 = 0.56$, but could also be broader due to the possible underestimate of the column densities below the completeness limit. Nevertheless, it is more than twice as broad as the width of the second lognormal ($\sigma_2 = 0.26$) and larger than in other nearby clouds like Maddalena, Auriga (Schneider et al. 2013), or Aquila (Schneider et al. 2015). This can be a sign of broadening by turbulence and external compressive forcing (see Federrath et al. 2010; Tremblin et al. 2012; Federrath & Klessen 2013). The power-law tail follows a slope of $s = -2.55$ or corresponding $\alpha = 1.78$ for a spherical density distribution. The deviation from the lognormal into the power-law occurs near $N_{\text{H}_2,\text{dev}} = 3.6 \times 10^{21} \text{ cm}^{-2}$

which is slightly below the recent values by Schneider et al. (2015) who found the transition into the power-law tail to be at $A_V \sim 4\text{--}5 \text{ mag}^4$ in their investigation of four low-mass and high-mass star forming regions, although it is higher than the result of Roccatagliata et al. (2015) who find the deviation to occur at $A_V \sim 1.2\text{--}2 \text{ mag}$ in the Serpens Core region.

From the *Herschel* data the center-south part of the cloud shows a PDF very similar to that of the entire cloud. Here again two peaks are present and the distribution above the completeness limit can be fitted by a double lognormal and a power-law tail. The width of the first fitted lognormal is narrower, the width of the second broader than those of the entire cloud with values of $\sigma_1 = 0.46$ and $\sigma_2 = 0.35$. The slope of the power-law is slightly flatter with $s = -2.43$, but leading to a comparable exponent $\alpha = 1.82$.

In the northern part of the cloud the double-peak lognormal profile of the PDF from *Herschel* is found again, but now there is no excess above the second lognormal at higher densities. The peak position of the first lognormal is lower ($N_{\text{H}_2, \text{peak1}} = 7.94 \times 10^{20} \text{ cm}^{-2}$) than in the center-south and in the whole cloud, but with similar width ($\sigma_1 = 0.55$). The peak position of the second lognormal ($N_{\text{H}_2, \text{peak2}} = 2.23 \times 10^{21} \text{ cm}^{-2}$) is lower than that of the whole cloud and its width ($\sigma_2 = 0.18$) is approximately half as broad.

Although it is not possible to strictly constrain the shape of the PDF below the completeness limit, one can say that the distribution above does not show just two components (lognormal and a power-law) but at least three because of the second peak that appears before the deviation into the power-law. This shape could be attributed to an initial turbulent cloud which was later compressed by an external driving agent. This agent can either be an ionization front, an expanding shell driven by winds, and/or supernovae or colliding flows. The initial lognormal form of the PDF of the cloud develops a second component caused by the dense compressed gas. This behavior was found in simulations by Tremblin et al. (2012) of an initial turbulent medium that is ionized and heated by an ionization source. They concluded that a double-peak is present when the ionized gas pressure dominates over the turbulent ram pressure of the cloud. Matsumoto et al. (2015) studied the evolution of turbulent molecular clouds swept by a colliding flow. They found that the PDF exhibits two peaks in the case when the Mach numbers of the initial turbulence and the colliding flow are of the same order $M = 10$ (model HT10F10; see their Figure 11b) and the line of sight is perpendicular to the colliding flow. Then the low column density peak represents the colliding flow and the higher column density peak the sheet cloud, respectively. Observationally, double-peak PDFs have been reported and recently studied by Schneider et al. (2012), Harvey et al. (2013), and Tremblin et al. (2014) for several nearby clouds exposed to an ionization source. Areas of the cloud close to the ionization front did show the predicted second peak in the PDF due to the compression induced by the expansion of the ionized gas into the molecular cloud. In the case of Lupus I the source of the compression is very likely the expanding HI shell around the USco subgroup of Sco-Cen (possibly together with a supernova that exploded within USco) and the wind bubble of the remaining B-stars of UCL pushing from the eastern and western side of the cloud, respectively. This scenario is discussed in more detail in Section 6.1.

⁴ $N(\text{H}_2)/A_V = 0.94 \times 10^{21} \text{ cm}^{-2} \text{ mag}^{-1}$ (Bohlin et al. 1978).

Lognormal PDFs indicate shock waves (Kevlahan & Pudritz 2009) or turbulence (e.g. Vazquez-Semadeni 1994; Federrath et al. 2010). Tremblin et al. (2012) have shown in a simulation of Stroemgren spheres advancing into turbulent regions that the region compressed by the ionization front also has a lognormal density PDF, but shifted to higher density due to the compression. A PDF of a region that includes compressed and undisturbed parts of the cloud will thus show a double-peak PDF.

The power-law tail that is seen in my PDFs could be explained by active star formation and the transition to a gravity dominated density regime represented by the star forming cores. This can be shown by comparing the PDFs of the two regions in the north and the center-south. In the north where there is almost no star formation and just one pre-stellar core and ≈ 20 unbound cores can be found (Rygl et al. 2013), the PDF shows no power-law tail in the high density regime. In the center-south instead where almost all the star formation activity takes place with plenty of very young bound cores, the PDF shows the power-law tail very clearly. Numerical studies have also shown that the PDF for an actively star forming region develops a clear deviation from the lognormal in the form of a power-law tail (Ballesteros-Paredes et al. 2011; Girichidis et al. 2014).

With LABOCA the PDF of Lupus I can be modeled as one lognormal with a power-law tail at high densities ($N_{\text{H}_2, \text{dev}} = 6.0 \times 10^{21} \text{ cm}^{-2}$). The peak of the lognormal distribution lies at $N_{\text{H}_2, \text{peak}} = 1.43 \times 10^{21} \text{ cm}^{-2}$ which is below the completeness limit of the LABOCA column density map. The width of the lognormal is broad ($\sigma = 0.56$), but uncertain due to the peak position and thus possibly even broader. The power-law slope ($s = -2.66$, $\alpha = 1.75$) is very similar to the value of the *Herschel* PDF indicating the star formation activity in the cloud.

The PDF of the center-south region shows the same behavior as the one for the whole cloud. The lognormal part is slightly broader ($\sigma = 0.60$), but the power-law slope ($s = -2.59$, $\alpha = 1.77$) and the deviation point ($6.0 \times 10^{21} \text{ cm}^{-2}$) are almost the same as in the whole cloud. In the northern part only a narrower lognormal is seen instead ($\sigma = 0.52$), indicating the lack of star formation activity and the dominance by the turbulence induced through the compression. In all three cases the positions of the peaks are very close to each other.

As was already seen in the column density map from LABOCA, its PDF shows only the dense cores and the intercore medium. The instrument is not sensitive to all the material that can still be probed with *Herschel*. With LABOCA I thus sample the second lognormal of the *Herschel* PDF and the power-law tail.

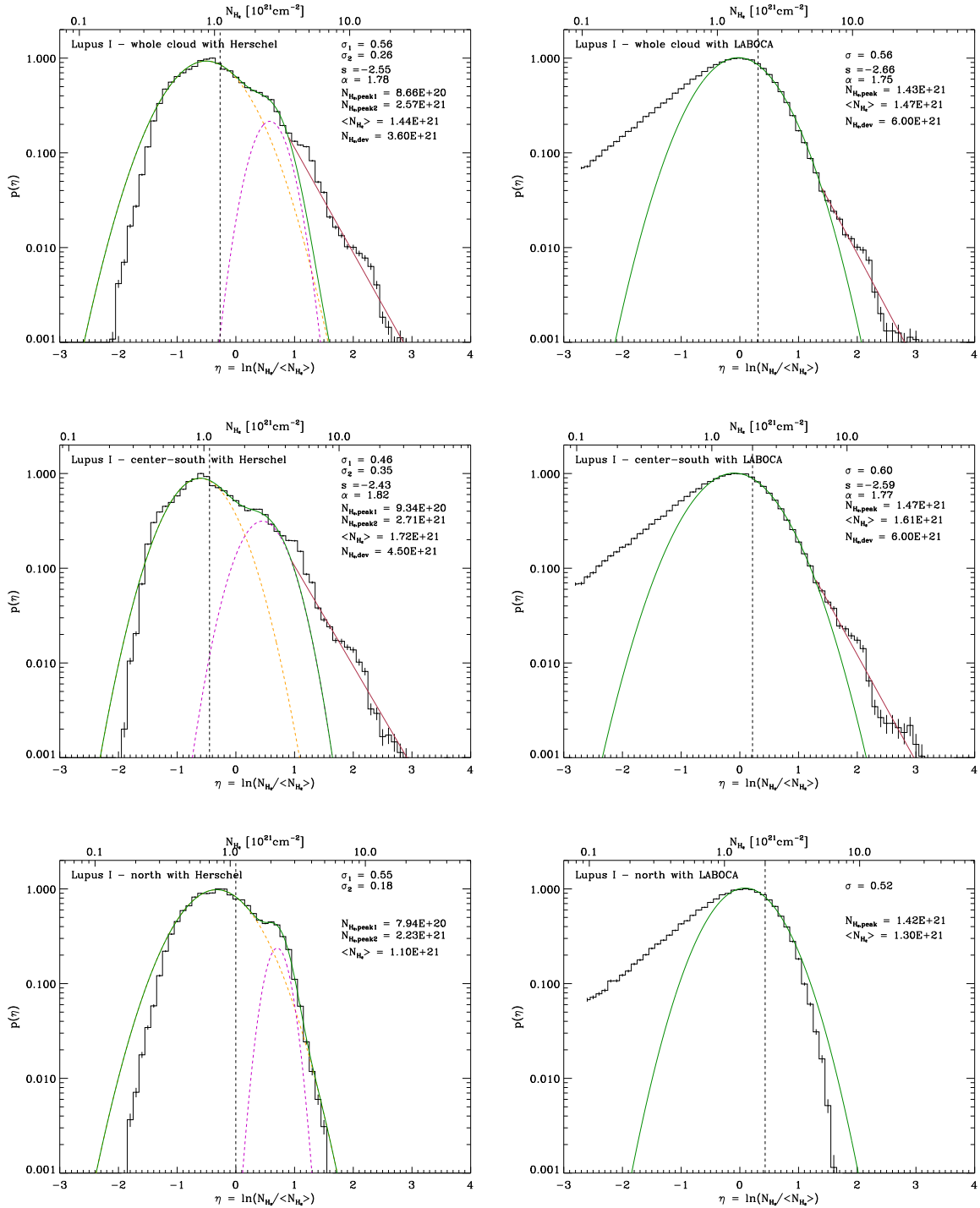


Figure 4.7: Column density PDFs of Lupus I and their model fits for the north and the center-south part of the cloud, as well as for the entire cloud. The error bars show the \sqrt{N} uncertainties. In case of *Herschel*, the two yellow and purple dashed lines show the fits of the two lognormals to the distribution around the first and second peak, respectively. Their superposition is represented by the solid green line. For LABOCA the solid green line shows the lognormal fit to the distribution around the peak. For all cases, the straight solid red line shows the power-law fit to the high-density tail of the PDF, if applicable. In each plot, I give the value of the dispersion(s) of the fitted lognormal(s) σ_i , the position(s) of the peak(s) of the lognormal(s) $N_{\text{H}_2, \text{peak}i}$, the slope of the fitted power-law tail s , the corresponding slope of an equivalent spherical density distribution α , the mean column density $\langle N_{\text{H}_2} \rangle$, and the deviation point from the lognormal to the power-law tail $N_{\text{H}_2, \text{dev}}$. The vertical dashed line marks the incompleteness limit (lowest closed contour) which is 1.1×10^{21} and $2 \times 10^{21} \text{ cm}^{-2}$ for the *Herschel* and LABOCA map, respectively.

4.2.2 Robustness of the PDF fit with respect to the bin size

I exemplarily chose the *Herschel* PDF of the whole cloud to study the effects of the bin size on the PDF fit. The results of the PDF fits for the four different bin sizes of 0.05, 0.1, 0.15, and 0.2 are shown in Figure 4.8. In all cases the widths of the two lognormals do not change significantly except for σ_2 at the largest bin size of 0.2 which increases by $\approx 20\%$ compared to the smaller bin sizes. The peak positions of both components, however, systematically shift to lower column densities with increasing bin size. Furthermore, the second peak becomes less prominent when the bin size is increased and I expect it to merge with the first peak for even larger bin sizes. The slope of the power-law remains almost constant with increasing bin size, except for the highest bin size where it is steeper than for the lowest. The deviation point into the power-law changes only for the highest bin size and is shifted by about 6% to a higher value of $3.85 \times 10^{21} \text{ cm}^{-2}$ which is a consequence of the steeper power-law tail. Therefore, the change of the fit parameters is not critically dependent on the bin size if it is not too small (< 0.05) or too big (> 0.2). The main features of the PDF (double-peak and power-law tail) still remain recognizable within the bin size interval I chose. However, a bin size of 0.1 seems to be the best compromise between maintaining the main features of the PDF and lowering the noise in the high density bins (see bin size of 0.05). Similar conclusions were presented by Schneider et al. (2015) who investigated the *Herschel* data of two low-mass and two high-mass star forming regions.

4.2.3 An alternative approach to fitting column density PDFs

In this section, I present an alternative approach to fit column density PDFs. Its main idea is to compute a cumulative density distribution (CDF) from the column density map and compare it with the CDF of a simulated distribution using a Kolmogorov-Smirnov test (KS test). The advantage of this method is that the data do not have to be binned in a histogram what reduces their information content. However, this approach turned out to be more complex and time-consuming (especially concerning computational time) than I thought beforehand and therefore I had to stop further investigation at a certain point. Nevertheless, I would like to report on the idea and my progress.

Here, I concentrate on the northern part of Lupus I. Since the PDF of this part shows a double-peak, I assumed that this is due to two different column density distributions that overlay each other. Hence, I created two random lognormal distributions with different widths $\sigma_{1,\text{sim}}$ and $\sigma_{2,\text{sim}}$ as well as different peak positions $N_{\text{H}_2,\text{peak1},\text{sim}}$ and $N_{\text{H}_2,\text{peak2},\text{sim}}$. Those two were then concatenated to one distribution of which the CDF was calculated. The number of values in each distribution was set to a percentage of a previously chosen total number of values that the joined distribution should have. I chose ten times the number of pixels in the *Herschel* column density map what yields about 1.5 million values. In the last step, the CDF of the simulated distribution was compared to the CDF of the *Herschel* column density map via the KS test to determine whether the distributions are similar to each other. The column density distribution is incomplete at the low column density end because of the sensitivity limit of *Herschel*. Therefore, I chose a lower limit of

$3.7 \times 10^{20} \text{ cm}^{-2}$ for the KS test, and the two distributions were only compared above it, as they diverge from each other below the limit.

Six free parameters are required to construct the simulated distributions for the northern part of the cloud. For the center-south part and the whole cloud, another two free parameters are added (size of power-law distribution and its slope). In principle, one could set up a grid of parameters, run all possibilities and test which set gives the best Kolmogorov statistic. However, the most critical aspect of this approach is the computational time. To test one set of parameters takes about 4–6 seconds. Reducing the number of free parameters to four by fixing the size of the two simulated lognormal distributions and testing ten different values for each free parameter, requires 10^4 comparisons which takes about 14 hours. Hence, a good guess for the possible parameter range is important to reduce computational time. I used the results of the fit to the PDF of the northern part, i.e. the two widths ($\sigma_1 = 0.55$, $\sigma_2 = 0.18$) and peak positions ($0.794 \times 10^{21} \text{ cm}^{-2}$, $2.23 \times 10^{21} \text{ cm}^{-2}$), as my initial guesses and explored the parameter space within ± 0.15 for σ_i and $\pm 0.15 \times 10^{21} \text{ cm}^{-2}$ for the peak positions. The size of the first lognormal distribution was varied between 86% and 94% of the total size of the simulated distribution.

The KS test is based on the calculation of the maximum vertical deviation $d_{\max} = \sup_{N_{\text{H}_2}} |\text{CDF}(N_{\text{H}_2})_{\text{sim}} - \text{CDF}(N_{\text{H}_2})_{\text{data}}|$ between the CDF of the simulated and the observed distribution. The parameter set that gives the smallest d_{\max} is considered as the best fit. In several runs, I determined step by step the best set of parameters and the result is shown in Figure 4.9. The left panel shows the two CDFs (black: observed, green: best fit simulated), the resulting best fit parameters of the two distributions, and the size of the first distribution (pt_1). The right panel shows the PDF of the best fit simulated distribution (green histogram) and of the observed column density map (black histogram). For comparison the fit directly to the PDF of the northern part (cf. bottom left panel of Figure 4.7) is shown as the solid green line. The four parameters describing the two lognormal distributions have higher values than in the PDF fit case. The difference varies between 2% and 10% which is within the assumed error of 10% for the PDF fit (see Section 4.2). The PDF fit to the observed column density distribution (green solid line) intersects all but three bins of the whole simulated distribution (green histogram in right panel of Figure 4.9).

This approach is in principle simple, but requires a-priori knowledge of the underlying distributions and a good guess for the initial parameter range. This can be obtained from the analysis of the observed PDF. Also a rough estimate of the peak positions, the widths and the power-law slope could be determined from the PDF without a fit. Then a grid of parameters can be set up. How fine the grid should be, depends on the available time. This heavy time dependence is, from my perspective, the biggest disadvantage of this approach. It renders this method impractical since the exploration of a finely spaced parameter grid takes several days or even weeks. In this aspect the PDF fit clearly has an advantage over the presented alternative approach. The fit is done in a few seconds and its results are in agreement with the results of the alternative approach.

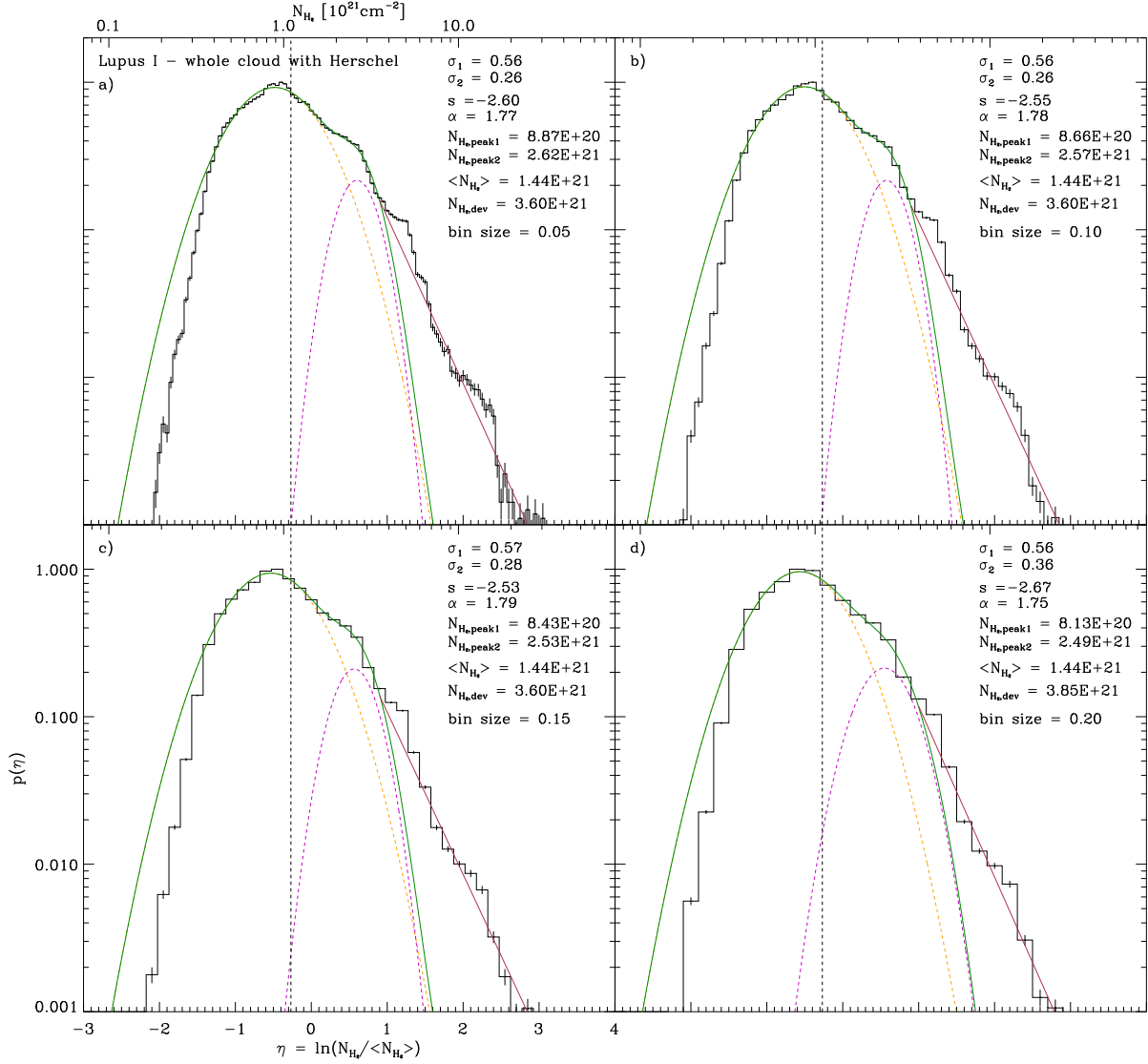


Figure 4.8: Fits to the column density PDF of the whole cloud with *Herschel*. The four panels show the PDF with four different bin sizes of a) 0.05, b) 0.1, c) 0.15, and d) 0.2. All other quantities as in Figure 4.7.

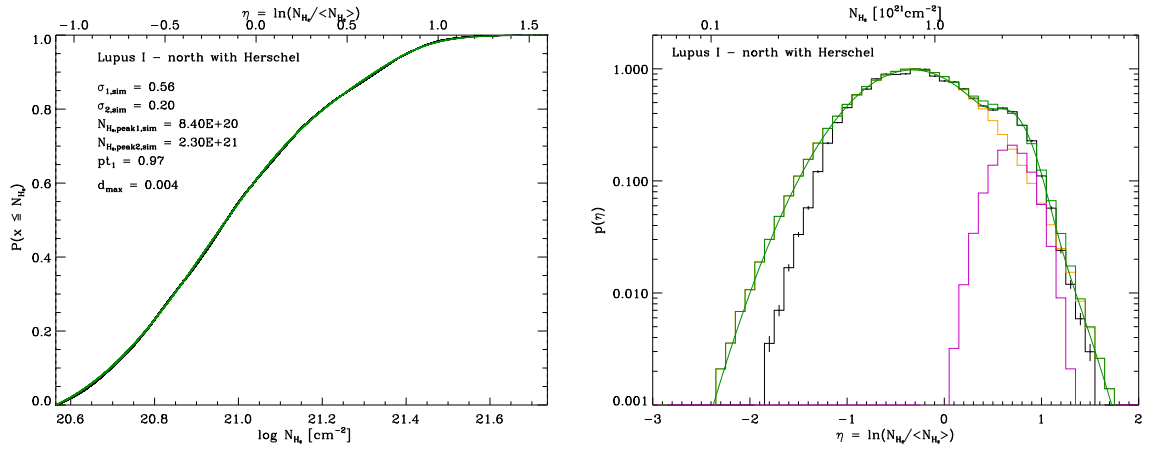


Figure 4.9: *Left*: Cumulative distribution functions of the best fit simulated distribution (green) and the observed distribution (black) for the northern part of Lupus I. The width $\sigma_{i,\text{sim}}$ and peak position $N_{\text{H}_2,\text{peak}i,\text{sim}}$ for each of the two simulated lognormal distributions that were concatenated are given in the upper left of the plot. The parameter pt_1 gives the size of the first simulated distribution in terms of percentage of the total number of values in the concatenated distribution. Accordingly, the size of the second simulated distribution is $1 - \text{pt}_1$. The KS test parameter d_{max} gives the goodness of the fit. It represents the maximum vertical deviation between the two CDFs. For the KS test the two distributions were compared with each other only above a completeness limit of $3.7 \times 10^{20} \text{cm}^{-2}$. *Right*: Column density PDF of the observed distribution (black; with \sqrt{N} error bars), the two simulated distributions (yellow and purple), and the concatenated distribution (green). The green solid line gives the fit to the PDF for comparison (see bottom left panel of Figure 4.7).

4.3 Distribution of cores in Lupus I from LABOCA

For the core analysis in the LABOCA map, I used the `Clumpfind` package (Williams et al. 1994). It decomposes the emission of the map into a set of clumps or cores contouring the data at given threshold levels. The results can be found in Table 4.3 and the distribution of the cores (represented by the white crosses) is shown in the left panel of Figure 4.10. The algorithm identified 15 different cores with masses between 0.07 and 1.71 M_{\odot} . Their total mass is 8.37 M_{\odot} and their total flux is 25.39 Jy. This corresponds to $\sim 5\%$ of the total mass of Lupus I (see Section 4.4) and $\sim 5\%$ of the total flux of the LABOCA map. For the computation of the core masses, I derived their temperatures from the *Herschel* SPIRE SED fit temperature map as the mean temperature within the ellipse representing a core and calculated the mass following Schuller et al. (2009)

$$M = \frac{d^2 F_{\nu} R}{B_{\nu}(T_d) \kappa_{\nu}} \quad (4.7)$$

where d is the distance to Lupus I, F_{ν} the total flux of the core, $R = 100$ the dust-to-gas ratio, and $\kappa_{\nu} = 1.32 \text{ cm}^2 \text{ g}^{-1}$ (see Section 4.1.6). Interestingly, all but one core are found in the center-south part of Lupus I. This confirms my interpretation of the column density maps, i.e. that active star formation is taking place in this part of Lupus I.

The distribution of the cores from the *Herschel* data (Rygl et al. 2013) agrees with this picture and the core distribution from my LABOCA map. The northern part of Lupus I is mainly populated by unbound cores and just one pre-stellar core, whereas the center-south is dominated by pre-stellar cores, many of which coincide with my LABOCA cores. However, a direct assignment is not easily possible since the *Herschel* coordinates can only be estimated from the source images in the paper of Rygl et al. (2013) and in some cases several *Herschel* sources seem to be on the position of one LABOCA source or vice versa.

Benedettini et al. (2012) found eight dense cores in Lupus I using high-density molecular tracers at 3 and 12 mm with the Mopra telescope (red diamonds in right panel of Figure 4.10), seven of which have one or more counterparts in my LABOCA map. The matches are given in Table 4.3. They classify five of their cores as very young protostars or pre-stellar cores (Lup1 C1-C3, C5, and C8) and the remaining three also as very likely to be protostellar or pre-stellar. For three of their cores (Lup1 C4, C6, and C7), they calculated a kinetic temperature of ≈ 12 K. This agrees within 20% with the core temperatures derived from the *Herschel* SPIRE SED fit temperature map.

Of the 17 young stellar objects found in Lupus I by the *Spitzer* c2d near-infrared survey (Chapman et al. 2007; Merín et al. 2008), 11 lie within the boundaries of the LABOCA map (blue boxes in right panel of Figure 4.10), but only one object (IRAS 15398–3359) clearly matches one of my LABOCA cores (#1). This is the well-known low-mass class 0 protostar IRAS 15398–3359 (inside the B228 core) which has a molecular outflow (see e.g. Oya et al. 2014; Dunham et al. 2014). Two other objects of the c2d survey are close, but offset by $\approx 0.5'$ to the center of our cores #3 and #5, respectively. Nevertheless, each of these two objects still lies within the boundaries of the corresponding ellipse representing the LABOCA core (see Table 4.3). Most of the LABOCA cores are potentially at a very

early evolutionary stage, i.e. without a protostar inside to heat it and eventually destroy the surrounding dust envelope to allow near-infrared radiation to escape. The only cores with a $70\ \mu\text{m}$ counterpart, which is a good proxy for a protostar inside a core, are #1 and #3. Therefore, I do not expect to find many *Spitzer* counterparts.

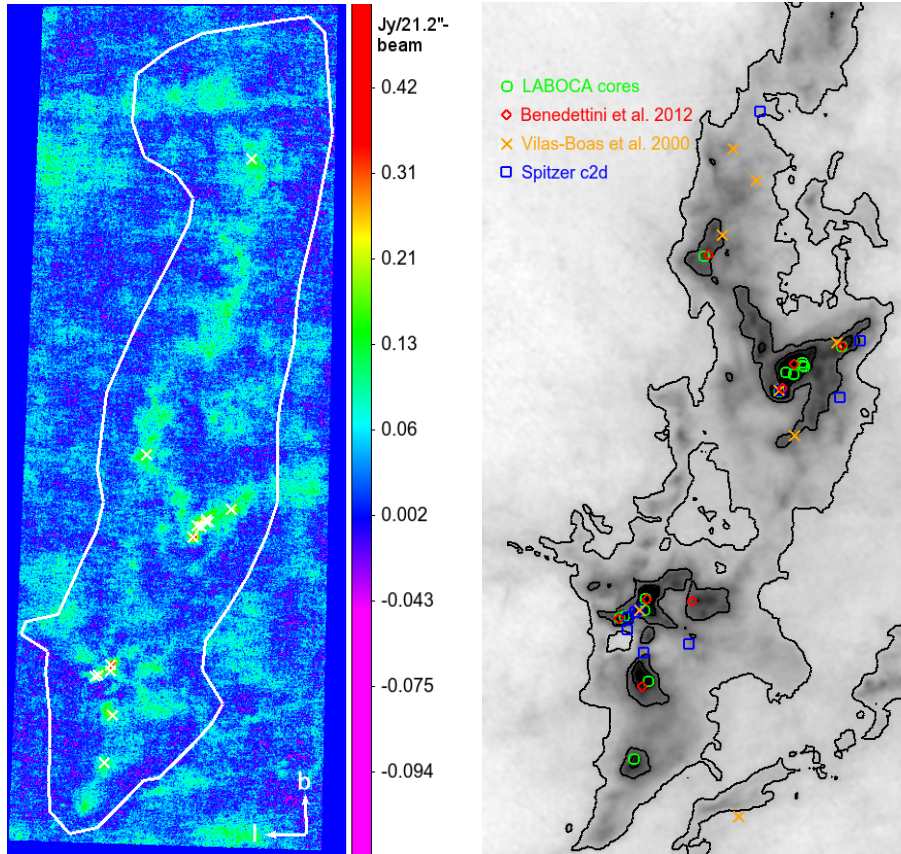


Figure 4.10: *Left*: Lupus I LABOCA $870\ \mu\text{m}$ map with square-root intensity scaling in units of $\text{Jy}/21.2''\text{-beam}$. The positions of the 15 cores that were found by `Clumpfind` are marked with white crosses. The white polygon indicates the common area within which the mass of the cloud was calculated from the LABOCA and *Herschel* column density maps (see Section 4.4). *Right*: *Herschel* column density map of the center-south region with contour levels of 1.1 , 4 , 7 , and $10 \times 10^{21}\ \text{cm}^{-2}$. The different symbols mark the center positions of the cores found with LABOCA and of objects found in other studies as discussed in Section 4.3.

Vilas-Boas et al. (2000) found 15 (14) condensations in C^{18}O (^{13}CO) with the 15 m SEST telescope. Eight cores lie within my LABOCA map (orange crosses in right panel of Figure 4.10), three of which (Lu7, Lu10, B228) coincide with LABOCA detected cores (#12, #5, and #1). Their C^{18}O excitation temperatures are 9, 11, and 10 K, respectively. This is $\approx 20\text{--}40\%$ lower than the temperatures from the *Herschel* map. For cores Lu7 and Lu10 they calculated a mass from C^{18}O of 11.7 and $3.1\ M_{\odot}$, respectively. This is a factor of ≈ 20 and ≈ 7 higher than the LABOCA masses. But the sizes of their condensations were on average larger than at least three times their beam size of $48''$.

The *Herschel* column density map of the center-south region with contour levels of 1.1, 4, 7, and $10 \times 10^{21} \text{ cm}^{-2}$ is displayed in the right panel of Figure 4.10. Overplotted are the LABOCA cores found in this study (green circles), as well as the above mentioned cores and YSOs found by Benedettini et al. (2012) (red diamonds), Vilas-Boas et al. (2000) (orange crosses), and the *Spitzer* c2d survey (blue boxes), respectively.

My findings confirm that Lupus I harbors a population of very young cores that are forming stars right now and probably have ages below 1 Myr. This could support the idea of an external shock agent, like the USco shell, sweeping up the cloud and triggering the simultaneous formation of new stars within the cloud.

Table 4.3: Parameters of the 15 cores detected in the LABOCA map with `Clumpfind` (see Figure 4.10). The beam size (HPBW) and area used to convert intensities into fluxes is $21.2''$ and 509 arcsec^2 , respectively. The total mass of all cores is $\approx 8 M_{\odot}$. Column 4 and 5 give the FWHM in x and y direction of the ellipses representing the cores. Columns 6, 7, and 8 give the core's peak intensity, total flux, and mass, respectively. The core temperature shown in column 9 was derived from the *Herschel* SPIRE SED fit temperature map as the mean temperature within the ellipse representing a core. The last column gives the matches to dense cores found by Benedettini et al. (2012).

#	Ra	Dec	a_x [$''$]	b_y [$''$]	I_{max} [Jy/beam]	F_{tot} [Jy]	M_{core} [M_{\odot}]	T_{core} [K]	Cp.
1	15:43:01.68	-34:09:08.9	58.22	44.38	1.37	5.61	1.71	14.0	Lup1 C4
2	15:44:59.85	-34:17:08.8	62.51	44.09	0.51	3.97	1.59	12.0	Lup1 C6
3	15:45:13.58	-34:17:08.8	46.56	33.45	0.33	1.48	0.40	15.0	Lup1 C7
4	15:45:16.02	-34:16:56.6	35.31	34.95	0.31	1.00	0.27	15.0	Lup1 C7
5	15:45:03.80	-34:17:57.3	57.22	42.24	0.28	1.41	0.46	13.5	Lup1 C6
6	15:42:52.86	-34:08:02.1	96.42	49.94	0.28	3.85	1.34	13.0	Lup1 C3
7	15:42:43.57	-34:08:14.2	70.62	44.38	0.25	1.64	0.57	13.0	Lup1 C3
8	15:42:44.55	-34:08:32.5	30.55	20.85	0.25	0.48	0.17	13.0	Lup1 C3
9	15:42:44.06	-34:08:44.6	36.82	19.26	0.24	0.49	0.17	13.0	Lup1 C3
10	15:42:50.42	-34:08:38.5	53.28	30.34	0.22	1.05	0.36	13.0	Lup1 C3
11	15:45:25.10	-34:24:01.8	42.46	69.57	0.22	1.63	0.53	13.5	Lup1 C8
12	15:42:23.02	-34:09:33.2	68.97	46.08	0.21	1.72	0.53	14.0	Lup1 C1
13	15:39:09.92	-33:25:30.9	27.24	27.70	0.20	0.34	0.07	17.0	-
14	15:45:55.75	-34:29:23.7	28.10	26.28	0.20	0.29	0.08	14.5	-
15	15:42:47.90	-33:53:15.3	43.80	19.59	0.19	0.43	0.12	15.0	Lup1 C2

4.4 Total mass estimates of Lupus I

To derive the total mass of the cloud from the three different column density maps, I defined a polygon around the filament (shown in left panel of Figure 4.10 on the LABOCA map) to derive the total mass always in the same area ($\approx 1 \text{ deg}^2$). The total gas and dust mass was then calculated via the formula

$$M_{\text{Lupus I}}^{\text{tot}} = \sum N_{\text{H}_2} \mu_{\text{H}_2} m_{\text{H}} A_{\text{p}} \quad (4.8)$$

with A_{p} the area of a pixel in cm^2 . As the common lower level I chose $N_{\text{H}_2} > 10^{21} \text{ cm}^{-2}$ which corresponds roughly to $A_{\text{V}} > 1 \text{ mag}$. The resulting total mass for Lupus I is $M_{\text{Lupus I}}^{\text{tot}} \approx 171 M_{\odot}$, $\approx 174 M_{\odot}$, and $\approx 164 M_{\odot}$ for the *Planck*, *Herschel*, and LABOCA data. This means that the total masses calculated from the three data sets agree with each other. Comparing the total mass of the cloud to the total mass in cores from LABOCA ($\approx 8 M_{\odot}$) one sees that only about 5% of the mass is concentrated in the densest condensations. Most of the dust and gas is in more diffuse components.

The most recent literature value for the total mass of Lupus I is from the *Herschel* data by Benedettini et al. (2015). They did a pixel-by-pixel modified blackbody fit to four *Herschel* bands (160, 250, 350, and $500 \mu\text{m}$) and derived a total mass from their column density map of $163 M_{\odot}$ for $A_{\text{V}} > 2 \text{ mag}$. The cloud area that is above this threshold of 2 mag is given with 0.32 deg^2 . In my work the cloud area above $1.88 \times 10^{21} \text{ cm}^{-2}$ (using the Bohlin et al. (1978) conversion factor) covers only 0.21 deg^2 . The total mass above this threshold is $109 M_{\odot}$. Scaling my value to the same area given in Benedettini et al. (2015), yields a total mass of $166 M_{\odot}$ which is in good agreement with their value.

In a previous work on the *Herschel* data of Lupus I, Rygl et al. (2013) calculated a total mass of $M = 830 M_{\odot}$ (for $A_{\text{V}} > 2 \text{ mag}$) which is higher by a factor of 4–5 compared to my value. They calculated the total mass in a much bigger area than this work ($\approx 4.5 \text{ deg}^2$ compared to my $\approx 1 \text{ deg}^2$) and used a different method to create their column density map as mentioned already in Sec. 4.1.8. Also Benedettini et al. (2015) pointed out that the original five band maps from which Rygl et al. (2013) derived their column density maps were produced with a different map-maker and older calibration files and they used a different opacity law.

Other literature values cover a wide range of total masses for Lupus I, depending on the tracer used and the size of the area that was considered. From the *Spitzer* c2d near-infrared extinction maps Merín et al. (2008) determined a total mass of $479 M_{\odot}$ for $A_{\text{V}} > 3$. Various CO measurements (e.g. Tachihara et al. 1996; Hara et al. 1999; Tothill et al. 2009) yielded values of $\approx 280\text{--}880 M_{\odot}$. Direct comparisons with my values are not always possible since all maps cover different parts of the Lupus I cloud complex and the material is not homogeneously distributed to allow scaling the mass with the area. But I note that my values agree with most of the literature values within a factor of 2–3 which is expected considering the uncertainties in the choice of the dust model, the dust-to-gas ratio and the CO-to- H_2 conversion factors.

4.5 Summary of the dust emission results

I have performed LABOCA continuum sub-mm observations of Lupus I that provide, for the first time, a direct view of the densest, coldest cloud clumps and cores at high angular resolution. I complemented these data with *Herschel* and *Planck* data from which I constructed column density and temperature maps. From the *Herschel* and LABOCA column density maps I calculated PDFs to characterize the density structure of the cloud.

The northern part of Lupus I is found to have, on average, lower densities, higher temperatures, and no active star formation. The center-south part harbors dozens of pre-stellar cores where density and temperature reach their maximum and minimum, respectively. My analysis of the column density PDFs from the *Herschel* data show double-peak profiles for all parts of the cloud, which I attribute to an external compression. In those parts with active star formation, the PDF shows a power-law tail at high densities. The PDFs I calculated from my LABOCA data trace the denser parts of the cloud showing one peak and a power-law tail. With LABOCA I find 15 cores with masses between 0.07 and $1.71 M_{\odot}$ and a total mass of $\approx 8 M_{\odot}$. The total gas and dust mass of the cloud is $\approx 164 M_{\odot}$ and hence $\sim 5\%$ of the mass is in cores. From the *Herschel* and *Planck* data I find a total mass of $\approx 174 M_{\odot}$ and $\approx 171 M_{\odot}$, respectively.

I find that the position, orientation, and elongated shape of Lupus I, the double-peak PDFs and the population of pre-stellar and protostellar cores might be explained by an external large-scale compression of the cloud. Possible agents of such a compression might be the advancing USco HI shell and the UCL wind bubble.

Chapter 5

Describing the gas kinematics in Lupus I using molecule emission

The results of the dust analysis presented in the previous chapter suggest a scenario of external compression of Lupus I from either USco or USco and UCL. Therefore, I proposed follow-up molecular line observations to further investigate this aspect because molecular lines are well suited to obtain kinematic information about the gas in Lupus I (see Section 2.3). Systematic differences within the cloud or between one side of the cloud and the other could reveal signs of interaction between the cloud and the surroundings, i.e. the HI shell of USco and the wind-blown bubble of UCL. In this chapter, I present $^{13}\text{CO}(J = 2 \rightarrow 1)$ and $\text{C}^{18}\text{O}(J = 2 \rightarrow 1)$ observations of three distinct regions within the Lupus I cloud. These regions will be called cut A, cut B, and cut C. They are marked in the right panel of Figure 3.1 on top of the LABOCA continuum map. Cuts A and C cross the main filament perpendicularly, cut B is more parallel to it but goes through the prominent class 0 protostar IRAS 15398–3359 in the center of the filament. Here, I present the analysis of the observational data and the comparison to the available HI data. The analysis of the CO and HI data was done by myself. The HI data was provided by my collaborator Daniel Kröll but analyzed by myself. I am also using the results from D. Kröll’s fit of an expanding homogeneous spherical shell model to the HI data of the USco region.

5.1 Spectra

All observed spectra are shown in Appendix A. The individual spectra are very complex, showing a variety of different line profiles. There are spectra with one, two or even three components. Many have asymmetric and non-Gaussian profiles. The average ^{13}CO and C^{18}O spectrum for each cut is shown in Figure 5.1. The solid lines represent the average ^{13}CO spectrum and the dotted lines the average C^{18}O spectrum multiplied by three. Cut A shows the lowest intensities of all three cuts in both lines. The averaged ^{13}CO line is very broad and asymmetric towards velocities lower than the velocity of the peak, i.e. 5.75 km s^{-1} . The peak intensity of the ^{13}CO line is 1.22 K. The ^{13}CO line of cut B is the

most narrow and has the highest peak intensity of all three cuts with a value of 4.44 K at $v_{\text{LSR}} = 5.02 \text{ km s}^{-1}$. For cut C the ^{13}CO line also peaks at $v_{\text{LSR}} = 5.02 \text{ km s}^{-1}$ with a peak intensity of 3.26 K. The averaged C^{18}O lines of cut B and cut C both peak at $v_{\text{LSR}} = 5.13 \text{ km s}^{-1}$ and have a peak intensity of 1.34 and 0.74 K, respectively.

The averaged spectra suggest the presence of a possible large-scale velocity gradient running along the filament's major axis from north-west (cut A) to south-east (cut C) of almost 1 km s^{-1} because the northern part of Lupus I has on average higher v_{LSR} velocities than the central and southern part. However, the behavior of this gradient throughout the cloud cannot be determined from these three cuts alone.

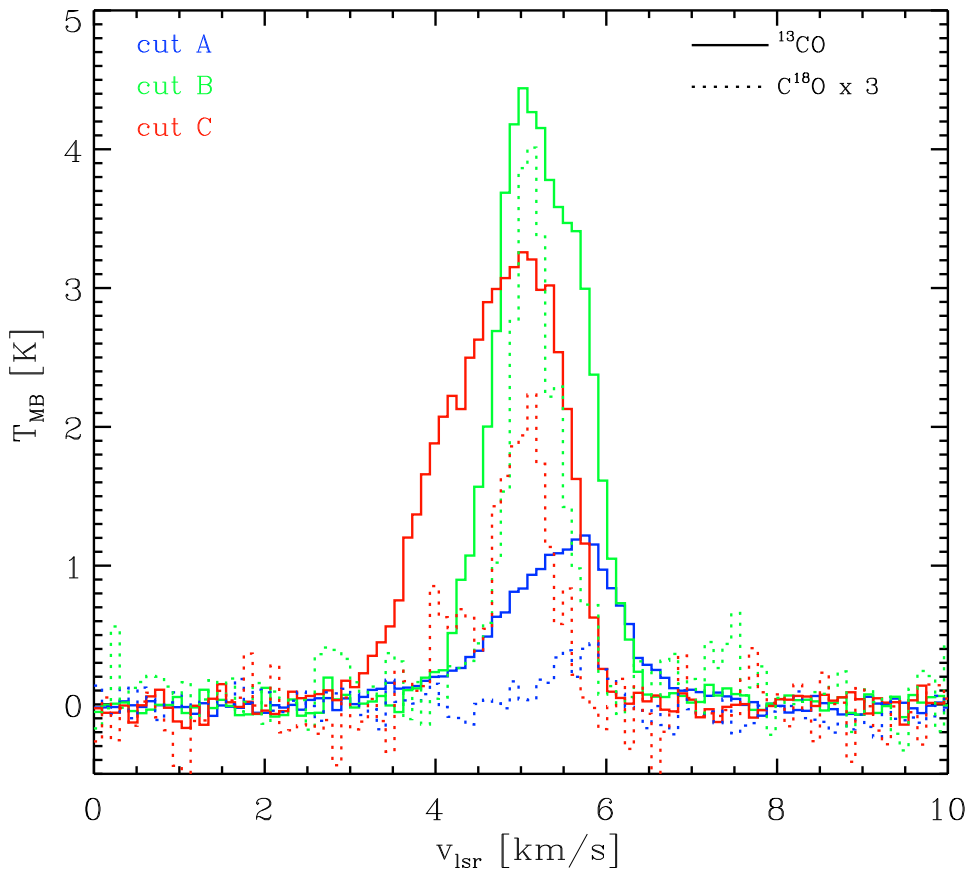


Figure 5.1: Average ^{13}CO and C^{18}O spectra of the three cuts. The integrated intensities (for $v_{\text{LSR}} = 0 - 10 \text{ km s}^{-1}$) of the ^{13}CO lines are 1.96, 5.69, and 5.55 K km s^{-1} for cut A, B, and C, respectively. Those of the C^{18}O lines are 1.22, and 0.50 K km s^{-1} for cut B and cut C, respectively.

5.2 Velocity channel maps

Velocity channel maps for each cut and molecular line are shown in Figures 5.2 to 5.4. The velocity range shown is $v_{\text{LSR}} = 3.2\text{--}6.8 \text{ km s}^{-1}$ and the channel separation is $\approx 0.1 \text{ km s}^{-1}$. The maps have been convolved with a Gaussian of two pixels or approximately one beam.

Cut A The main ^{13}CO emission in cut A is at velocities of $v_{\text{LSR}} = 5.5\text{--}6.2 \text{ km s}^{-1}$ with the highest intensities between 5.9 and 6.1 km s^{-1} . The emission is concentrated on the center of the cut and extends to about $10'$ around the center in the channels with highest intensities. At $v_{\text{LSR}} = 6.4 \text{ km s}^{-1}$ the spatial extent of the emission is decreased to $\sim 2'$ around the center. Between $v_{\text{LSR}} = 3.4\text{--}2.8 \text{ km s}^{-1}$ a narrow emission patch appears north-east of the center. Its peak intensity is about one third ($\approx 2 \text{ K}$) of the maximum intensity of the entire cut (at 6 km s^{-1}). The C^{18}O emission appears only in the channels $v_{\text{LSR}} = 5.1\text{--}6.3 \text{ km s}^{-1}$ with a peak intensity of $\approx 2 \text{ K}$ at 5.9 km s^{-1} . Spatially, the C^{18}O emission region is limited to about $2'$ around the very center of the cut.

Cut B The highest intensities of the three cuts are found in cut B. Most of the emission is at $v_{\text{LSR}} = 4.7\text{--}5.8 \text{ km s}^{-1}$ with peak intensities of up to $\approx 7.5 \text{ K}$ between 4.9 and 5.1 km s^{-1} . Between $v_{\text{LSR}} = 4.2\text{--}6 \text{ km s}^{-1}$ a second emission region at the south-eastern edge is apparent and is spatially separated from the center. This second region has its emission peak in the 4.8 km s^{-1} channel. The bulk of the C^{18}O emission lies between $v_{\text{LSR}} = 4.9\text{--}5.4 \text{ km s}^{-1}$ and hence in the same range as the ^{13}CO emission. It is concentrated on the center of the cut and no emission is found at either edge.

Cut C Within cut C several spatially distinct emission regions can be seen in ^{13}CO and C^{18}O . The highest intensity of $\approx 6 \text{ K}$ is seen at a velocity of $v_{\text{LSR}} = 5.1 \text{ km s}^{-1}$ at a location north-east of the center. A second intensity peak of $\approx 5 \text{ K}$ at 4.2 km s^{-1} can be found in the center of the cut. In contrast to the other two cuts, the ^{13}CO and C^{18}O emission peaks do not overlap, but are located at opposite ends of the cut. C^{18}O emission is found at three positions within the cut. For $v_{\text{LSR}} = 4.2\text{--}5.0 \text{ km s}^{-1}$ there is emission in the center. For $v_{\text{LSR}} = 4.8\text{--}5.3 \text{ km s}^{-1}$ emission appears south-west of the center where it also has its peak with an intensity of about 4 K . At the position where ^{13}CO has its highest emission, C^{18}O emission is in the velocity range of $v_{\text{LSR}} = 5.1\text{--}5.5 \text{ km s}^{-1}$ with a peak intensity of about 3 K at 5.3 km s^{-1} .

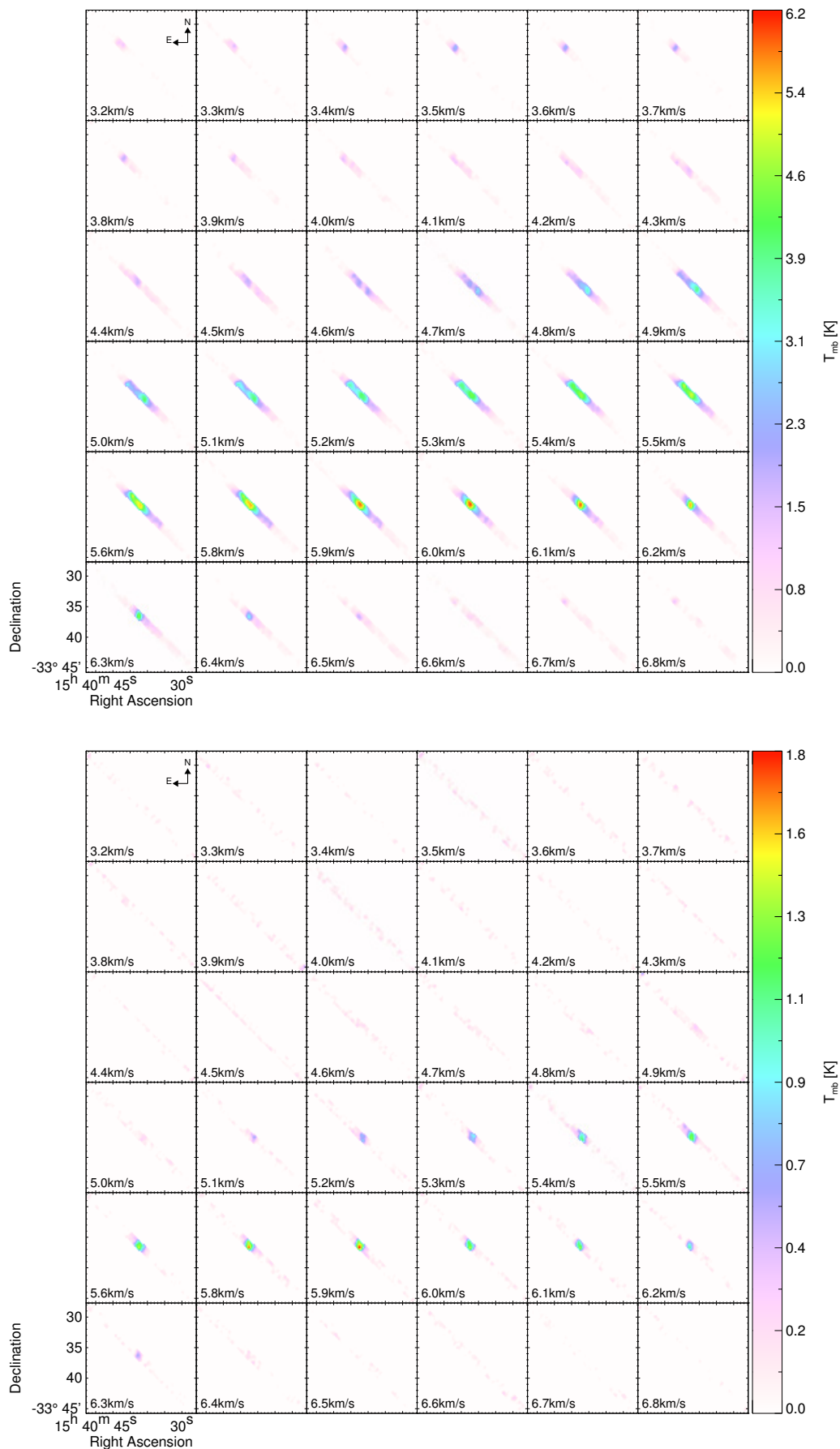


Figure 5.2: Velocity channel map of cut A in the ^{13}CO (upper panel) and the C^{18}O (lower panel) line. The velocity of each channel is given in the lower left of each plot panel. A Celestial compass is displayed in the upper- and leftmost panel. The intensity scale is given in main-beam temperature T_{mb} .

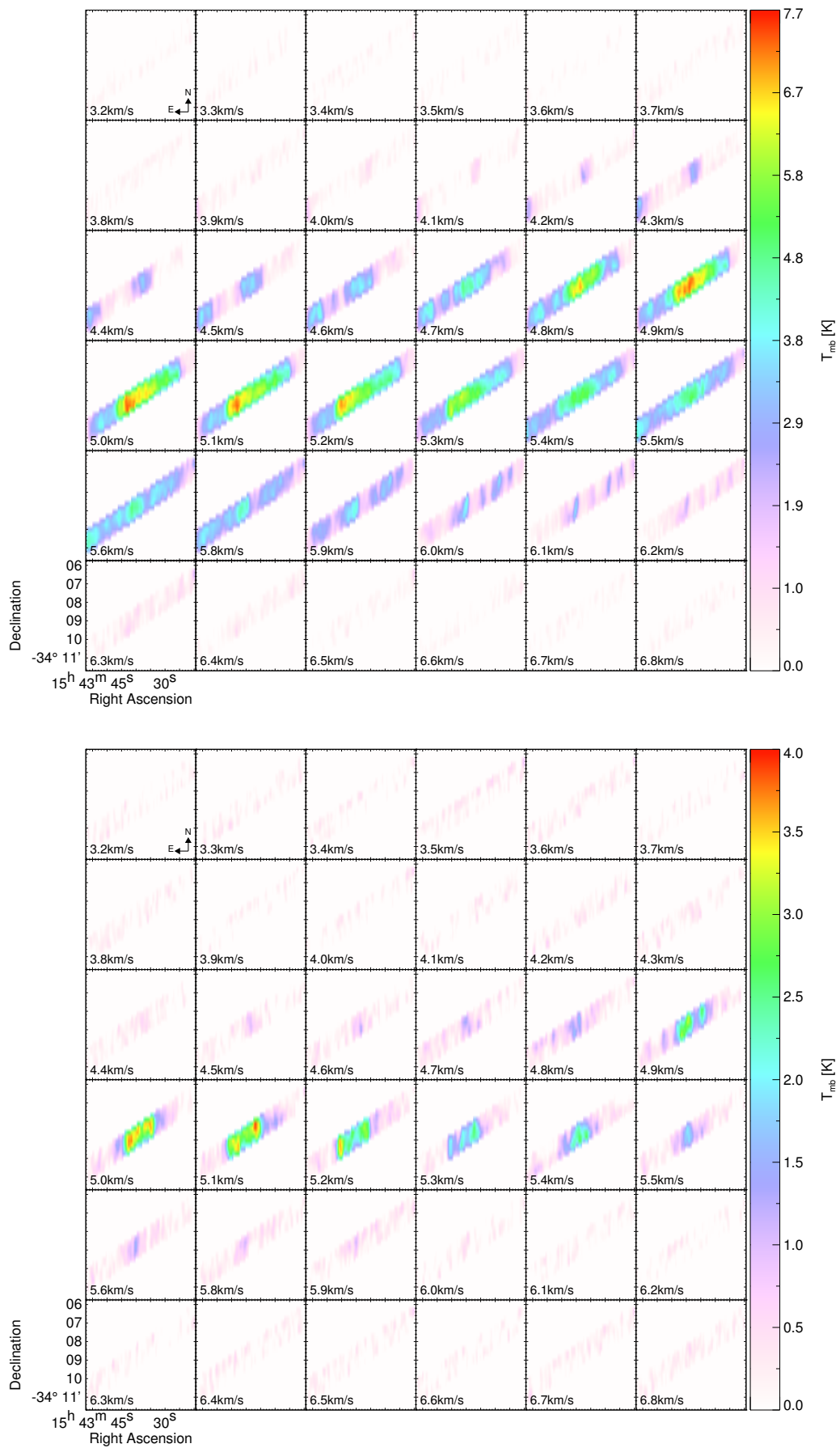


Figure 5.3: Same as Figure 5.2 but for cut B.

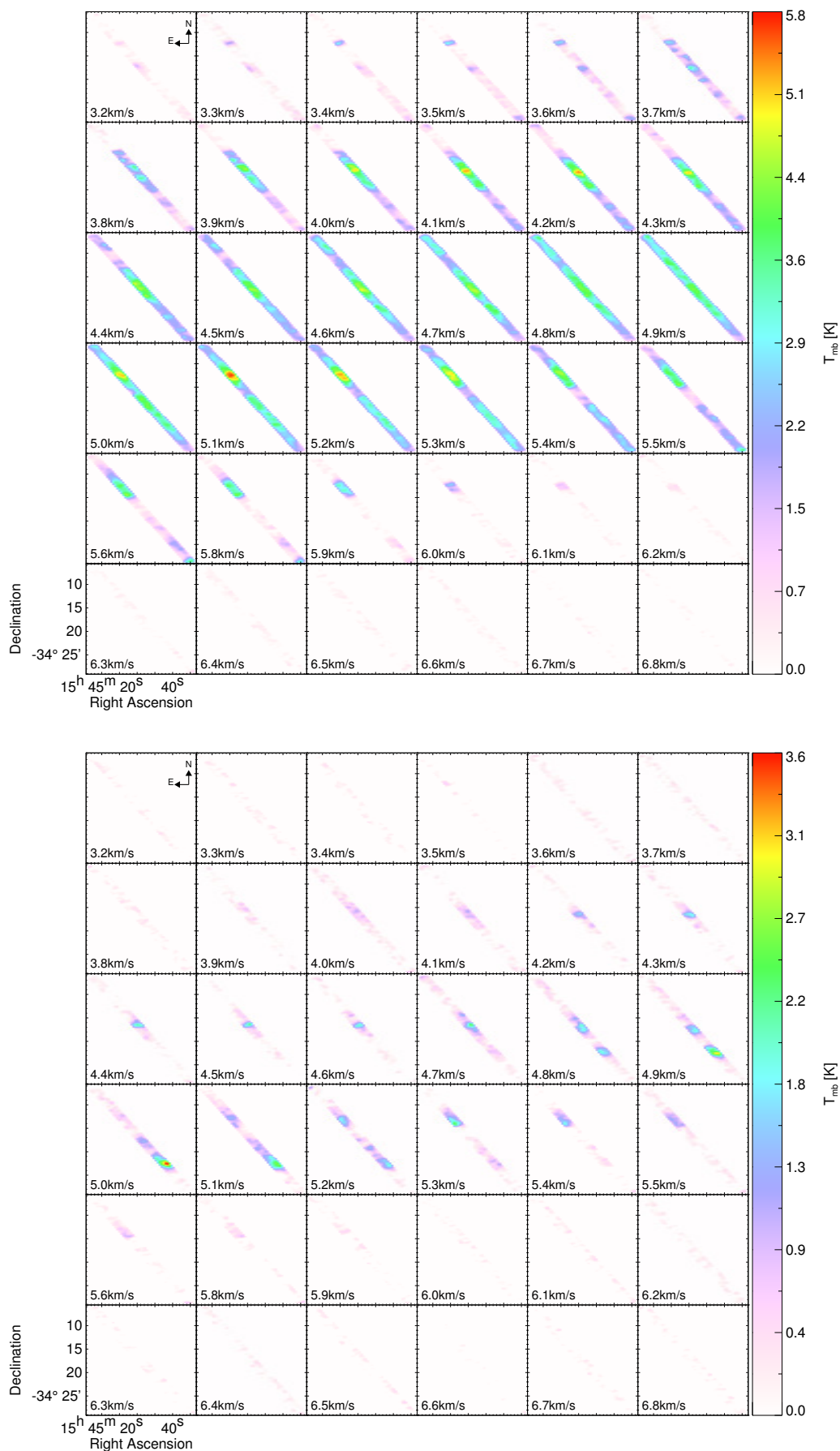


Figure 5.4: Same as Figure 5.2 but for cut C.

5.3 PV diagrams

In PV diagrams different velocity components that are present in a cloud and may overlay each other, can often be disentangled (see e.g. Hacar et al. 2013). The PV diagrams of the three cuts along a line through the center of each cut are presented in Figure 5.5. The x-axis gives the position along this line. The white crosses mark the velocity of the peak intensity at each x-position. The cutoff for the peak intensity marks is set to 1 K in ^{13}CO for all three cuts and 0.5 K in C^{18}O for cuts B and C. The C^{18}O cutoff for cut A is 0.3 K.

Cut A Two velocity components are present in this cut. One main component in the center of the cut which is traced by both isotopologues and extends from $v_{\text{LSR}} \approx 5\text{--}6.5 \text{ km s}^{-1}$ in velocity space. Moreover, there is a second component that is apparent only in ^{13}CO at the north-eastern edge of the cut (on the left of the PV diagram). It ranges between $v_{\text{LSR}} \approx 3.2\text{--}4 \text{ km s}^{-1}$ and might be a sub-filament of Lupus I with a different gas velocity. The ^{13}CO data suggest that there is also a third, very faint component at velocities of $v_{\text{LSR}} = 6.5\text{--}7 \text{ km s}^{-1}$ at the north-eastern edge of the cut.

Cut B The C^{18}O and ^{13}CO PV diagrams of cut B reveal that this cut is one coherent structure in velocity space where most of the gas has velocities of $v_{\text{LSR}} = 4.5\text{--}6 \text{ km s}^{-1}$. There are, however, signs of two other ^{13}CO components present at the south-eastern edge of the cut (on the left of the diagram). They are located at positions between $0'$ and $6'$ and separated in velocity by about 1 km s^{-1} . The first component extends between 5.4 and 5.9 km s^{-1} and is coherent in velocity. The second one shows a south-east to north-west velocity gradient: the velocity increases by more than 1 km s^{-1} from 4.3 to 5.4 km s^{-1} between the positions of $1'$ to $\sim 5'$. Both components could be sub-filaments of Lupus I with a different gas velocity that overlay each other at those positions. Although the intensities at those positions are very low, the C^{18}O data also suggest the presence of these two components. Finally, it is interesting to note that although the center of the cut harbors the class 0 protostar, and known outflow source IRAS 15398–3359 (LABOCA continuum emission is shown in Figure 5.6), there are no signs of infall or outflows apparent in the PV diagram.

Cut C The PV diagram of cut C is the most complex and reveals three structures separated both in velocity and position space. Those three structures are present in both the ^{13}CO and the C^{18}O data. The structure in the center of the cut shows a steep velocity gradient of about 1 km s^{-1} from south-west (on the right of the PV diagram) to north-east (on the left of the PV diagram) on a length scale of about $7'$ or 0.3 pc . In both tracers the velocity decreases from about 5.1 to 4 km s^{-1} . This might be a sign of infall motion in the pre-stellar core present at this position (see Figure 5.6). The other two structures are located on opposite sides of the center. The structure north-east of the center has velocities between $v_{\text{LSR}} = 4.3\text{--}6.2 \text{ km s}^{-1}$ in ^{13}CO and shows a decreasing velocity gradient away from the center which is, however, not present in the C^{18}O data. The peak of the ^{13}CO emission is found within this structure north-east of the center. The third structure is located south-west of the center. Both tracers confirm that it is coherent in velocity space with $v_{\text{LSR}} = 4.6\text{--}5.3 \text{ km s}^{-1}$. The C^{18}O emission has its peak within this third structure whereas the ^{13}CO emission is weaker than in the structure north-east of the center.

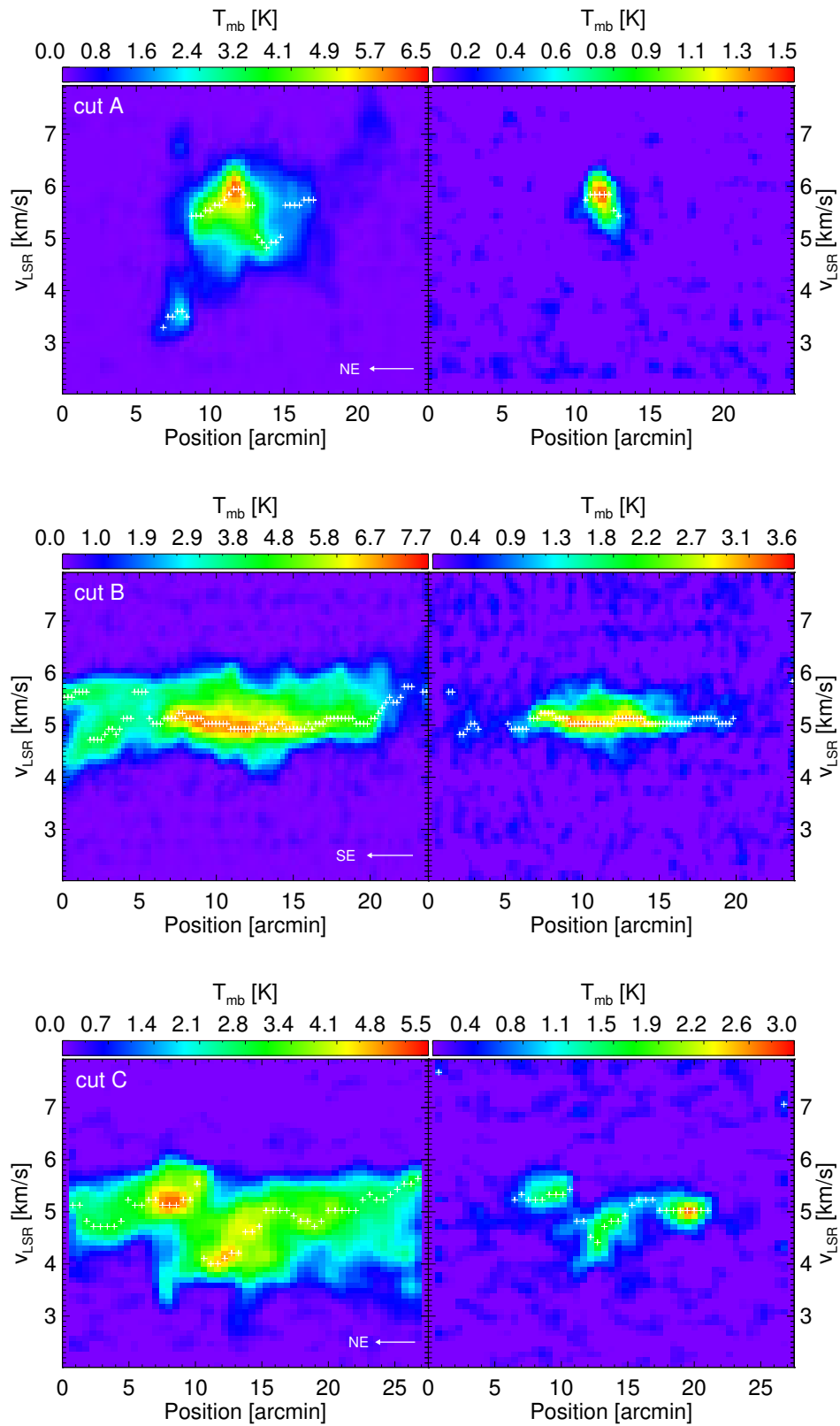


Figure 5.5: Position-velocity diagrams of cut A, B, and C (from top to bottom) in ^{13}CO (left panel) and C^{18}O (right panel) along a line through the middle of the cut. The x-axis gives the position along this line. The white arrow in the bottom right corner indicates the orientation of the cut in the Celestial coordinate frame. The white crosses mark the velocity of the peak intensity at each x-position. The cutoff is set to 1 K in ^{13}CO for all three cuts and 0.5 K in C^{18}O for cuts B and C. The C^{18}O cutoff for cut A is 0.3 K. All maps have been convolved with a Gaussian of two pixels or approximately one beam.

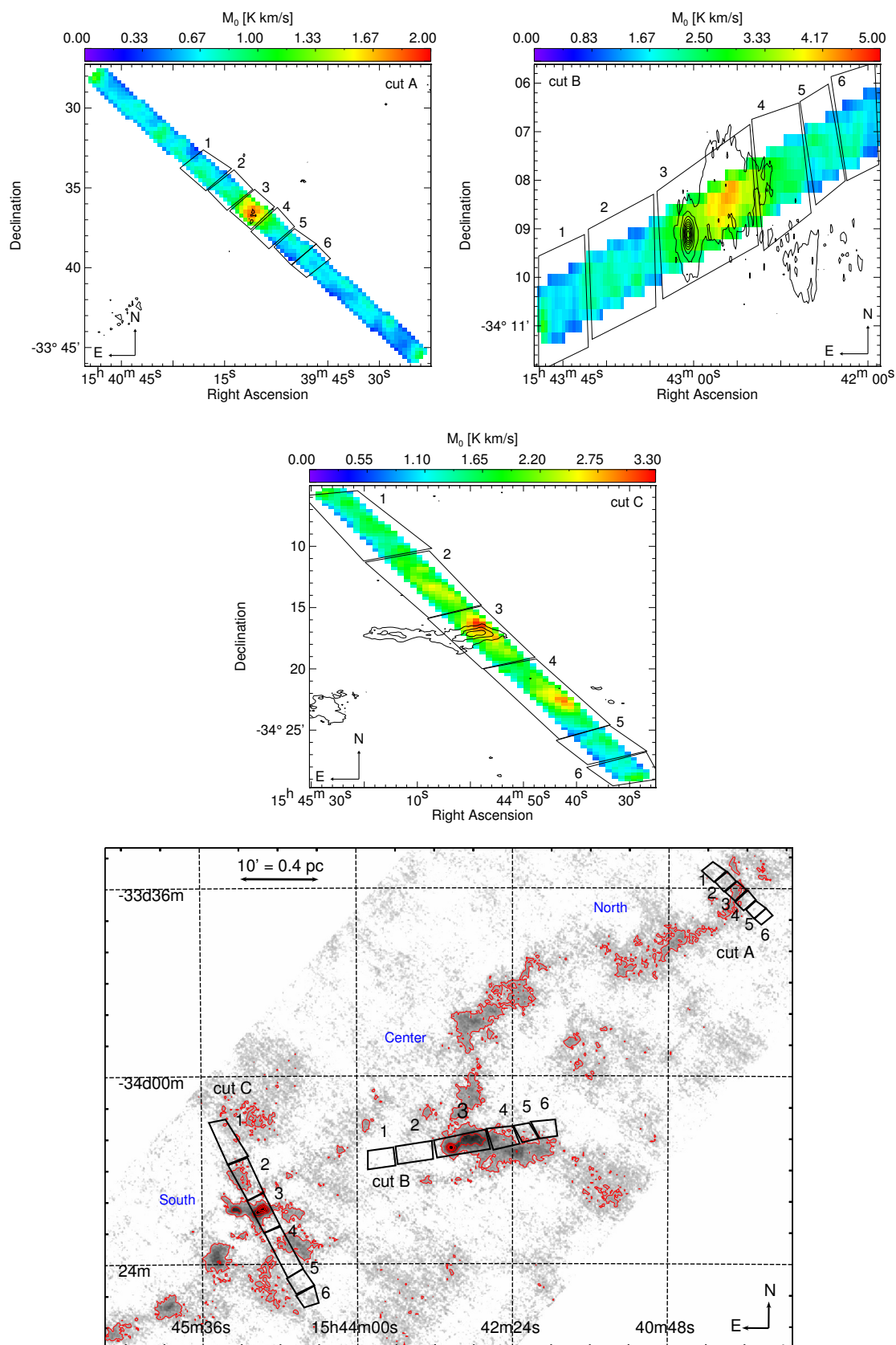


Figure 5.6: Integrated $C^{18}O$ intensity maps of cut A, B (top row), and C (middle row). The six boxes into which each cut was divided are shown, as well as the contours of the LABOCA $870 \mu\text{m}$ continuum emission. Levels are from 10%–100% of the peak intensity of 1.37 Jy/beam . The bottom panel shows the dust column density map from LABOCA with red contour levels of 0.3, 1, 1.7, 2.3, and $3 \times 10^{22} \text{ cm}^{-2}$.

5.4 Moment maps

The three moment maps of each cut calculated for both ^{13}CO and C^{18}O are shown in Figures 5.7 and 5.8. For visualization purposes the maps have been convolved with a Gaussian of two pixels or approximately one beam. This reduces the noise, but also leads to some unwanted edge effects because of the neighboring NaN values.

The zeroth moment is the integrated intensity of the line

$$M_0 [\text{K km s}^{-1}] = \Delta v \sum_v T_{\text{mb},v} \quad (5.1)$$

with Δv the width of a velocity channel and $T_{\text{mb},v}$ the main-beam temperature at velocity channel v . The first moment is the intensity-weighted velocity of the line or mean (also centroid) velocity of the gas. It is given by

$$M_1 [\text{km s}^{-1}] = \frac{\sum_v T_{\text{mb},v} v}{M_0} \quad (5.2)$$

Finally, the second moment

$$M_2 [\text{km s}^{-1}] = \sqrt{\frac{\sum_v T_{\text{mb},v} (v - M_1)^2}{M_0}} \quad (5.3)$$

represents the velocity dispersion of the gas along the LOS. If the spectrum consisted of just one single Gaussian line, M_0 would represent the area, M_1 the mean, and M_2 the standard deviation of this Gaussian. To take into account the entire emission of the cloud, I chose an integration range of $v = 0\text{--}10 \text{ km s}^{-1}$. The channel width is $\Delta v = 0.1 \text{ km s}^{-1}$. These moment maps can be created with the `GO MOMENTS` task of the `CLASS` software.

Cut A The integrated emission of both lines is concentrated on the center of the cut and decreases off-center. The central region shows similar mean velocities (about 5.5 km s^{-1}) in both tracers. The velocity dispersion is smaller in ^{13}CO ($\approx 3 \text{ km s}^{-1}$) than in C^{18}O ($\approx 5 \text{ km s}^{-1}$). The increased velocity dispersion in ^{13}CO at both ends of the cut is probably a numerical artifact, because the integrated intensity at these pixels was already too low.

Cut B High values of the integrated ^{13}CO intensities are present almost everywhere throughout cut B. The emission increases from the edges towards the center where it peaks at about 11 K km s^{-1} . A similar picture is drawn by the C^{18}O emission. Both lines peak at the same position slightly north-west of the center. This peak position, however, does not agree with the position of the $870 \mu\text{m}$ continuum emission peak from LABOCA which is located further south-east of the CO peaks (see Figure 5.6). Both isotopologues reveal a homogeneous mean velocity of about 5.5 km s^{-1} within the cut. The velocity dispersion is lower where the integrated emission is higher and thus increases from the center towards the edges. It ranges between $3\text{--}5 \text{ km s}^{-1}$ for ^{13}CO and $5\text{--}7 \text{ km s}^{-1}$ for C^{18}O .

Cut C Several "islands" of enhanced integrated ^{13}CO and C^{18}O emission are present in cut C. Moreover, the peak of the emission in each line does not overlap. The peak of the integrated ^{13}CO emission is found north-east of the center whereas the C^{18}O peak is located in the center of the cut. At the position of the ^{13}CO peak there is no enhanced C^{18}O emission. Another C^{18}O peak appears in the south-western part of the cut where instead no enhanced ^{13}CO emission is seen. The mean velocity of the C^{18}O gas is not homogeneous but oscillates within the cut between $\approx 4.6\text{--}5.3\text{ km s}^{-1}$. The mean velocity of ^{13}CO is homogeneous in the center ($\approx 4.5\text{ km s}^{-1}$) but is increased at both edges of the cut with values between 5 and 5.3 km s^{-1} . The velocity dispersion of the gas is approximately constant in the central part of the cut but again higher at both edges. In the center of cut C the velocity dispersion of ^{13}CO is about 3 km s^{-1} ; that of the C^{18}O gas about 5 km s^{-1} . At the edges it is $4\text{--}4.5\text{ km s}^{-1}$ for ^{13}CO and $6\text{--}7.5\text{ km s}^{-1}$ for C^{18}O .

The spectra of each cut do not show single, perfectly Gaussian shaped lines in most cases. Thus, an interpretation of the mean velocity and the velocity dispersion map of the gas might be misleading. The method used for the calculation of the moment maps does not account for the superposition of different velocity components, saturation of lines, line blending or possible self-absorption. Hence, the assumption of a single Gaussian line for the spectrum might in many cases not be a good approximation.

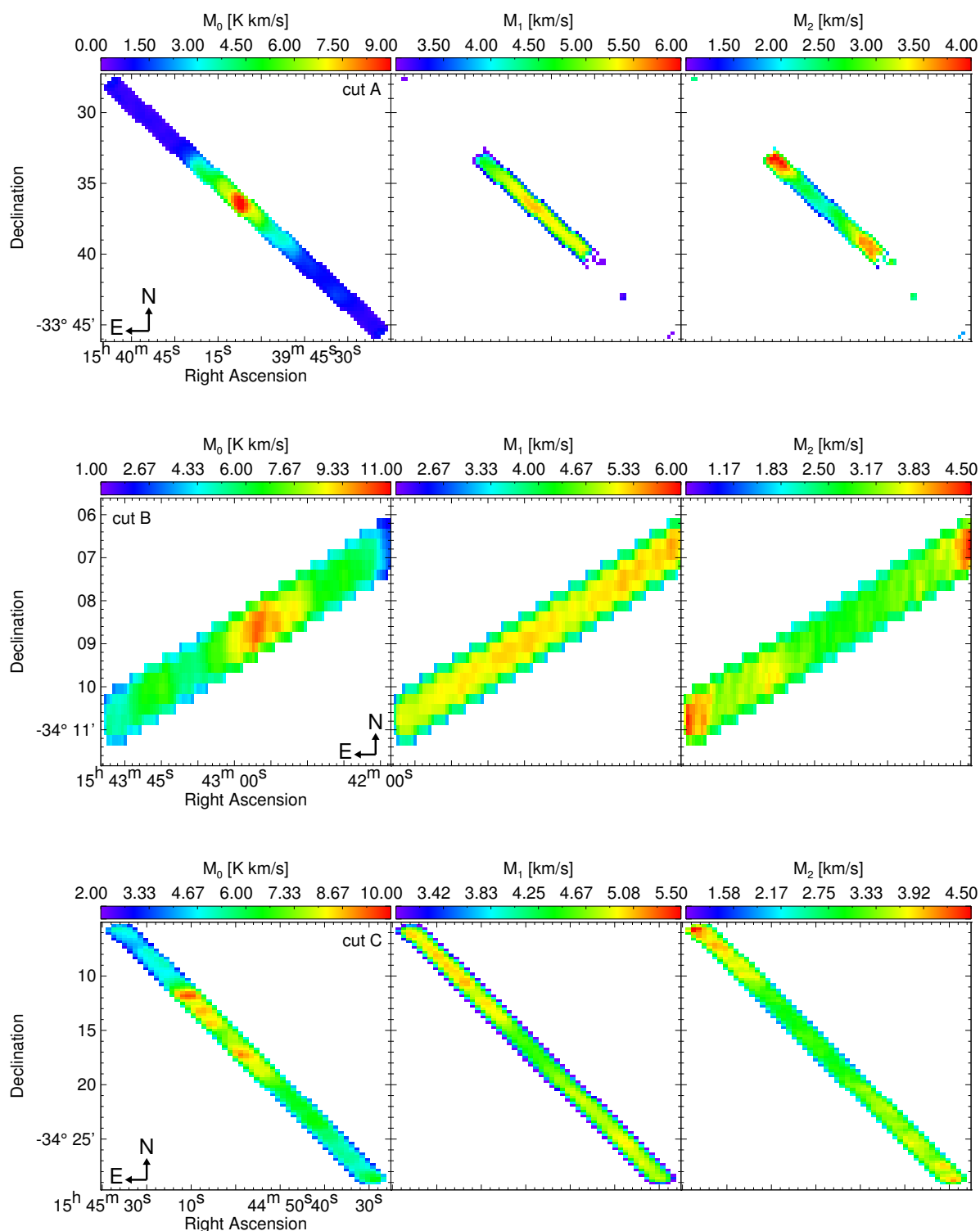
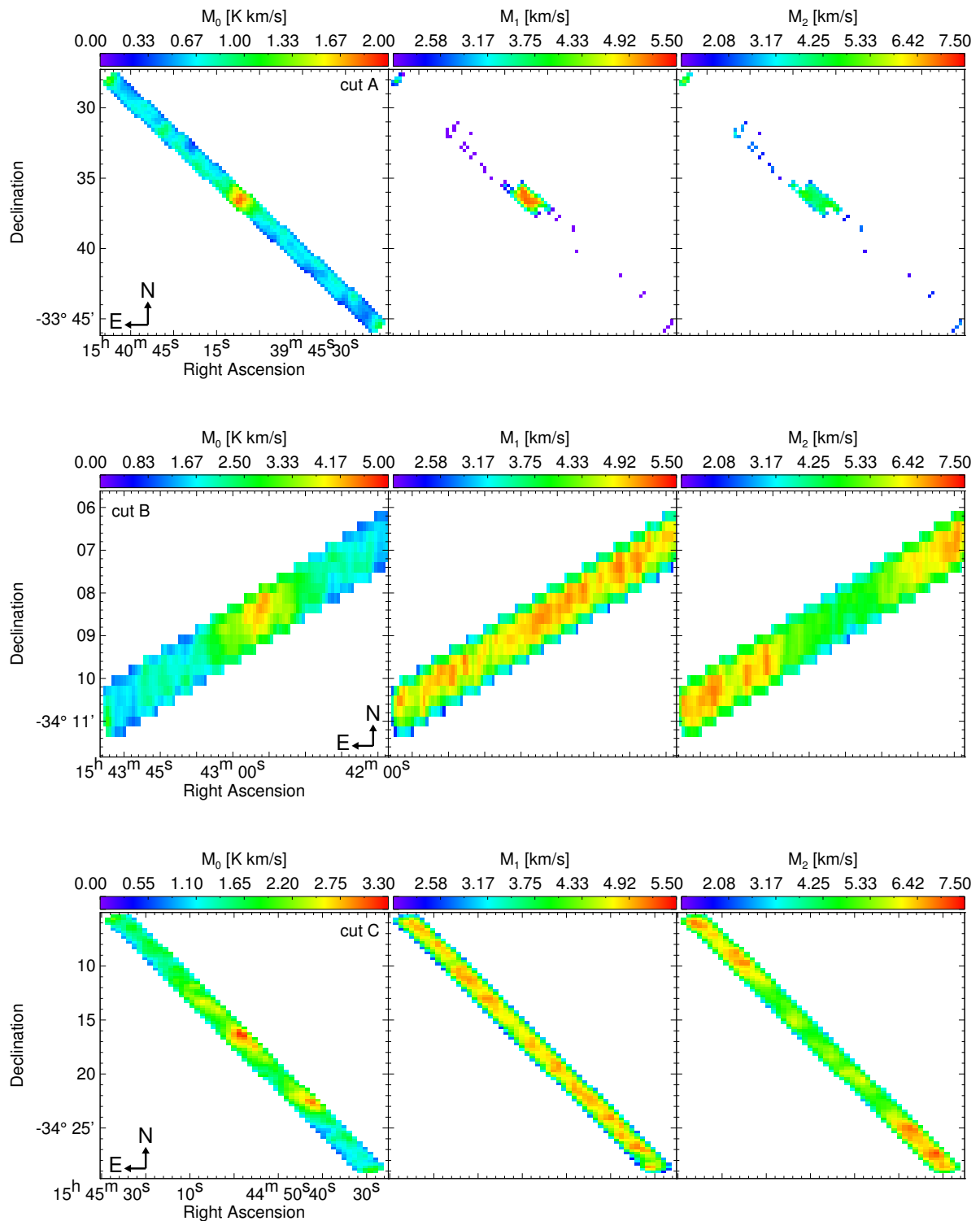


Figure 5.7: ^{13}CO moment maps of cut A, B, and C (from top to bottom). The left panel shows the integrated intensity M_0 , the middle panel the centroid velocity M_1 , and the right panel the velocity dispersion M_2 of the gas. Pixels where a moment was not calculated are left blank. All maps were convolved with a Gaussian of two pixels or about one beam. As an effect of that the edge pixels have seemingly lower values because they are neighboring to NaN values.

Figure 5.8: Same as Figure 5.7 but for $C^{18}O$.

5.5 LTE analysis

For the following calculations of optical depth, excitation temperature, and column density only spectra with a S/N > 4 were selected. This assures that both lines are clearly detected and reduces possible confusion. Constants of the ^{13}CO and C^{18}O line that are needed for these calculations are listed in Table 5.1. This analysis is based on LTE conditions (see also Section 2.2.2). The excitation temperature T_{ex} is assumed to be equal to the kinetic temperature of the gas and to be the same for all transitions and both CO isotopologues. This assumption holds as long as the temperature distribution along the LOS is uniform. Typically, this is not the case and will thus lead to errors that have to be taken into account. For simplicity of notation I define $\tau_{13} = \tau(^{13}\text{CO})$ and $\tau_{18} = \tau(\text{C}^{18}\text{O})$.

5.5.1 Optical depth

The H_2 column density map calculated from dust emission showed that almost all of Lupus I has column densities below $1 \times 10^{23} \text{ cm}^{-2}$. Therefore, the criterion of optical thinness is fulfilled for C^{18}O . Adopting a constant abundance ratio of ^{13}CO to C^{18}O one can estimate the optical depth of the ^{13}CO gas (see e.g. Myers et al. 1983; Ladd et al. 1998). With that the optical depths of both lines are connected via

$$\tau_{13} = \kappa \times \tau_{18} \quad (5.4)$$

with $\kappa = \frac{[^{13}\text{CO}]}{[\text{C}^{18}\text{O}]}$ the relative abundance ratio of the given isotopologues. Here I adopt a constant abundance ratio of $\kappa = 7.3$ (Wilson & Rood 1994, local ISM). Then the optical depth τ_{13} can be approximated by the lines' intensity ratio

$$\frac{T_{\text{mb}}^{13}(v)}{T_{\text{mb}}^{18}(v)} = \frac{1 - \exp(-\tau_{13})}{1 - \exp(-\tau_{13}/\kappa)} \quad (5.5)$$

with $T_{\text{mb}}^{13}(v)$ and $T_{\text{mb}}^{18}(v)$ the main-beam temperature of the corresponding line at velocity channel v . In principle this relation is valid for every velocity channel. Here, I chose $T_{\text{mb}}^{18}(v) = T_{\text{peak}}^{18}$ the peak brightness temperature of the C^{18}O line. Then $T_{\text{mb}}^{13}(v) = T_{\text{peak}}^{13}$ is the corresponding brightness temperature of ^{13}CO at the velocity channel of the C^{18}O peak intensity. The resulting equation for the optical depth of τ_{13} is transcendent and can only be solved numerically. It is illustrated in the top panel of Figure 5.9. This method breaks down when the line ratio approaches unity which I also find at a few pixels of cut C. There the C^{18}O line is very strong compared to the rest of the cut and the resulting τ_{13} is even ten times higher than in the rest of the cut. The resulting optical depth maps for C^{18}O are shown in the left panels of Figure 5.10. Pixels that had a too small S/N to calculate an optical depth are left blank.

Cut A The optical depth was calculated only in the area of highest integrated intensity, i.e. in the very center of the cut and hence the filament. τ_{13} has values below 3 except for three pixels. Its mean and median is 1.9. This shows that in the northern part of the cloud ^{13}CO is only very moderately optically thick and C^{18}O is clearly optically thin.

Cut B For this cut the optical depth was calculated for about 60% of the pixels. The emission was too low at both edges of the cut to obtain spectra with a $\text{S/N} > 4$. τ_{13} (τ_{18}) ranges between 1.6 (0.2) and 11.5 (1.6) with a mean and median of 5.1 (0.7). Most of the cut has an optical depth close to the mean value. Therefore, the central part of the cloud, represented by cut B, is on average more optically thick by a factor of about 2.5 than the northern part (cut A).

Cut C Within cut C the optical depth was calculated only for three "islands" in the center of the cut because of the low C^{18}O emission elsewhere. In the south-western part of the cut, τ_{13} displays values of up to 20 because of the high intensity of the C^{18}O line relative to that of ^{13}CO . At some pixels the method could not be applied because the C^{18}O intensity was even higher than that of ^{13}CO . Then the ratio of the two brightness temperatures is below one and Equation 2.25 is not solvable. This might come from either ^{13}CO becoming optically thick or ^{13}CO self-absorption which leads to plateaus or double-peaks in the line profile and thus a lower peak intensity in the spectrum than in reality. Some of the ^{13}CO spectra in this area show a characteristic self-absorption dip with the C^{18}O line peaking at the position of the dip. Surprisingly, neither the *Herschel* dust column density map nor the LABOCA map reveal any particularly dense core in this region (see Figure 5.6). A dense pre-stellar core is, however, present in the center of cut C. Nevertheless, the ^{13}CO optical depth at its position is not significantly above the median of the cut which is 5.1 and thus similar to cut B.

Molecular clouds typically have an optical depth τ_{13} of below one at the edges and up to four in the central and most dense regions or cores (Carlhoff et al. 2013). In the case of Lupus I this applies for cut A. The other two cuts are above this typical value. C^{18}O is below one almost everywhere within all three cuts. Furthermore, there are pixels in cut C where the spectra suggest that C^{18}O becomes optically thick or shows self-absorption dips. Vilas-Boas et al. (2000) have analyzed 15 cores in Lupus I observing $\text{C}^{18}\text{O}(1-0)$ and $^{13}\text{CO}(1-0)$ line with the 15 m Swedish-ESO Submillimeter Telescope (SEST) at La Silla in Chile. They have found optical depths τ_{18} between < 0.1 and 0.57. Similar values have been calculated by Hara et al. (1999) for 12 cores in Lupus I from $\text{C}^{18}\text{O}(1-0)$ observations. These findings are in agreement with my results.

Table 5.1: Constants of the $^{13}\text{CO}(2-1)$ and $\text{C}^{18}\text{O}(2-1)$ lines that are needed for the calculations in this chapter. ν_0 is the line's rest frequency, $T_\nu = h\nu_0/k_B$ the corresponding brightness temperature, μ is the molecule's dipole moment, and B_{rot} its rotational constant.

Line	ν_0 [GHz]	T_ν [K]	μ [D]	B_{rot} [10^{10} Hz]
$^{13}\text{CO}(2-1)$	220.3986765	10.577469	0.122	5.509967
$\text{C}^{18}\text{O}(2-1)$	219.5603568	10.537236	0.110	5.489009

5.5.2 Excitation temperature

After determining the optical depth, one can calculate the corresponding excitation temperature by reorganizing Equation 2.19 to

$$T_{\text{ex}}(\tau) = \frac{T_\nu^{18}}{\ln \left\{ 1 + \left[\frac{T_{\text{peak}}^{18}}{T_\nu^{18}} (1 - \exp(-\tau_{18}))^{-1} + J(T_{\text{bg}})/T_\nu^{18} \right]^{-1} \right\}} \quad (5.6)$$

with $T_\nu = \frac{h\nu_0}{k_B}$, and $T_{\text{bg}} = 2.73$ K the temperature of the cosmic microwave background (CMB). I used the C^{18}O line for the calculation of T_{ex} because it is more reliable to use the optically thin line. The behavior of T_{ex} in dependence of τ is shown in Figure 5.9. T_{ex} becomes independent of τ_{18} for optical depths of more than $\approx 4-5$. This is expected as one probes just the outermost layer of a cloud once it is dense enough and becomes optically thick. The resulting T_{ex} maps are displayed in the middle panels of Figure 5.10.

Cut A The excitation temperature in cut A has a mean of 11.3 K and a median of 10.8 K. Most of the pixels have a temperature between 10 and 11 K, but there are also several pixels above 12 K (north-eastern edge of the center) and around 9 K (south-western edge of the center).

Cut B In cut B the excitation temperature has a mean and a median of 11.0 K and 11.2 K which is just slightly above that of cut A. The data suggest the presence of a temperature gradient across the cut. T_{ex} increases from the north-western towards the south-eastern end of the cut by about 2–3 K from ≈ 10 to 13 K.

Cut C The excitation temperature in this cut differs significantly from that of the other two cuts. This is puzzling at first, since the integrated line intensities are similar to those of cut B. The mean and median T_{ex} are 8.5 and 8.4 K, respectively. This is a 3 K difference to the other two cuts and the maximum excitation temperature is just 11 K. This is not only seen in the south-western part of the cut where the calculations of the optical depth are not reliable, but also in the center. Probably, this is an effect of the very complex spectra within cut C. Often the ^{13}CO spectrum has a plateau or shows a dip. This is a hint

towards optical thickness and self-absorption and thus the ^{13}CO line intensity is probably underestimated in those cases. Also the C^{18}O line intensity is in general lower than in cut B. This will lead to an overestimation of the optical depths and to an underestimation of T_{ex} . I will discuss these effects in more detail in Section 5.5.4.

The excitation temperatures of the CO gas in the three cuts are significantly lower than the previously obtained dust temperatures. The mean of the dust temperature within the same area in which excitation temperatures have been obtained is 16.8, 14.7, and 14.7 K for cut A, cut B, and cut C, respectively. These values are 5.5, 3.6, and 6.2 K higher than the corresponding mean T_{ex} . The dust temperatures of cut A are higher than in the other two cuts. This trend, however, is not confirmed by the excitation temperatures. Cuts B and C have similar dust temperatures but very different excitation temperatures.

The excitation temperatures calculated in my analysis are comparable to previous findings from different CO and molecular observations of Lupus I. Four of the cores (C3 - C6) found by Benedettini et al. (2012) with high-density molecular tracers at 3 and 12 mm with the Mopra telescope are at least partially in cuts B and C. Using NH_3 they calculated a kinetic temperature of 12.6 and 12.3 K for cores C4 (in cut B) and C6 (in cut C), respectively. Averaging the excitation temperature in my maps within the approximate extent of each core, which I define as a circle centered at the position and with a radius that is given in their work, I find values of 11.8 and 8.8 K for core C4 and C6, respectively. Hence, the temperatures agree in case of cut B where the difference is about 6%. This is, however, just a very crude approximation and parts of the cores are already outside my map.

Tachihara et al. (1996) adopted a constant excitation temperature of 13 K for the whole cloud in their analysis of $^{13}\text{CO}(1-0)$. But Tothill et al. (2009) found even lower excitation temperatures than this work from their analysis of $\text{CO}(4-3)$ and $^{13}\text{CO}(2-1)$. Throughout most of the cloud they find excitation temperatures of 7–9 K and slightly warmer ends of the filament with $T_{\text{ex}} = 10-12$ K. The excitation temperatures of the 15 cores found in $\text{C}^{18}\text{O}(1-0)$ and $^{13}\text{CO}(1-0)$ by Vilas-Boas et al. (2000) range between 7 and 16 K with a mean and a median of 10.2 and 10.0 K, respectively. These values are closer to the average of about 11 K I found in cuts A and B.

5.5.3 Column density and PDFs

The previous determination of the excitation temperatures allows to calculate the C^{18}O column density using Equation 2.42. The factor $\tau_{18}/(1 - \exp(-\tau_{18}))$ corrects the integrated intensity for possible opacity broadening (see Goldsmith & Langer 1999). But this effect should be in any case small for the C^{18}O line because τ_{18} stays below unity in most pixels.

The corresponding H_2 column density simply follows, assuming a constant abundance ratio of $[\text{C}^{18}\text{O}]/[\text{H}_2] = 1.7 \times 10^{-7}$ (Haworth et al. 2013). The three column density maps are shown in the right panels of Figure 5.10.

Cut A The H_2 column density in cut A is the lowest of the three cuts. The mean and median are 3.4 and $3.5 \times 10^{21} \text{ cm}^{-2}$, respectively. The maximum column density is $5.5 \times 10^{21} \text{ cm}^{-2}$. The median is about 2.5 times smaller than that of cut B and that of cut C.

Cut B The values of the column density within cut B range between $2.2 \times 10^{20} \text{ cm}^{-2}$ and $2.2 \times 10^{22} \text{ cm}^{-2}$ with a median of $9.5 \times 10^{21} \text{ cm}^{-2}$. These high values might be due to the protostellar core present in the cut.

Cut C This cut shows column densities similar to cut B. The minimum, maximum, and mean of $6.2 \times 10^{20} \text{ cm}^{-2}$, $4.3 \times 10^{22} \text{ cm}^{-2}$, and $1.0 \times 10^{22} \text{ cm}^{-2}$, respectively, are higher than in cut B, but the median of $8.8 \times 10^{21} \text{ cm}^{-2}$ is again lower by $\approx 6\%$.

The column density distribution in the three cuts is in agreement with the results of the dust analysis. Cut A in the northern part of Lupus I has the on average lowest column density. Cut B and cut C have a similar range of column densities which is significantly higher than in cut A. This is most likely because of the pre- and protostellar cores that lie within each of those cuts. In general I note that the column densities from CO are higher than those from dust emission.

Tachihara et al. (1996) found a mean H_2 column density of $N(\text{H}_2) = 3.8 \times 10^{21} \text{ cm}^{-2}$ for the whole Lupus I cloud. They calculated it from the $^{13}\text{CO}(1-0)$ line. Hara et al. (1999) lists values between 2.5 and $5.7 \times 10^{21} \text{ cm}^{-2}$ for the 12 cores they observed in $\text{C}^{18}\text{O}(1-0)$. The 15 cores observed by Vilas-Boas et al. (2000) have column densities between 2 and $14 \times 10^{21} \text{ cm}^{-2}$. The values I found in the three cuts fall within the range spanned by the previous results. The median of cut A is close to the mean of Tachihara et al. (1996) and roughly in the middle of the range determined by Hara et al. (1999). The median values of the other two cuts are close to the upper limit of the range spanned by the cores observed by Vilas-Boas et al. (2000).

The column density PDFs calculated for the three cuts are shown in Figure 5.11. However, they have a very low statistics of 53, 239, 184 pixels in cut A, B, and C, respectively. Only the PDF of cut B has a recognizable shape. It could be lognormal, but a power-law would probably also represent a possible fit because of the large error bars. The PDF of cut A is systematically shifted towards lower column densities what could be expected from the previously calculated lower mean column density value. The PDF of cut C probes the largest range of different column density values. The PDF of cut B is cut off at $\sim \eta = 1$ whereas cut C shows another three bins above that value. But this feature might be due to the unreliable pixels in the south-west of cut C because the pre-stellar core in the middle of the cut does not show such high column densities. The PDFs calculated from CO are in general shifted towards higher column densities compared to the PDFs of the dust.

Finally, I also carried out the LTE analysis based on the averaged spectra of cut B and cut C (see Figure 5.1). Due to a low S/N the averaged C¹⁸O spectrum of cut A was not used for further analysis. The resulting quantities for cut B and cut C are summarized in Table 5.2. It is interesting to note that the excitation temperature for cut B is about 9 K which is almost 3 K lower than the mean of T_{ex} calculated for all pixels separately. This value is closer to that of cut C than the previously calculated one. The column density calculated from the averaged spectra of cut B is $1.1 \times 10^{22} \text{ cm}^{-2}$ which is comparable to the previously calculated median value of $9.5 \times 10^{21} \text{ cm}^{-2}$. The integrated ¹³CO intensity is comparable in both cuts whereas the integrated C¹⁸O intensity is lower by more than half. The corresponding peak intensities display a similar behavior (note that T_{peak}^{13} describes the ¹³CO intensity at the position of the C¹⁸O peak). The averaged spectra of cut B and C suggest that there is a different velocity dispersion in those two cuts. The ¹³CO linewidth for instance is narrower in cut B than in cut C which is, however, not the case for C¹⁸O. Therefore, the two cuts might have different critical densities for a line to become optically thick. This could explain the different optical depths and excitation temperatures found in both cuts despite similar integrated ¹³CO intensities.

Table 5.2: Results of the LTE analysis for the averaged spectra of cut B and cut C (see Figure 5.1). Columns two and three give the peak brightness temperature of the C¹⁸O line and the ¹³CO intensity at the position of the C¹⁸O peak, respectively. Columns four and five give the integrated line intensity of C¹⁸O and ¹³CO, respectively. Columns six and seven give the optical depths of C¹⁸O and ¹³CO, respectively. Columns eight and nine show the excitation temperature T_{ex} and the H₂ column density.

Cut	T_{peak}^{18} [K]	T_{peak}^{13} [K]	$\int T_{\text{mb}}^{18} dv$ [K km s ⁻¹]	$\int T_{\text{mb}}^{13} dv$ [K km s ⁻¹]	τ_{18}	τ_{13}	T_{ex} [K]	N(H ₂) [10 ²¹ cm ⁻²]
B	1.34	4.27	1.22	5.69	0.34	2.47	9.18	10.9
C	0.74	3.21	0.50	5.55	0.19	1.41	8.71	4.7

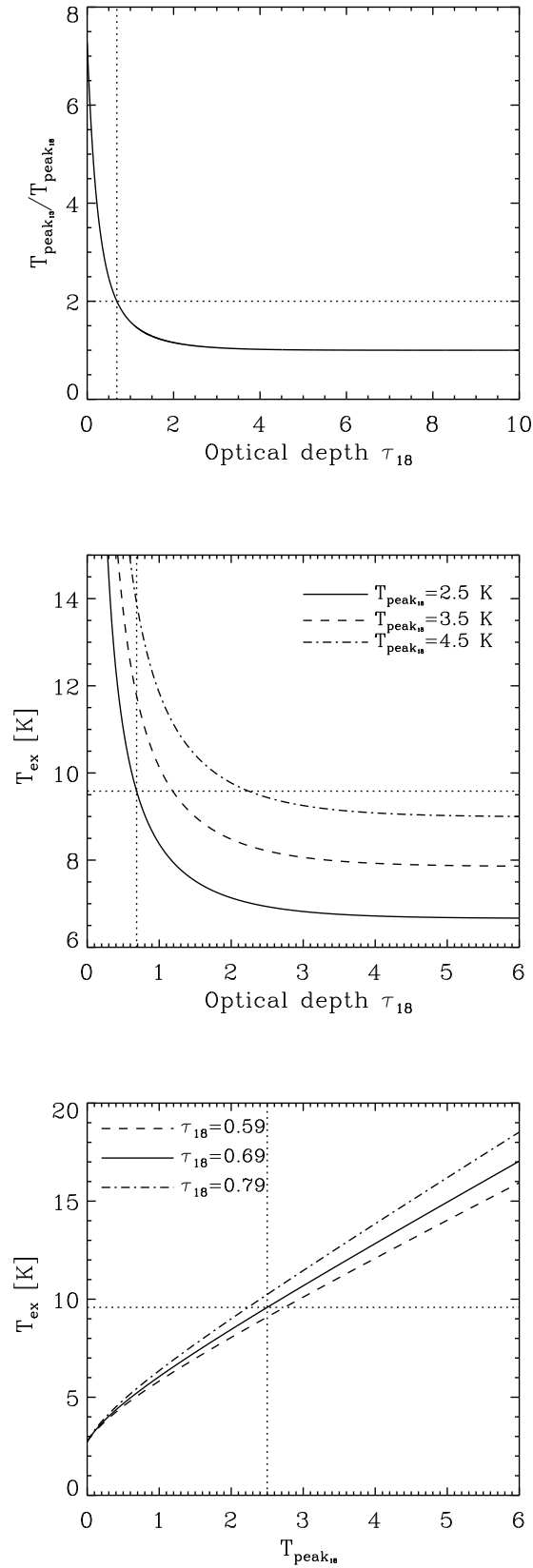


Figure 5.9: *Top*: Dependence of the optical depth on the line peak temperature ratio (Equation 5.5). *Middle*: Excitation temperature T_{ex} for three different peak temperatures of $T_{\text{peak}}^{18} = 2.5$ K (solid), 3.5 K (dashed), and 4.5 K (dash-dotted). Note that at some point T_{ex} becomes independent of τ . In the three cases here it happens for values above ~ 4 –5. *Bottom*: Plot of T_{ex} against T_{peak}^{18} for three different optical depths of $\tau_{18} = 0.59$ (dashed), 0.69 (solid), and 0.79 (dash-dotted). The horizontal and vertical dotted lines in each plot mark exemplary values discussed in Section 5.5.4.

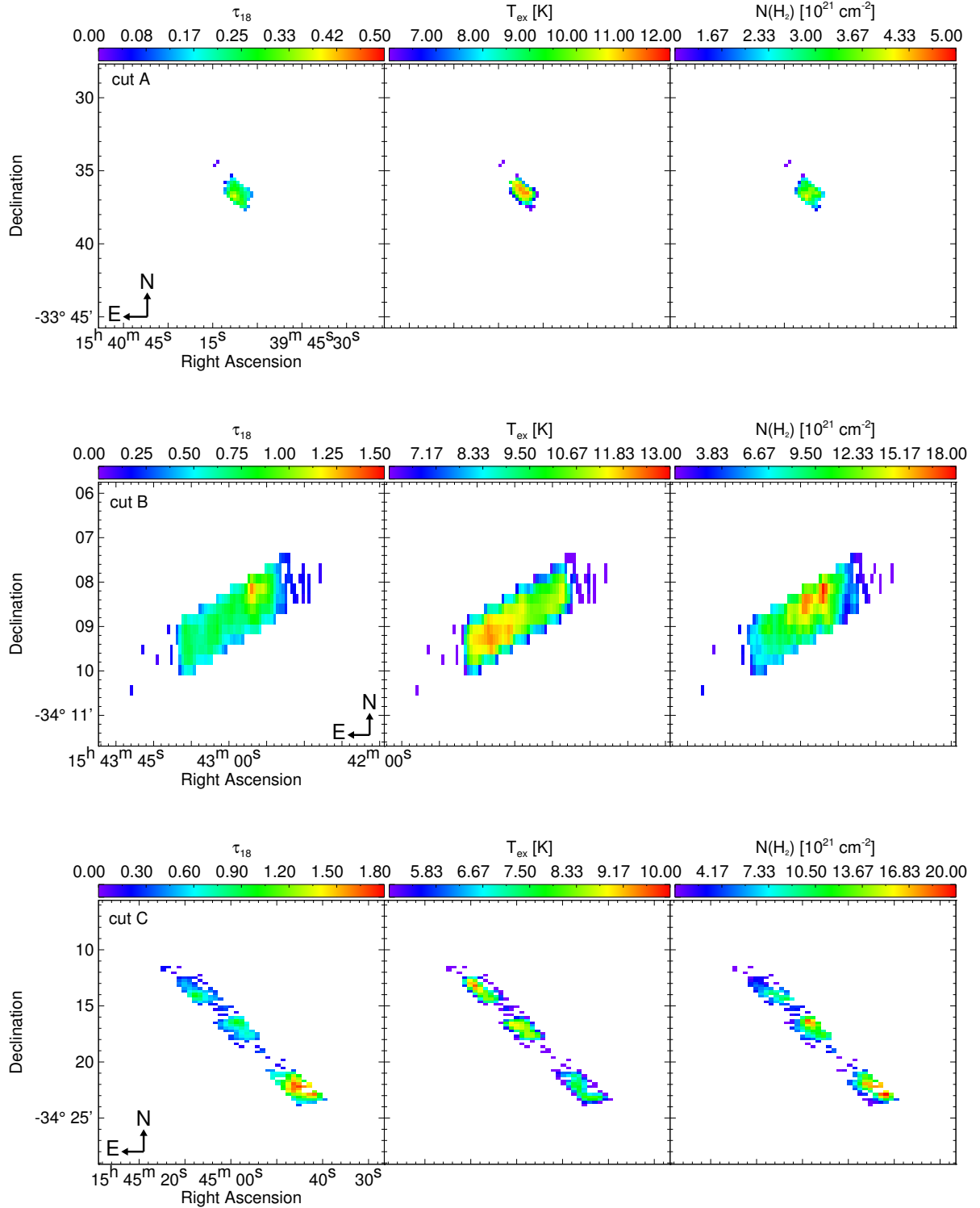


Figure 5.10: Results of the LTE analysis for cut A, B, and C (from top to bottom). The left panel shows the optical depth τ_{18} , the middle panel the excitation temperature T_{ex} , and the right panel the H_2 column density. τ_{13} can easily be calculated by multiplying the colorbar values of τ_{18} by $\kappa = 7.3$. The intensity scaling stays the same. All maps were convolved with a Gaussian of two pixels or about one beam. As an effect of that the edge pixels have seemingly lower values because they are neighboring to NaN values. Pixels within each cut for which the ^{13}CO and the C^{18}O spectrum had a $S/N < 4$ are left blank.

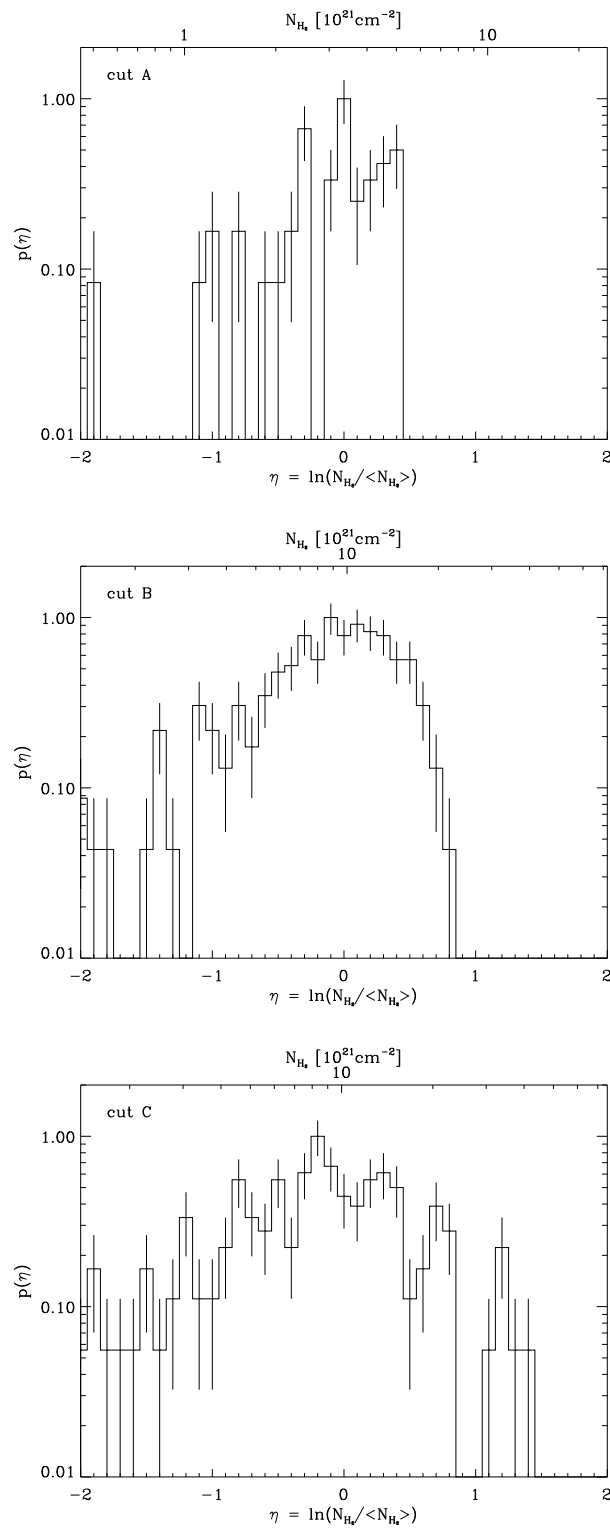


Figure 5.11: Column density PDF of cut A, B, and C (from top to bottom), respectively. Error bars are \sqrt{N} uncertainties.

5.5.4 Errors of the LTE analysis

The LTE analysis is prone to high errors. The uncertainties of the previously calculated quantities can even reach a factor of ten. Therefore, the results do not necessarily resemble the real physical conditions in the cloud. Instead, they rather yield lower or higher limits. In this section, I shortly discuss possible error sources and connections between them.

In reality, molecular clouds are not isothermal slabs of gas, but rather display substructures at different densities and temperatures. Hence, LTE conditions can most likely not be assumed. Instead, a non-LTE approach would be required to include more accurate assumptions of the physical parameters in the cloud. This, however, requires numerical simulations of radiation transfer. In LTE one assumes a single temperature for the whole cloud and the same excitation temperature for both CO isotopes. If there was a temperature gradient along the LOS, the real ratio between the intensities of the ^{13}CO and C^{18}O line would be missed, which would lead to an under- or overestimation of the optical depth and thus the excitation temperature.

For positions where ^{13}CO becomes optically thick and the line profile deviates significantly from a Gaussian, e.g. showing a plateau, the ^{13}CO peak temperature is underestimated. This leads to a lower ratio of the two peak temperatures and thus to an overestimated optical depth and underestimated excitation temperature. This effect can be seen at many pixels of cut C.

In the calculation of the optical depth, I used the C^{18}O peak as a reference to build the brightness temperature ratio of Equation 5.5 because it is the optically thin line and hence less affected by opacity broadening. I adapted the corresponding brightness temperature of ^{13}CO at the velocity of the C^{18}O peak. In many cases the ^{13}CO peak position does not agree with the C^{18}O peak position. Depending on the ^{13}CO line profile this might also lead to a significant underestimation of the ^{13}CO peak intensity if it is missed.

The two optical depths τ_{13} and τ_{18} are assumed to be connected through the abundance ratio of ^{13}C and ^{18}O . Here, I assumed that this ratio is constant. In reality it is known to vary in our Galaxy and depends on the Galactocentric radius (see e.g. Wilson & Rood 1994). Also within such a local molecular cloud like Lupus I the abundance ratio may already vary. The value of κ is not well determined and the literature lists different values for similar regions and conditions. Thus, a factor of at least two for the uncertainty is reasonable.

Figure 5.9 illustrates the behavior of the different calculated quantities and how small changes in one of them can lead to large errors in the others. As a starting point, I exemplarily chose two typical peak brightness temperatures of $T_{\text{peak}}^{13} = 5 \text{ K}$ and $T_{\text{peak}}^{18} = 2.5 \text{ K}$ such that their ratio is exactly two. A ratio of two yields an optical depth of $\tau_{18} = 0.69$. These two values are marked by the dotted lines in the top panel. In the next step one can calculate T_{ex} . The middle panel displays its behavior in dependence of τ_{18} for three different C^{18}O peak temperatures of 2.5 (solid line), 3.5 (dashed), and 4.5 K (dash-dotted). The resulting value $T_{\text{ex}} = 9.6 \text{ K}$ for the chosen $T_{\text{peak}}^{18} = 2.5 \text{ K}$ is again marked by the two dotted lines intersecting each other on the solid curve. In the case that the ^{13}CO intensity is underestimated and should actually be higher, the optical depth is overestimated. Keeping

$T_{\text{peak}}^{18} = 2.5$ K constant and increasing T_{peak}^{13} one would move along the solid line towards higher T_{ex} . An increase of T_{peak}^{13} by 20% leads to a decrease of τ_{18} by 25% and thus an increase of T_{ex} by more than 1 K or 11%. In the following, I compare two pixels with each other that have the same optical depth, i.e. the same peak temperature ratio. The bottom panel of Figure 5.9 shows T_{ex} in dependence of T_{peak}^{18} for three different constant optical depths of 0.59 (dashed line), 0.69 (solid), and 0.79 (dash-dotted). The higher the two intensities the higher the resulting excitation temperature for the same optical depth. In my example of $\tau_{18} = 0.69$ the increase of T_{peak}^{18} by 1 K (2 K) causes an increase of T_{ex} by 1.1 K (4.3 K). T_{ex} is linearly correlated to T_{peak}^{18} for a constant τ_{18} within a typical (as seen in the spectra of the three cuts) T_{peak}^{18} peak intensity range of 2 to 5 K (see bottom panel). The higher τ_{18} the steeper the slope of this correlation.

Three different variables enter in Equation 2.42 to calculate the column density. Besides the optical depth and the excitation temperature there is also the integrated intensity of the C¹⁸O line. Hence, there is a combined effect of the errors that cannot be predicted in a simple manner.

To conclude, the interpretation of the LTE results has been carried out under the assumption that the inferred excitation temperatures represent lower limits and thus the resulting H₂ column densities represent upper limits. In addition, these three cuts just cover a very small portion of the entire cloud and hence any conclusions drawn from the here presented results might not represent the conditions of the whole cloud. Nevertheless, from the results I have obtained through the dust analysis I have reasons to believe that each of the three cuts might represent the conditions in the corresponding part of Lupus I where it is located, i.e. northern, central, and southern part.

5.6 Determination of different velocity components

The velocity channel maps and the PV diagrams already revealed that there are several velocity components present in the three CO cuts through Lupus I. In this section, I analyze how they behave within one cut and within the cloud to find out if there are systematic differences especially between one side of a cut and the other. This could reveal signs of interaction between the cloud and the surroundings, i.e. the HI shell of USco and the wind-blown bubble of UCL.

For this, each cut was divided into six boxes that are shown in Figure 5.6. In each of these boxes an average ^{13}CO and C^{18}O spectrum of all pixels within the box was calculated. These spectra are presented in Figure 5.12. The top row shows the average ^{13}CO spectra, the bottom those of C^{18}O . Each column represents one cut.

Then for each component present in the averaged spectrum of one box its peak position and FWHM were determined in two ways. First empirically from the spectra (see results in Table 5.3) and then using multi-component (up to three) Gaussian fitting (see results in Table 5.4). These peak positions and FWHM were then plotted into one diagram per cut (see Figure 5.13) what made it easier to find and group similar velocity components. In the next step, a mean peak position and a mean FWHM was determined for each group of velocity components. All values discussed below refer to the empirically determined results. The Gaussian fits to the spectra are presented in Figures 5.14 to 5.19.

Cut A For boxes 2–4 a C^{18}O line could be recognized within cut A. In the center of the cut (box 3) the peak velocity is 5.9 km s^{-1} . North-east and south-west next to the center (boxes 2 and 4) the peak velocity is lower by 0.4 and 0.5 km s^{-1} , respectively. There is a difference in the FWHM between box 2 and boxes 3 and 4 of about a factor of two. However, the spectrum of box 2 is also the one with the lowest integrated intensity. Thus the errors in the determination might be higher. For box 2 the Gaussian fitting method yields a FWHM of 0.55 km s^{-1} which is higher by 0.15 km s^{-1} than the empirically determined value. In cut A there is one group of ^{13}CO peak velocity components. The peak velocities within the group range between $v_{\text{LSR}} = 5.4\text{--}5.9 \text{ km s}^{-1}$ with a mean of 5.6 km s^{-1} . The ^{13}CO FWHM range between 0.9 and 1.8 km s^{-1} with a mean of 1.2 km s^{-1} which is almost twice the mean of the C^{18}O FWHM. In box 1 there are also two other ^{13}CO components present with peak velocities of 3.5 and 6.7 km s^{-1} . In those boxes where both a C^{18}O and a ^{13}CO line are present the peak positions agree well with each other whereas the ^{13}CO lines are roughly twice as wide as the C^{18}O lines. The ^{13}CO peak velocities at the two edges of the cloud (box 1 and 6) are significantly different. At the edge towards USco the peak velocity is 5.3 km s^{-1} , whereas it is 5.8 km s^{-1} at the edge towards UCL. The FWHM, however, are similar. Furthermore, both edges do not show significant amounts of C^{18}O emission.

Cut B In cut B there is one group of C^{18}O peak velocities. The three values of the group (boxes 2–4) range between 5.0 and 5.2 km s^{-1} with a mean of 5.1 km s^{-1} . The highest corresponding FWHM of 0.6 km s^{-1} is found in the center of the cut (box 3). In

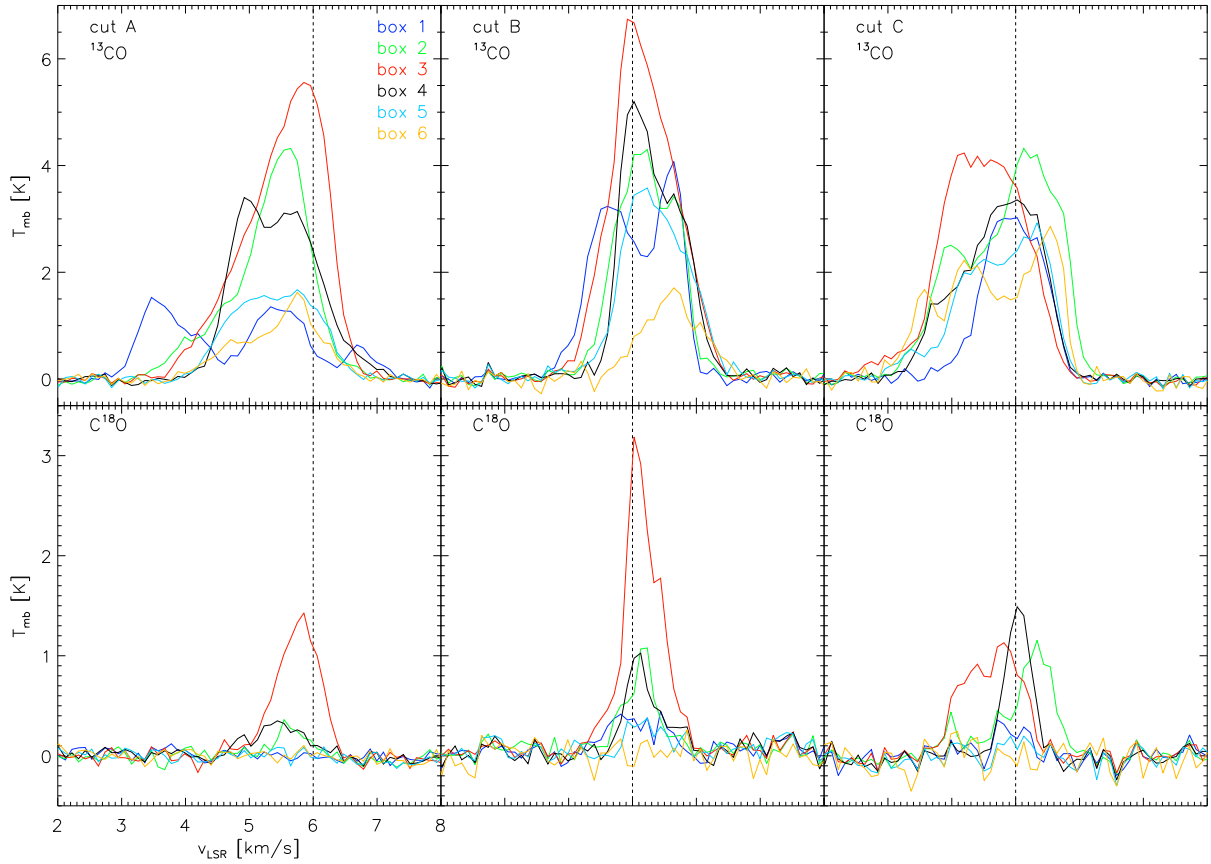


Figure 5.12: Averaged spectra within the six boxes into which each cut was divided. The top row shows the average ^{13}CO spectra; the bottom those of C^{18}O . Each column represents one of the three cuts. The different colors denote the six boxes from 1 to 6. The vertical dashed line marks for orientation $v_{\text{LSR}} = 6 \text{ km s}^{-1}$ for cut A and $v_{\text{LSR}} = 5 \text{ km s}^{-1}$ for cuts B and C.

the other two boxes next to it the FWHM is 0.2 and 0.1 km s^{-1} lower, respectively. The mean of all three FWHM is 0.5 km s^{-1} which is 0.2 km s^{-1} lower than in cut A. In ^{13}CO there are two groups of peak velocities present. One with a mean at 5.7 km s^{-1} , the other at 5.0 km s^{-1} . The high velocity group has a narrower FWHM with a mean of 0.7 km s^{-1} than the low velocity group with a mean of 1.0 km s^{-1} . In those boxes where both a C^{18}O and a ^{13}CO line are present the peak positions agree well with each other. The corresponding linewidths for boxes 2 and 3 are different by about a factor of two. For box 4 they are different by 30% but agree within the error of $\pm 0.2 \text{ km s}^{-1}$. The two edges of cut B can only be compared in ^{13}CO since the C^{18}O emission is limited to the central part of the cut. Box 6 at the north-western end of the cut has just one high velocity component at 5.7 km s^{-1} with a FWHM of 1.0 km s^{-1} . The same high velocity component is also present in box 1 at the other end. This component, however, has a FWHM that is less than half as wide (0.4 km s^{-1}) as that of the corresponding component in box 6. However, the other component in box 1 at 4.6 km s^{-1} has again a FWHM of 0.9 km s^{-1} and thus comparable to that in box 6.

Within box 3 there are two of the cores found by Benedettini et al. (2012). They fitted the CS(2–1) spectra of cores Lup1 C3 and Lup1 C4 with Gaussians and obtained peak positions of 5.14 and 5.16 km s^{−1}, respectively. Similar values were also obtained from their fits to the other high density tracers like N₂H⁺. This agrees well with my results in C¹⁸O. The empirically determined peak position is 5.0 km s^{−1}, the one from the Gaussian fitting is 5.14 km s^{−1}.

Cut C Within cut C there are two groups of C¹⁸O peak velocities present. The first one has a mean of 5.0 km s^{−1}, the second one is at 4.2 km s^{−1}. Both groups show similar means of the FWHM of 0.6 and 0.5 km s^{−1}. In these boxes where both lines are present, the peak velocities of C¹⁸O and ¹³CO agree with each other within the errors. In these cases the FWHM of the C¹⁸O line is lower by a factor of 2–5 than that of ¹³CO.

In ¹³CO there are three groups of peak velocities. The first group has a mean of 3.5 km s^{−1}, the second one 4.2 km s^{−1}, and the third group 5.2 km s^{−1}. The means of the peak velocity of the intermediate and high velocity group in ¹³CO agree with those of the corresponding groups identified in C¹⁸O. The highest ¹³CO peak velocities of the two boxes 1 and 6 at the edges of the cut show a difference of 0.5 km s^{−1} which is higher than the assumed error of ±0.2 km s^{−1}. The corresponding FWHM behave the opposite way. The ¹³CO spectrum of box 1 has a linewidth that is twice as wide as that of the high velocity component in box 6. However, there are also two other components present in box 6 with lower peak velocities but higher linewidths.

For this cut one can compare the C¹⁸O results of box 3 with the results obtained by Benedettini et al. (2012) for their core Lup1 C6 which covers a large portion of the pixels in box 3. They fitted the CS(2–1) spectrum of the core with two Gaussian components for which they obtain peak velocities of 4.2 and 4.94 km s^{−1}, respectively. This agrees with my empirically determined results ($v_{p_1} = 4.4$, $v_{p_2} = 4.8$ km s^{−1}) and even better with the ones obtained from the Gaussian fitting ($v_{p_1}^G = 4.22$, $v_{p_2}^G = 4.86$ km s^{−1}). Their corresponding linewidths are 0.54 and 1.1 km s^{−1}, respectively. This agrees with my results only for the lower velocity component. For the higher velocity component their linewidth is higher by about 36%. However, Benedettini et al. (2012) do not rule out the possibility of self-absorption that may be the cause of the CS(2–1) double-peak. Thus, this might also be the case for C¹⁸O.

Both methods, the empirical determination and the Gaussian fitting, yield results that agree with each other within the errors in most cases. An exception is cut A where non-Gaussian shaped lines and lines that showed double-peaks were fitted with two Gaussians. In the empirical method these were treated as one single line. Also the empirical method was done more conservatively and boxes where lines could not be easily recognized by eye were omitted. In some of those cases the Gaussian fitting helped to obtain a result.

I find that where both a C¹⁸O and a ¹³CO line are present, the mean of the C¹⁸O peak positions and that of the ¹³CO peak positions agree with each other within ±0.2 km s^{−1}

(dotted and dashed horizontal lines in Figure 5.13). But in those cases there is a clear separation in the means of the FWHM of the $C^{18}O$ and ^{13}CO lines with a difference of $0.5\text{--}0.8\text{ km s}^{-1}$. This is expected since the more optically thin line ($C^{18}O$) should be narrower. The empirical results suggest to find the highest $C^{18}O$ linewidth in the center of each cut and an equal or lower one off-center. This trend, however, is not supported by the results of the Gaussian fitting. No $C^{18}O$ line was identified at the edges of the cuts (or just at one edge using Gaussian fitting) and hence a comparison between the two ends is not possible with this tracer. Furthermore, the $C^{18}O$ peak positions of cut A, as well as their mean, are systematically higher than those of cut B and cut C. The means are 5.6 , 5.1 , and 5.0 km s^{-1} for cut A, B, and C, respectively. This suggests the presence of velocity gradient in the cloud. But the data do not show evidence for systematically higher linewidths on one side of Lupus I. Also between the cuts no such trend can be seen.

Table 5.3: Empirically determined values of peak position (v_{p_i}) and FWHM (Δv_i) of the different components in each averaged spectrum of one box in a cut. Note that in ^{13}CO for cut A box 1, cut B box 6, and for cut C boxes 2, 3, 5, and 6, as well as in C^{18}O for cut C boxes 2 and 3 the velocity peaks are not ordered with increasing velocity. This is due to the grouping of components in velocity performed in the analysis. For cut A boxes 4 and 5 the double-peak is likely due to optical thickness of the line. Therefore an interpolation was done to create one single peak line.

Box		C^{18}O [km s $^{-1}$]				^{13}CO [km s $^{-1}$]					
#	v_{p_1}	Δv_1	v_{p_2}	Δv_2	v_{p_1}	Δv_1	v_{p_2}	Δv_2	v_{p_3}	Δv_3	
cut A											
1	–	–	–	–	5.3	1.0	3.5	1.0	6.7	0.5	
2	5.5	0.4	–	–	5.6	1.0	–	–	–	–	
3	5.9	0.8	–	–	5.9	1.4	–	–	–	–	
4	5.4	0.8	–	–	5.4	1.3	–	–	–	–	
5	–	–	–	–	5.4	1.8	–	–	–	–	
6	–	–	–	–	5.8	0.9	–	–	–	–	
\emptyset	5.6	0.7	–	–	5.6	1.2	3.5	1.0	6.7	0.5	
cut B											
1	–	–	–	–	4.6	0.9	5.7	0.4	–	–	
2	5.2	0.4	–	–	5.2	1.0	5.7	0.5	–	–	
3	5.0	0.6	–	–	4.9	1.1	–	–	–	–	
4	5.1	0.5	–	–	5.0	0.7	5.7	0.7	–	–	
5	–	–	–	–	5.2	1.3	–	–	–	–	
6	–	–	–	–	–	–	5.7	1.0	–	–	
\emptyset	5.1	0.5	–	–	5.0	1.0	5.7	0.7	–	–	
cut C											
1	–	–	–	–	5.0	1.2	–	–	–	–	
2	5.3	0.6	4.0	0.2	5.1	1.5	4.0	0.9	–	–	
3	4.8	0.7	4.4	0.7	–	–	4.2	1.7	–	–	
4	5.0	0.5	–	–	5.0	1.5	–	–	–	–	
5	–	–	–	–	5.3	0.7	4.5	1.1	3.4	0.6	
6	–	–	–	–	5.5	0.6	4.2	1.1	3.6	0.7	
\emptyset	5.0	0.6	4.2	0.5	5.2	1.1	4.2	1.2	3.5	0.7	

Table 5.4: Values of peak positions ($v_{p_i}^G$) and FWHM (Δv_i^G) of the different components in each averaged spectrum of one box within a cut determined from multi-component Gaussian fitting (see Figures 5.14 to 5.19). Velocity peaks are grouped in the same way as in the empirical analysis (see Table 5.3) and thus not always ordered by increasing velocity.

Box #	C^{18}O [km s $^{-1}$]				^{13}CO [km s $^{-1}$]					
	$v_{p_1}^G$	Δv_1^G	$v_{p_2}^G$	Δv_2^G	$v_{p_1}^G$	Δv_1^G	$v_{p_2}^G$	Δv_2^G	$v_{p_3}^G$	Δv_3^G
cut A										
1	–	–	–	–	5.45	1.03	3.68	0.97	6.76	0.53
2	5.65	0.55	–	–	5.60	0.83	4.96	1.73	–	–
3	5.77	0.76	–	–	5.95	0.76	5.27	1.44	–	–
4	5.45	0.94	–	–	5.63	1.22	4.86	0.56	–	–
5	–	–	–	–	5.86	0.88	4.96	1.00	–	–
6	–	–	–	–	5.76	0.87	4.75	0.87	–	–
\emptyset	5.62	0.75	–	–	5.71	0.93	4.75	1.10	6.76	0.53
cut B										
1	5.03	1.08	–	–	4.71	0.97	5.62	0.48	–	–
2	5.14	0.63	–	–	5.13	1.00	5.75	0.30	–	–
3	5.14	0.66	–	–	5.15	1.19	–	–	–	–
4	5.13	0.63	–	–	5.00	0.53	5.64	0.74	–	–
5	5.25	0.81	–	–	5.34	1.21	–	–	–	–
6	–	–	–	–	–	–	5.62	1.10	–	–
\emptyset	5.14	0.76	–	–	5.07	0.98	5.66	0.66	–	–
cut C										
1	4.93	0.55	–	–	4.97	1.09	–	–	–	–
2	5.35	0.57	4.51	1.31	5.25	1.12	4.02	0.90	–	–
3	4.86	0.65	4.22	0.55	–	–	4.50	1.51	–	–
4	5.04	0.45	–	–	5.15	0.88	4.34	1.31	–	–
5	–	–	–	–	5.35	0.63	4.50	1.12	3.28	0.44
6	–	–	–	–	5.51	0.60	4.35	1.41	3.51	0.29
\emptyset	5.05	0.56	4.37	0.93	5.25	0.86	4.34	1.25	3.40	0.37

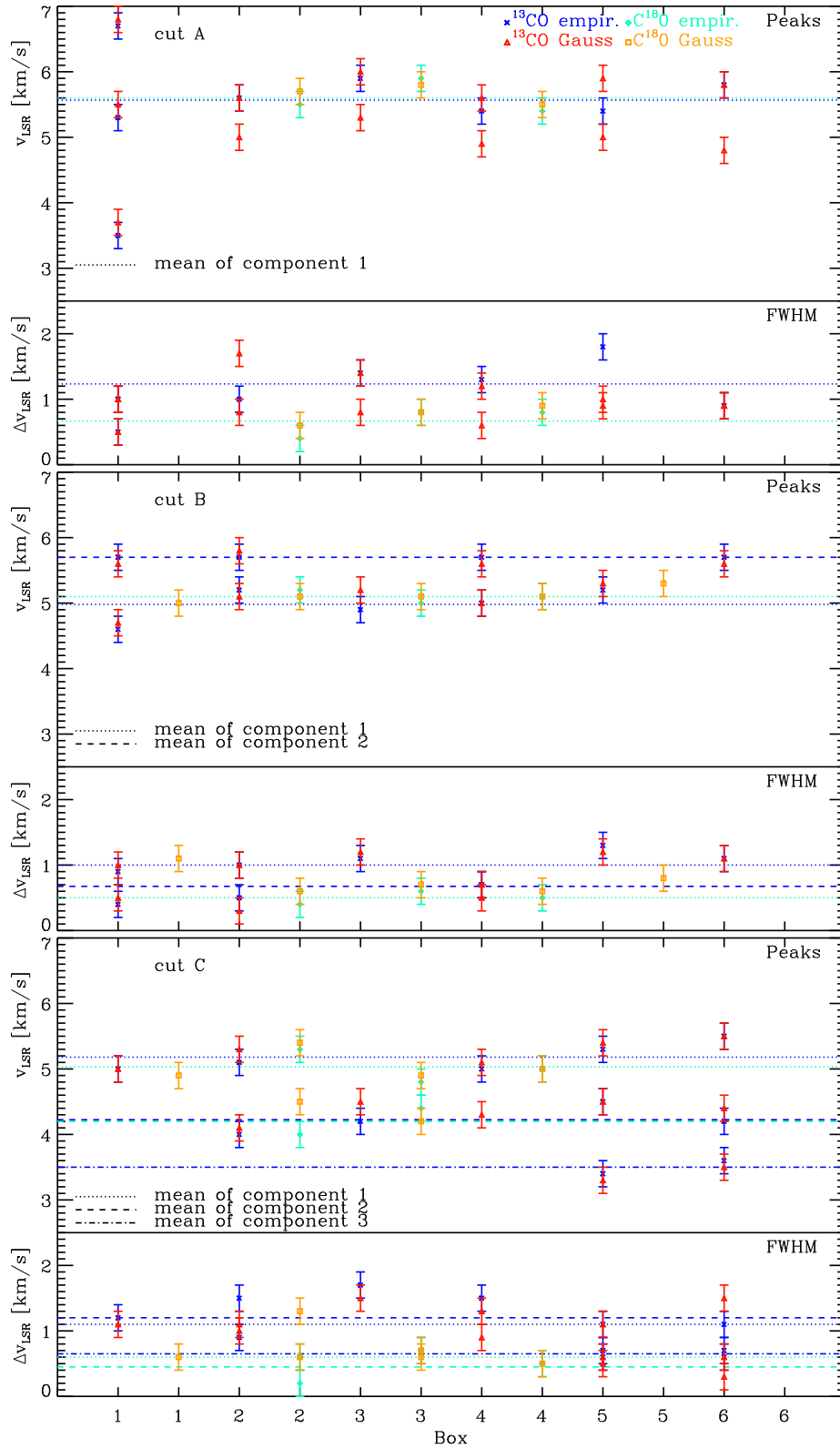


Figure 5.13: Peak velocities and FWHM for each component in an averaged spectrum of one box (1 to 6) within one cut. Blue crosses and cyan diamonds mark the empirically determined values of peak position and FWHM directly from the spectra for ^{13}CO and C^{18}O , respectively. Their values can be found in Table 5.3. The red triangles and the orange boxes mark those values as determined from multi-component Gaussian fits to each spectrum (see Figures 5.14 to 5.19 and Table 5.4). The dotted, the dashed and the dashed-dotted lines mark the average of the empirically determined component 1, 2, and 3, respectively. Error bars are $\pm 0.2 \text{ km s}^{-1}$.

5.6.1 Non-thermal motions

To estimate the non-thermal motion of the gas, which in general is associated to turbulence, one can calculate the non-thermal velocity dispersion from the measured linewidth by subtracting the thermal component. For this, I follow the standard assumption that the thermal and non-thermal components are independent from each other (see e.g. Myers 1983). Then the non-thermal velocity dispersion σ_{NT} is

$$\sigma_{\text{NT}} = \sqrt{\frac{\Delta v^2}{8 \ln 2} - \frac{k_{\text{B}} T_{\text{kin}}}{m}} \quad (5.7)$$

with Δv the measured linewidth, k_{B} the Boltzmann constant, T_{kin} the kinetic gas temperature (here I adopt 10 K), and m the mass of the observed molecule ($m_{^{13}\text{CO}} = 29 \text{ u}$, $m_{\text{C}^{18}\text{O}} = 30 \text{ u}$). Dividing σ_{NT} by the isothermal sound speed $c_{\text{s}} = 0.19 \text{ km s}^{-1}$ for a 10 K ISM gas, gives a direct measure of non-thermality of the component. For the measured linewidths of ^{13}CO in the three cuts, the ratio $\sigma_{\text{NT}}/c_{\text{s}}$ is between 2 and 4.5. That means the gas would be supersonic. But the measured ^{13}CO linewidth is known to have a significant contribution from opacity broadening in an optical depth regime above $\tau_{13} > 1-2$ and should therefore be corrected (Phillips et al. 1979). However, C^{18}O is not severely affected by this problem because of $\tau_{18} < 1$ in most cases. For this molecule the measured linewidths are between 0.4 and 0.8 km s^{-1} . This yields a ratio of $\sigma_{\text{NT}}/c_{\text{s}}$ between 0.9 and 1.8. Hence, most of the C^{18}O gas within the three cuts is in the transonic regime ($1 < \sigma_{\text{NT}}/c_{\text{s}} < 2$) what means that these regions of Lupus I are not quiescent, but have a significant level of turbulence. Typically, the gas of a quiescent cloud resides in the sub-sonic regime as found e.g. by Hacar & Tafalla (2011) for L1517. In Lupus I this signature of turbulence might have been imprinted on the gas by the large-scale interaction with the HI shell of USco and the wind-blown bubble of UCL. However, these three cuts do not sample the entire cloud. It might still be possible that the observed linewidths are just lower or upper limits to the level of turbulence present in Lupus I.

5.6.2 Comparison to other molecular observations of Lupus I

So far no simulations have been performed that predict the behavior of the CO lines in scenarios of colliding flows. Hence, I am not able to compare my results to theoretical models. However, there are several observational papers in the literature that report on velocity gradients present in the molecular gas of Lupus I. Tachihara et al. (2001) found a velocity gradient in ^{12}CO of $\approx 0.25 \text{ km s}^{-1} \text{ pc}^{-1}$ along the long axis of the cloud. They detected gas velocities from 4 km s^{-1} in the south ($b = 15^\circ$) to 6 km s^{-1} in the northern part of the cloud ($b = 18^\circ$). Vilas-Boas et al. (2000) reported a velocity gradient of about $0.3 \text{ km s}^{-1} \text{ pc}^{-1}$ along the long axis of Lupus I. They observed several cores within the cloud in $^{13}\text{CO}(1-0)$ and $\text{C}^{18}\text{O}(1-0)$.

Tothill et al. (2009) observed Lupus I in both $^{13}\text{CO}(2-1)$ and $\text{CO}(4-3)$. They did not observe a smooth velocity gradient along the long axis of the filament but rather two large clumps at the north-western and south-eastern end of it. Their velocities differ by about

3 km s^{-1} , while the central part of Lupus I lies at an intermediate velocity. Moreover, they reported on a coherent velocity gradient of about $1 \text{ km s}^{-1} \text{ pc}^{-1}$ running across the central part of the filament (perpendicular to the long axis). Further, they found an increased linewidth at the edge of Lupus I which is facing USco compared to the gas behind it.

Benedettini et al. (2012) conducted CS(2–1) observations of the central and of a portion of the southern part of Lupus I. They found that the gas velocity increased from the north-west of the central part to the south of the filament by more than 1 km s^{-1} from 4.3 to 5.9 km s^{-1} . In the southern part they also saw a horizontal velocity gradient where the gas velocity increased perpendicular to the long axis of the filament from 3.9 km s^{-1} at the edge towards USco to 6 km s^{-1} at the edge towards UCL. They reported that the CS(2–1) peak velocity increased from 4.4 to 5.5 km s^{-1} in the southern part of Lupus I. This agrees with my C^{18}O observations in cut C (Figure 5.4). Their field-of-view covers approximately the portion of cut C between $10'$ and $20'$ (see PV-diagram in Figure 5.5) where this gradient is present. Their observations, however, do not include the component in the north-eastern part of cut C which has slightly higher velocities than that in the south-western part.

The velocity structure of the gas in Lupus I is very complex. At many positions there are several components along the line-of-sight and its distinction is not always easy. In addition, optical depth effects play also an important role. An increased ^{13}CO linewidth for instance as found by Tothill et al. (2009) might just be an effect of the opacity broadening of the line as it becomes optically thick. Furthermore, the linewidths they found are in general very high and mostly above 2 km s^{-1} . This is at least twice the values I calculated from the CO data. This might be explained by the spatial resolution ($\text{HPBW} = 3.3'$) of their $^{13}\text{CO}(2-1)$ observations which is almost seven times worse than that of my data. Thus, they might not have been able to spatially resolve the different velocity components present in the gas and might just have seen very broad lines as the result of a superposition of several shifted components. Hence, the results from an optically thick tracer (like ^{12}CO) or one that becomes optically thick in dense portions of Lupus I (^{13}CO) might be misleading concerning velocity gradients and variations in linewidths. A good example for this effect can be seen in cut C. In the PV diagram (Figure 5.5) the velocity of the peak intensity is marked with a white cross for each position along the cut. Regarding the peak positions, ^{13}CO suggests the presence of two large velocity gradients. One running from the north-eastern edge towards the center and the other running from the center to the south-western end of the cut. However, the C^{18}O data reveal that there is just one velocity gradient in the center of the cut, i.e. inside the prestellar core that resides there. In the north-eastern and the south-western part of the cut there are two separated velocity components that have no gradient but are coherent in velocity. Thus, ^{13}CO can be misleading in this case because the peak temperature may shift between different velocity components that are present throughout the cut (compare Figure 5.12). Either the ^{13}CO components must be differentiated or the optically thin tracer C^{18}O should be used instead because velocity gradients appearing in the (possibly) optically thick tracer may not necessarily be present in the (more) optically thin tracer.

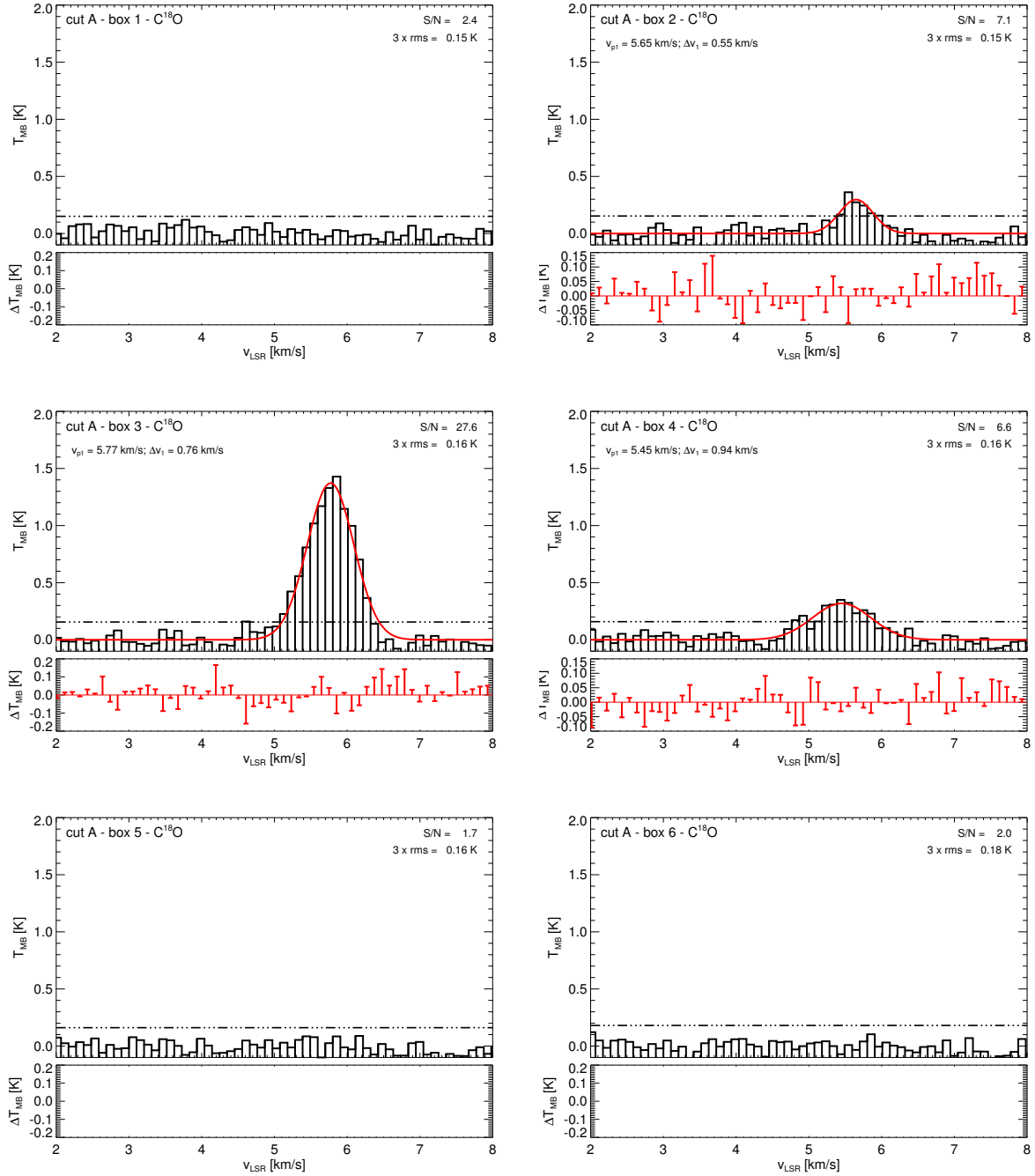


Figure 5.14: Histograms of the average $C^{18}O$ spectra of the six boxes across cut A with a bin size of 0.1 km s^{-1} . The black dash-dotted line marks the $3 \times \text{rms}$ limit. The values of $3 \times \text{rms}$ and the signal-to-noise ratio S/N are given in the upper right of the plot. The red solid line shows the Gaussian fit to the spectrum. If more than one component was fitted, each one of them is represented by a blue dashed line and the red solid line is their sum. The residuals of the fit are given by the red bars in the small plot below the spectrum. Peak positions v_{pi} and FWHM Δv_i of each component in one box are given in the upper left of the plot. A summary of all these values can be found in Table 5.4 where they are denoted by an upper index G. The numbering of the components is done according to the grouping performed in the empirical analysis (see Table 5.3 and Figure 5.13) and thus not always in increasing order.

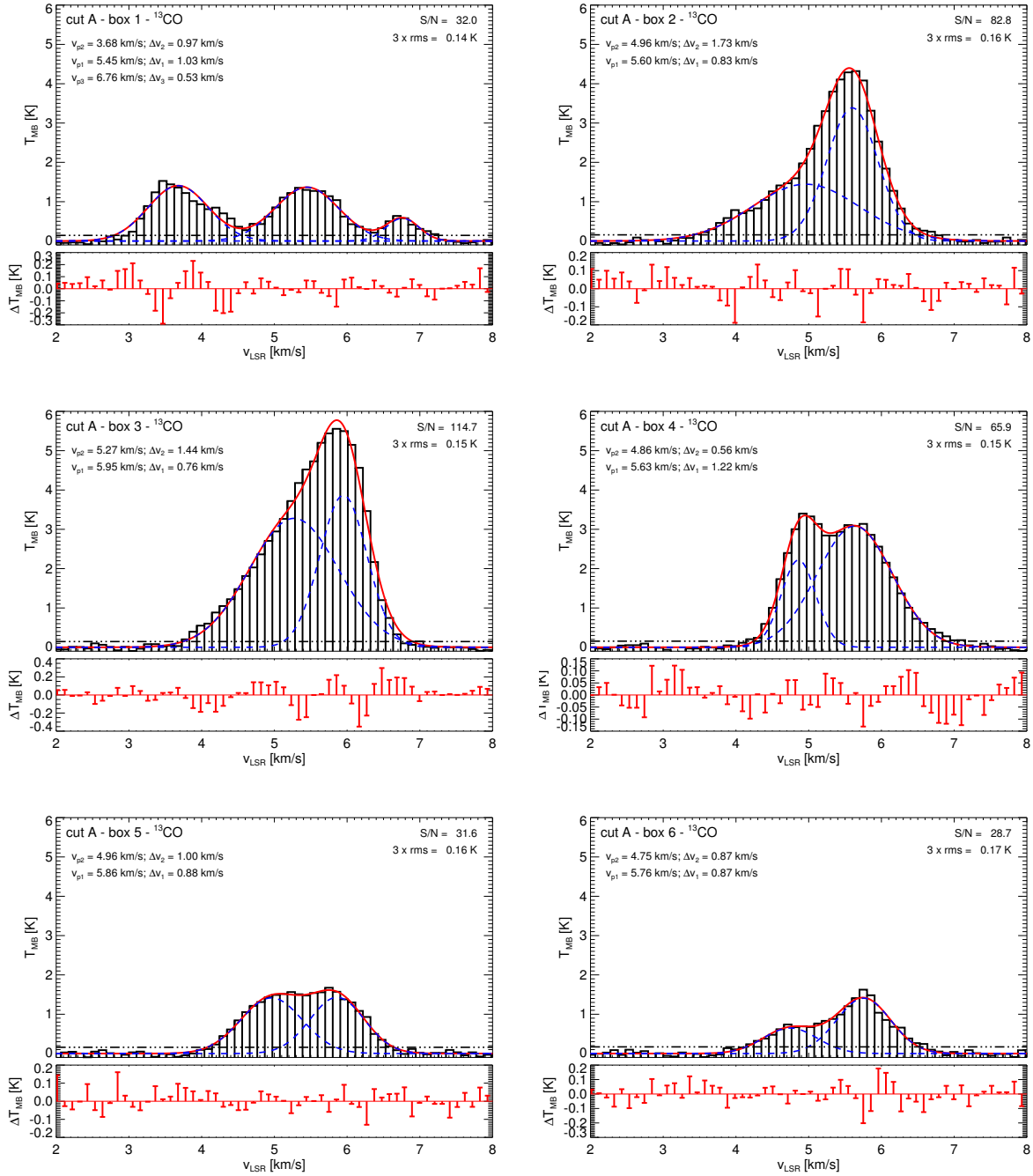


Figure 5.15: Histograms of the average ^{13}CO spectra of the six boxes across cut A with a bin size of 0.1 km s^{-1} . The black dash-dotted line marks the $3 \times \text{rms}$ limit. The values of $3 \times \text{rms}$ and the signal-to-noise ratio S/N are given in the upper right of the plot. The red solid line shows the Gaussian fit to the spectrum. If more than one component was fitted, each one of them is represented by a blue dashed line and the red solid line is their sum. The residuals of the fit are given by the red bars in the small plot below the spectrum. Peak positions v_{p_i} and FWHM Δv_i of each component in one box are given in the upper left of the plot. A summary of all these values can be found in Table 5.4 where they are denoted by an upper index G. The numbering of the components is done according to the grouping performed in the empirical analysis (see Table 5.3 and Figure 5.13) and thus not always in increasing order.

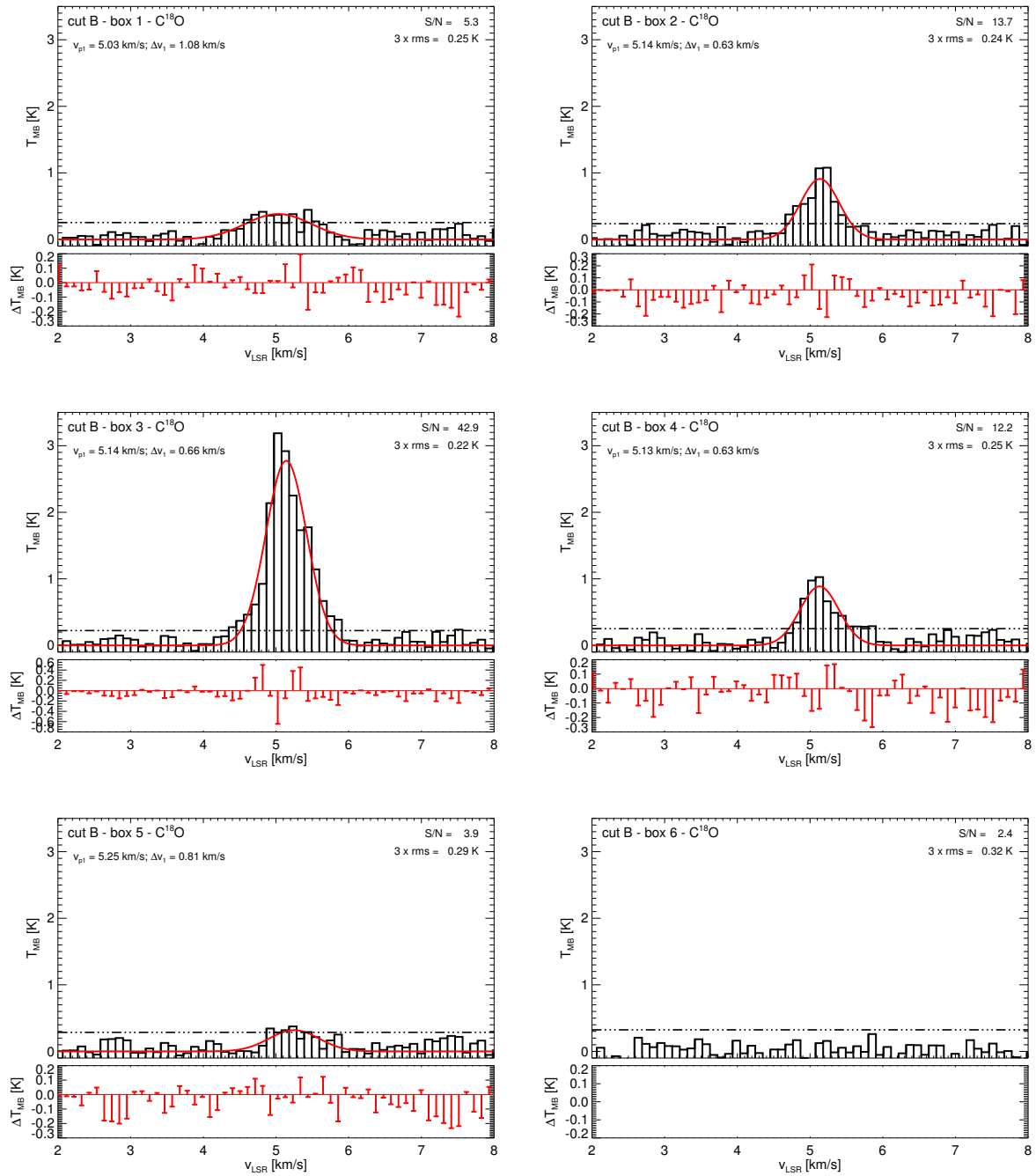


Figure 5.16: Same as Figure 5.14 but for cut B.

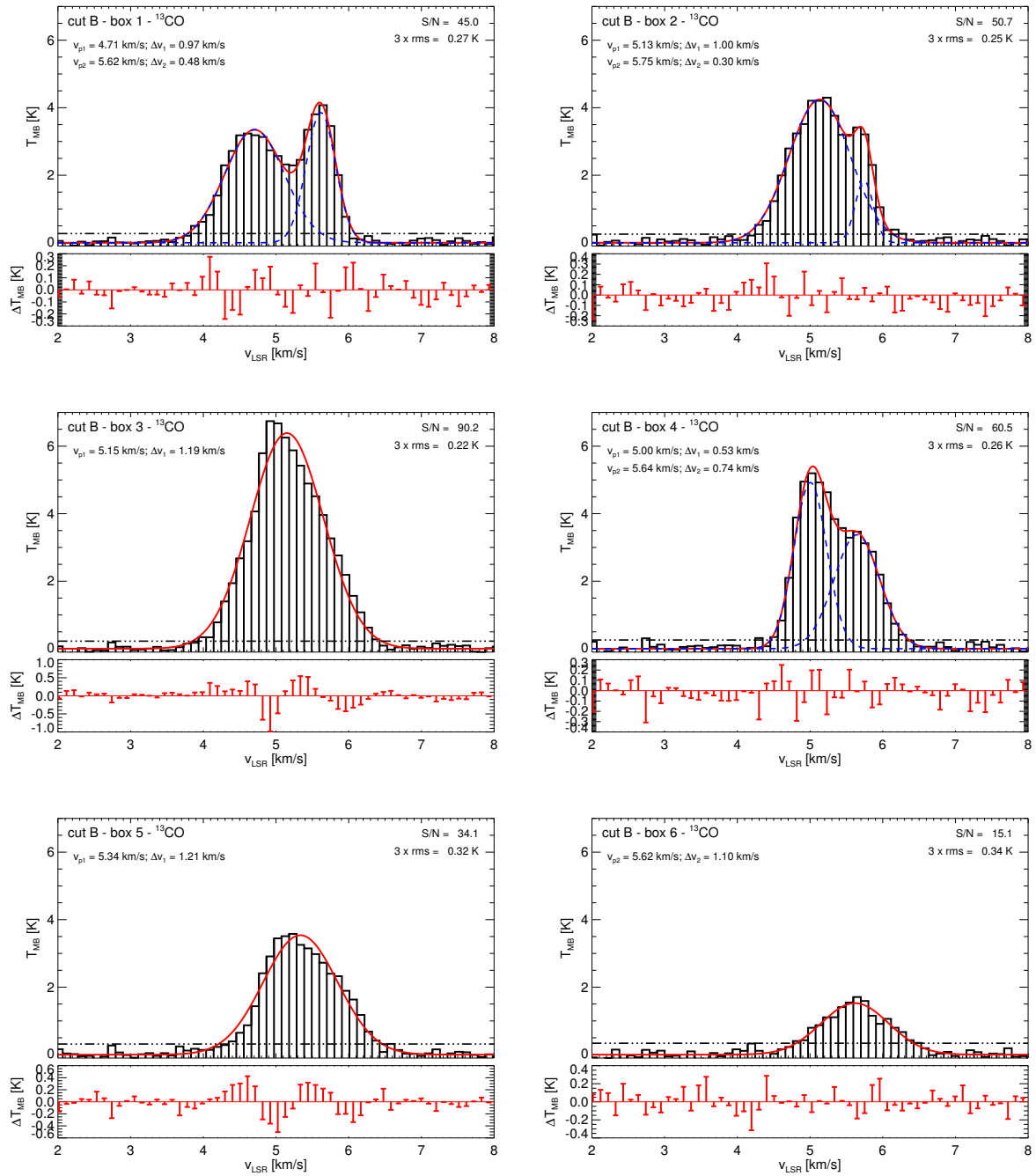


Figure 5.17: Same as Figure 5.15 but for cut B.

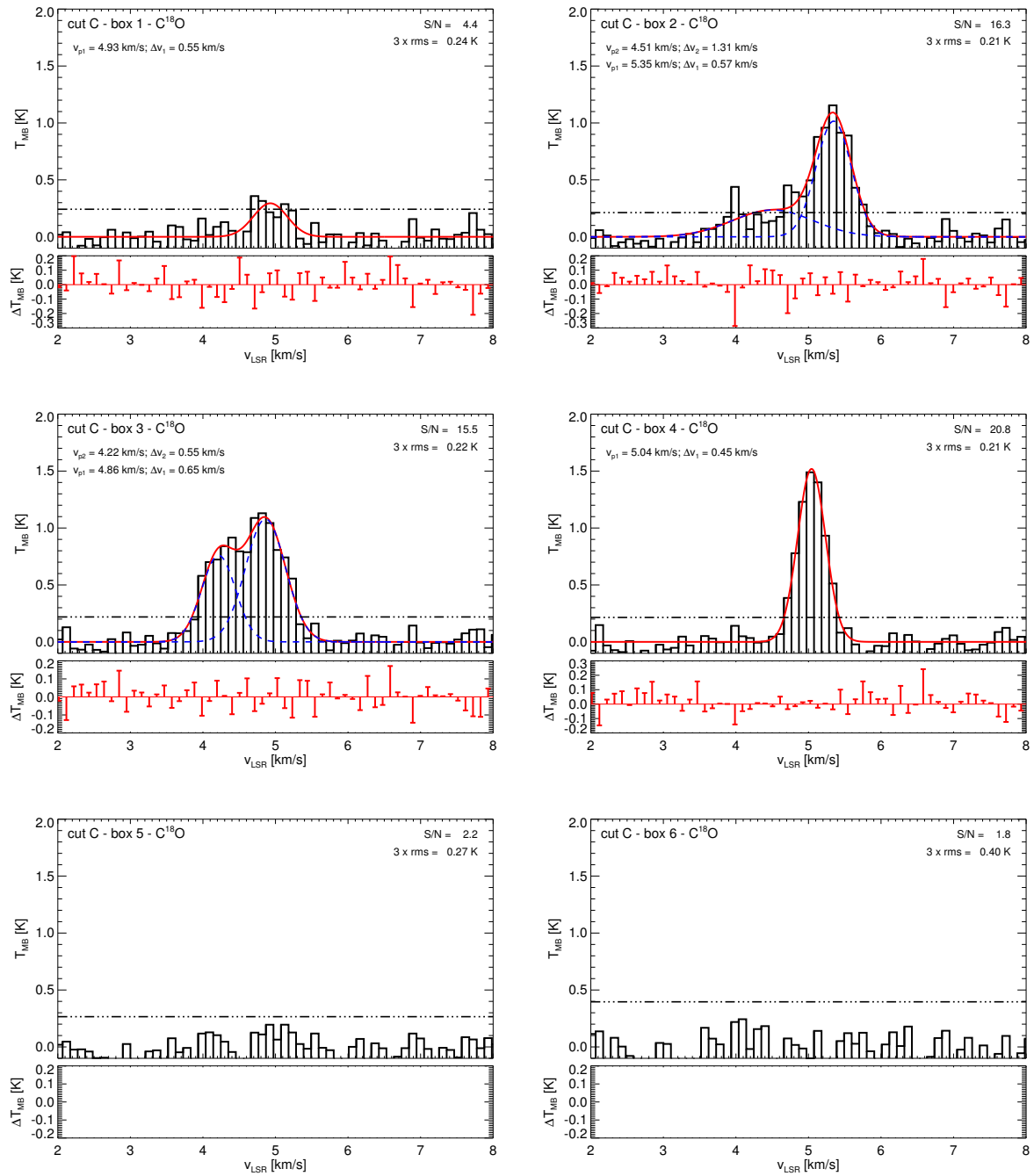


Figure 5.18: Same as Figure 5.14 but for cut C.

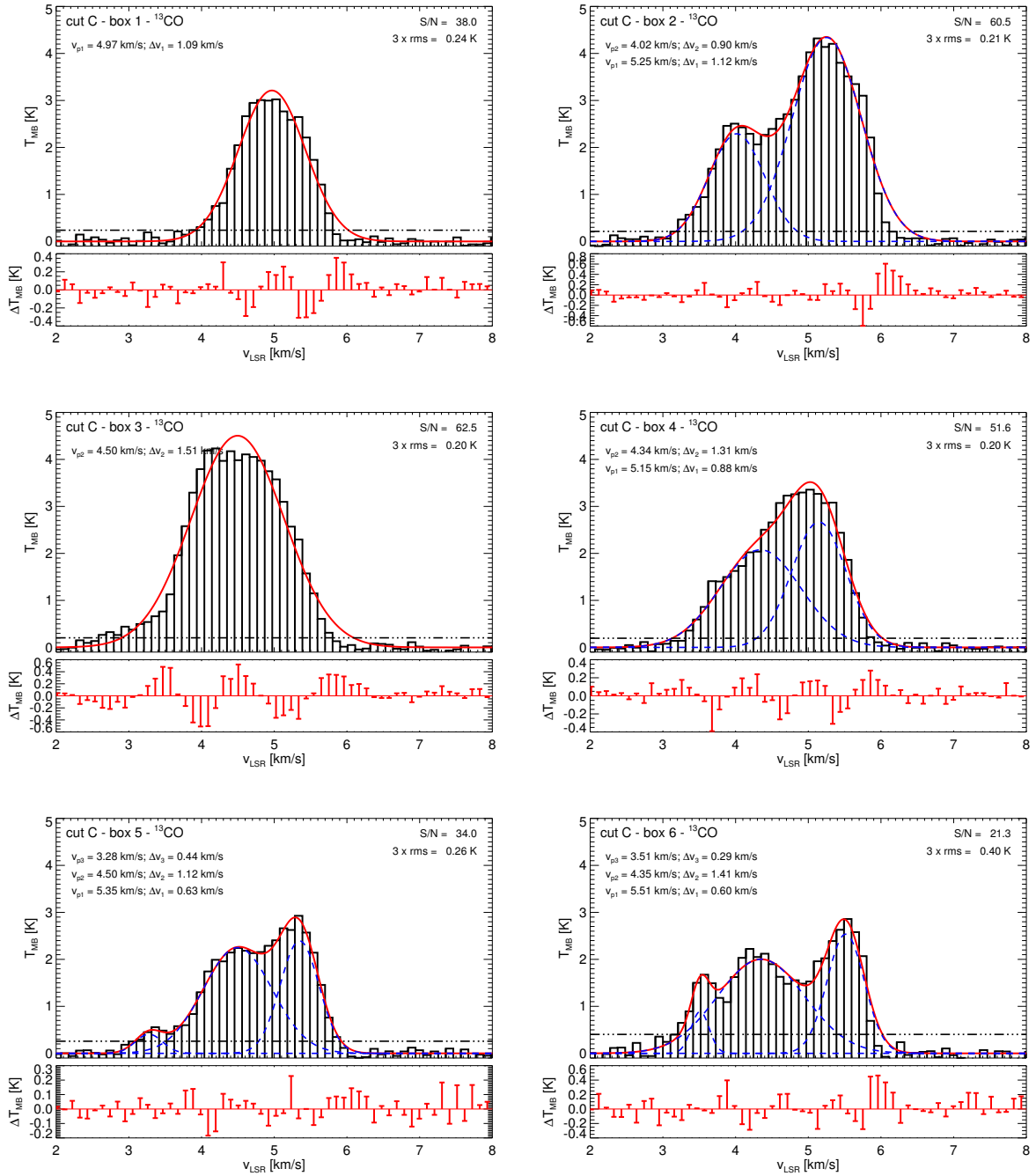


Figure 5.19: Same as Figure 5.15 but for cut C.

5.7 Summary of the kinematic results

From my C¹⁸O observations I can confirm that the northern part of Lupus I represented by cut A has significantly higher gas velocities than the center and the southern part (cuts B and C). This difference is about half the value that has been reported in the literature (0.5 compared to 1 km s⁻¹). However, the data do not allow to detect a possible gradient along the long axis of the filament because they do not cover the cloud in between the cuts. Within the cuts only in the center of cut C a significant gas velocity gradient is evident. Not separating the different velocity components within the cuts may result in a false identification of seemingly large velocity gradients. This is especially true for the more optically thick ¹³CO. The gradient could be as large as 3 km s⁻¹ pc⁻¹ in cut A if one compared $v_{p_2} = 3.5$ and $v_{p_3} = 6.7$ km s⁻¹ with each other (see Table 5.3). Therefore, special care has to be taken in the analysis and interpretation. In all three cuts the non-thermal component of the linewidth is in the transonic regime. Thus, a significant level of turbulence is present in those regions and possibly the whole cloud. This might be due to the compression from the USco HI shell and the UCL wind-blown bubble. However, the data do not indicate increased linewidths at the edges of the cuts. Neither C¹⁸O nor ¹³CO shows such a behavior.

5.8 Comparison to the HI data

In this section, I compare my results from the CO analysis to the HI data of Lupus I. The atomic hydrogen data are part of the GASS HI survey (McClure-Griffiths et al. 2009; Kalberla et al. 2010). They have a spatial resolution of $14.4'$ which corresponds to a length scale of 0.6 pc at the distance of Lupus I. The velocity resolution is $\approx 0.8 \text{ km s}^{-1}$. A velocity channel map for $v_{\text{LSR}} = 0\text{--}8 \text{ km s}^{-1}$ and an HI column density map are shown in Figure 5.20. Black contours represent the integrated $\text{C}^{18}\text{O}(1\text{--}0)$ emission observed by Hara et al. (1999).

The HI emission lies in the same velocity range as the CO emission, i.e. mainly between $v_{\text{LSR}} = 3\text{--}7 \text{ km s}^{-1}$. The peak emission is at $v_{\text{LSR}} = 5 \text{ km s}^{-1}$ which agrees with the velocity of the CO emission peaks in cuts B and C. Both, the channel map and the column density map, reveal that the HI emission and the CO emission do not spatially agree with each other. The highest column density is located at the north-western end of Lupus I. Two other slightly lower peaks are found further south-west. In the central and the southern part of Lupus I there is less HI emission than in the north. Between $b = 15^\circ 30'\text{--}17^\circ$ and $l = 338^\circ 30'\text{--}339^\circ 30'$ there is a deficit in HI emission around the center-south of Lupus I in the form of a little hole. The HI emission, in general, is enhanced at the Galactic west side of Lupus I and has a deficit on its east side. The average HI column density for Lupus I is $\langle N_{\text{H}} \rangle = 5.5 \times 10^{20} \text{ cm}^{-2}$. This means that the atomic to molecular fraction is less than unity for both parts of the cloud assuming the averaged H_2 column densities derived from dust emission of $1.10 \times 10^{21} \text{ cm}^{-2}$ and $1.72 \times 10^{21} \text{ cm}^{-2}$ for the north and the center-south, respectively (see Table 4.2). Using the mean H_2 column density from the CO analysis would decrease the ratio even further. However, given the large uncertainties in the determination of these values, the ratio could also well be around or above unity. Benedettini et al. (2015), for example, reported a ratio of $\langle N_{\text{H}} \rangle / \langle N_{\text{H}_2} \rangle \approx 1.6$ calculated from their *Herschel* column density maps and the HI data of de Geus (1992).

Most likely Lupus I marks a transition region between the molecular and atomic phase of HI. At those places in the cloud where the atomic hydrogen emission is decreased, the molecular emission is enhanced and vice versa (see bottom panel of Figure 5.20). Also my own C^{18}O analysis showed that its emission is almost negligible in cut A (north) and significantly higher in cuts B and C, i.e. in the center and the south of Lupus I. This may explain why the northern part of the cloud is different from the center and the south. The north might not have build enough dense molecular material yet to start the star formation process. Therefore, the north is quiescent. The lower dust column densities seen there might be another reason for a higher fraction of atomic material. As H_2 forms predominantly on the surface of dust grains the formation efficiency may be lower where less dust is available within the cloud. In the central and southern part of Lupus I the molecular to atomic portion of the material is significantly higher. The C^{18}O emission is strongest whereas the HI emission has a deficit. Active star formation and high CO column densities ($N(\text{H}_2) \approx 10^{22} \text{ cm}^{-2}$) can be seen. Heiner et al. (2015) have created synthetic HI and CO observations from a numerical simulation of decaying turbulence in the thermally bistable neutral medium. They find a power-law tail in the column density

PDF when molecular clouds have formed. This tail, however, only appears in the PDFs of the molecular material and not the HI. Hence, they conclude that the molecule formation is directly correlated with gravitational infall. The dust PDF of the northern part of Lupus I does not show a power-law tail. Thus, the gravitational infall might not yet be significant to convert as much atomic material into molecular one as is apparent in the center-south. Another explanation might be that the molecular material that has already formed in the north is still CO dark because there is not yet enough column density to provide sufficient shielding for CO from destructive UV radiation. The average H₂ column density in the north as calculated from the *Herschel* column density map is $1.1 \times 10^{21} \text{ cm}^{-2}$ and thus lower than the required value for CO shielding ($\sim 10^{22} \text{ cm}^{-2}$). My CO data yielded an H₂ column density of $3.5 \times 10^{21} \text{ cm}^{-2}$ for cut A. Somewhat higher than that from the dust analysis, but still lower than the required 10^{22} cm^{-2} . I conclude, that this particular configuration of the atomic and molecular material in and around Lupus I and the co-moving CO and HI gas velocities suggest that the formation of the cloud is linked to the large-scale feedback of the USco and the UCL subgroups of Sco-Cen.

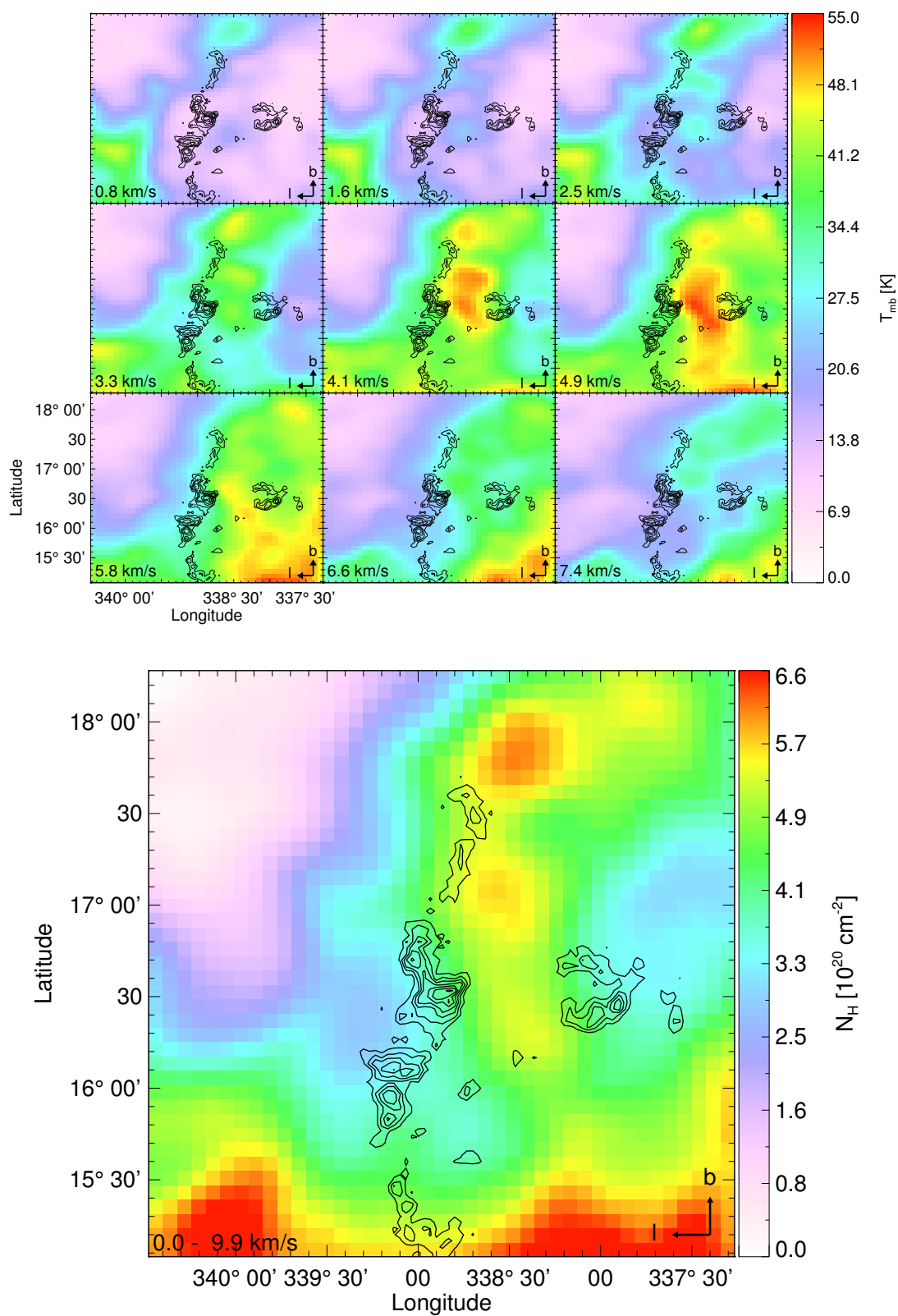


Figure 5.20: *Top*: HI channel maps for a velocity range of $v_{\text{LSR}} = 0.8\text{--}7.4 \text{ km s}^{-1}$. Black contours show the integrated $\text{C}^{18}\text{O}(1-0)$ emission observed by Hara et al. (1999). They start at 0.3 K km s^{-1} with a step size of 0.3 K km s^{-1} . *Bottom*: HI column density map calculated from the integrated emission for $v_{\text{LSR}} = 0\text{--}10 \text{ km s}^{-1}$.

Chapter 6

Lupus I in context of the star formation history of Sco-Cen

In the previous chapters, I have presented several arguments that Lupus I is a special molecular cloud whose formation history is mainly influenced by external drivers. In this chapter, I discuss those arguments placing Lupus I in the context of its surroundings and the formation history of the two neighboring subgroups, USco and UCL, and their large-scale feedback. In a last step, I test the plausibility of the proposed scenario with a geometrical model.

6.1 Surroundings of Lupus I

The *Planck* data are best suited to study the dust surroundings of Lupus I (see Figure 6.1). These observations at 350, 550, and 850 μm cover the whole sky at a resolution of 5'. Lupus I lies on the Galactic eastern edge of a ring-like dust ridge (labeled in bottom panel of Figure 6.1) that extends from about $b = +10^\circ$ to $b = +25^\circ$ in Galactic latitude with a center at about $l = 345^\circ$, $b = +17.5^\circ$. The ridge is $\sim 5^\circ$ wide, which corresponds to ~ 13 pc at the distance of Lupus I. In addition to Lupus I, it consists of several small molecular clouds extending north of Lupus I and then bending towards the east connecting with the ρ Ophiuchus molecular cloud on the opposite site of Lupus I. No dust emission is seen in the *Planck* maps farther west of Lupus I. The same is true for the inside of the dust ridge: between ρ Ophiuchus and Lupus I a roundish dust void is seen. However, these two dust voids on either side of Lupus I are filled with hot, X-ray emitting gas that can be seen with ROSAT (top left in Figure 6.1). The bottom panel in Figure 6.1 shows the dust emission seen by *Planck* in 350 μm . Overlaid in white are the contours of the ROSAT diffuse X-ray emission at 3/4 KeV¹. Inside USco the contours follow the edge of the dust ridge indicating that the hot X-ray gas might be in contact with the cold dust. On the western

¹The very strong X-ray emission seen near the position of the B2IV star southwest of Lupus I (κ Cen; $l = 326.872^\circ$, $b = +14.754^\circ$) is neither related to the star nor to Sco-Cen, but most likely caused by the quasar [VV2006] J150255.2–415430.

side of Lupus I, the contours mark the outline of the second roundish X-ray emission seen in ROSAT. The cyan dots mark the remaining early B-type stars of UCL. Both contours seem to wrap around Lupus I what might be a sign that the cloud is embedded in hot ISM.

These dust voids and the observed X-ray gas might be explained by the cumulative feedback of the massive stars in the USco and UCL subgroups of Sco-Cen. Their creation has been interpreted in a scenario of propagating molecular cloud formation and triggered cloud collapse and star formation taking place within the last 17 Myr in the UCL and USco subgroups of Scorpius-Centaurus (see de Geus 1992; Preibisch & Zinnecker 2007). The expansion of the UCL HI shell that started ~ 17 Myr ago and was driven by winds of the massive stars and supernova explosions, has probably cleared out almost all the dust and molecular material west of Lupus I; however, the observed X-ray gas on that side is probably not related to the supernova explosions because the X-ray luminosity of supernova-heated superbubbles dims via expansion losses and mixing with entrained gas on a timescale of typically less than a million years (Krause et al. 2014). The shell today has a radius of ~ 110 pc (as seen from HI data; de Geus 1992), generally consistent (compare, e.g. Baumgartner & Breitschwerdt 2013; Krause et al. 2013) with the inferred age of the stellar group, about 17 million years. Therefore, this X-ray gas is probably currently heated by the remaining B-stars of UCL. Six of the stars southwest of Lupus I ($325^\circ < l < 335^\circ$ and $+10^\circ < b < +15^\circ$; see bottom panel in Figure 6.1) lie at positions that makes it likely that they are the sources of this wind bubble.

The USco HI shell started its expansion ~ 5 Myr ago powered by the winds of the OB-stars and quite possibly a recent supernova explosion, about 1.5 Myr ago, as suggested by the detection of the 1.8 MeV gamma-ray line towards the USco subgroup and the detection of the pulsar PSR J1932+1059 (Diehl et al. 2010, and references therein). What now forms the above-mentioned dust ridge is probably the remaining material of the USco parental molecular cloud that was swept up by the advancing USco shell leaving the dust void filled with X-ray gas. From simulations, large-scale oscillations of the hot, X-ray emitting gas (Krause et al. 2014) are expected because the energy source is never exactly symmetric.

Figure 6.2 shows the USco HI shell as observed today. I have created an HI column density map of USco and the surroundings of Lupus I which is shown in the top panel. The black and white contours represent the dust emission at $850 \mu\text{m}$ and the CO(1–0) emission from *Planck*, respectively. The blue and black labeled dots represent early B-type stars in USco and UCL, respectively. The model fit to the HI data done by Daniel Kröll yields a shell expansion velocity of $\sim 7 \text{ km s}^{-1}$ and a thickness of ~ 6 pc. The current inner and outer radius is ~ 30 pc and ~ 36 pc, respectively. Both radii of the USco shell are indicated by the two black circles. East and west of Lupus I there are not only dust voids, but also clear HI voids and the atomic material is concentrated in the same area as the dust ridge. A further zoom on Lupus I (bottom panel of Figure 6.2), i.e. the ring-like dust ridge and the areas east and west of it, reveals a complicated distribution of atomic, molecular, and dust material. Whereas the CO emission is always found in regions of dust emission, there are several areas within the ring-like dust ridge where there is HI emission but neither dust nor CO are present. The layering of atomic and molecular material as can be seen in Lupus I (dense CO is surrounded by HI), is also found in other places in the

shell around Lupus I. Although, there are certain positions at which HI emission peaks coincide with CO emission peaks. In this part of the shell where Lupus I is located the molecular material is found preferably behind the atomic one, i.e. closer to the inner edge of the shell. However, local turbulence and inhomogeneities mix the material into complex configurations leading to different atomic to molecular fractions inside the shell.

The comparison of my CO data to the HI data showed that the emission of both tracers lies in the same velocity range. This means that Lupus I is probably co-moving with the atomic material in the shell what would agree with the formation within the shell wall. Dawson et al. (2011b) have found that expanding supershells are capable of accumulating big amounts of material when they sweep through the ISM. Thus, they have a greatly increased density within their walls which leads to very fast chemical timescales. For such a shell they estimate a transition timescale from atomic to molecular material of $\sim 10^6$ – 10^7 yr (see also Koyama & Inutsuka 2000; Bergin et al. 2004; Heitsch & Hartmann 2008; Clark et al. 2012). The estimated age of the USco shell is ~ 5 Myr and hence it should have had sufficient time to accumulate locally enough atomic material and produce molecular material at the position of Lupus I in its wall. From the dust analysis I found that the total mass of Lupus I is only $\sim 170 M_{\odot}$. This is at least two orders of magnitude lower than the estimated total mass of the USco shell ($\sim 10^4$ – $10^5 M_{\odot}$) calculated from the HI model fit of D. Kröll. If the atomic material was homogeneously distributed within the shell, then at least $\sim 10^3 M_{\odot}$ would have been swept up at the current position of Lupus I which is enough to create a $\sim 10^2 M_{\odot}$ molecular cloud. Furthermore, the analysis of the LABOCA data has revealed many pre- and protostellar cores. This suggests that the formation timescale of the cloud and the onset of star formation should be on the order of even less than 2 Myr which is still in agreement with the atomic-to-molecular transition timescale. Matthews et al. (2014) have found that the large-scale magnetic field is perpendicular to the Lupus I filament, i.e. it points in the direction of the USco shell expansion. This might have favored the accumulation of cold, dense atomic gas along the field lines and promoted fast molecule formation (Hartmann et al. 2001; Vázquez-Semadeni et al. 2011).

On the western side of Lupus I there is the UCL wind bubble. The X-ray observations suggest that it could be colliding with the USco HI shell right at the position of Lupus I, squeezing it in between. This wind bubble might have provided a counter-pressure to the expanding USco shell and thus favored this position for an additional compression of the shell material. In this way a new molecular cloud could have been created there and it might explain why not more very young star forming clouds (except ρ Oph that was pre-existing) are seen distributed within the wall of the USco shell.

This view is also supported by the results of the column density PDFs of the dust emission. They have a double-peak profile over the whole extent of the cloud. Together with the dust column density map this shows that Lupus I consists of a dense layer in the center of the filament which is surrounded by much more diffuse material. Simulations have shown that this is consistent with the idea of a two-sided compression through colliding flows (see Matsumoto et al. 2015). Then the molecular cloud is created in a dense and thin sheet layer which is surrounded by the diffuse material of the colliding flows. A significant

level of turbulence is also present in the cloud, as indicated by transonic linewidths in the C¹⁸O data of all three parts of Lupus I. Hence, this turbulence might have been injected by the collision process.

6.2 Geometrical model for the interaction zone

To check the consistency of the scenario that Lupus I might be located in the interaction zone of the USco HI shell and the UCL wind bubble, I have created a simple geometrical model. The observer is in the origin of the coordinate system which is a 3D Cartesian representation of the Galactic coordinate system with

$$\begin{pmatrix} x \\ y \\ z \end{pmatrix} = \begin{pmatrix} r \sin \theta \cos \phi \\ r \sin \theta \sin \phi \\ r \cos \theta \end{pmatrix} \quad (6.1)$$

where $\theta = 90^\circ - b$, $\phi = l$, and r is the distance. The x-axis is defined by the direction to the Galactic center. Both HI shell and wind bubble are represented by a sphere. I place the center of the USco sphere at $(l, b) = (347^\circ, +25^\circ)$ and a distance of 145 pc. I assume a radius of ~ 30 pc, which is the inner shell radius from the HI model fit of Daniel Kröll, because Lupus I seems to be located between the inner and outer shell edge but closer to the inner edge as seen in the observations.

I estimate the average projected position of the B-stars southwest of Lupus I that might be responsible for the wind bubble to be $(l, b) = (331^\circ, +12^\circ)$. This also agrees with the center of a circle I placed in the ROSAT image enclosing the X-ray emission in this region. The average distance from us to the stars of the UCL subgroup is about 5 pc smaller than that to USco (de Zeeuw et al. 1999) and thus I place the center of the UCL sphere at 140 pc.

Therefore, in my model the UCL wind bubble is placed below and slightly in front of the USco HI shell with respect to us. By increasing the radius of the UCL sphere its expansion toward USco and Lupus I is simulated. Figure 6.3 shows the configuration of the model in a perspective view. Figure 6.4 shows the model in a side projection (top panel) and a projection from above (bottom panel). The black sphere in the figures represents the USco shell. The green sphere represents the stage at which the UCL bubble touches the fixed USco sphere (touch point is marked by a magenta cross). The position of Lupus I is marked by three red asterisks that represent the top, middle, and bottom of the main filament, respectively. I have plotted the cloud at three different distances of 150, 140, and 130 pc along the red line which is the line-of-sight between observer and Lupus I. The black and the green solid lines are the LOS between the observer and the corresponding sphere. The model shows that the expansion of the UCL sphere goes in the direction of Lupus I which would eventually be crossed by the sphere.

In a next step the geometrical model is related to the observed velocities of HI (shell) and CO (Lupus I). The model fit of D. Kröll to the HI data of the USco shell yields the line-of-sight velocity at each position on the surface of the shell as would be observed from

earth (for details about the model see upcoming paper by Kröll et al., in preparation). In Figure 6.3 all points on the surface of the USco sphere that have a model velocity between $3\text{--}6\text{ km s}^{-1}$ are marked by cyan dots. This represents the CO velocity range I have observed in Lupus I. The green UCL sphere intersects these points on the black USco sphere. This means that the UCL wind bubble might interact with the USco HI shell at positions that have a similar gas velocity to Lupus I.

The Lupus I cloud and the USco HI shell have similar observed velocities and thus it seems reasonable that Lupus I is expanding with the USco shell. This means that the cloud should be expected close to those locations on the HI shell that have similar velocities. In this work I assume a distance to Lupus I of 150 pc which is the commonly used distance for this cloud. Then the closest position on the shell with a similar velocity would be even just ~ 1 pc away from Lupus I.

The latest distance determination for Lupus I was done by Lombardi et al. (2008b) who used extinction maps from the Two Micron All Sky Survey (2MASS) and combined them with *Hipparcos* and Tycho parallaxes to obtain the distance to the Lupus complexes based on a maximum likelihood approach. They did not determine the distance to the Lupus I cloud itself but to all Lupus clouds as a whole. In their sample only six stars out of 186 were located towards Lupus I and thus their method was strongly biased towards the other Lupus clouds. Therefore, it is not really sure whether their resulting distance of 155 ± 8 pc is valid for Lupus I. Smaller distances can also be found in the literature (see e.g. Comerón 2008, and references therein) and maybe the determination of another more reliable value should be considered. In my model case a distance to Lupus I of 140 pc would place the cloud closer to the touch point (~ 5 pc) of the two spheres than for 150 pc (~ 10 pc) and it would still be very close (< 5 pc) to possible points on the USco shell with similar velocities.

My geometrical model is subject to large uncertainties that I want to discuss shortly. The distance to Lupus I has an uncertainty of possibly even ± 20 pc but my chosen value of 150 pc is more likely an upper limit. The model fit to the HI data has several free parameters. In context of my model the distance to the center of the USco shell and its radius are the most relevant ones. They have an error of ± 20 pc and ± 2 pc. A change of those two parameters already influences the resulting distribution of the LOS velocities on the shell. Finally, the choice of position and size of the UCL sphere is another source of uncertainty. The distance to UCL of 140 pc is an average for all stars of the subgroup. Thus, it might not be representative for the stars I assume to be the driver of the wind bubble. The secular parallaxes of de Bruijne (1999) measured for the individual B-stars suggest that they might be farther away than 140 pc. From that I estimate the uncertainty in this distance to be of order ± 15 pc. As the X-ray emission is proportional to the density squared, it is often only observable for the densest regions because of a not high enough instrument sensitivity. This means that the more diffuse emission remains hidden from the observer and thus a possible wind bubble could be larger or have a different center of origin.

However, within the uncertainties that I assume my purely geometrical model has a configuration in which the UCL wind bubble intersects at the same time the USco HI shell at positions that have LOS velocities similar to those of Lupus I and the location of the cloud itself. The model does not represent the real situation accurately which is much more complicated and certainly has a more complex geometry. But even such a simple model shows that the observational data do not exclude the idea that Lupus I is indeed in an interaction zone between the USco HI shell and the UCL wind bubble. Moreover, this model indicates that Lupus I can be expanding with the USco shell and that the cloud most likely is located at the edge of the inner shell which is consistent with the observations. As a next step following this model a more realistic scenario could be created by performing numerical simulations.

The results I have presented in this work suggest that Lupus I was and is strongly affected by large-scale external compressing forces coming from the expansion of the USco HI shell and the UCL wind bubble. The cloud was most likely formed out of the atomic material swept up by the USco shell and is now expanding with the shell. The collision with the UCL wind bubble might have been the factor that enhanced a local inhomogeneity and the density in the USco shell at a position that favored the formation of Lupus I.

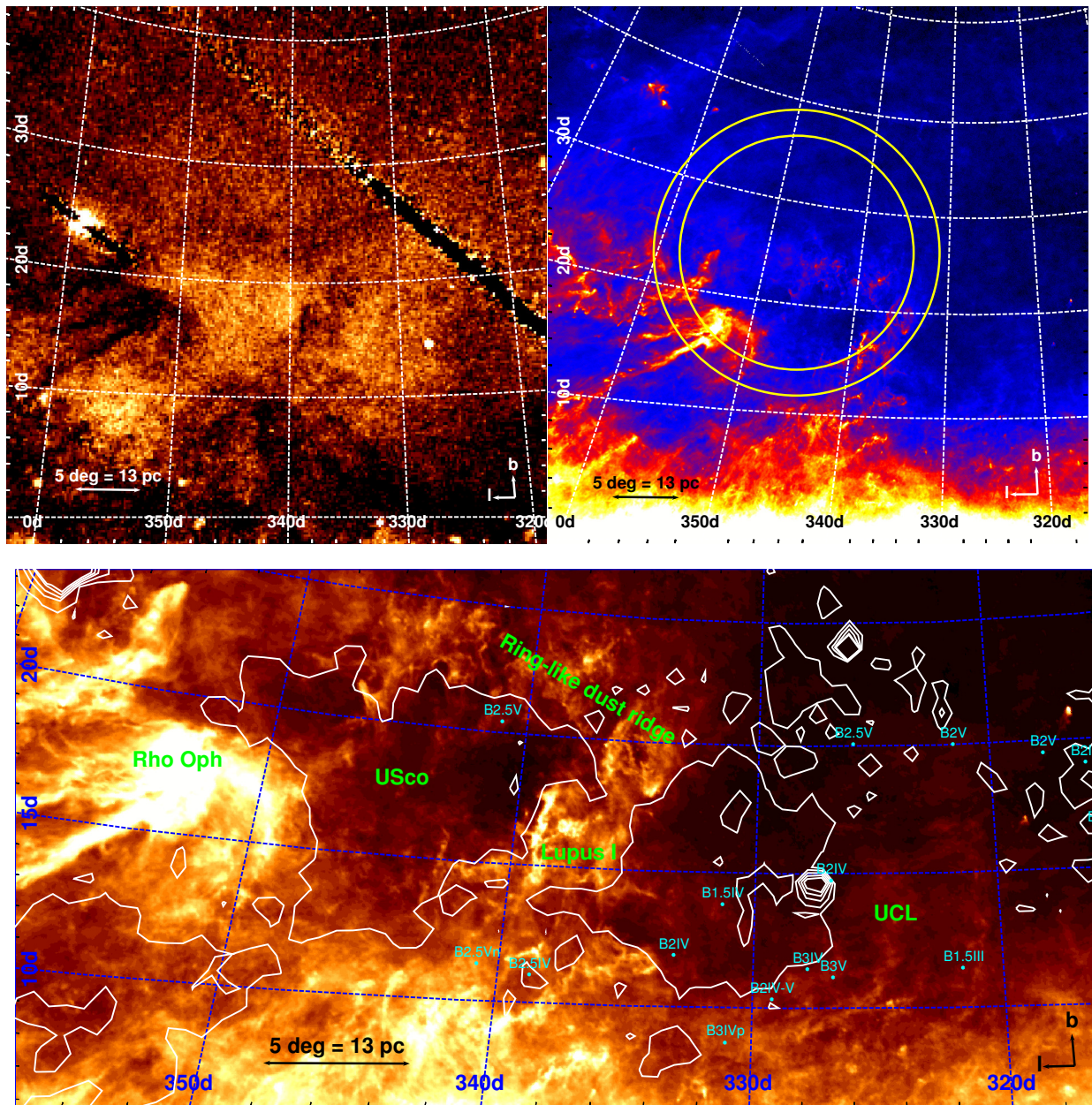


Figure 6.1: *Top*: Surroundings of Lupus I in X-rays (ROSAT 3/4 KeV, left) and dust emission (*Planck* 850 μm , right). There are two X-ray bubbles on either side of the Lupus I ridge and both Lupus I and ρ Ophiuchus as well as the little cloudlets north of them seen in dust emission have X-ray shadows. The yellow dashed circles in the right image give the position of the inner and outer edge of the USco HI shell determined from the model fit. The center lies at $l = 347^\circ$, $b = 25^\circ$ and the inner and outer radius is 12° and 15° , respectively. *Bottom*: Surroundings of Lupus I seen in dust emission (*Planck* 350 μm). The white contours mark the X-ray emission (ROSAT 0.8 KeV) from $0.27\text{--}1 \times 10^{-3}$ counts/s. The cyan dots mark the positions of the B1-B3 stars of UCL from the *Hipparcos* catalog. Labels are given in green.

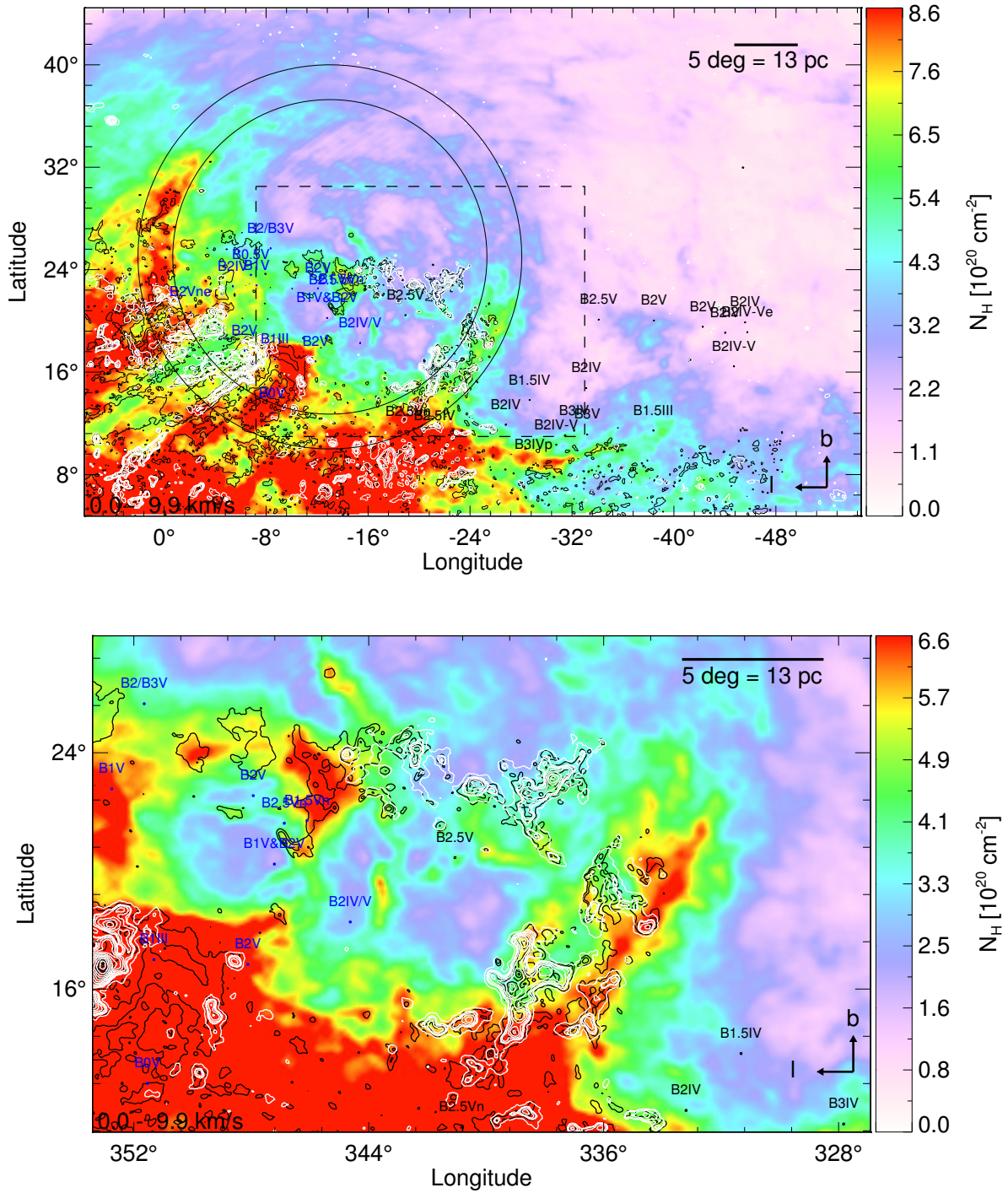


Figure 6.2: *Top*: HI column density map of USco and the surroundings of Lupus I calculated from the integrated emission for $v_{\text{LSR}} = 0\text{--}10\text{ km s}^{-1}$. The two black circles indicate the inner and outer radius of the USco shell from the model fit. The black and white contours represent the dust emission at $850\ \mu\text{m}$ and the CO(1–0) emission from *Planck*, respectively. The blue and black labeled dots represent early B-type stars in USco and UCL, respectively. *Bottom*: Zoom into the region indicated as a dashed black box in the top panel.

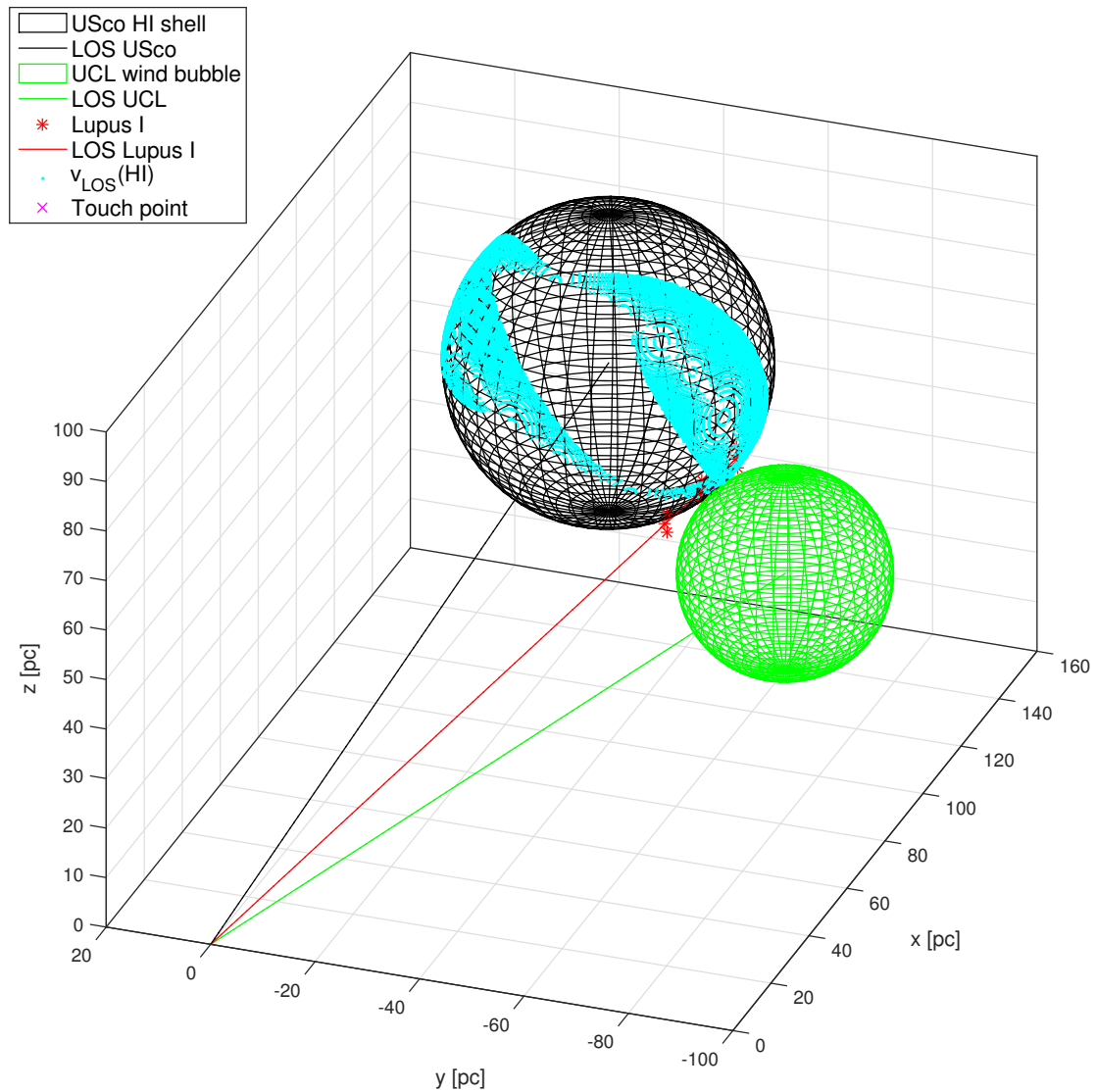


Figure 6.3: Geometrical model of the possible interaction zone between the USco HI shell (black sphere) and the UCL wind bubble (green sphere). The observer is in the origin of the coordinate system. The position of Lupus I is marked by three red asterisks that represent the top, middle, and bottom of the main filament, respectively. The cloud is plotted at three different distances of 150, 140, and 130 pc along the red line which is the line-of-sight from us to Lupus I. The black and the green solid lines are the LOS from the observer to the corresponding sphere. The cyan dots mark those positions on the USco shell that have LOS velocities between 3 and 6 km s^{-1} , i.e. similar to Lupus I. They were calculated from the model fit to the HI data of USco. The magenta cross marks the touch point between the USco and UCL sphere.

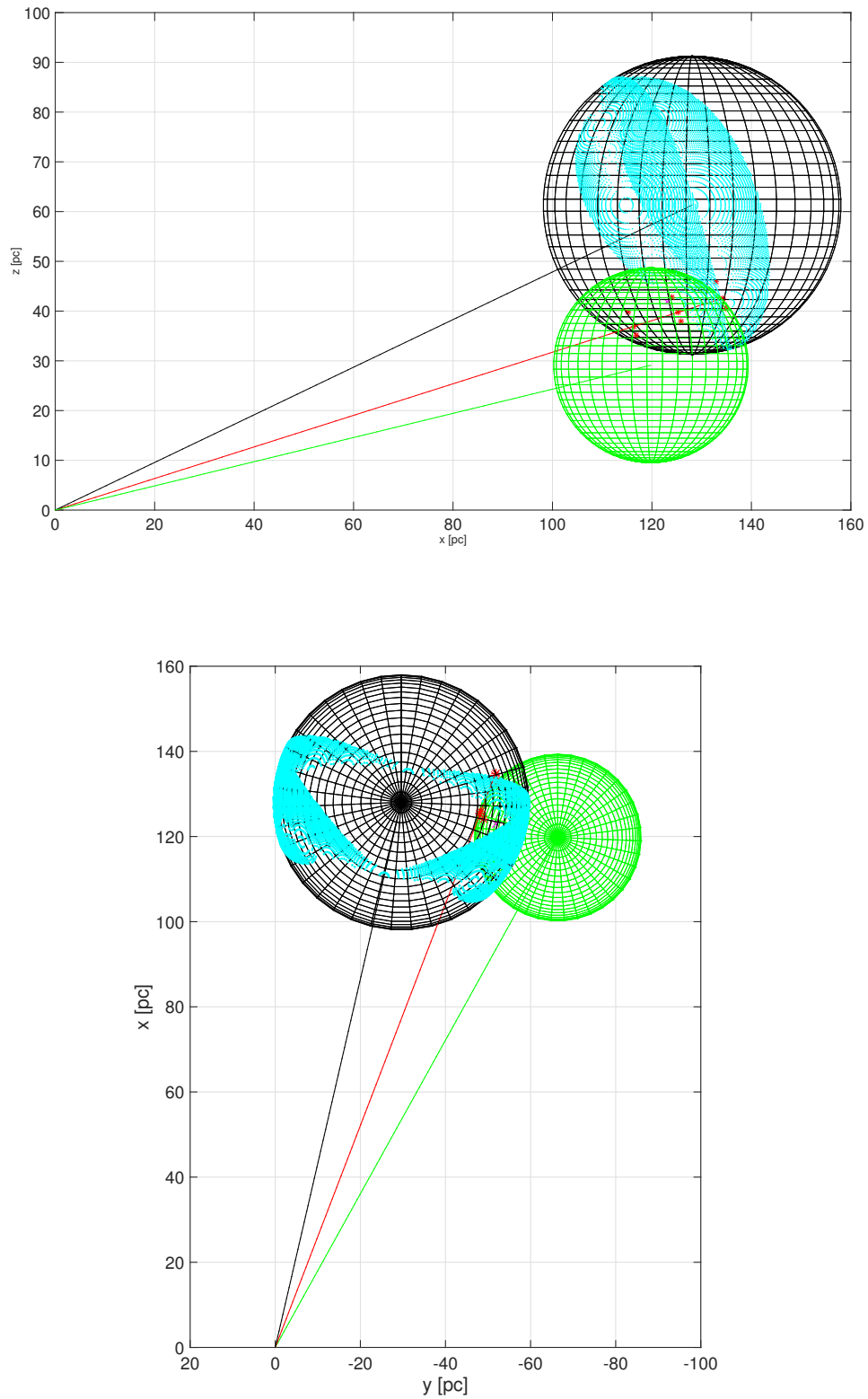


Figure 6.4: Same as Figure 6.3 but now shown in a side projection (top panel) and a projection from above (bottom panel).

Chapter 7

Summary and outlook

In the current picture of the dynamic ISM, molecular cloud formation is attributed to collisions of large-scale flows in the ISM that can be driven by stellar feedback processes, i.e. UV-radiation, winds, and supernovae. One possible example of such a formation process is the Lupus I molecular cloud. It is found between the Upper-Scorpius and the Upper-Centaurus-Lupus subgroups of the Scorpius-Centaurus OB association at a location where an expanding HI shell around USco appears to interact with a bubble currently powered by the winds of the remaining B-stars of UCL. Because it is close, Lupus I is a good candidate to study how such a collision process may form and influence new dense clouds in the ISM.

For this work, I performed new sub-mm continuum observations and C¹⁸O and ¹³CO molecular line observations of Lupus I at the APEX telescope (see Chapter 3). I complemented those with archival multi-wavelength observations of Lupus I and its surroundings to characterize the physical properties of the cloud and find possible tracers of an interaction between the cloud and the expanding shell or bubble.

From my LABOCA sub-mm continuum observations of Lupus I as well as from archival *Herschel* and *Planck* data of far-infrared and sub-mm dust emission I created column density maps of the cloud (Section 4.1). In addition I calculated a temperature map from an SED fit using the three SPIRE bands of *Herschel*. All maps suggest that the cloud can be divided into two distinct regions. The northern part that has on average lower densities and higher temperatures as well as no active star formation and the center-south part with dozens of pre-stellar cores where density and temperature reach their maximum and minimum, respectively.

From the LABOCA and *Herschel* maps I derived column density PDFs for the entire cloud as well as for the two above mentioned regions separately (see Section 4.2). The *Herschel* PDF of Lupus I showed a double-peak profile with a power-law tail. The power-law can be attributed to the star formation activity in the center-south part of the cloud since it disappears in the PDF of the northern part. However, the double-peak profile is conserved throughout the cloud and possibly arises due to the large-scale compressions from the cumulative massive star feedback of the Sco-Cen subgroups. Such a sign for compression in the PDF was previously found in both observations and simulations of

advancing ionization fronts, also supported by simulations of colliding turbulent flows. With LABOCA, I probe the denser parts of Lupus I, and find one lognormal and the power-law tail for the whole cloud and the center-south. The PDF of the northern part shows only the lognormal behavior.

The distribution of the 15 cores that were detected in my LABOCA map confirms that only the center-south part of Lupus I is actively forming stars whereas the north is quiescent (see Section 4.3). The cores have masses between 0.07 and $1.71 M_{\odot}$ and a total mass of $\approx 8 M_{\odot}$. As the cloud has a total gas and dust mass of $\approx 164 M_{\odot}$ (from LABOCA for $N_{\text{H}_2} > 10^{21} \text{ cm}^{-2}$) this means that $\sim 5\%$ of the mass is in cores. All of those cores are pre-stellar or protostellar confirming that we are witnessing a large star formation event. The total mass of Lupus I calculated from *Herschel* and *Planck* for $N_{\text{H}_2} > 10^{21} \text{ cm}^{-2}$ was $\approx 174 M_{\odot}$ and $\approx 171 M_{\odot}$, respectively (Section 4.4).

The age of the population of young stellar objects suggests a compression event about 1–2 Myr ago that lead to rather simultaneous onset of star formation in Lupus I. This large-scale compression might be the reason for the position, orientation and elongated shape of Lupus I, as well as the double-peak PDFs and the population of very young pre-stellar cores I found.

In a next step, I performed follow-up molecular line observations to investigate the kinematics of the gas in Lupus I. With the SHeFI receiver at APEX, I did observations of the $J = 2 \rightarrow 1$ line of ^{13}CO and C^{18}O at three distinct cuts across the Lupus I cloud (Section 3.2). Cut A is located in the north, cut B in the center, and cut C in the south of the filament. Cuts A and C cross the main filament perpendicularly, cut B is more parallel to it and goes through the prominent class 0 protostar IRAS 15398–3359 in the center of the filament. For each cut about 600 individual spectra have been obtained in each CO line that show a variety of complex line profiles (Appendix A). There are spectra with one, two or even three components. Many have asymmetric and non-gaussian profiles.

The averaged spectra of each cut showed that the northern part of Lupus I, represented by cut A, has significantly higher gas velocities than the center and the southern part represented by cuts B and C, respectively (see Section 5.1). Most of the gas in cuts B and C has peak velocities of $\sim 5 \text{ km s}^{-1}$ whereas in cut A they are $\sim 5.8 \text{ km s}^{-1}$. This indicates that there might be a velocity gradient along the main filament of Lupus I which is on the order of $0.25 \text{ km s}^{-1} \text{ pc}^{-1}$. However, due to a lack of observational data in between the three cuts this should be confirmed by further observations.

The integrated intensity map of cut A demonstrated that the bulk of the ^{13}CO and C^{18}O emission is concentrated on the very center of the filament and is the lowest of all three cuts (Section 5.4). In cut B both lines have high integrated intensities at almost every position within the cut. The peaks of the integrated emission of both isotopologues do spatially agree with each other. Cut C instead shows several islands of enhanced integrated CO emission and the peaks of the integrated ^{13}CO and C^{18}O emission are spatially separated from each other.

The LTE analysis (see Section 5.5) showed that the C^{18}O line is optically thin almost everywhere within the three cuts. The optical depth of the ^{13}CO line has average values of $\tau_{13} \sim 3$ in cut A and $\tau_{13} \sim 5$ in the other two cuts. The excitation temperatures I found are

on average ~ 11 K for cuts A and B, and ~ 9 K for cut C. This agrees well with previous findings for Lupus I. However, these T_{ex} are lower by $\sim 30\%$ than the corresponding dust temperatures. The inferred H_2 column densities and PDFs are shifted towards significantly higher values than for the dust but relative to each other show the same tendency. The north has the lowest column densities with a median of $3.5 \times 10^{21} \text{ cm}^{-2}$. The center and the south have similar median values that are higher by a factor of about 2.5 than that in the north.

Velocity channel maps and PV diagrams revealed that the CO emission in Lupus I is mainly found at velocities of $v_{\text{LSR}} = 3\text{--}6 \text{ km s}^{-1}$ (see Sections 5.2 and 5.3). In addition, each cut is composed of several LOS components that overlay each other. This is a sign of complex kinematics of the gas in the cloud. To analyze how these various components behave within one cut and within the cloud each cut was divided into six boxes (Section 5.6). In each of these boxes an average ^{13}CO and C^{18}O spectrum of all pixels within the box was calculated. Then for each component present in the averaged spectrum of one box its peak position and FWHM were determined in two ways: empirically from the spectra and using multi-component Gaussian fitting.

I found that where both a C^{18}O and a ^{13}CO line are present, the mean of the C^{18}O peak positions and that of the ^{13}CO peak positions agree with each other within $\pm 0.2 \text{ km s}^{-1}$. In those cases, however, there is a clear separation between the means of the FWHM of the C^{18}O and ^{13}CO lines, with a difference of $0.5\text{--}0.8 \text{ km s}^{-1}$. This is expected since the more optically thin line (C^{18}O) should be narrower. The C^{18}O linewidth is highest in the center of each cut and equal or lower off-center. However, no C^{18}O emission is found at the edges of the cuts and hence a comparison between those was not possible with the optically thin tracer. Further, the C^{18}O peak positions of cut A, as well as their mean, are systematically higher than those of cut B and cut C. The means are 5.6 , 5.1 , and 5.0 km s^{-1} for cut A, B, and C, respectively. Therefore, there might be a velocity gradient along the long axis of Lupus I but only half as large as previous observations have suggested.

From my data, I did not find evidence for systematically increased linewidths on one side of Lupus I. Also between the cuts no such trend can be seen. Furthermore, a significant gas velocity gradient has been revealed solely in the center of cut C which is most likely related to the pre-stellar core found at this position and possible infall motions. The confusion of distinct velocity components present in Lupus I might just mimic previously reported velocity gradients across the main filament. This may be a result of low spatial resolution and the use of a not optically thin tracer. In all three cuts the non-thermal component of the linewidth is in the transonic regime. Thus, a significant level of turbulence is present in those regions and possibly the whole cloud. This might be due to the compression from the USco HI shell and the UCL wind-blown bubble.

A comparison of my CO data to the available HI data yielded that the emission of both tracers lies in the same velocity range (see Section 5.8). Moreover, C^{18}O emission peaks located in the center-south of Lupus I coincide with deficits in HI emission whereas the position of the HI emission peak in the north shows a deficit in C^{18}O emission. This might resemble two different stages in the transition between atomic and molecular material. In the north a smaller fraction of atomic hydrogen has been converted into molecular

hydrogen and subsequently into dense CO. Therefore, this part of the cloud is quiescent. The center-south of the cloud has instead enough molecular material to actively form stars. This could also be a consequence of the lower dust column density in the northern part of Lupus I. A smaller amount of dust particles reduces the formation efficiency of molecular hydrogen and provides less shielding from destructive UV radiation.

Analyzing the surroundings of Lupus I (see Section 6.1), I found that the cloud lies on the eastern edge of a ring-like, ~ 13 pc wide dust ridge that extends from about $b = +10^\circ$ to $b = +25^\circ$ in Galactic latitude with a center at about $l = 345^\circ$, $b = +17.5^\circ$. No dust emission and almost no atomic hydrogen is seen farther west and east of Lupus I. However, these two voids on either side of Lupus I are filled with hot, X-ray emitting gas observed with ROSAT (Figure 6.1). This might be a sign that the cloud is embedded in hot ISM.

These dust voids and the observed X-ray gas could be explained with the cumulative feedback of the massive stars in the USco (on the Galactic east side of Lupus I) and UCL (west side of Lupus I) subgroups of Sco-Cen. About 17 Myr ago the expansion of the UCL HI shell started which was driven by winds of the massive stars and supernovae explosions. This expansion has probably cleared out almost all the dust and molecular material west of Lupus I. But the observed X-ray gas on that side is most likely currently heated by the remaining B-stars of UCL. Six of these stars, southwest of Lupus I, are located at positions that favor them as the sources of this wind bubble.

On the east side of Lupus I the USco HI shell started its expansion ~ 5 Myr ago powered by the winds of the OB-stars and quite possibly a recent supernova explosion, about 1.5 Myr ago. The above-mentioned dust ridge is probably the remaining material of the USco parental molecular cloud that was swept up by the advancing USco shell leaving the dust void filled with X-ray gas.

A comparison of the large-scale HI, CO, and dust emission in the USco shell and in the vicinity of Lupus I revealed that the molecular material is always found in regions of dust emission and both of those components are preferentially found behind the outer edge of the atomic shell, i.e. further inwards (Figure 6.2). This would be the expected configuration if molecular material was produced inside the expanding HI shell. However, this picture is not found in all parts of the shell. Thus, it is rather likely that local turbulence and inhomogeneities mix the material into complex configurations where each part of the shell wall may have different atomic to molecular fractions.

The CO velocities of Lupus I are in the same range as the HI velocities of the USco shell and thus the cloud is probably co-moving with the shell what would agree with the formation within the shell wall. The timescale of the transition between atomic and molecular material in such a massive shell with $M \approx 10^4\text{--}10^5 M_\odot$ (estimated from the model fit to the HI data by D. Kröll) was estimated to be $\sim 10^6\text{--}10^7$ yr. This is consistent with the age of the USco shell (~ 5 Myr) and the age of the young stellar objects in Lupus I (< 2 Myr). Furthermore, about ten times more material than the mass of Lupus I should have been swept up in the shell at the position of Lupus I which should have allowed the creation of a $\sim 170 M_\odot$ cloud.

On the western side of Lupus I there is the UCL wind bubble. From the X-ray observations it looks like it could be colliding with the USco HI shell right at the position of

Lupus I, squeezing it in between. This wind bubble might have provided a counter-pressure to the expanding USco shell and thus favored this position for an additional compression of the shell material. In this way a new molecular cloud could have been created there and it might explain why not more very young star forming clouds (except ρ Oph that was pre-existing) are seen distributed within the wall of the USco shell. This view can also be supported by the morphology of the dust column density maps and their double-peak PDFs. They show that Lupus I consists of a dense layer in the center of the filament which is surrounded by much more diffuse material. Simulations have shown that this is consistent with the idea of a two-sided compression through colliding flows where the molecular cloud is created in a dense and thin sheet layer which is surrounded by the diffuse material of the colliding flows. The transonic $C^{18}O$ linewidths found in Lupus I might be a sign of turbulence that has been injected by the collision process.

I constructed a geometrical model which showed that the observational data do not exclude the idea that Lupus I is indeed in an interaction zone between the USco HI shell and the UCL wind bubble (see Section 6.2). In the model two spheres represent the shell and the bubble. The USco sphere was placed at 145 pc, the UCL sphere 5 pc in front of it (with respect to us) what corresponds to the average distance to each subgroup. The calculated touch point of the two spheres is close to the possible position of Lupus I and is located in a region on the USco sphere that has similar predicted line-of-sight HI velocities to that of the CO gas in Lupus I. This model also indicated that Lupus I can be expanding with the USco shell and that the cloud most likely is located at the edge of the inner shell which is consistent with observations.

I conclude that the results I have presented in this work suggest that Lupus I was and is strongly affected by large-scale external compressing forces coming from the expansion of the USco HI shell and the UCL wind bubble. The cloud was most likely formed out of the atomic material swept up by the USco shell and is now expanding with the shell. The collision with the UCL wind bubble might have been the factor that enhanced a local inhomogeneity and the density in the USco shell at a position that favored the formation of Lupus I.

To further test the here presented formation scenario of Lupus I, my observational results should be compared to dedicated numerical simulations. I have calculated the physical properties of the cloud, i.e. its density, mass, and temperature. Furthermore, the molecular line data revealed the kinematical behavior of the cloud and the level of turbulence present. The properties of the expanding HI shell of USco have been constrained by the available HI data and the model fit. This includes the expansion velocity, size, mass, density, and predicted LOS velocities with respect to us. The full stellar population has already been investigated and the distances to the individual stars, i.e. the massive early types, are known from the *Hipparcos* data. With that, the X-ray and the γ -ray data, the energy input of these stars can be calculated and with a population synthesis model one can predict the IMF of the USco and UCL subgroups. This information should allow to set up a numerical simulation where the initial conditions are reasonably well constrained. The initial stellar population of USco would follow from the population synthesis model and their approximate birth positions could be traced back from proper motion data. The

B-stars that probably drive the current expansion of the UCL wind bubble could be placed accordingly. Then the expansion of the USco shell could be simulated and the effects on the shell material during the collision with the wind bubble. However, the initial density of the surrounding medium should not be assumed homogeneous because we know from observations that it has been pre-structured by the expansion of the UCL HI shell. In this way it might be possible to obtain constraints on whether a cloud like Lupus I can be created and how much the counterpressure of the wind bubble contributes to a more effective molecular cloud formation. The realization of a simulation that includes all those observational constraints might not yet be feasible, but the results of this work build a good basis to discuss promising and realistic ideas.

Appendix A

CO spectra of cut A, B, and C

In the appendix I present all ^{13}CO and C^{18}O spectra that have been observed for the three cuts in Lupus I. Each figure consists of 10×10 plots that are ordered according to the image coordinate system of the corresponding map of a cut. A raster of each map with the x- and y-coordinates of the pixels is shown at the beginning of a section. The ^{13}CO spectra are plotted in blue, the C^{18}O spectra in red. The corresponding pixel coordinates to which these spectra belong, are given in the upper left corner of a plot (x left, y right). The dashed vertical line marks $v_{\text{LSR}} = 5 \text{ km s}^{-1}$.

A.1 cut A

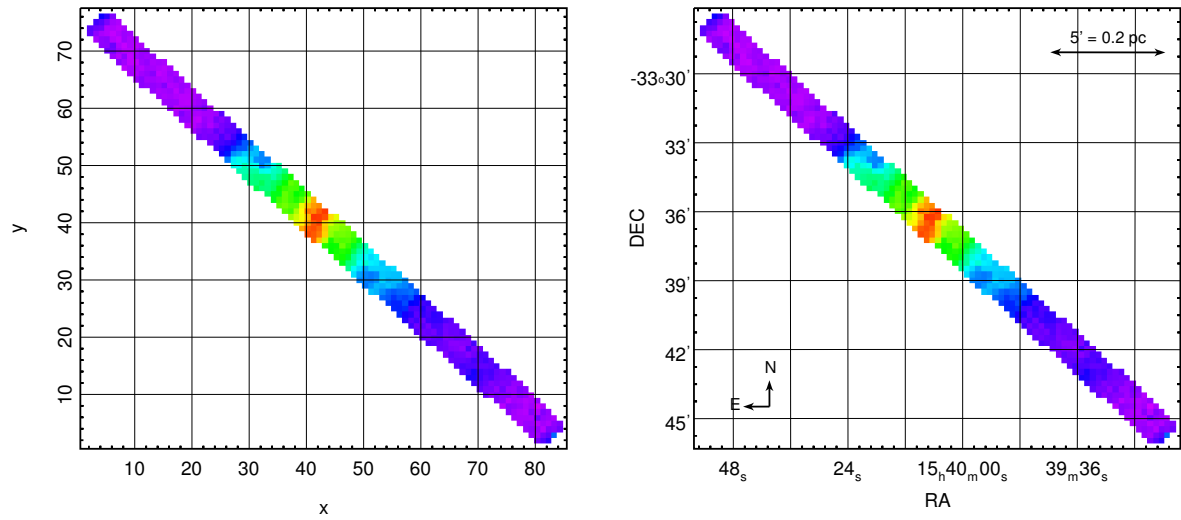


Figure A.1: *Left*: Raster map of the CO spectra in cut A. Background image is the integrated ^{13}CO emission. *Right*: Same map as in the left panel, but with an Celestial coordinate grid (J2000), a compass, and a scale.

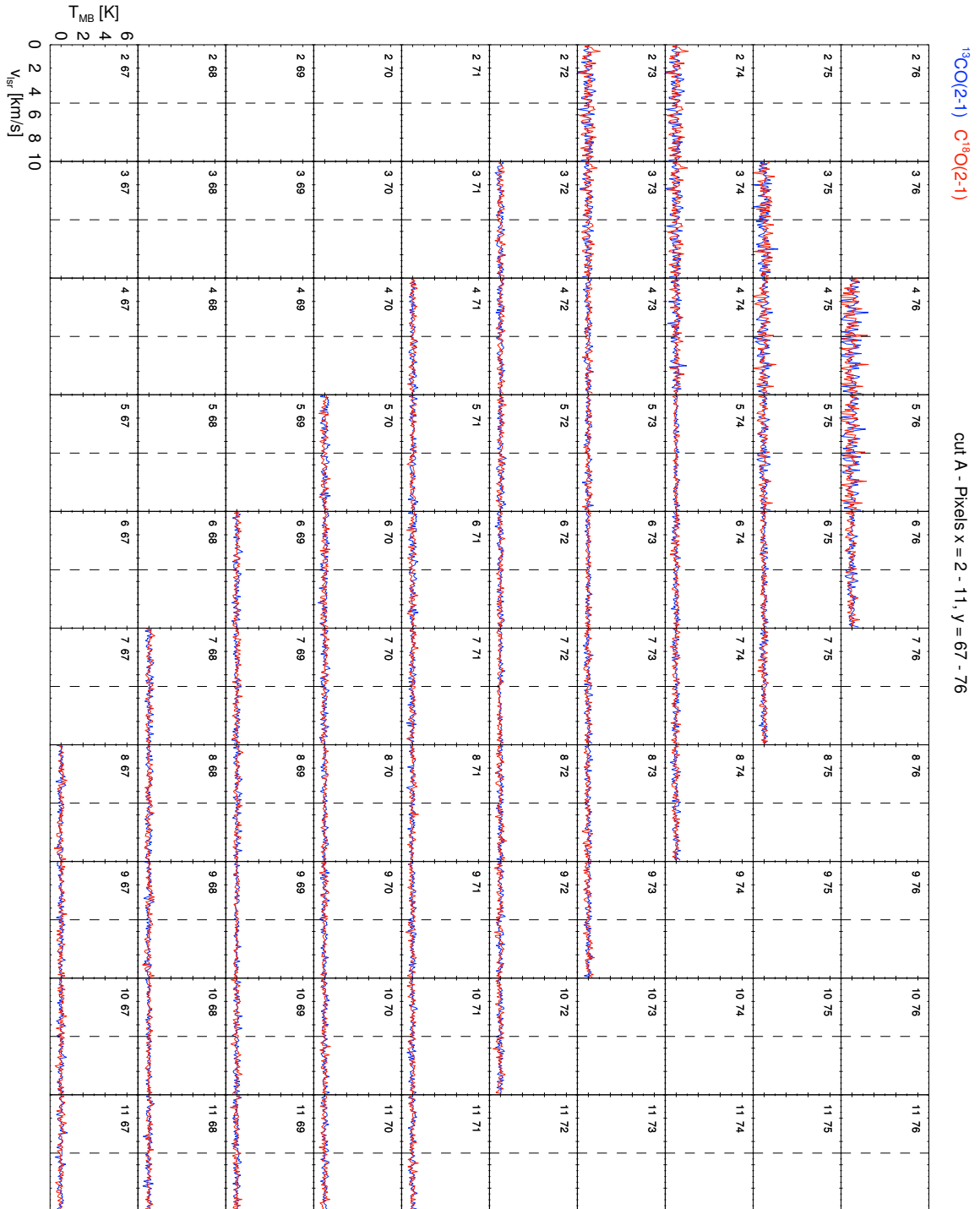


Figure A.2: ^{13}CO (blue) and C^{18}O (red) spectra of cut A. The corresponding pixel coordinates to which these spectra belong, are given in the upper left corner of each plot (x left, y right). The position of the pixel can be found in Figure A.1. The x-axis gives the v_{LSR} velocity in km s^{-1} , the y-axis the main-beam temperature T_{mb} in Kelvin. The dashed vertical line marks $v_{\text{LSR}} = 5 \text{ km s}^{-1}$.

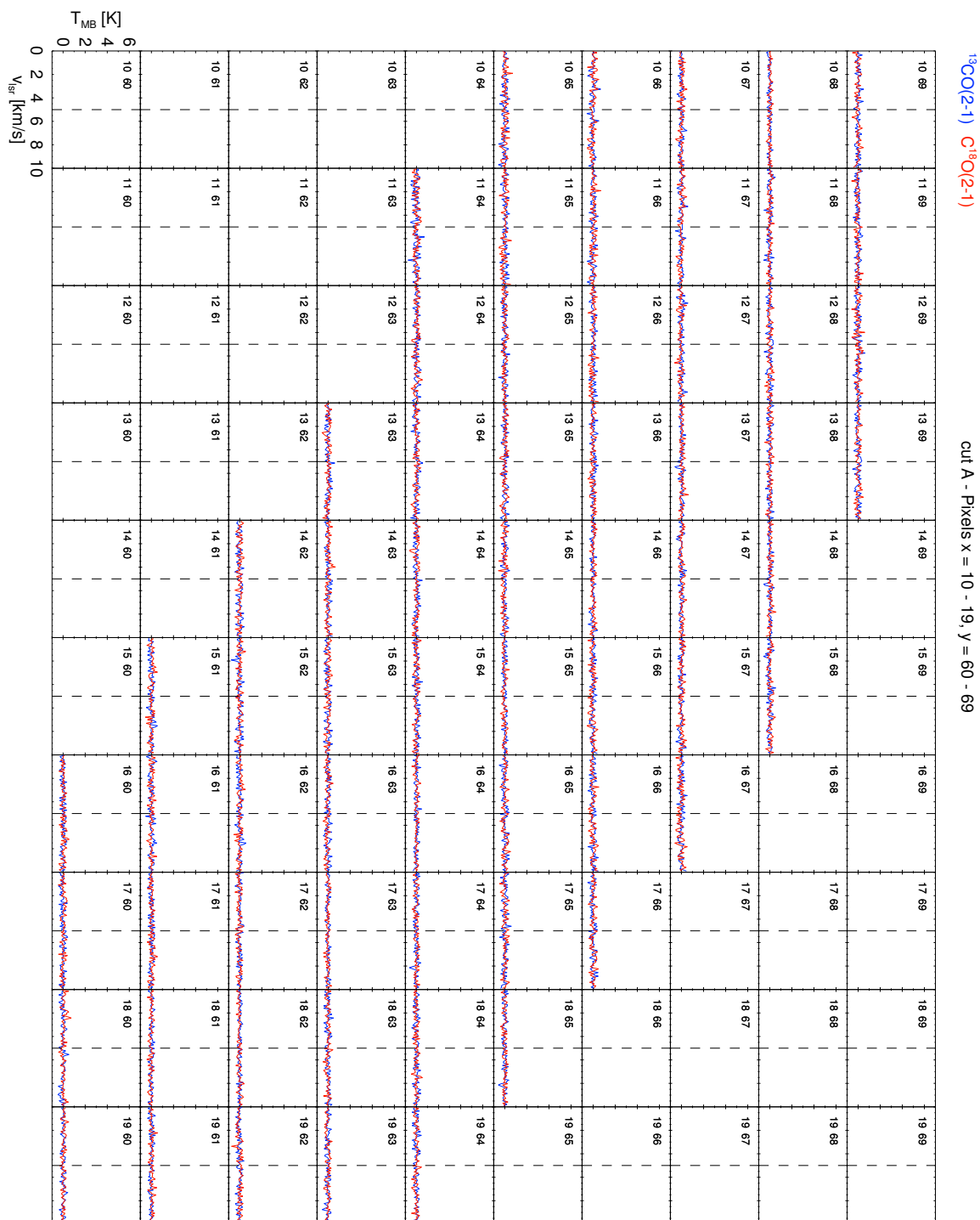


Figure A.3: Figure A.2 continued.

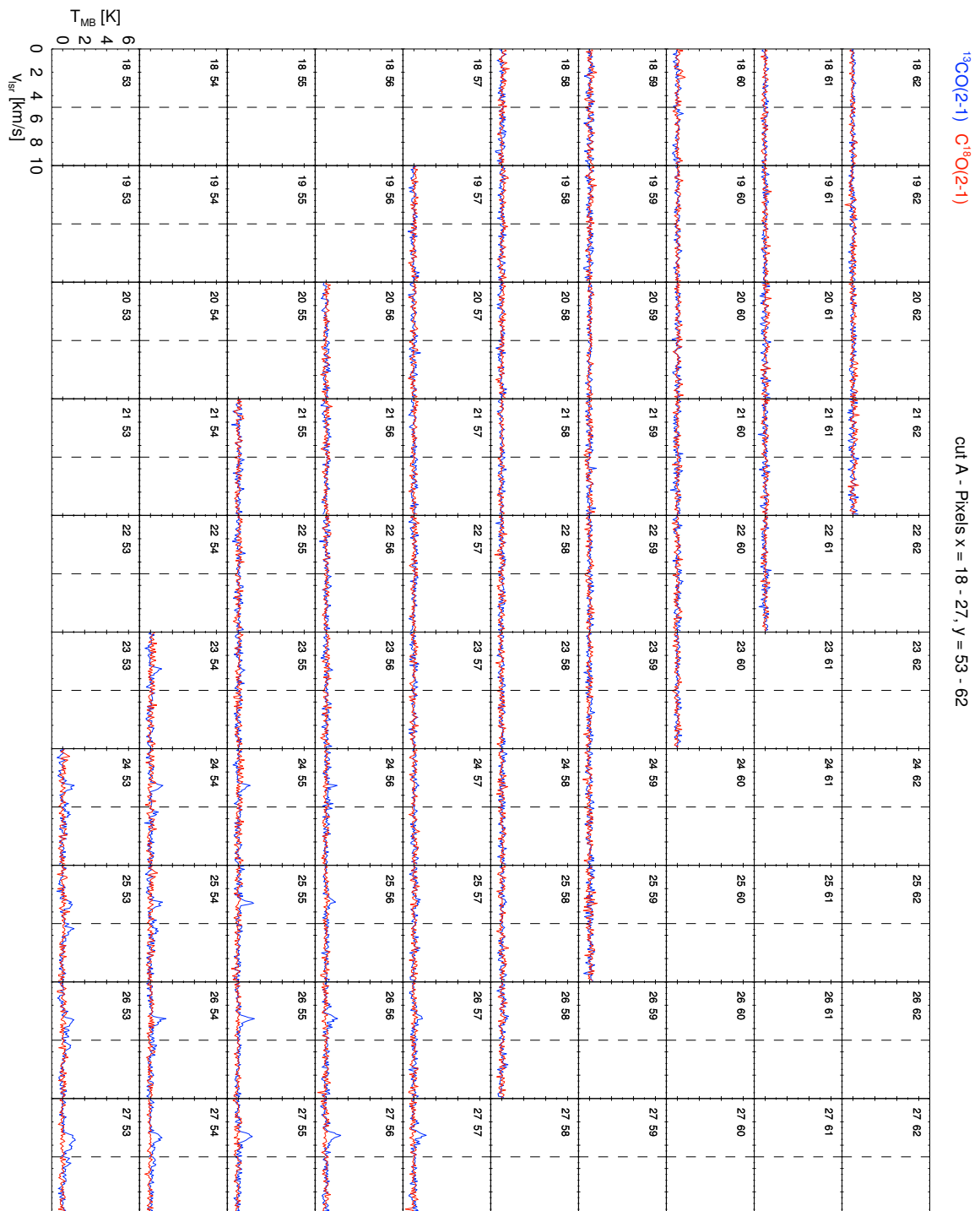


Figure A.4: Figure A.2 continued.

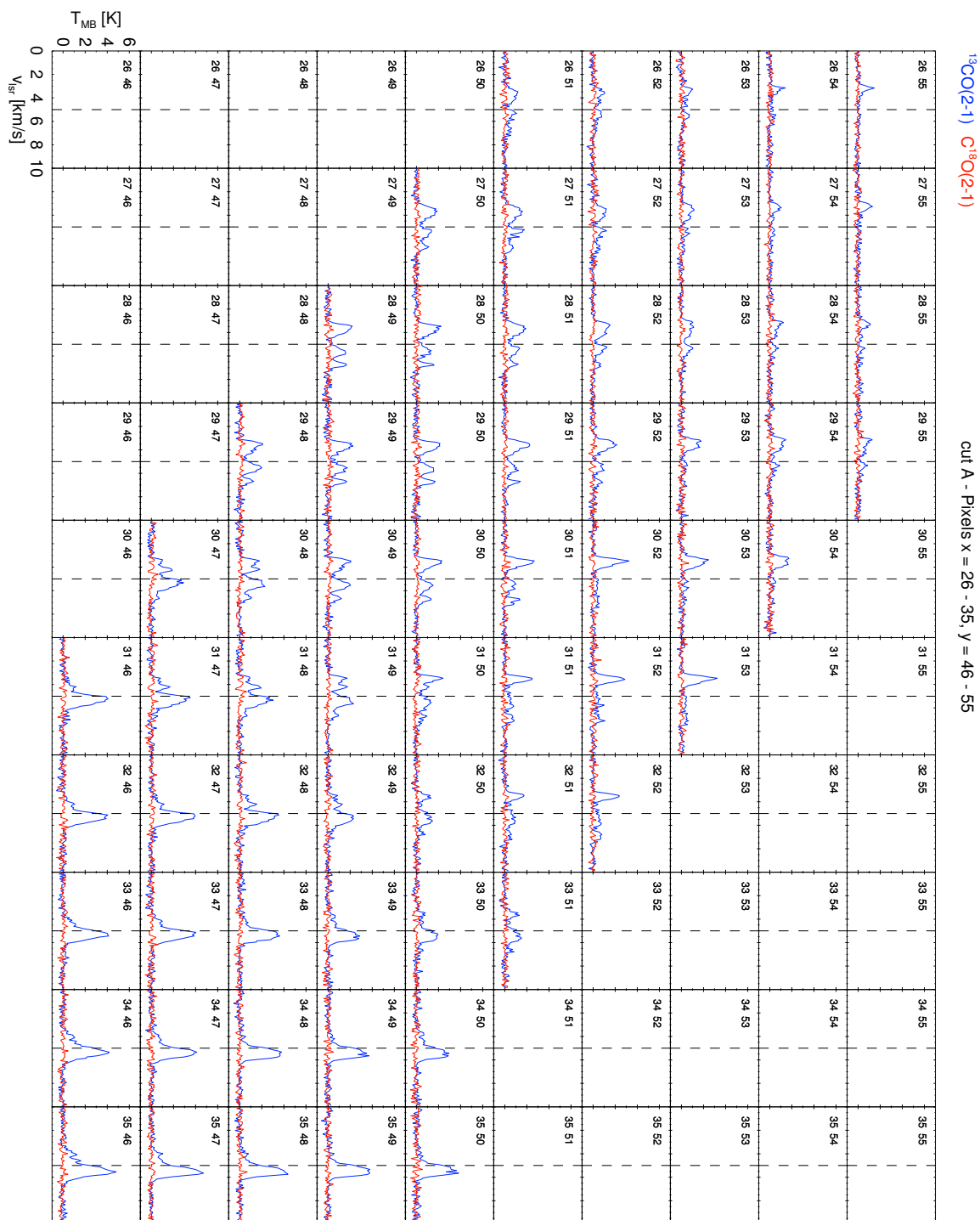


Figure A.5: Figure A.2 continued.

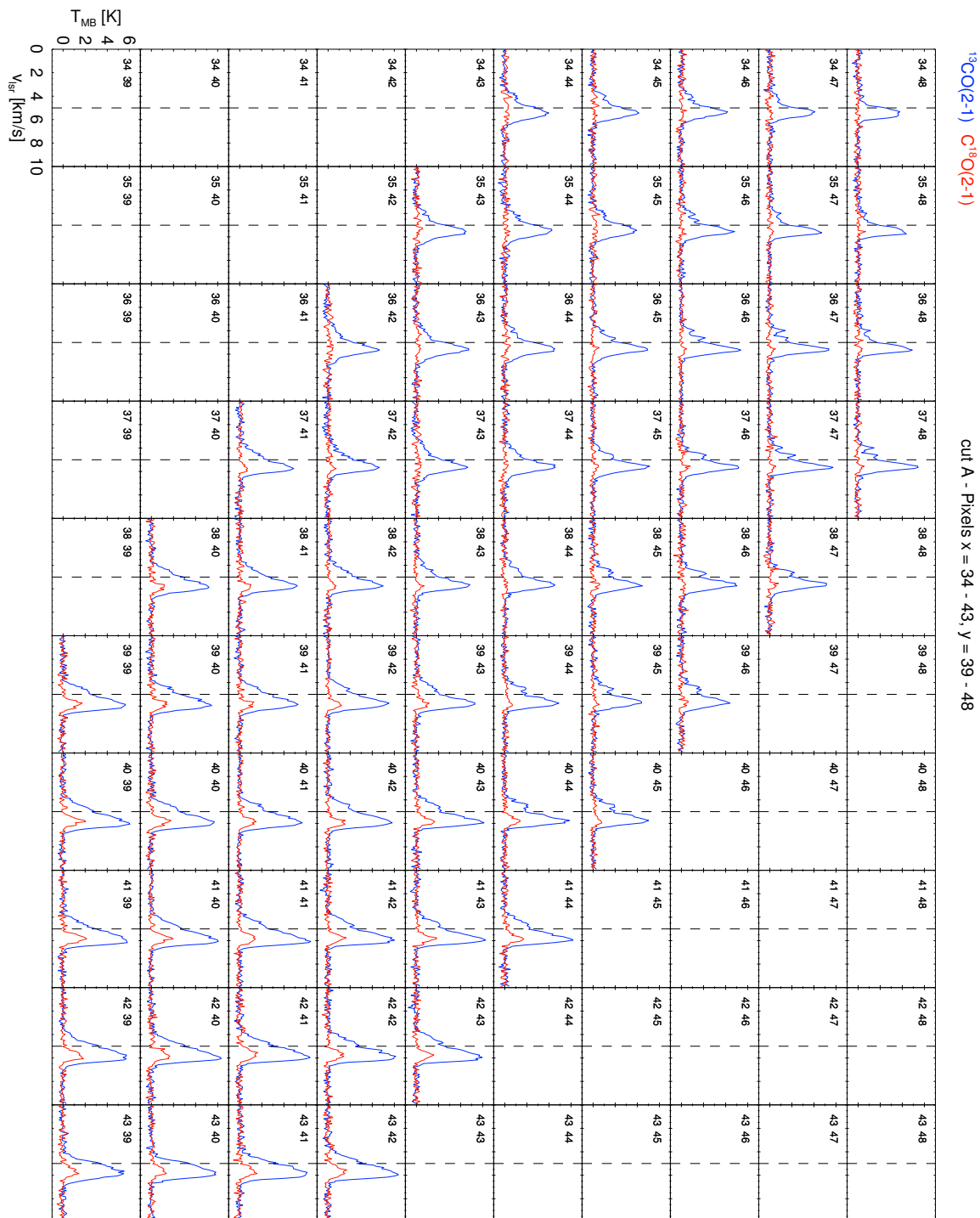


Figure A.6: Figure A.2 continued.

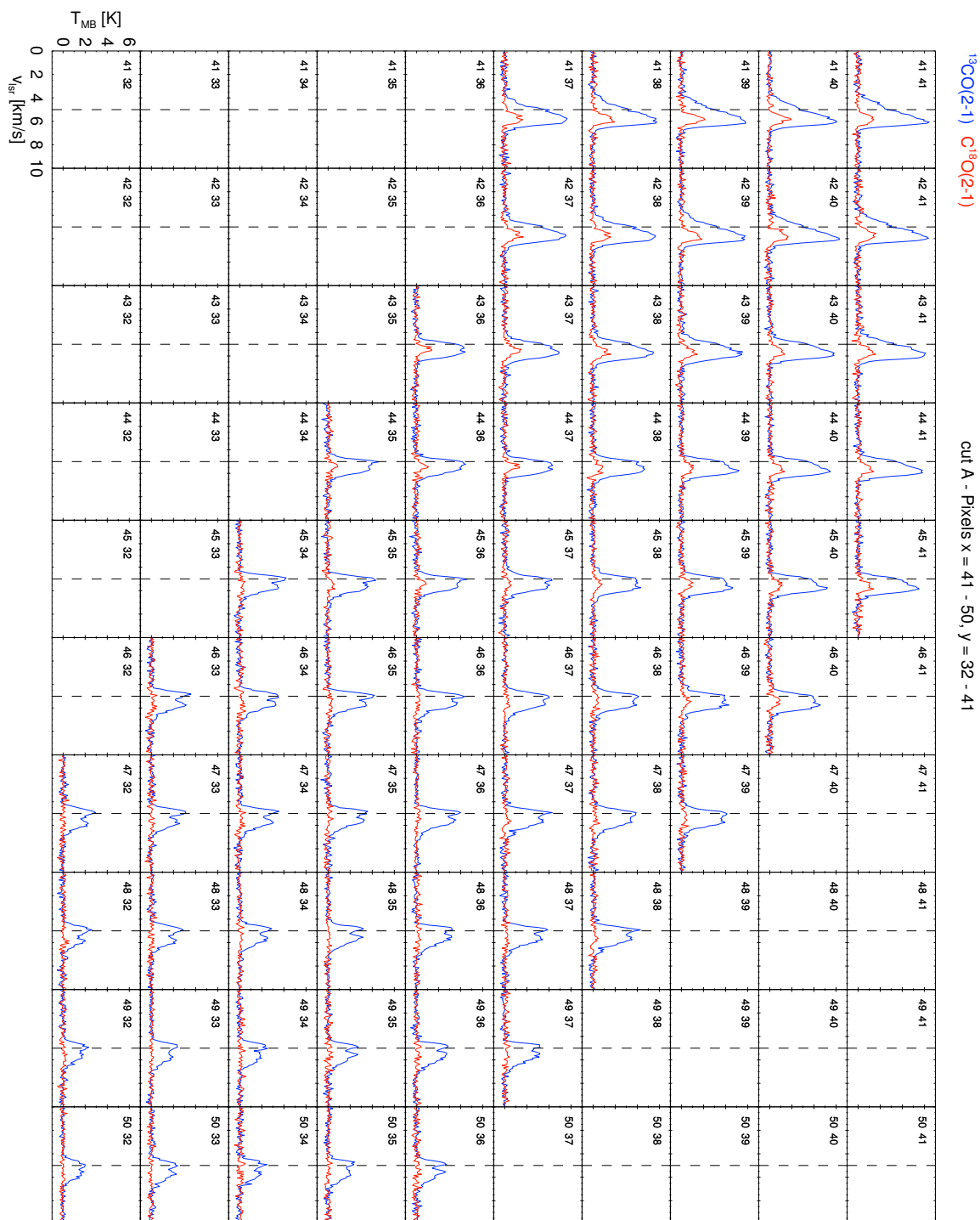


Figure A.7: Figure A.2 continued.

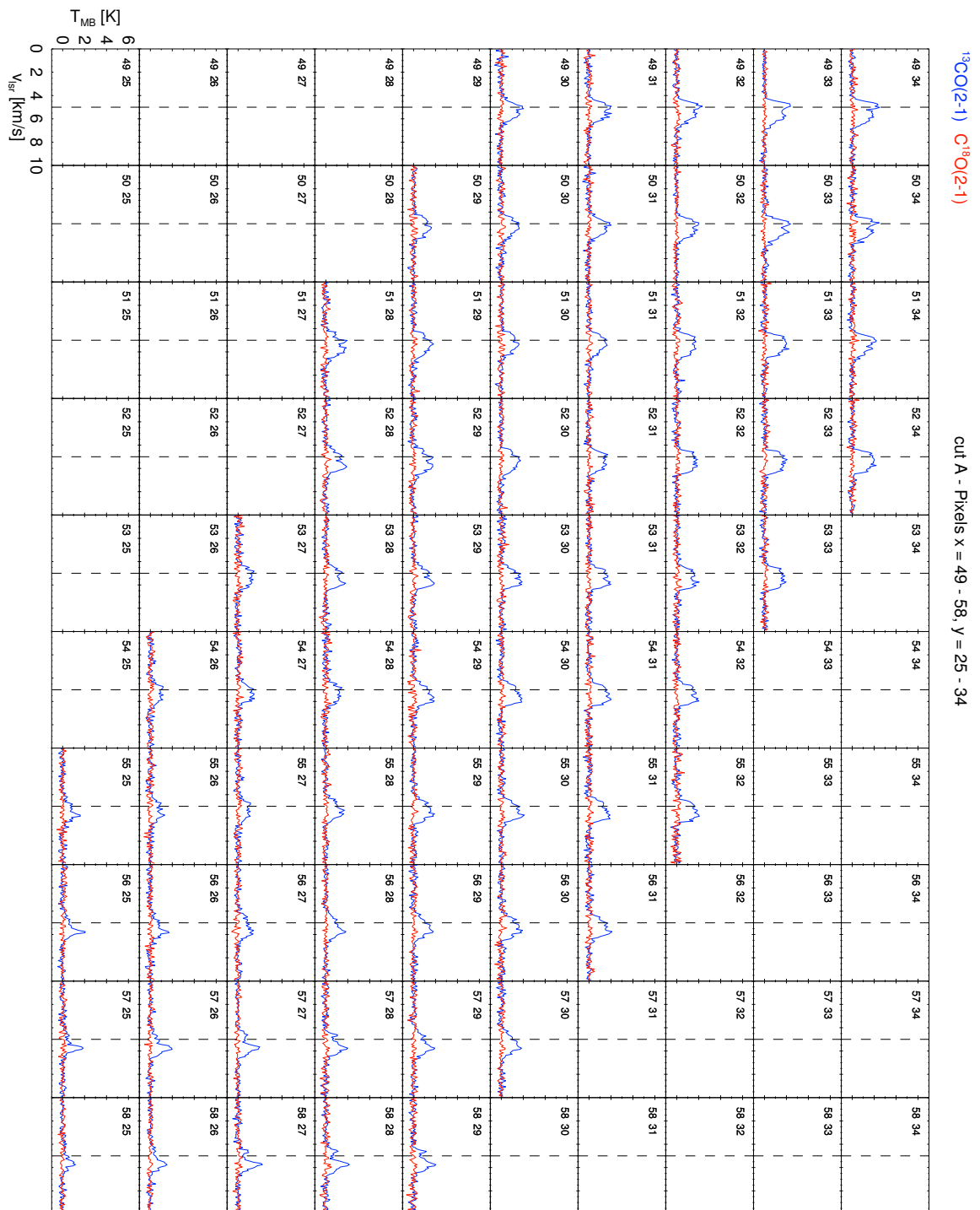


Figure A.8: Figure A.2 continued.

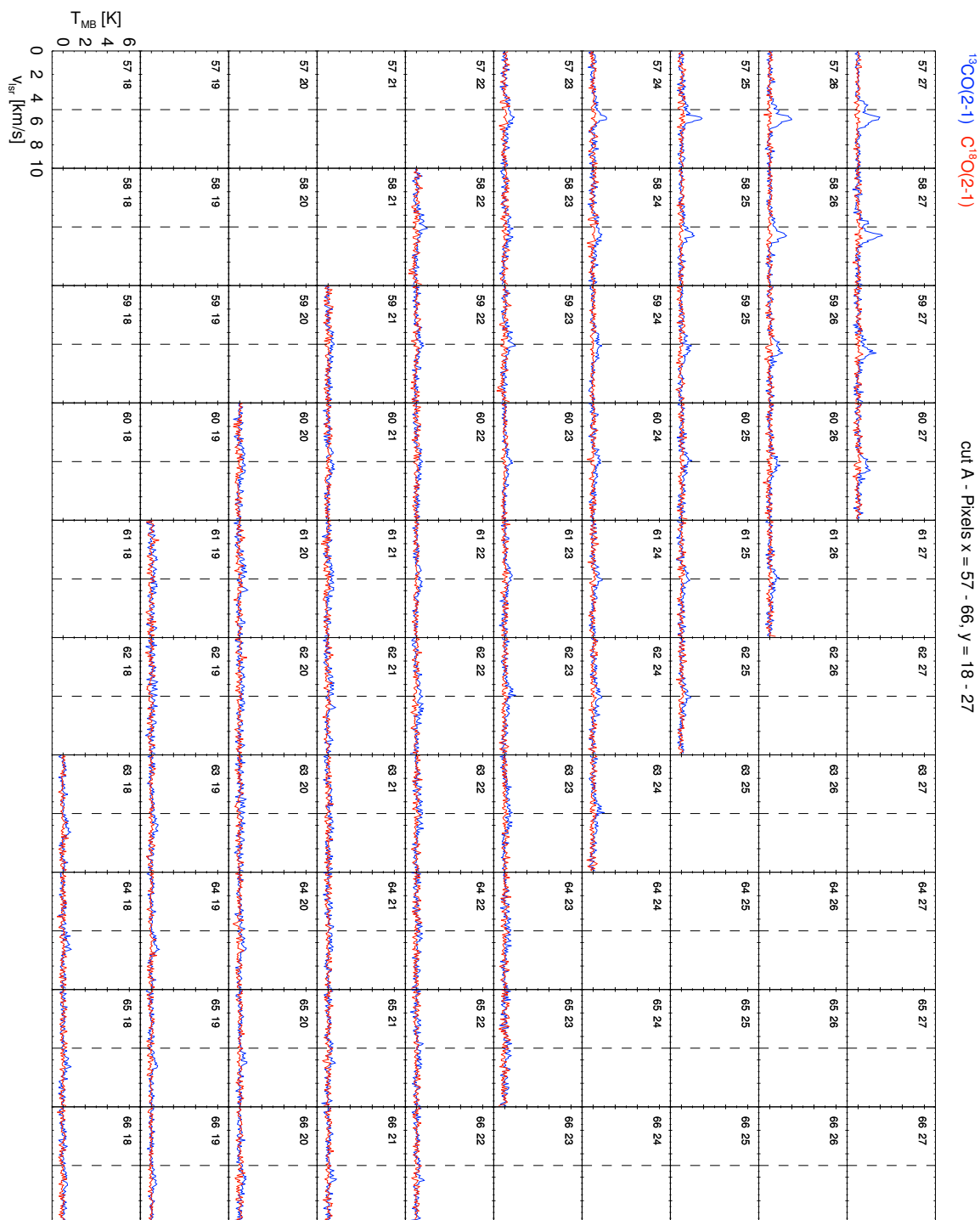


Figure A.9: Figure A.2 continued.

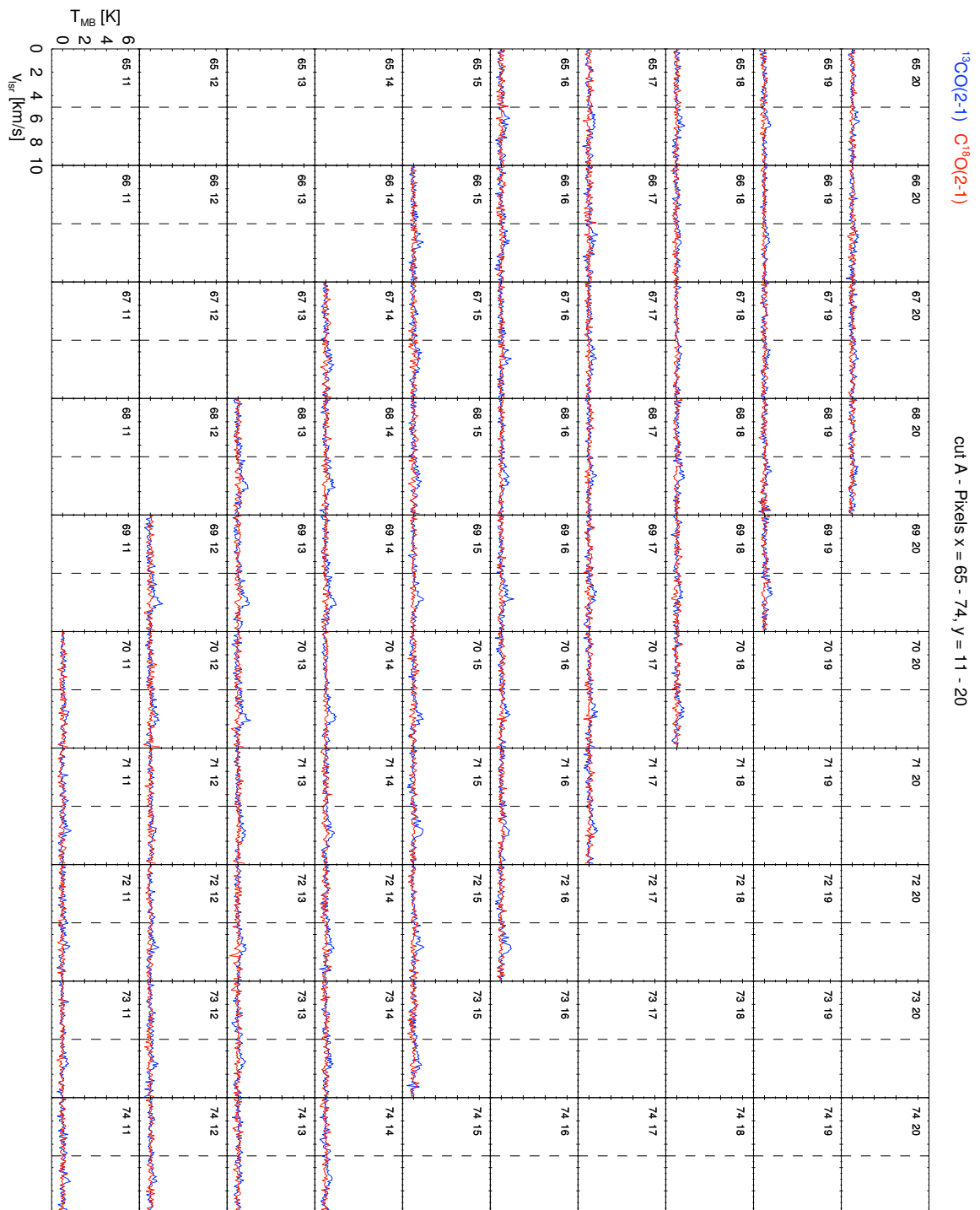


Figure A.10: Figure A.2 continued.

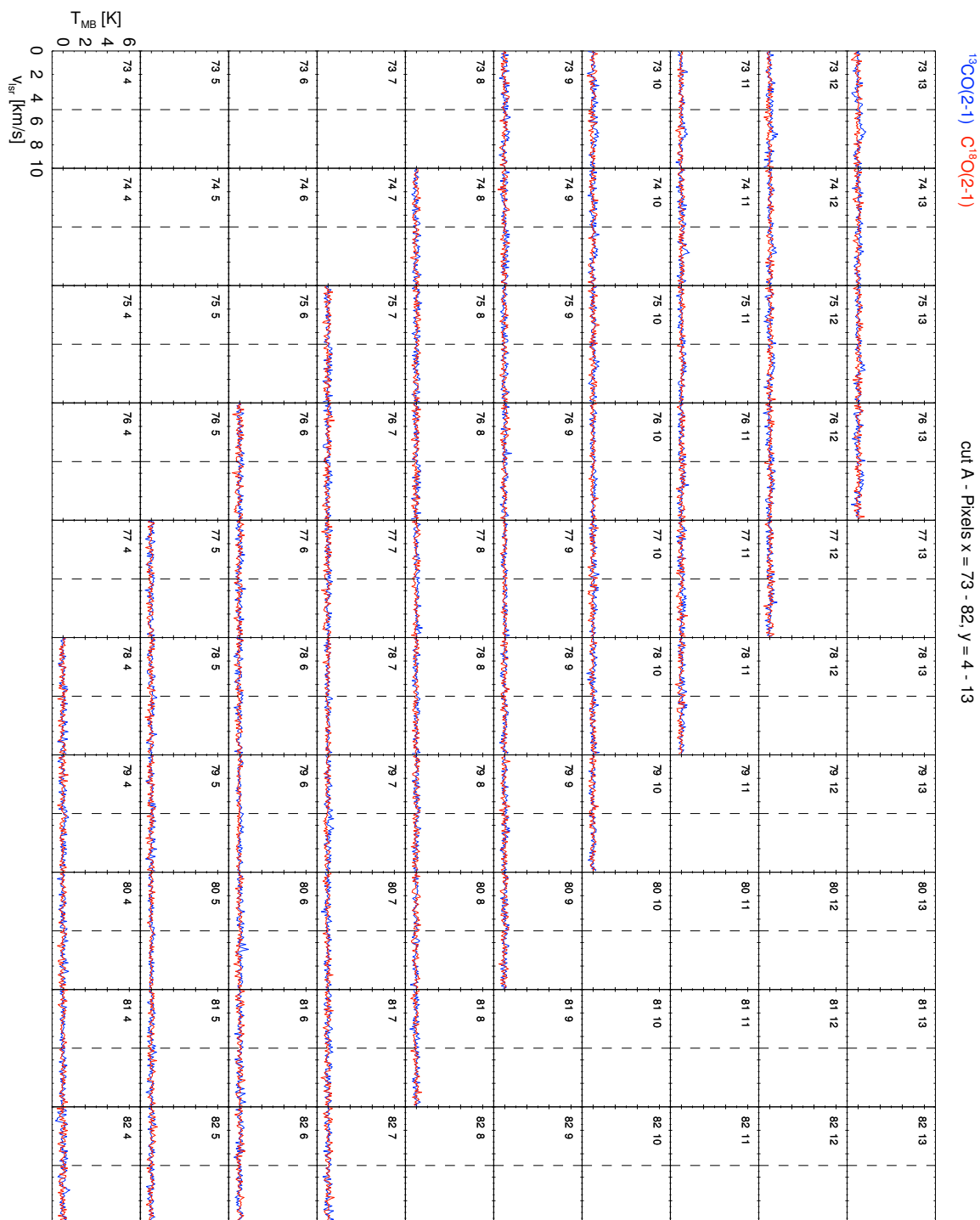


Figure A.11: Figure A.2 continued.

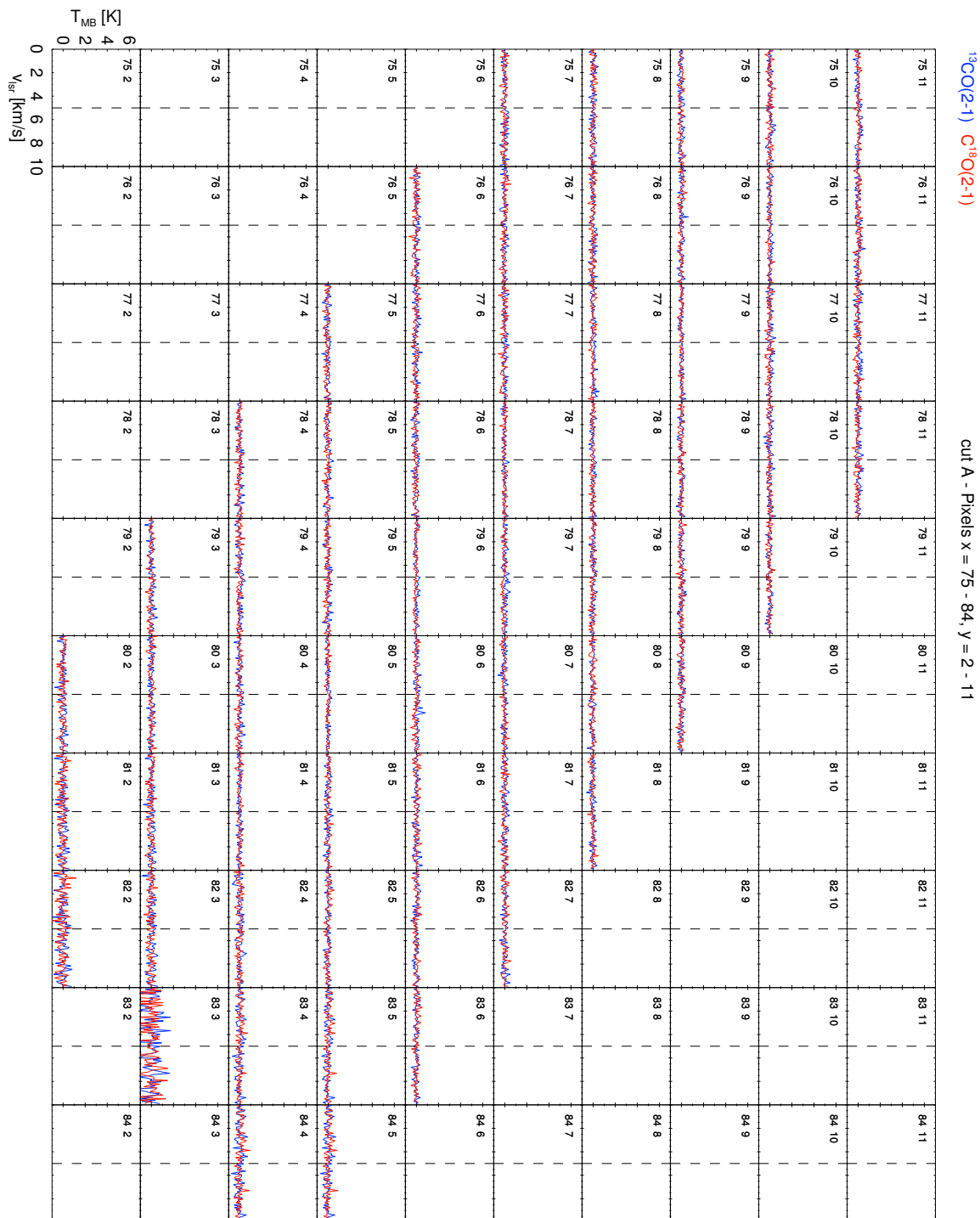


Figure A.12: Figure A.2 continued.

A.2 cut B

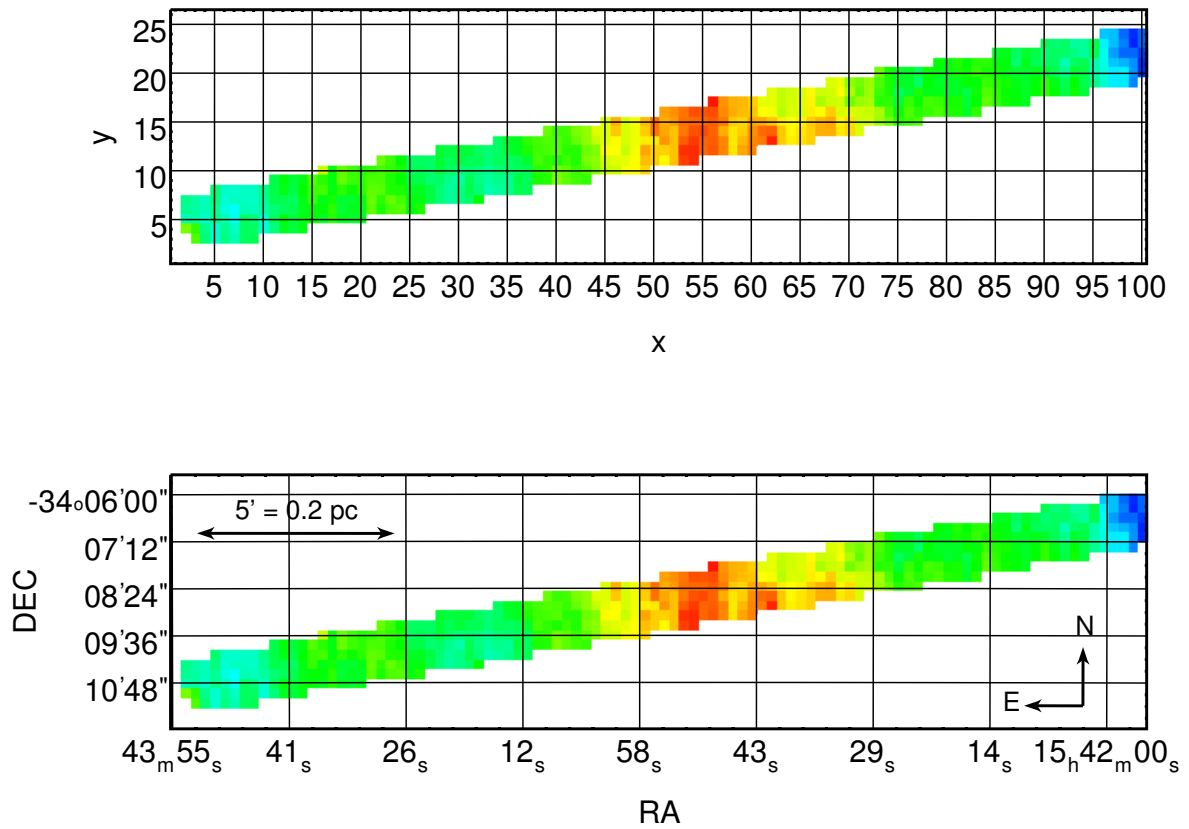


Figure A.13: *Left*: Raster map of the CO spectra in cut B. Background image is the integrated ^{13}CO emission. *Right*: Same map as in the left panel, but with an Celestial coordinate grid, a compass, and a scale.

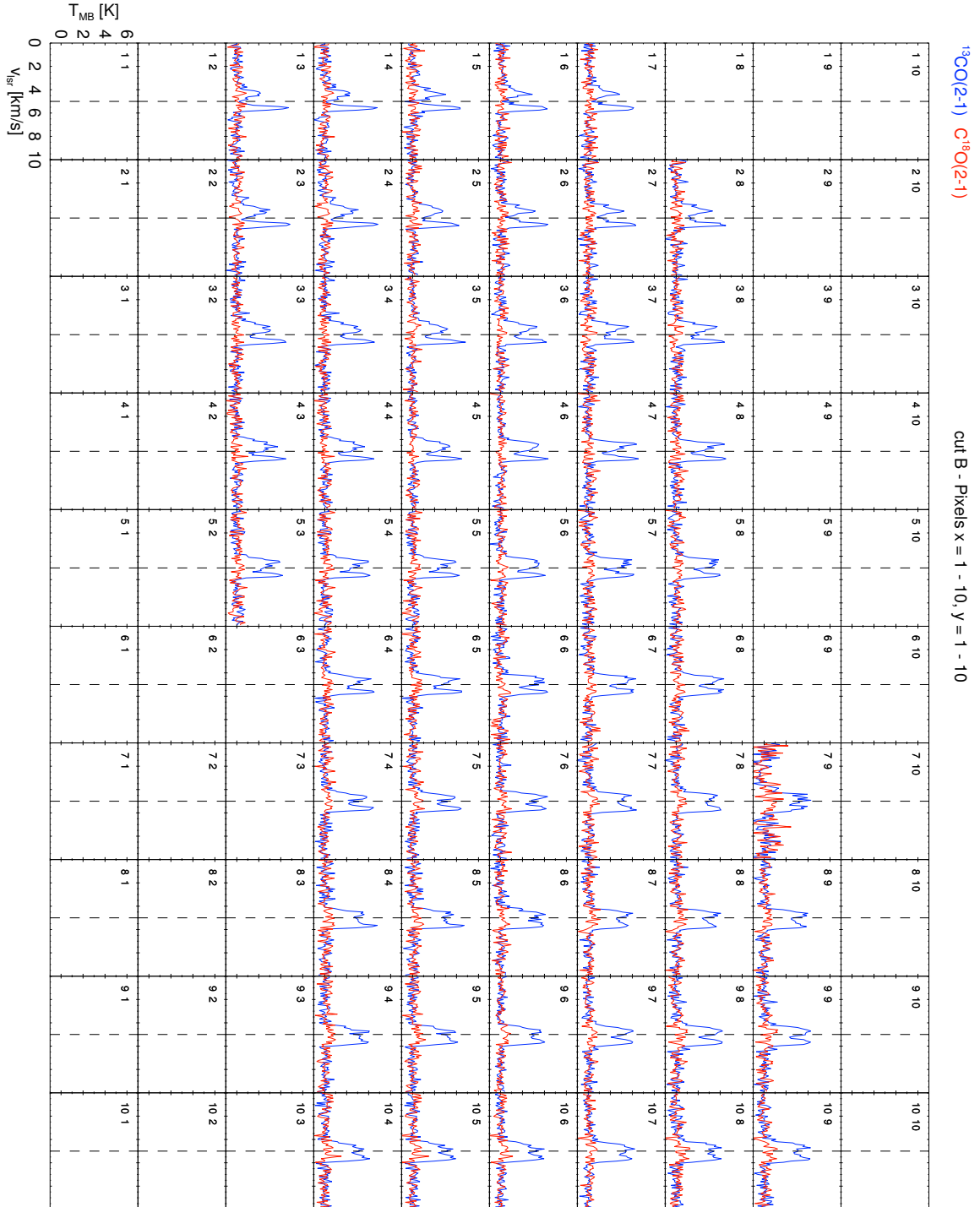


Figure A.14: ^{13}CO (blue) and C^{18}O (red) spectra of cut B. The corresponding pixel coordinates to which these spectra belong, are given in the upper left corner of each plot (x left, y right). The position of the pixel can be found in Figure A.13. The x-axis gives the v_{LSR} velocity in km s^{-1} , the y-axis the main-beam temperature T_{mb} in Kelvin. The dashed vertical line marks $v_{\text{LSR}} = 5 \text{ km s}^{-1}$.

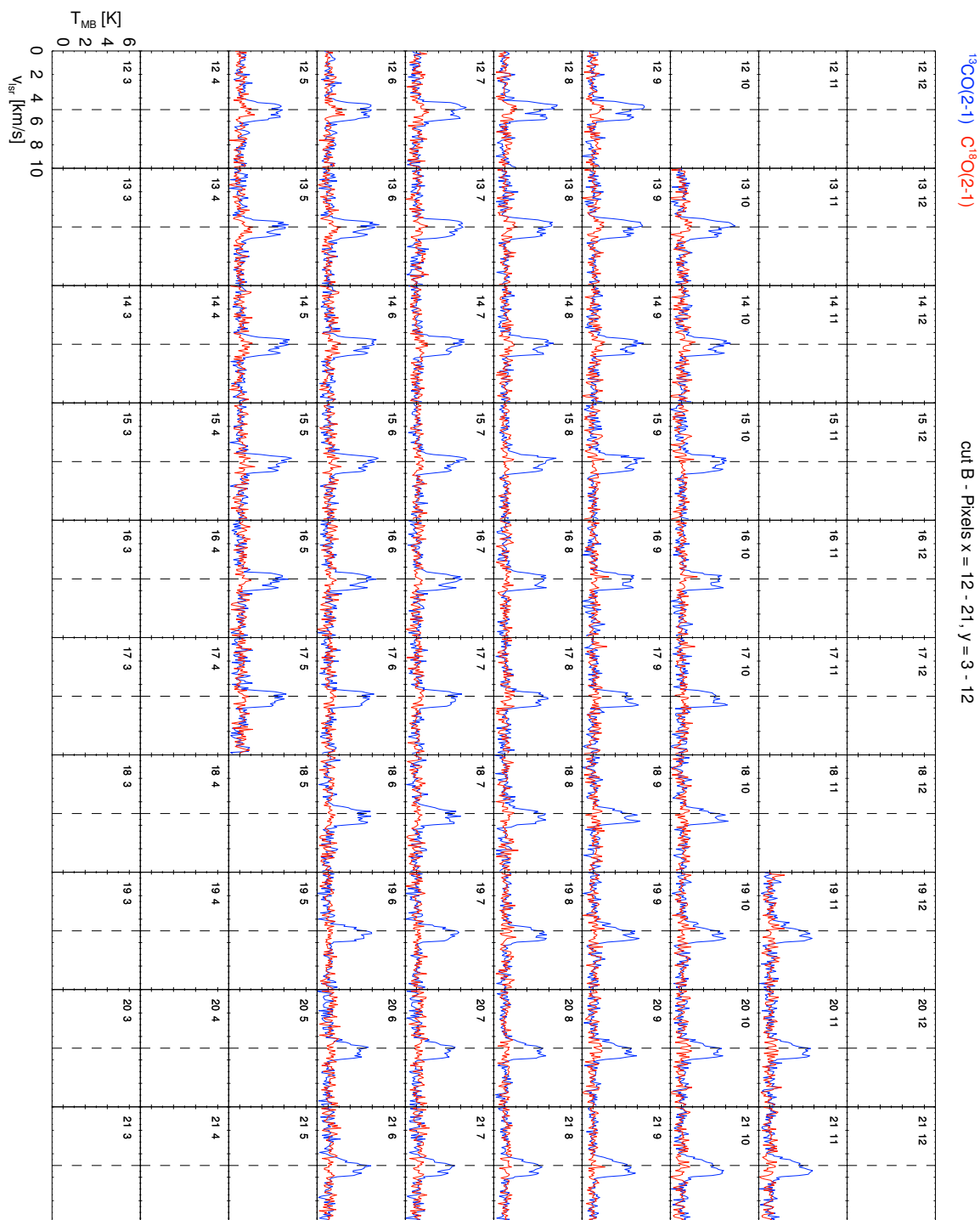


Figure A.15: Figure A.14 continued.

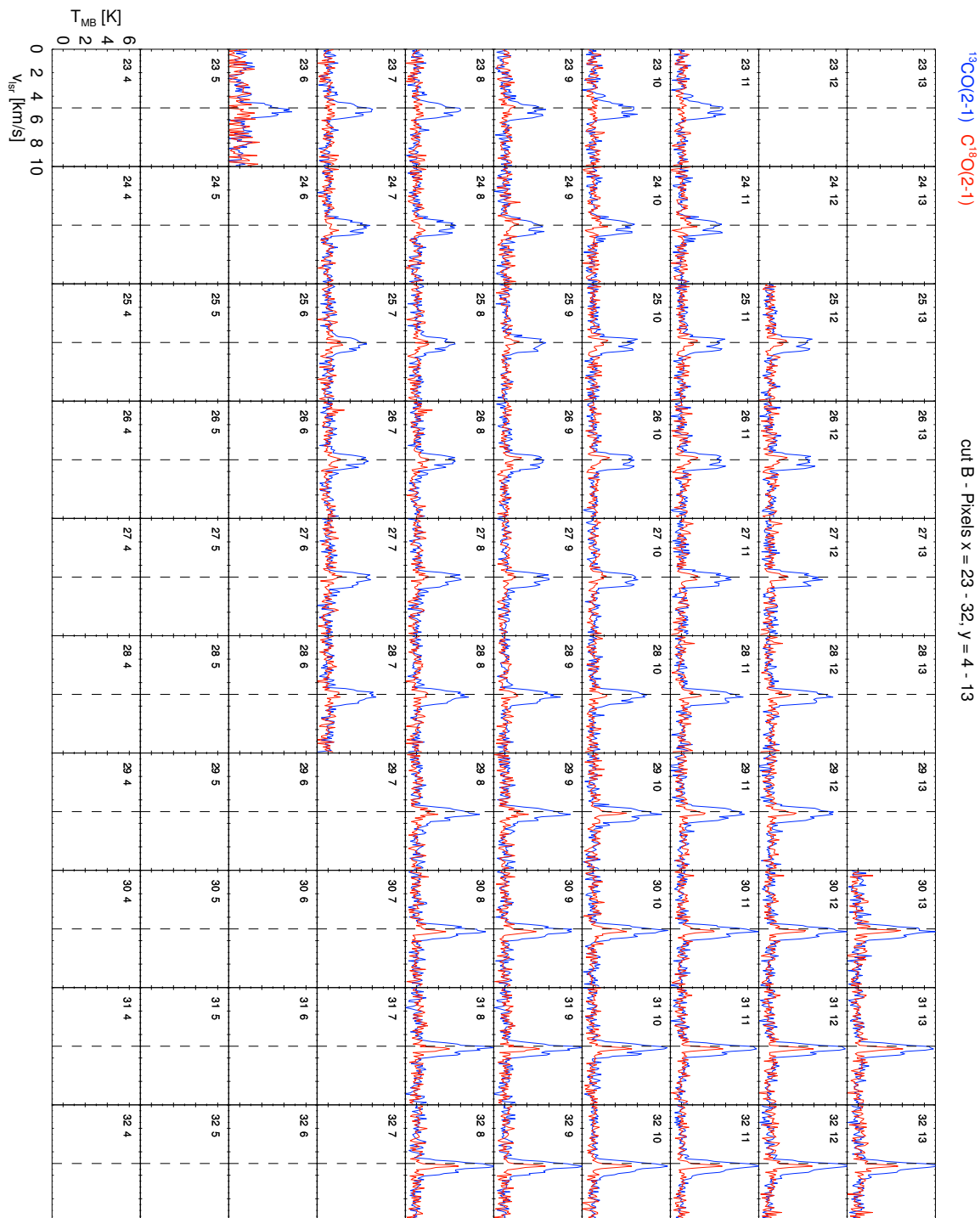


Figure A.16: Figure A.14 continued.

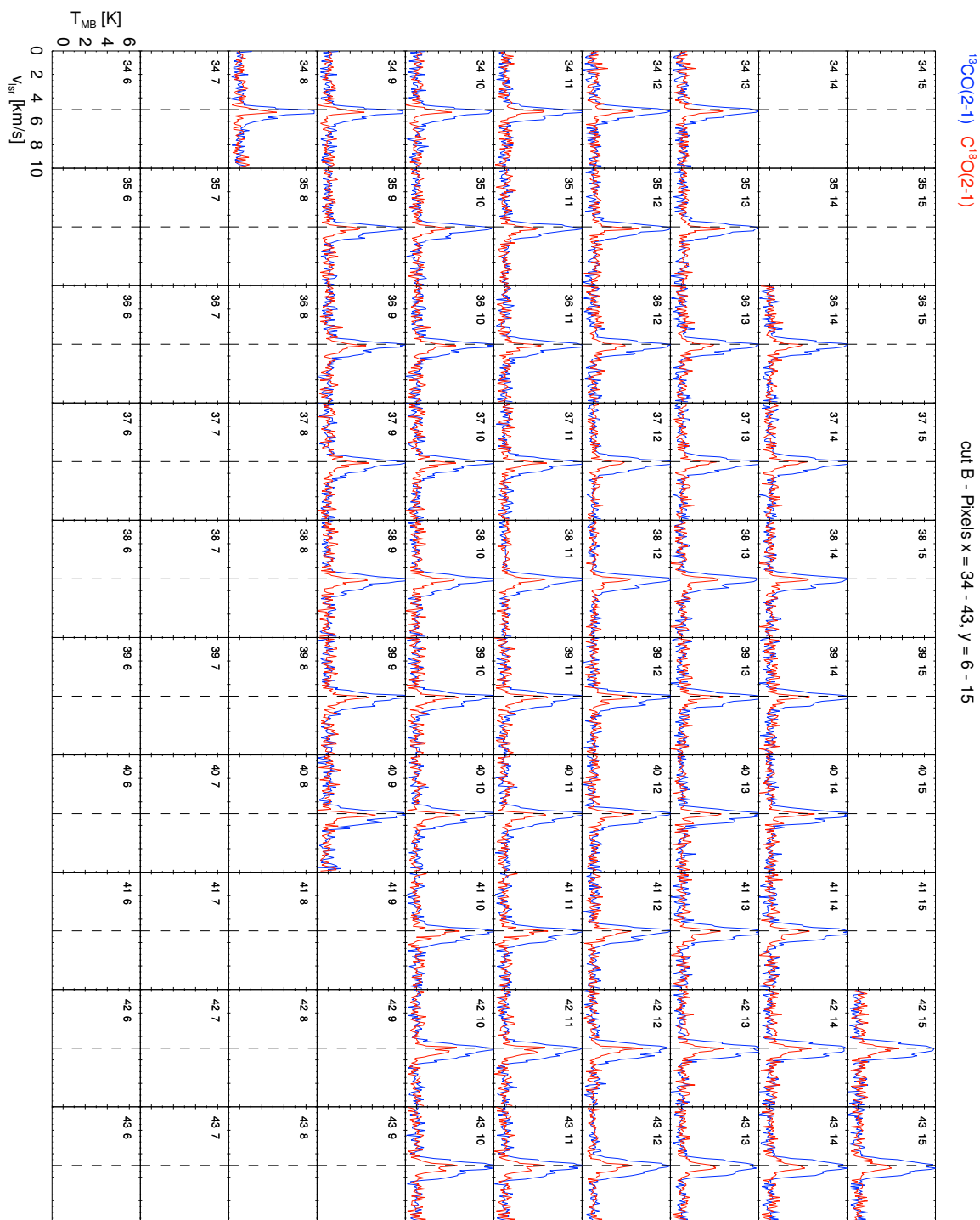


Figure A.17: Figure A.14 continued.

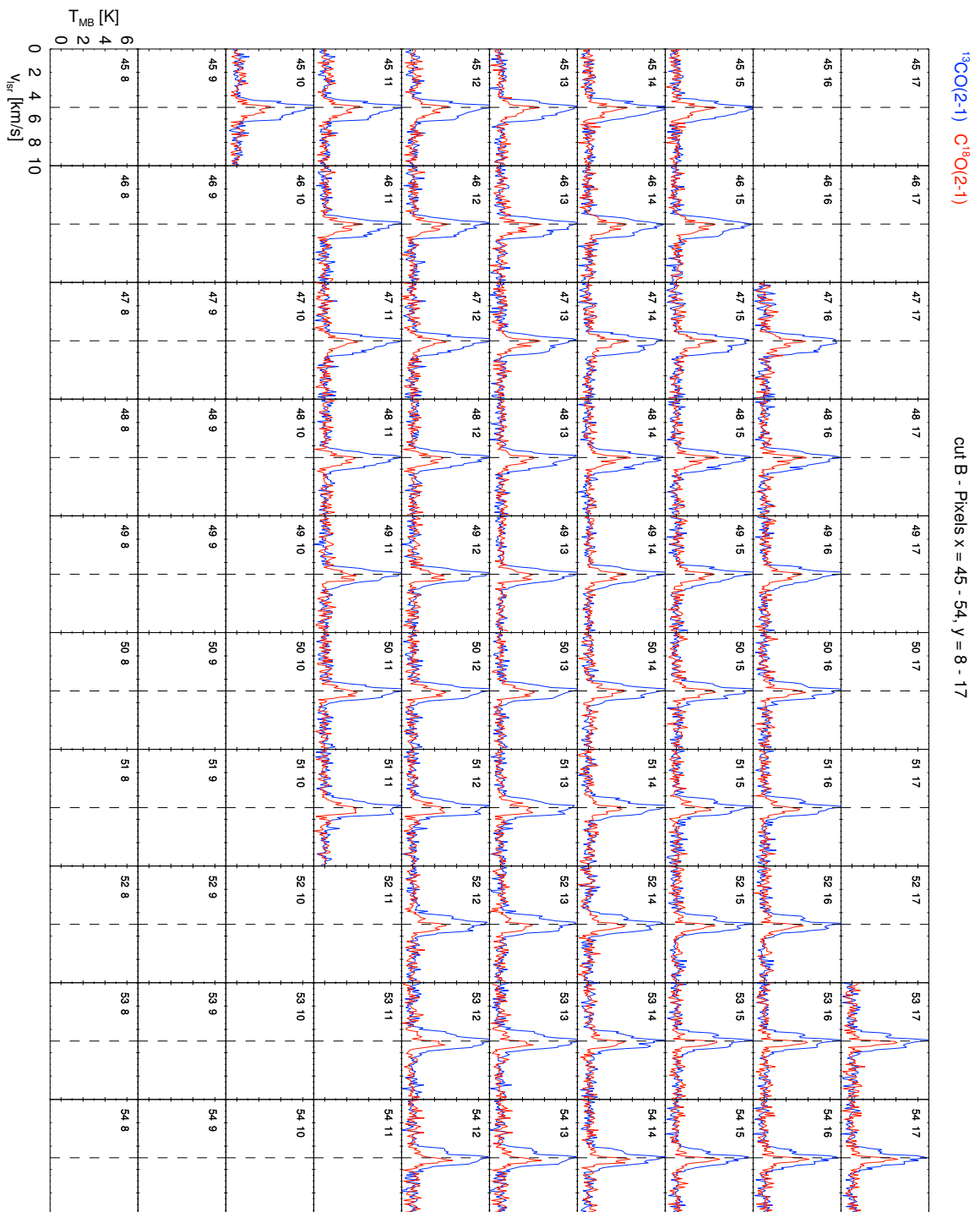


Figure A.18: Figure A.14 continued.

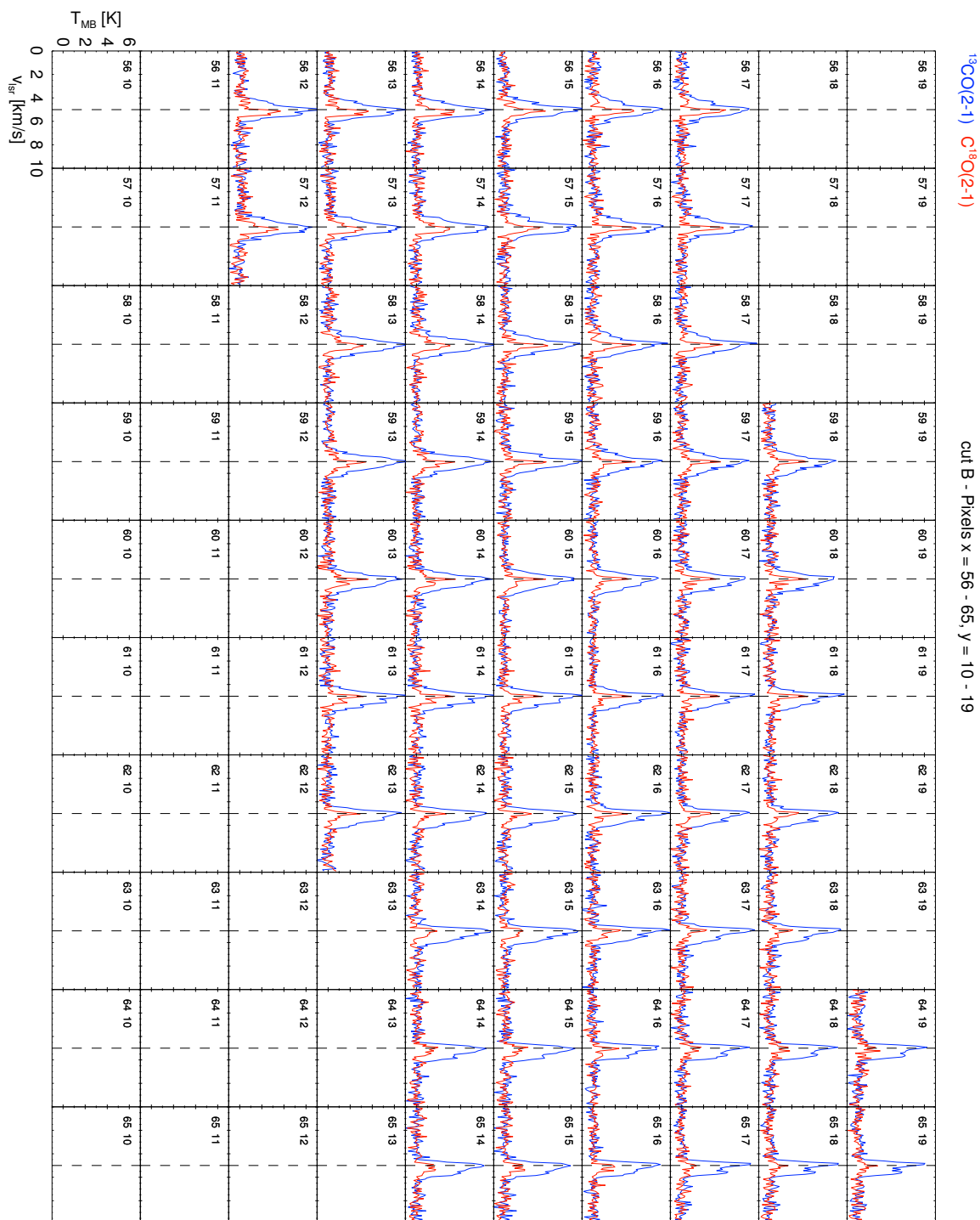


Figure A.19: Figure A.14 continued.

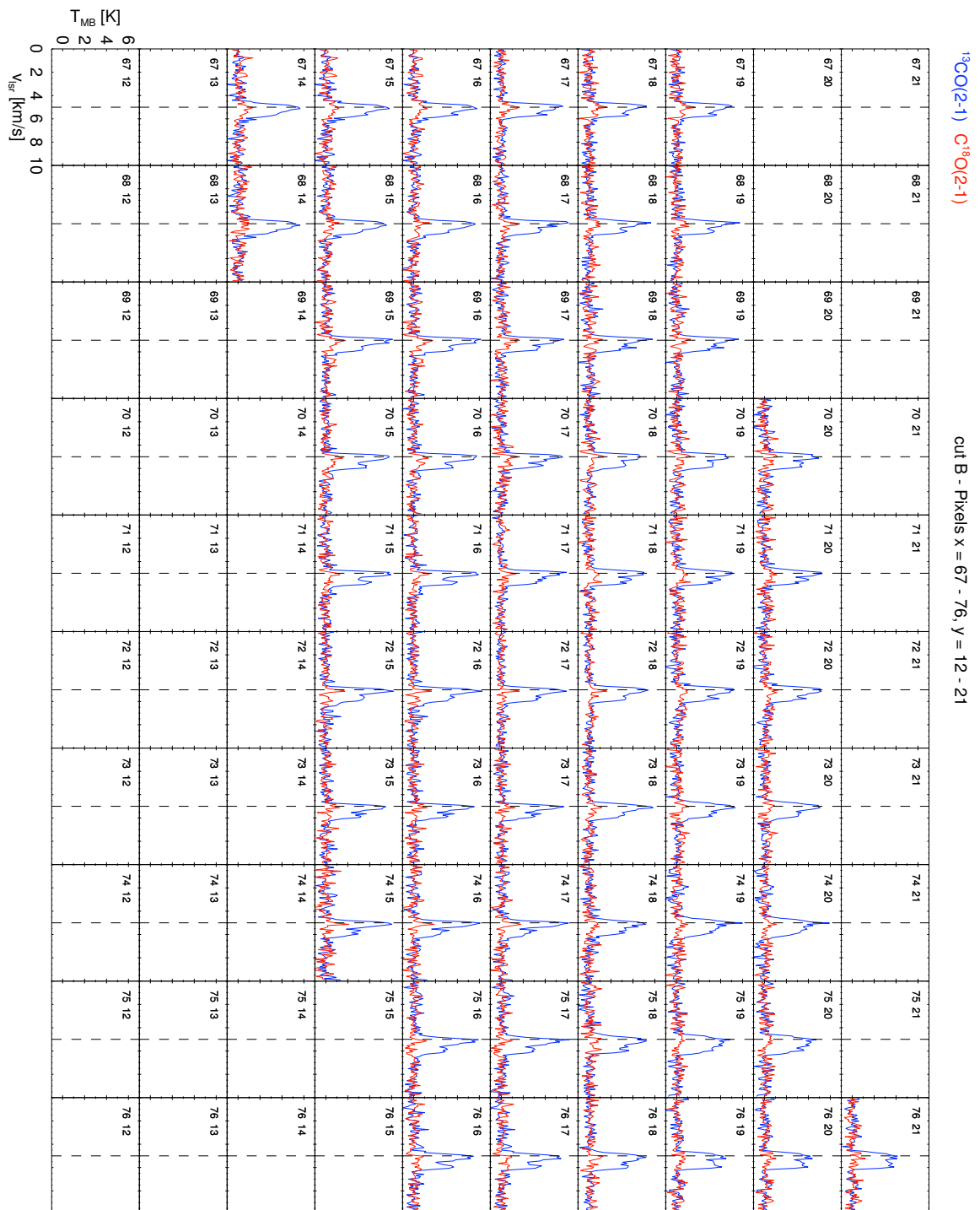


Figure A.20: Figure A.14 continued.

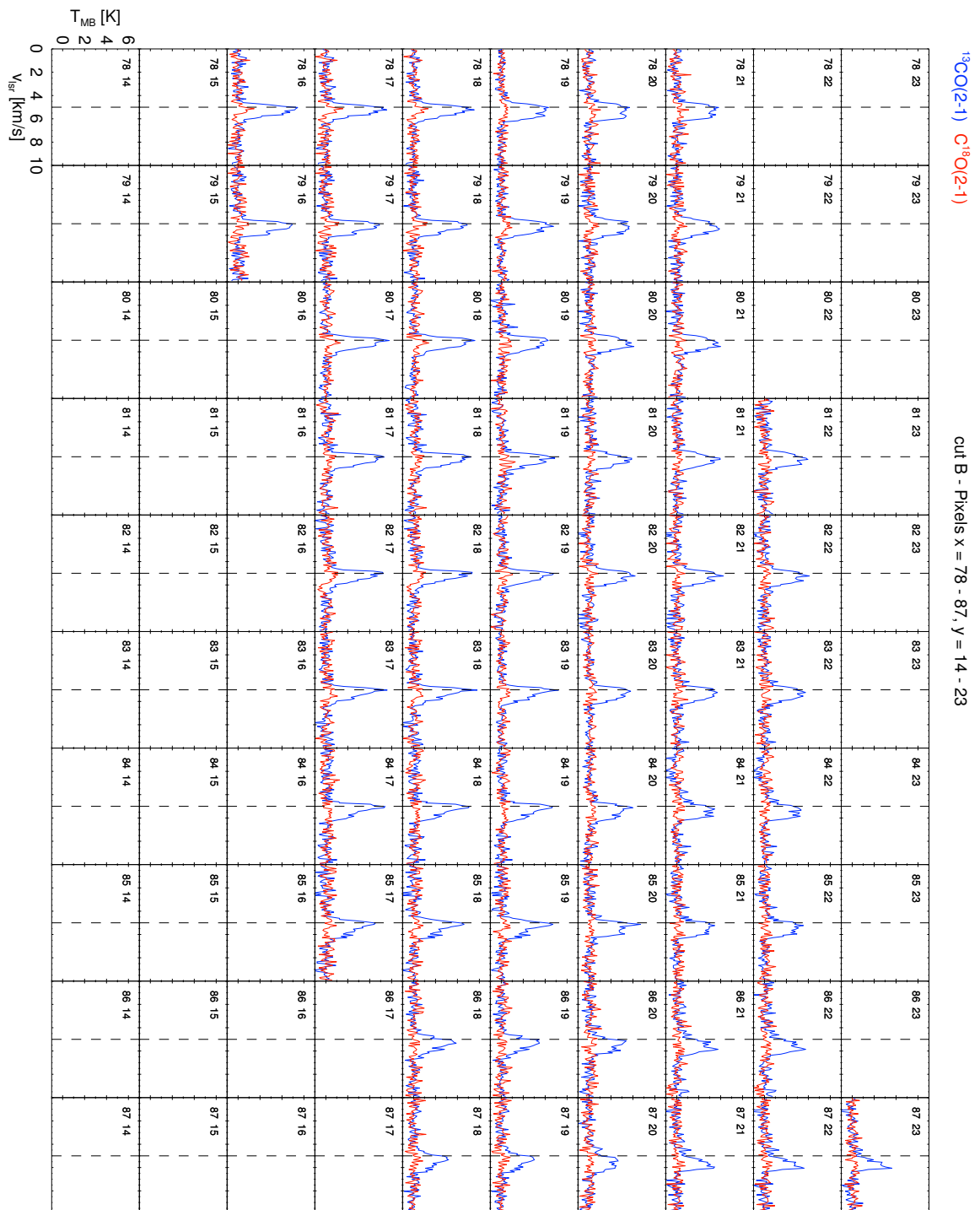


Figure A.21: Figure A.14 continued.

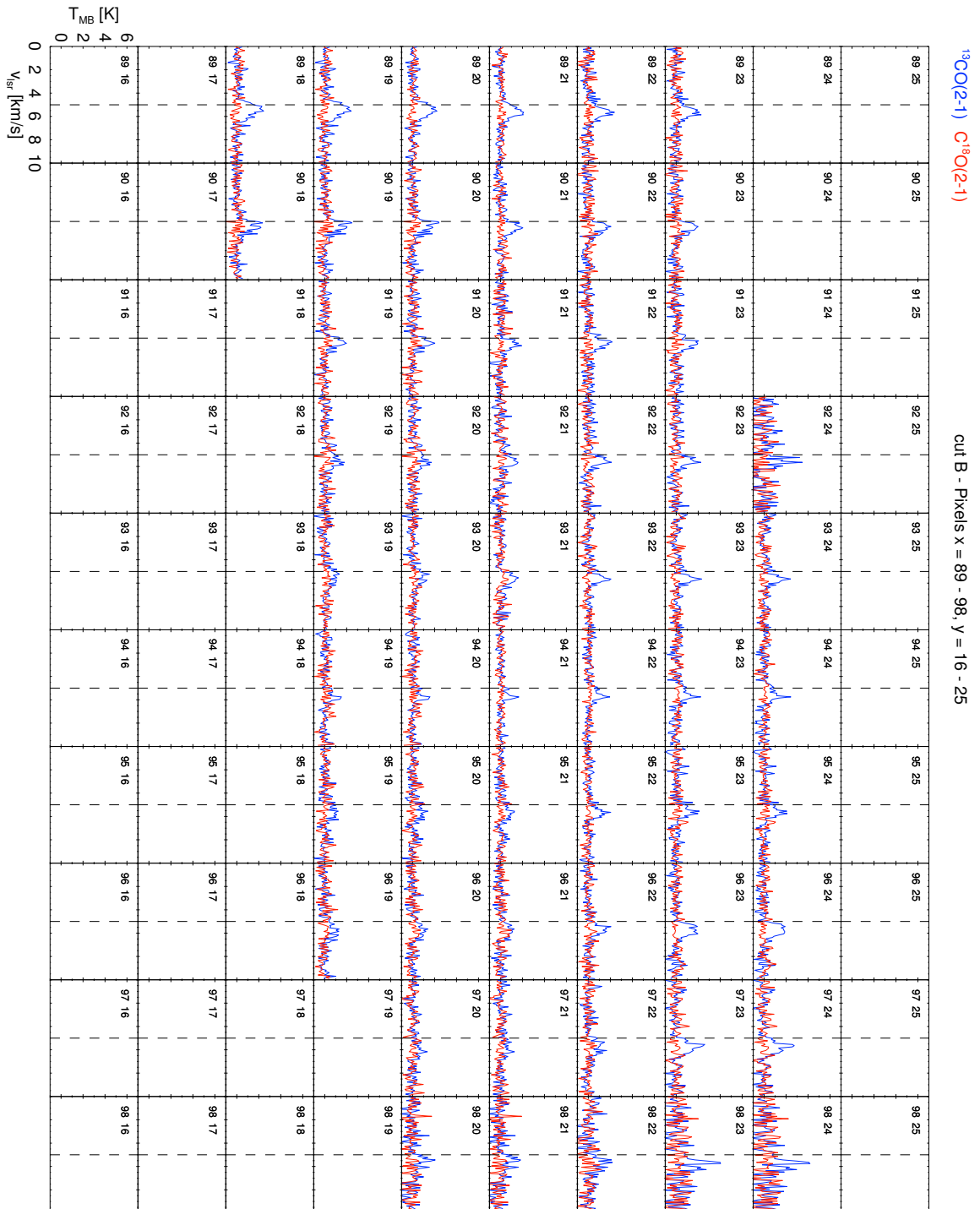


Figure A.22: Figure A.14 continued.

A.3 cut C

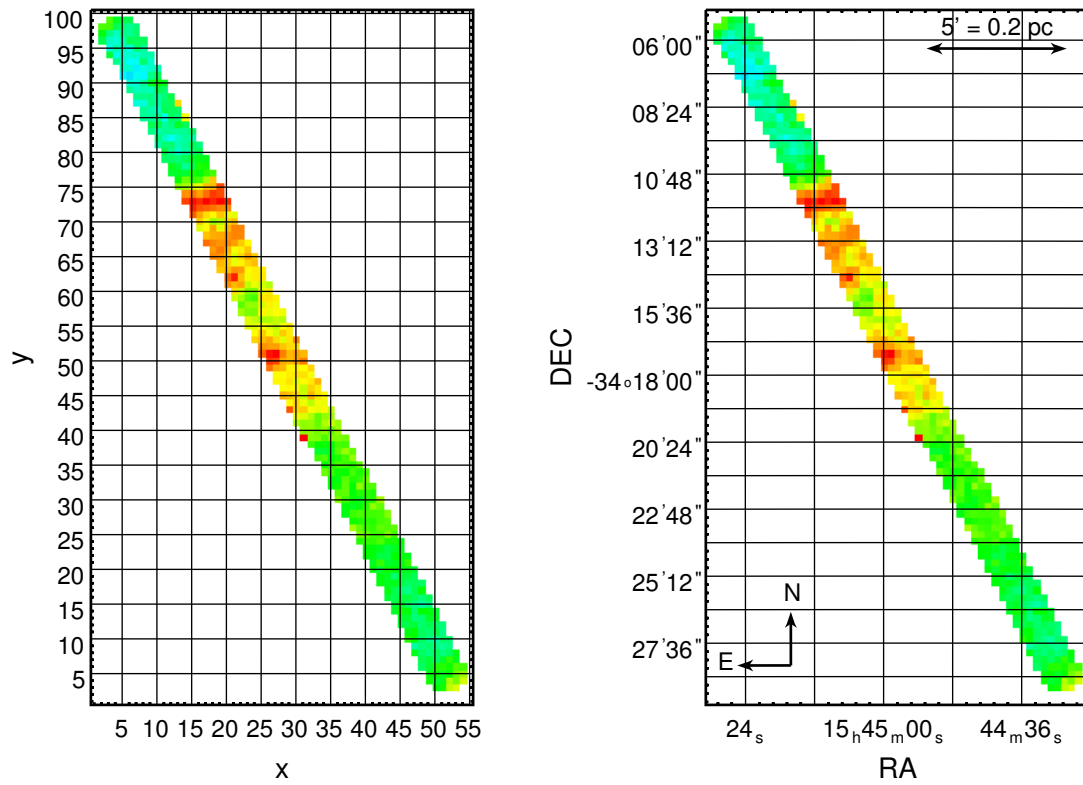


Figure A.23: *Left*: Raster map of the CO spectra in cut C. Background image is the integrated ^{13}CO emission. *Right*: Same map as in the left panel, but with an Celestial coordinate grid, a compass, and a scale.

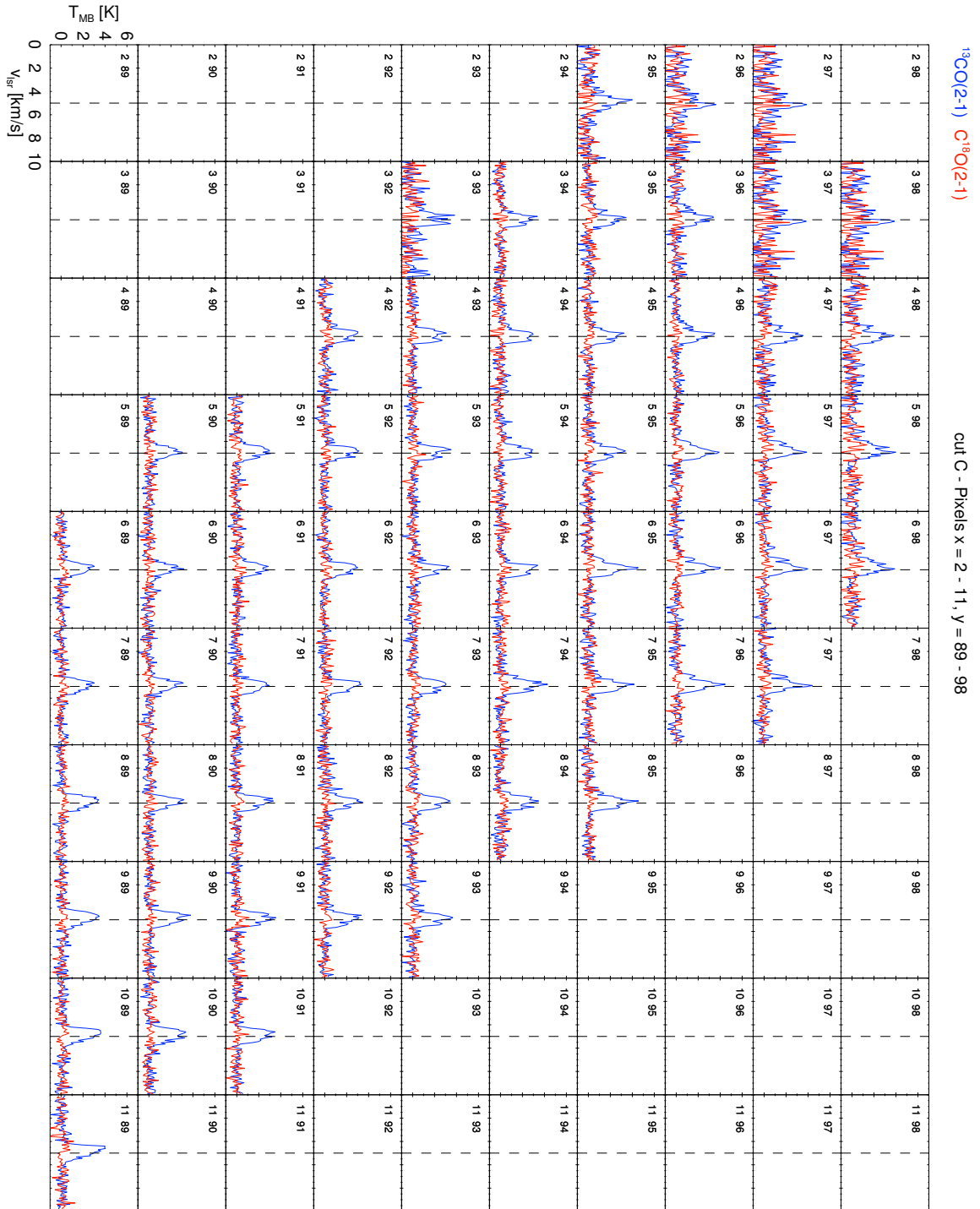


Figure A.24: ^{13}CO (blue) and C^{18}O (red) spectra of cut C. The corresponding pixel coordinates to which these spectra belong, are given in the upper left corner of each plot (x left, y right). The position of the pixel can be found in Figure A.23. The x-axis gives the v_{LSR} velocity in km s^{-1} , the y-axis the main-beam temperature T_{mb} in Kelvin. The dashed vertical line marks $v_{\text{LSR}} = 5 \text{ km s}^{-1}$.

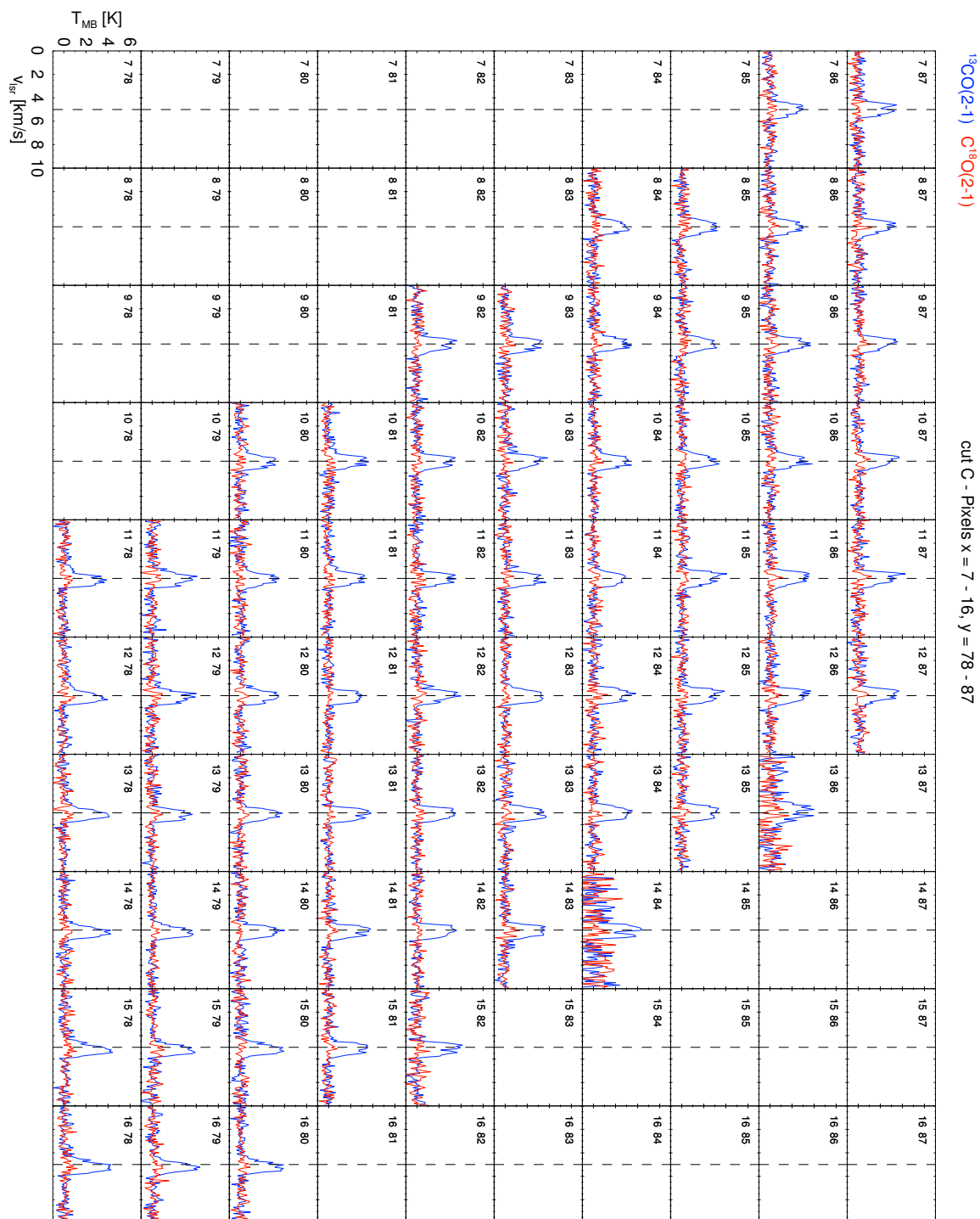


Figure A.25: Figure A.24 continued.

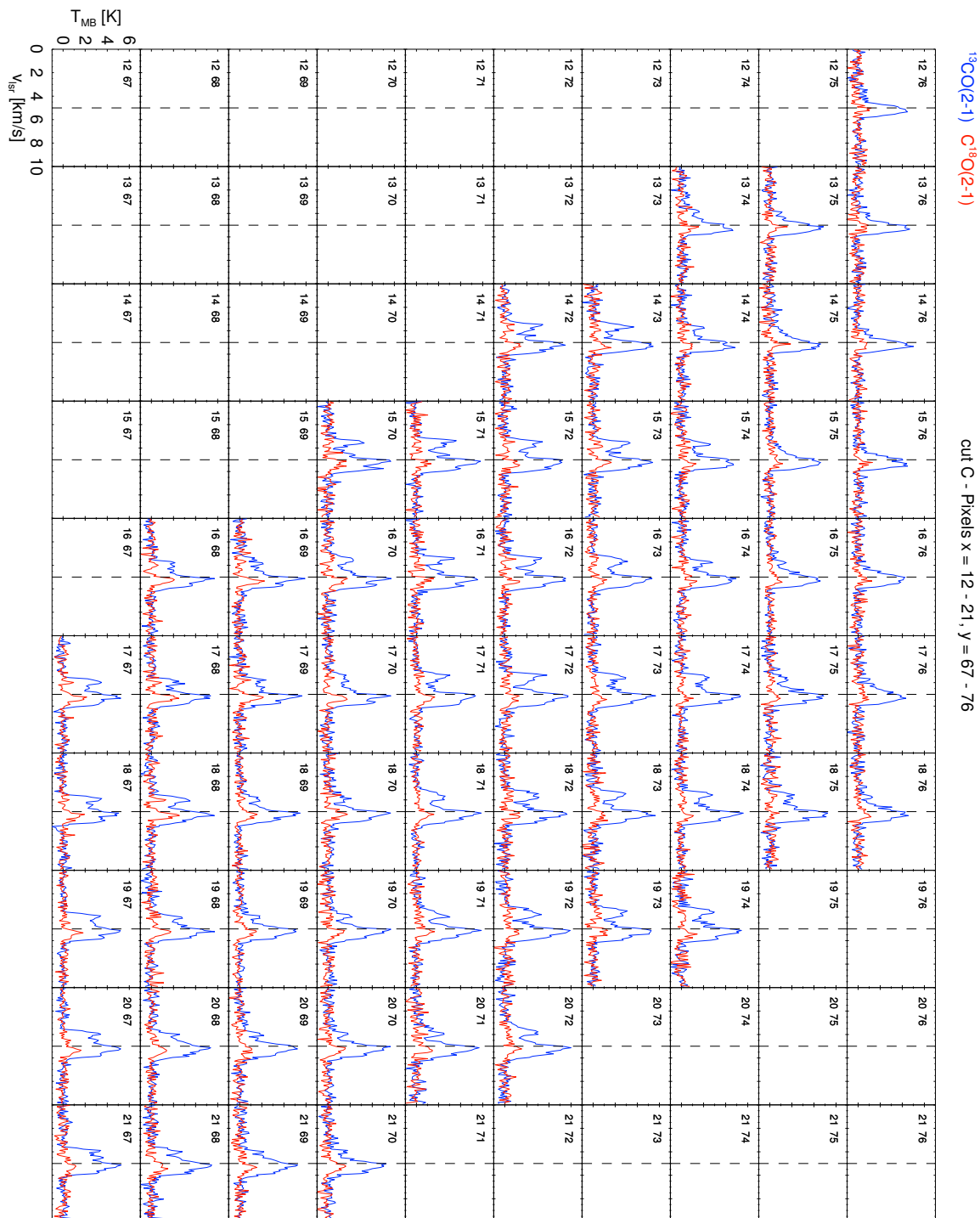


Figure A.26: Figure A.24 continued.

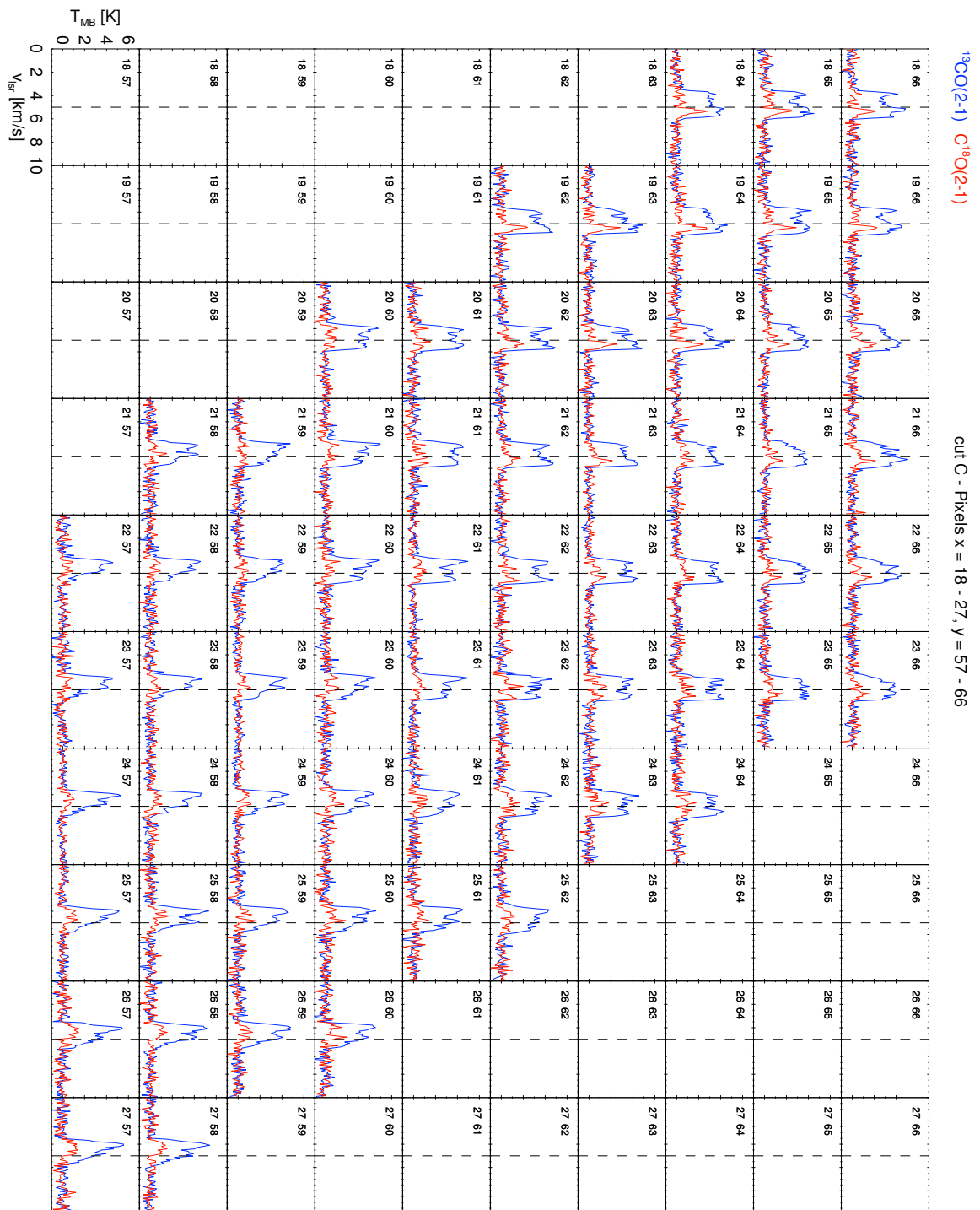


Figure A.27: Figure A.24 continued.

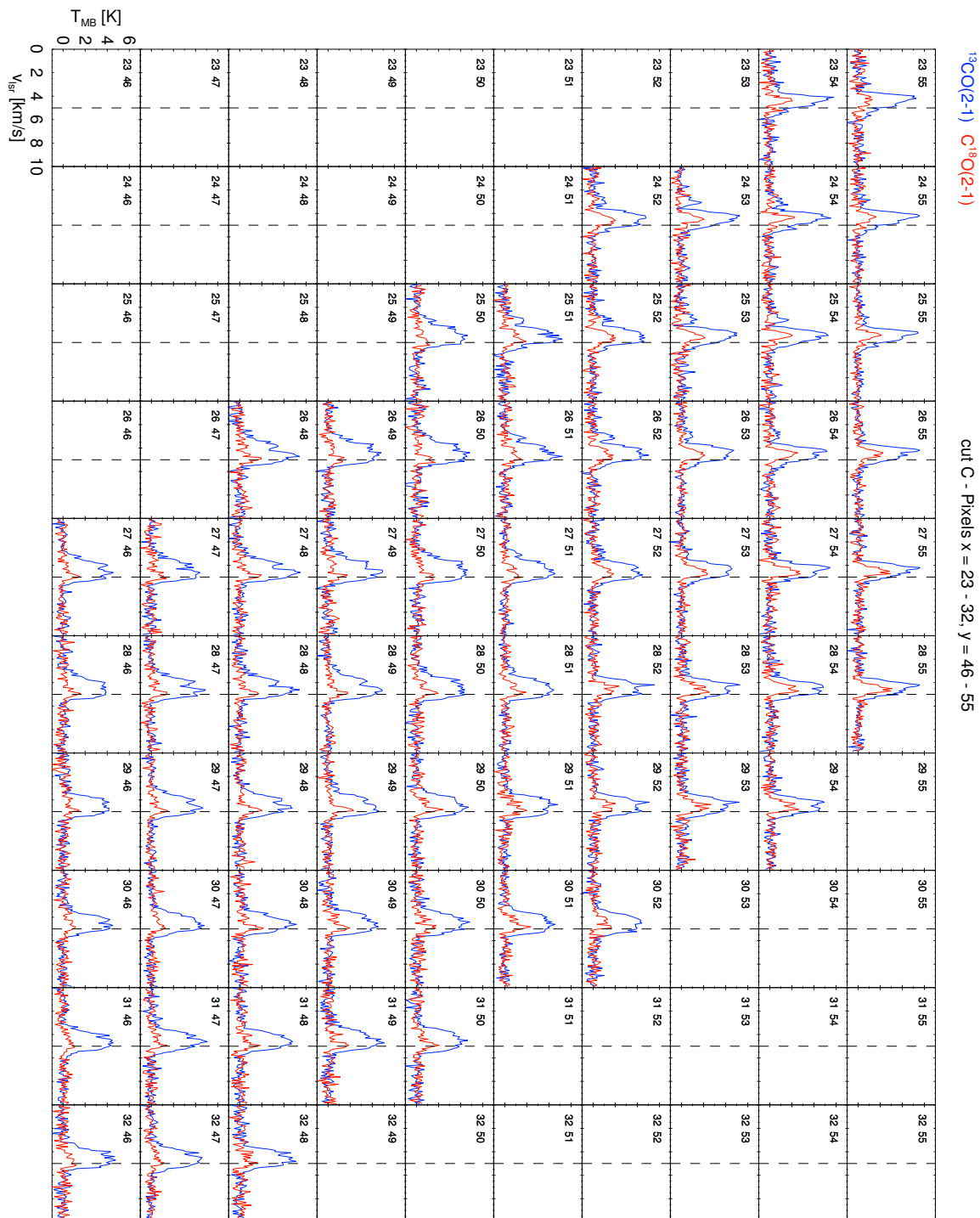


Figure A.28: Figure A.24 continued.

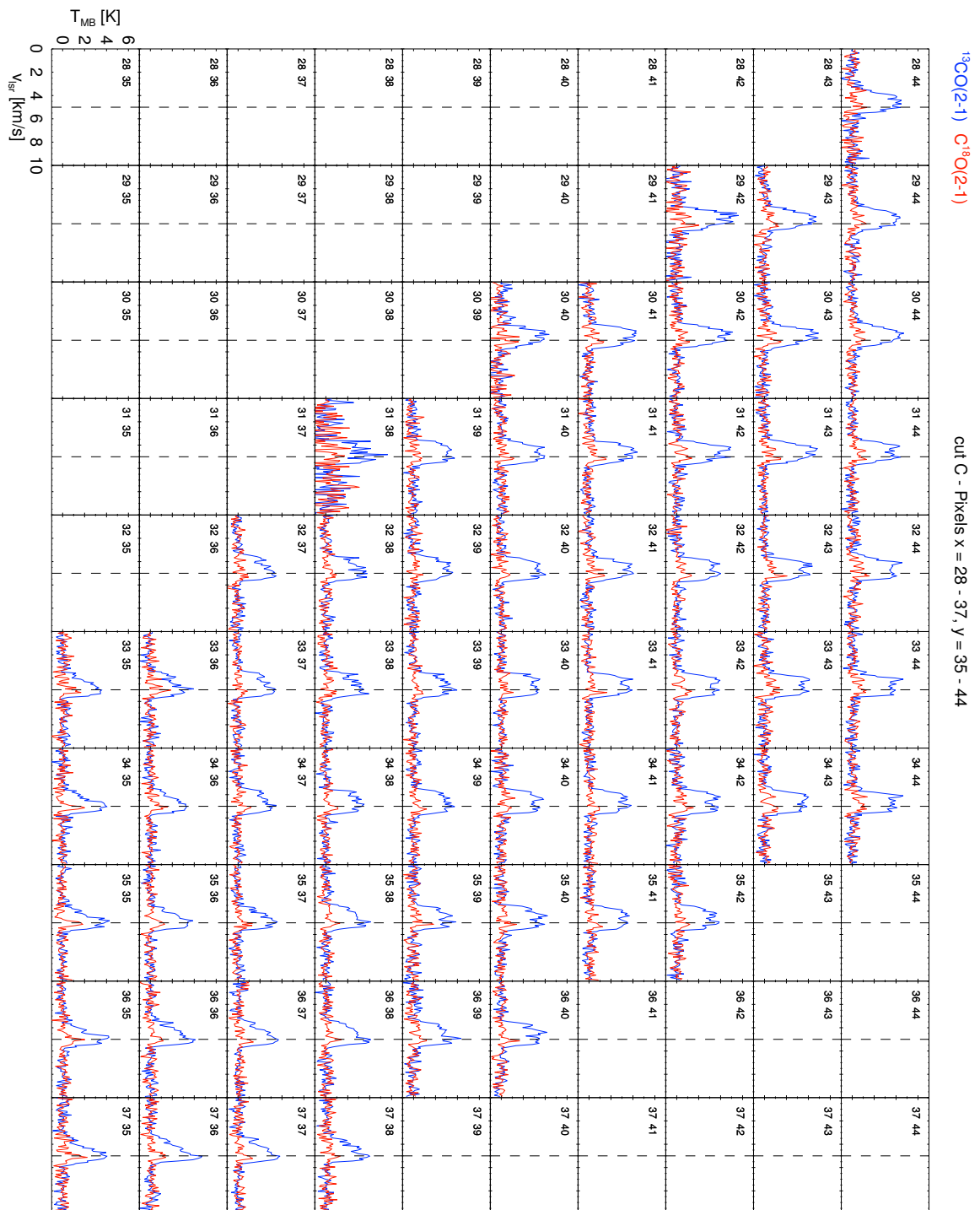


Figure A.29: Figure A.24 continued.

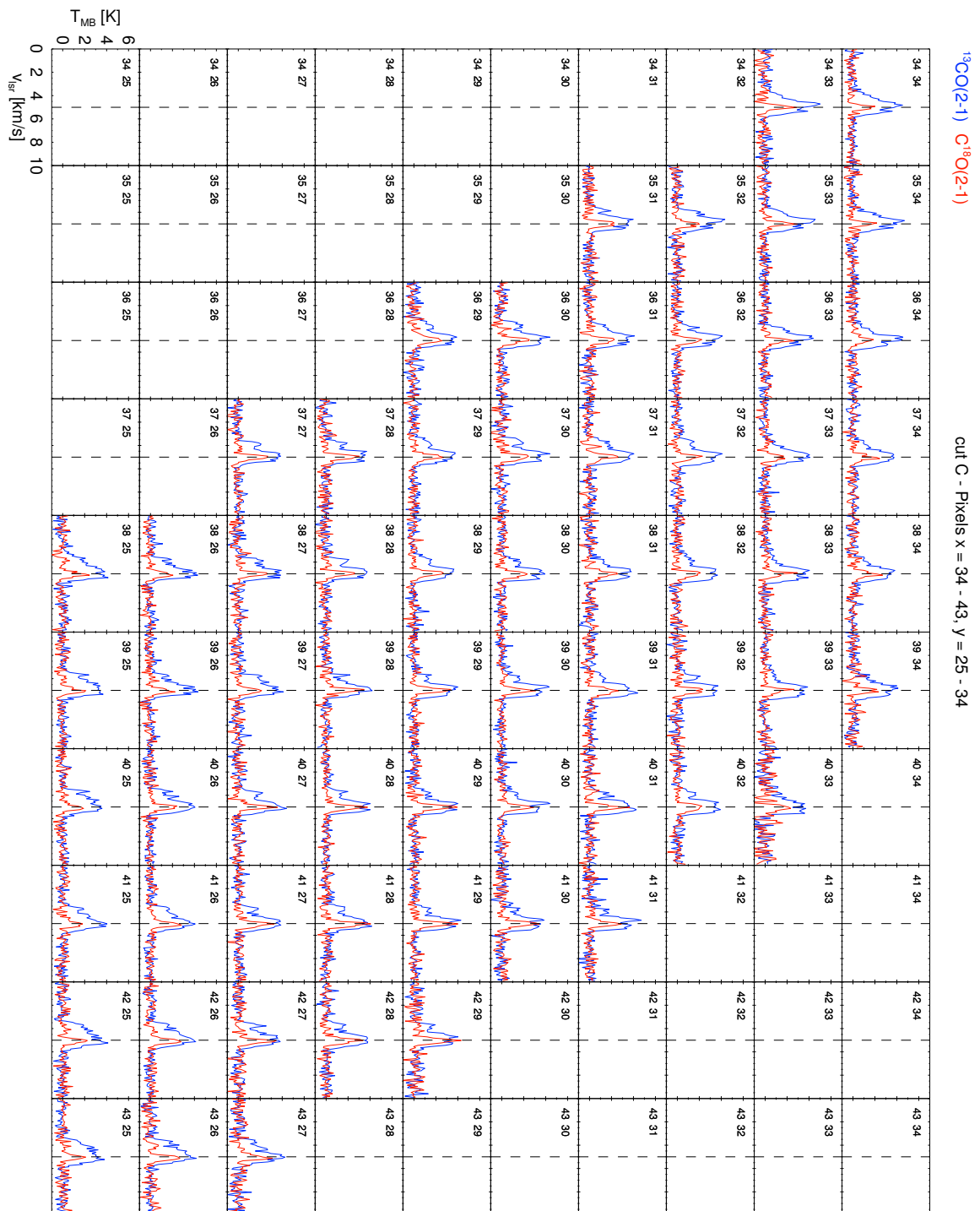


Figure A.30: Figure A.24 continued.

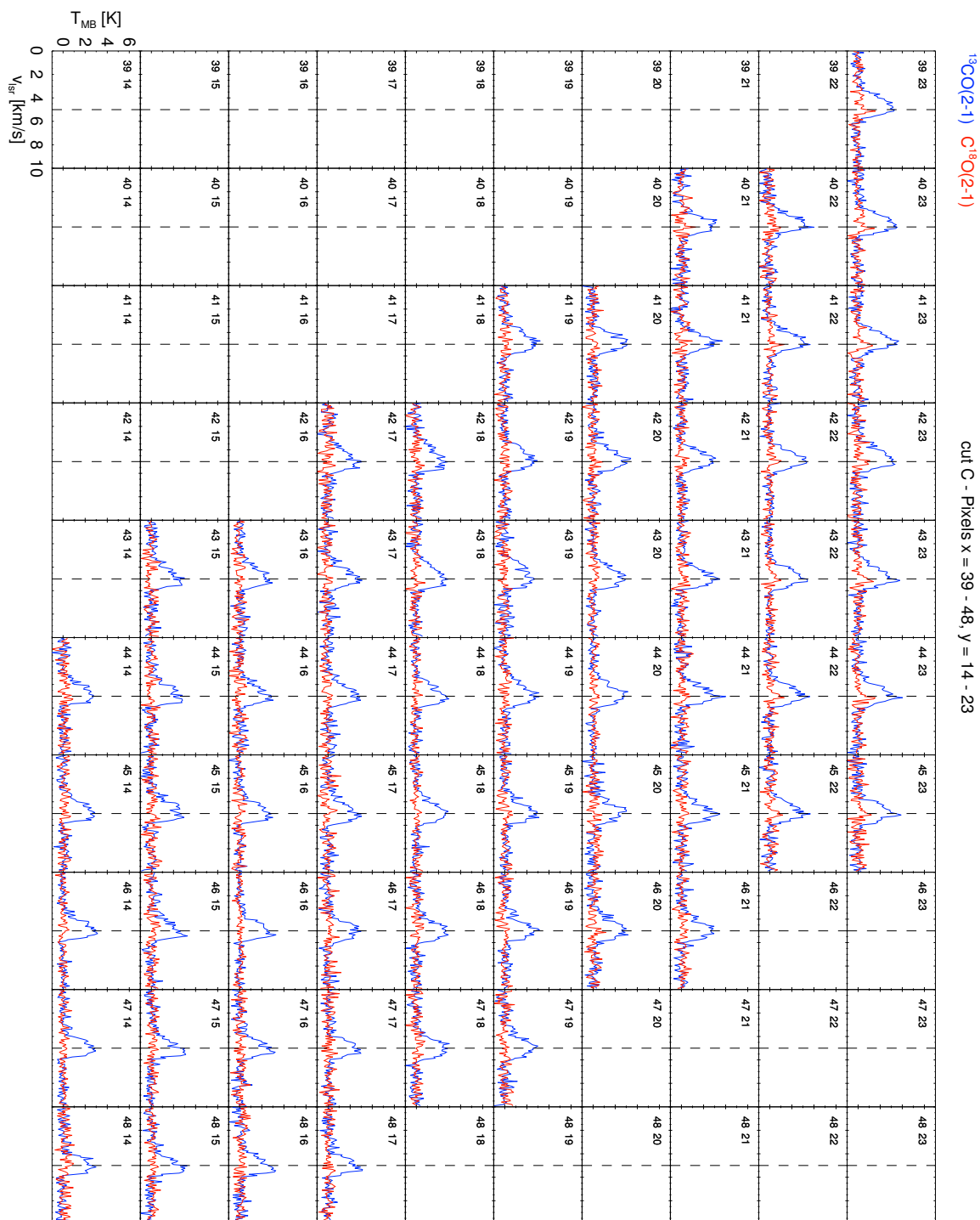


Figure A.31: Figure A.24 continued.

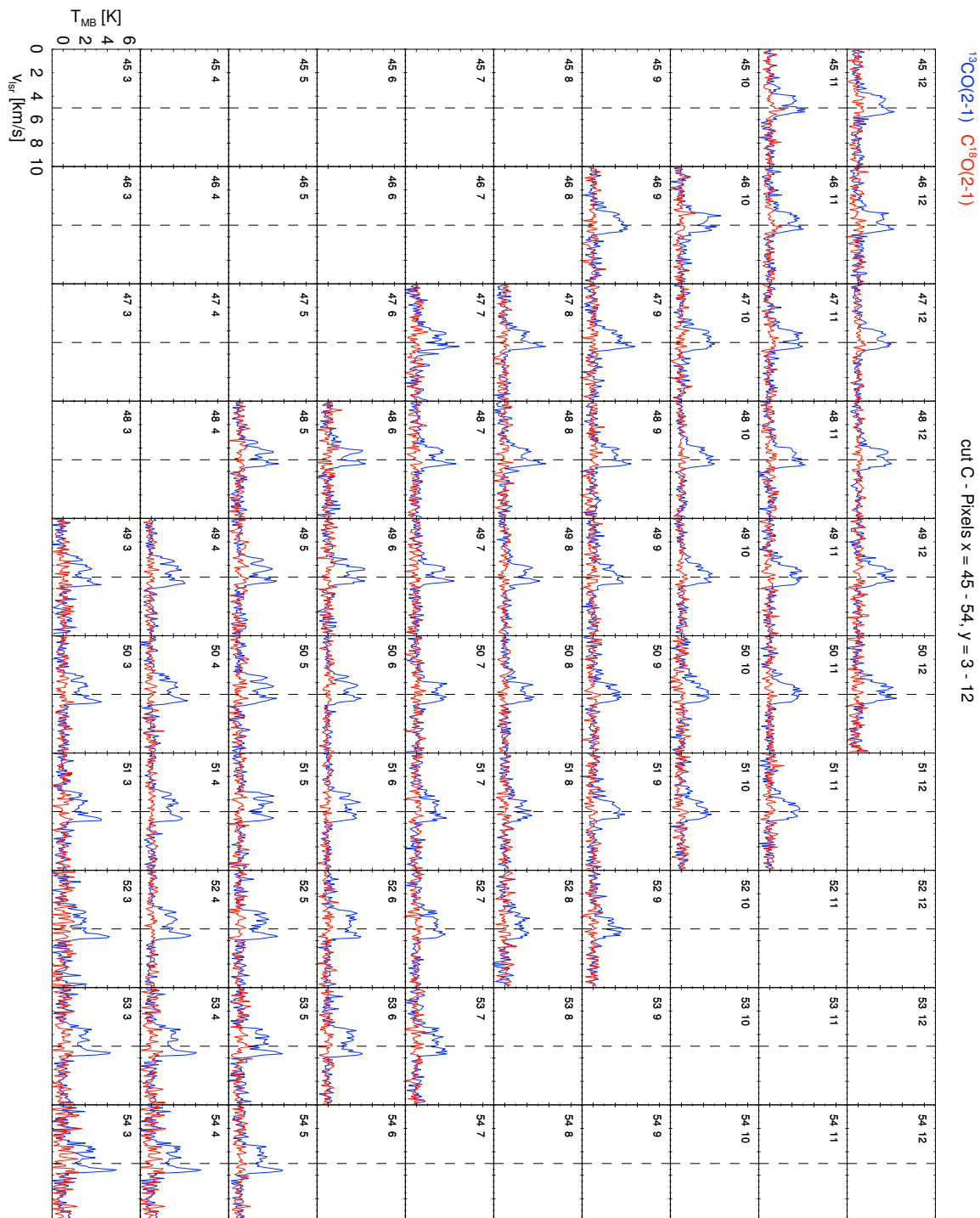


Figure A.32: Figure A.24 continued.

List of Figures

1.1	Integrated CO emission of the Milky Way	3
1.2	Dust extinction in the Milky Way	5
1.3	Life cycle of the ISM	7
1.4	Molecular cloud formation in the colliding flow model	8
1.5	Structure of molecular clouds	10
1.6	Optical and far-infrared image of Sco-Cen	18
1.7	Overview of the Lupus I cloud	21
2.1	Transmission windows in the earth's atmosphere	24
2.2	APEX telescope and the Llano de Chajnantor plateau	25
3.1	Setup of the LABOCA and APEX-1 observations	40
3.2	Reduction process of the LABOCA map	44
4.1	Map and histogram of the dust temperatures in Lupus I	47
4.2	<i>Herschel</i> column density maps for different dust models	49
4.3	<i>Herschel</i> column density and temperature maps from the SED fit with three, four, and five bands	53
4.4	Comparison of SED fits performed with three and with four bands for four selected pixels in the column density map	54
4.5	Column density maps of Lupus I from <i>Herschel</i> , LABOCA, and <i>Planck</i>	55
4.6	Column density PDFs of Lupus I	57
4.7	Column density PDFs of Lupus I	61
4.8	<i>Herschel</i> column density PDFs for different bin sizes	64
4.9	KS test of the northern part	65
4.10	Cores and YSOs in Lupus I	67
5.1	Average ^{13}CO and C^{18}O spectra of the three cuts	72
5.2	Velocity channel maps of cut A	74
5.3	Velocity channel maps of cut B	75
5.4	Velocity channel maps of cut C	76
5.5	PV diagrams of the three cuts	79
5.6	Division of each cut into boxes	80
5.7	^{13}CO moment maps of the three cuts	83

5.8	$C^{18}O$ moment maps of the three cuts	84
5.9	Dependencies of τ_{18} , T_{ex} , and T_{peak}^{18}	91
5.10	Results of the LTE analysis for the three cuts	92
5.11	Column density PDFs of the three cuts	93
5.12	Averaged spectra within the six boxes into which each cut was divided	97
5.13	Peak velocities and FWHM for each component in a box of one cut	102
5.14	Gaussian fits to the average $C^{18}O$ spectra of the boxes in cut A	105
5.15	Gaussian fits to the average ^{13}CO spectra of the boxes in cut A	106
5.16	Gaussian fits to the average $C^{18}O$ spectra of the boxes in cut B	107
5.17	Gaussian fits to the average ^{13}CO spectra of the boxes in cut B	108
5.18	Gaussian fits to the average $C^{18}O$ spectra of the boxes in cut C	109
5.19	Gaussian fits to the average ^{13}CO spectra of the boxes in cut C	110
5.20	HI channel and column density map of Lupus I	114
6.1	Surroundings of Lupus I in X-rays and dust emission	121
6.2	HI column density maps of USco and surroundings of Lupus I	122
6.3	Perspective view of the geometrical model of interaction zone USco - UCL	123
6.4	Projections of the geometrical model of interaction zone USco - UCL	124
A.1	Raster map of the CO spectra in cut A	132
A.2	CO spectra of cut A	133
A.13	Raster map of the CO spectra in cut B	144
A.14	CO spectra of cut B	145
A.23	Raster map of the CO spectra in cut C	154
A.24	CO spectra of cut C	155

List of Tables

1.1	Phases and components of the gaseous ISM	4
1.2	Properties of molecular clouds	11
2.1	Peak of the blackbody spectrum for different temperatures.	28
3.1	Details of the molecular line maps obtained for Lupus I with APEX-1 . . .	42
3.2	Zero-level offsets for the <i>Herschel</i> maps obtained from the cross-correlation with Planck and IRAS.	43
4.1	Parameters of the column density maps created from the <i>Herschel</i> SED fit	48
4.3	Parameters of the 15 cores detected in the LABOCA map with Clumpfind	68
5.1	Constants of the $^{13}\text{CO}(2-1)$ and $\text{C}^{18}\text{O}(2-1)$ molecular line transitions . . .	87
5.2	Results of the LTE analysis for the averaged spectra of cut B and cut C . .	90
5.3	Empirically determined values of peak position and FWHM of the different components in each averaged spectrum of a box within a cut	100
5.4	Peak positions and FWHM of the different components in each averaged spectrum of a box within a cut from the Gaussian fit	101

List of Abbreviations

ALMA	Atacama Large Millimeter Array
APEX	Atacama Pathfinder EXperiment
CMF	Core mass function
CSO	Caltech Submillimeter Observatory
FFTS	Fast Fourier Transform Spectrometer
FoV	Field of view
FTS	Fourier Transform Spectrometer
FWHM	Full width at half maximum
FWHP	Full Width To Half Power
GMC	Giant Molecular Cloud
Herschel	Herschel Space Observatory
Hipparcos	Hipparcos Space Astrometry Mission
HPBW	Half power beam width
IMF	Initial mass function
ISRF	InterStellar Radiation Field
JCMT	James Clerk Maxwell Telescope
LABOCA	LARge BOlometer CAmera
LCC	Lower-Centaurus-Crux
LMC	Large Magellanic cloud
LO	Local oscillator

LOS	Line of sight
LSR	Local Standard of Rest
LTE	Local Thermodynamical Equilibrium
MC	Molecular cloud
NANTEN2	NANTEN2 Observatory
OTF	On the fly
PACS	Photodetector Array Camera and Spectrometer
PDF	Probability Density Function
Planck	Planck Space Observatory
PWV	Perceptible Water Vapor
Sco-Cen	Scorpius-Centaurus
SFR	Star formation rate
SHeFI	Swedish HEterodyne Facility Instrument
SOFIA	Stratospheric Observatory For Infrared Astronomy
SPIRE	Spectral and Photometric Imaging REceiver
STO	Stratospheric Terahertz Observatory
UCL	Upper-Centaurus-Lupus
USco	Upper-Scorpius

Bibliography

- C. Alves de Oliveira, et al. (2014). ‘Herschel view of the large-scale structure in the Chamaeleon dark clouds’. *A&A* **568**:A98.
- P. André, et al. (2014). ‘From Filamentary Networks to Dense Cores in Molecular Clouds: Toward a New Paradigm for Star Formation’. *Protostars and Planets VI* pp. 27–51.
- P. André, et al. (2010). ‘From filamentary clouds to prestellar cores to the stellar IMF: Initial highlights from the Herschel Gould Belt Survey’. *A&A* **518**:L102.
- P. Andre & T. Montmerle (1994). ‘From T Tauri stars to protostars: Circumstellar material and young stellar objects in the rho Ophiuchi cloud’. *ApJ* **420**:837–862.
- G. Aniano, et al. (2011). ‘Common-Resolution Convolution Kernels for Space- and Ground-Based Telescopes’. *PASP* **123**:1218–1236.
- E. Audit & P. Hennebelle (2005). ‘Thermal condensation in a turbulent atomic hydrogen flow’. *A&A* **433**:1–13.
- J. Ballesteros-Paredes & L. Hartmann (2007). ‘Remarks on Rapid vs. Slow Star Formation’. *Revista Mexicana de Astronomia y Astrofisica* **43**:123–136.
- J. Ballesteros-Paredes, et al. (1999). ‘Turbulent Flow-driven Molecular Cloud Formation: A Solution to the Post-T Tauri Problem?’. *ApJ* **527**:285–297.
- J. Ballesteros-Paredes, et al. (2011). ‘Gravity or turbulence? - II. Evolving column density probability distribution functions in molecular clouds’. *MNRAS* **416**:1436–1442.
- R. Banerjee, et al. (2009). ‘Clump morphology and evolution in MHD simulations of molecular cloud formation’. *MNRAS* **398**:1082–1092.
- C. Battersby, et al. (2014). ‘The Comparison of Physical Properties Derived from Gas and Dust in a Massive Star-forming Region’. *ApJ* **786**:116.
- V. Baumgartner & D. Breitschwerdt (2013). ‘Superbubble evolution in disk galaxies. I. Study of blow-out by analytical models’. *A&A* **557**:A140.
- A. Belloche, et al. (2011). ‘The end of star formation in Chamaeleon I?. A LABOCA census of starless and protostellar cores’. *A&A* **527**:A145.

- M. Benedettini, et al. (2012). ‘Multiline spectral imaging of dense cores in the Lupus molecular cloud’. *MNRAS* **419**:238–250.
- M. Benedettini, et al. (2015). ‘Filaments in the Lupus molecular clouds’. *MNRAS* **453**:2036–2049.
- E. A. Bergin, et al. (2004). ‘Molecular Cloud Formation behind Shock Waves’. *ApJ* **612**:921–939.
- J.-P. Bernard, et al. (2010). ‘Dust temperature tracing the ISRF intensity in the Galaxy’. *A&A* **518**:L88.
- A. Blaauw (1964). ‘The Scorpio-Centaurus association’. In F. J. Kerr (ed.), *The Galaxy and the Magellanic Clouds*, vol. 20 of *IAU Symposium*, p. 50.
- P. Blasi (2014). ‘Recent developments in cosmic ray physics’. *Nuclear Physics B Proceedings Supplements* **256**:36–47.
- L. Blitz, et al. (2007). ‘Giant Molecular Clouds in Local Group Galaxies’. *Protostars and Planets V* pp. 81–96.
- L. Blitz & P. Thaddeus (1980). ‘Giant molecular complexes and OB associations. I - The Rosette molecular complex’. *ApJ* **241**:676–696.
- R. C. Bohlin, et al. (1978). ‘A survey of interstellar H I from L-alpha absorption measurements. II’. *ApJ* **224**:132–142.
- E. Brinks (1990). ‘The cool phase of the interstellar medium - Atomic gas’. In H. A. Thronson, Jr. & J. M. Shull (eds.), *The Interstellar Medium in Galaxies*, vol. 161 of *Astrophysics and Space Science Library*, pp. 39–65.
- J. R. Burke & D. J. Hollenbach (1983). ‘The gas-grain interaction in the interstellar medium - Thermal accommodation and trapping’. *ApJ* **265**:223–234.
- A. Burkert & L. Hartmann (2004). ‘Collapse and Fragmentation in Finite Sheets’. *ApJ* **616**:288–300.
- A. Burkert & L. Hartmann (2013). ‘The Dependence of Star Formation Efficiency on Gas Surface Density’. *ApJ* **773**:48.
- L. Cambr esy (1999). ‘Mapping of the extinction in giant molecular clouds using optical star counts’. *A&A* **345**:965–976.
- P. Carlhoff, et al. (2013). ‘Large scale IRAM 30 m CO-observations in the giant molecular cloud complex W43’. *A&A* **560**:A24.
- S. Cazaux & A. G. G. M. Tielens (2004). ‘H₂ Formation on Grain Surfaces’. *ApJ* **604**:222–237.

- G. Chabrier (2003). ‘The Galactic Disk Mass Function: Reconciliation of the Hubble Space Telescope and Nearby Determinations’. *ApJL* **586**:L133–L136.
- N. L. Chapman, et al. (2007). ‘The Spitzer c2d Survey of Large, Nearby, Interstellar Clouds. IV. Lupus Observed with MIPS’. *ApJ* **667**:288–302.
- S. B. Charnley & S. B. Rodgers (2009). ‘Theoretical Models of Complex Molecule Formation on Dust’. In K. J. Meech, J. V. Keane, M. J. Mumma, J. L. Siefert, & D. J. Werthimer (eds.), *Bioastronomy 2007: Molecules, Microbes and Extraterrestrial Life*, vol. 420 of *Astronomical Society of the Pacific Conference Series*, p. 29.
- P. C. Clark, et al. (2012). ‘How long does it take to form a molecular cloud?’. *MNRAS* **424**:2599–2613.
- F. Comerón (2008). *Handbook of Star Forming Regions, Volume II*, p. 295. ed. B. Reipurth, ASP Monograph Publications.
- P. S. Conti, et al. (2008). *From Luminous Hot Stars to Starburst Galaxies*. Cambridge University Press.
- T. M. Dame, et al. (2001). ‘The Milky Way in Molecular Clouds: A New Complete CO Survey’. *ApJ* **547**:792–813.
- T. M. Dame, et al. (1987). ‘A composite CO survey of the entire Milky Way’. *ApJ* **322**:706–720.
- J. R. Dawson (2013). ‘The Supershell - Molecular Cloud Connection: Large-Scale Stellar Feedback and the Formation of the Molecular ISM’. *PASA* **30**:25.
- J. R. Dawson, et al. (2011a). ‘Molecular Clouds in Supershells: A Case Study of Three Objects in the Walls of GSH 287+04-17 and GSH 277+00+36’. *ApJ* **741**:85.
- J. R. Dawson, et al. (2011b). ‘Supershells as Molecular Cloud Factories: Parsec Resolution Observations of H I and $^{12}\text{CO}(J = 1-0)$ in GSH 287+04-17 and GSH 277+00+36’. *ApJ* **728**:127.
- J. R. Dawson, et al. (2015). ‘A Young Giant Molecular Cloud Formed at the Interface of Two Colliding Supershells: Observations Meet Simulations’. *ApJ* **799**:64.
- J. H. J. de Bruijne (1999). ‘Structure and colour-magnitude diagrams of Scorpius OB2 based on kinematic modelling of Hipparcos data’. *MNRAS* **310**:585–617.
- E. J. de Geus (1992). ‘Interactions of stars and interstellar matter in Scorpio Centaurus’. *A&A* **262**:258–270.
- P. T. de Zeeuw, et al. (1999). ‘A HIPPARCOS Census of the Nearby OB Associations’. *AJ* **117**:354–399.

- R. Diehl, et al. (2010). ‘Radioactive ^{26}Al from the Scorpius-Centaurus association’. *A&A* **522**:A51.
- C. L. Dobbs, et al. (2014). ‘Formation of Molecular Clouds and Global Conditions for Star Formation’. *Protostars and Planets VI* **1312.3223**:3–26.
- B. T. Draine (2003). ‘Interstellar Dust Grains’. *ARA&A* **41**:241–289.
- B. T. Draine (2011). *Physics of the Interstellar and Intergalactic Medium*. Princeton University Press.
- B. T. Draine & A. Li (2007). ‘Infrared Emission from Interstellar Dust. IV. The Silicate-Graphite-PAH Model in the Post-Spitzer Era’. *ApJ* **657**:810–837.
- M. M. Dunham, et al. (2014). ‘Molecular Outflows Driven by Low-mass Protostars. I. Correcting for Underestimates When Measuring Outflow Masses and Dynamical Properties’. *ApJ* **783**:29.
- B. G. Elmegreen & J. Scalo (2004). ‘Interstellar Turbulence I: Observations and Processes’. *ARA&A* **42**:211–273.
- N. J. Evans, II, et al. (2009). ‘The Spitzer c2d Legacy Results: Star-Formation Rates and Efficiencies; Evolution and Lifetimes’. *ApJS* **181**:321–350.
- N. J. Evans, II, et al. (2014). ‘Star Formation Relations in Nearby Molecular Clouds’. *ApJ* **782**:114.
- C. Federrath & R. S. Klessen (2012). ‘The Star Formation Rate of Turbulent Magnetized Clouds: Comparing Theory, Simulations, and Observations’. *ApJ* **761**:156.
- C. Federrath & R. S. Klessen (2013). ‘On the Star Formation Efficiency of Turbulent Magnetized Clouds’. *ApJ* **763**:51.
- C. Federrath, et al. (2010). ‘Comparing the statistics of interstellar turbulence in simulations and observations. Solenoidal versus compressive turbulence forcing’. *A&A* **512**:A81.
- K. M. Ferrière (2001). ‘The interstellar environment of our galaxy’. *Reviews of Modern Physics* **73**:1031–1066.
- G. B. Field, et al. (1969). ‘Cosmic-Ray Heating of the Interstellar Gas’. *ApJL* **155**:L149.
- P. C. Frisch & J. D. Slavin (2003). ‘The Chemical Composition and Gas-to-Dust Mass Ratio of Nearby Interstellar Matter’. *ApJ* **594**:844–858.
- B. Gaczkowski, et al. (2015). ‘Squeezed between shells? The origin of the Lupus I molecular cloud. APEX/LABOCA, Herschel, and Planck observations’. *A&A* **584**:A36.

- B. M. Gaensler, et al. (2008). ‘The Vertical Structure of Warm Ionised Gas in the Milky Way’. *PASA* **25**:184–200.
- M. Galametz, et al. (2012). ‘Mapping the cold dust temperatures and masses of nearby KINGFISH galaxies with Herschel’. *MNRAS* **425**:763–787.
- J. E. Gaustad, et al. (2001). ‘A Robotic Wide-Angle H α Survey of the Southern Sky’. *PASP* **113**:1326–1348.
- P. Girichidis, et al. (2014). ‘On the Evolution of the Density Probability Density Function in Strongly Self-gravitating Systems’. *ApJ* **781**:91.
- P. F. Goldsmith, et al. (2008). ‘Large-Scale Structure of the Molecular Gas in Taurus Revealed by High Linear Dynamic Range Spectral Line Mapping’. *ApJ* **680**:428–445.
- P. F. Goldsmith & W. D. Langer (1999). ‘Population Diagram Analysis of Molecular Line Emission’. *ApJ* **517**:209–225.
- G. C. Gómez & E. Vázquez-Semadeni (2014). ‘Filaments in Simulations of Molecular Cloud Formation’. *ApJ* **791**:124.
- I. A. Grenier, et al. (2005). ‘Unveiling Extensive Clouds of Dark Gas in the Solar Neighborhood’. *Science* **307**:1292–1295.
- M. J. Griffin, et al. (2010). ‘The Herschel-SPIRE instrument and its in-flight performance’. *A&A* **518**:L3.
- R. Güsten, et al. (2006). ‘The Atacama Pathfinder EXperiment (APEX) - a new submillimeter facility for southern skies -’. *A&A* **454**:L13–L16.
- A. Hacar (2013). *Formacion de nucleos densos en las nubes moleculares de Tauro y Perseo*. Ph.D. thesis, Universidad Complutense de Madrid. <http://eprints.ucm.es/21554/1/T34482.pdf>.
- A. Hacar & M. Tafalla (2011). ‘Dense core formation by fragmentation of velocity-coherent filaments in L1517’. *A&A* **533**:A34.
- A. Hacar, et al. (2013). ‘Cores, filaments, and bundles: hierarchical core formation in the L1495/B213 Taurus region’. *A&A* **554**:A55.
- L. M. Haffner, et al. (2009). ‘The warm ionized medium in spiral galaxies’. *Reviews of Modern Physics* **81**:969–997.
- A. Hara, et al. (1999). ‘A Study of Dense Cloud Cores and Star Formation in Lupus: C¹⁸O J = 1-0 Observations with NANTEN’. *PASJ* **51**:895–910.
- J. Hartmann (1904). ‘Investigations on the spectrum and orbit of delta Orionis.’. *ApJ* **19**:268–286.

- L. Hartmann, et al. (2001). ‘Rapid Formation of Molecular Clouds and Stars in the Solar Neighborhood’. *ApJ* **562**:852–868.
- P. M. Harvey, et al. (2013). ‘A First Look at the Auriga-California Giant Molecular Cloud with Herschel and the CSO: Census of the Young Stellar Objects and the Dense Gas’. *ApJ* **764**:133.
- T. J. Haworth, et al. (2013). ‘Assessing molecular line diagnostics of triggered star formation using synthetic observations’. *MNRAS* **431**:3470–3484.
- C. Heiles & T. H. Troland (2003). ‘The Millennium Arecibo 21 Centimeter Absorption-Line Survey. II. Properties of the Warm and Cold Neutral Media’. *ApJ* **586**:1067–1093.
- J. S. Heiner, et al. (2015). ‘Molecular cloud formation as seen in synthetic H I and molecular gas observations’. *MNRAS* **452**:1353–1374.
- F. Heitsch & L. Hartmann (2008). ‘Rapid Molecular Cloud and Star Formation: Mechanisms and Movies’. *ApJ* **689**:290–301.
- M. Heyer & T. M. Dame (2015). ‘Molecular Clouds in the Milky Way’. *ARA&A* **53**:583–629.
- M. H. Heyer, et al. (2001). ‘The Equilibrium State of Molecular Regions in the Outer Galaxy’. *ApJ* **551**:852–866.
- D. Hollenbach & E. E. Salpeter (1971). ‘Surface Recombination of Hydrogen Molecules’. *ApJ* **163**:155.
- E. P. Hubble (1922). ‘The source of luminosity in galactic nebulae.’. *ApJ* **56**:400–438.
- S.-i. Inutsuka, et al. (2015). ‘The formation and destruction of molecular clouds and galactic star formation. An origin for the cloud mass function and star formation efficiency’. *A&A* **580**:A49.
- R. D. Jeffries, et al. (2011). ‘No wide spread of stellar ages in the Orion Nebula Cluster’. *MNRAS* **418**:1948–1958.
- M. Jura (1975). ‘Interstellar clouds containing optically thin H₂’. *ApJ* **197**:575–580.
- M. Juvela, et al. (2013). ‘Estimation of high-resolution dust column density maps. Comparison of modified black-body fits and radiative transfer modelling’. *A&A* **553**:A113.
- J. Kainulainen, et al. (2011). ‘Probing the evolution of molecular cloud structure. II. From chaos to confinement’. *A&A* **530**:A64.
- J. Kainulainen, et al. (2009). ‘Probing the evolution of molecular cloud structure. From quiescence to birth’. *A&A* **508**:L35–L38.

- P. M. W. Kalberla, et al. (2010). ‘GASS: the Parkes Galactic all-sky survey. II. Stray-radiation correction and second data release’. *A&A* **521**:A17.
- R. C. Kennicutt, Jr. (1998). ‘The Global Schmidt Law in Star-forming Galaxies’. *ApJ* **498**:541–552.
- N. Kevlahan & R. E. Pudritz (2009). ‘Shock-generated Vorticity in the Interstellar Medium and the Origin of the Stellar Initial Mass Function’. *ApJ* **702**:39–49.
- R. S. Klessen (2011). ‘Star Formation in Molecular Clouds’. In C. Charbonnel & T. Montmerle (eds.), *EAS Publications Series*, vol. 51 of *EAS Publications Series*, pp. 133–167.
- R. S. Klessen & S. C. O. Glover (2014). ‘Physical Processes in the Interstellar Medium’. *ArXiv e-prints* **1412.5182**.
- R. S. Klessen, et al. (2000). ‘Gravitational Collapse in Turbulent Molecular Clouds. I. Gasdynamical Turbulence’. *ApJ* **535**:887–906.
- J. Koda, et al. (2009). ‘Dynamically Driven Evolution of the Interstellar Medium in M51’. *ApJL* **700**:L132–L136.
- H. Koyama & S.-I. Inutsuka (2000). ‘Molecular Cloud Formation in Shock-compressed Layers’. *ApJ* **532**:980–993.
- M. Krause, et al. (2014). ‘Feedback by massive stars and the emergence of superbubbles. II. X-ray properties’. *A&A* **566**:A94.
- M. Krause, et al. (2013). ‘Feedback by massive stars and the emergence of superbubbles. I. Energy efficiency and Vishniac instabilities’. *A&A* **550**:A49.
- P. Kroupa (2001). ‘On the variation of the initial mass function’. *MNRAS* **322**:231–246.
- H. Krüger, et al. (2015). ‘Sixteen Years of Ulysses Interstellar Dust Measurements in the Solar System. I. Mass Distribution and Gas-to-dust Mass Ratio’. *ApJ* **812**:139.
- M. R. Krumholz (2014). ‘The big problems in star formation: The star formation rate, stellar clustering, and the initial mass function’. *Physics Reports* **539**:49–134.
- M. L. Kutner, et al. (1977). ‘The molecular complexes in Orion’. *ApJ* **215**:521–528.
- M. L. Kutner & B. L. Ulich (1981). ‘Recommendations for calibration of millimeter-wavelength spectral line data’. *ApJ* **250**:341–348.
- C. J. Lada (1987). ‘Star formation - From OB associations to protostars’. In M. Peimbert & J. Jugaku (eds.), *Star Forming Regions*, vol. 115 of *IAU Symposium*, pp. 1–17.
- E. F. Ladd, et al. (1998). ‘C¹⁸O and C¹⁷O Observations of Embedded Young Stars in the Taurus Molecular Cloud. I. Integrated Intensities and Column Densities’. *ApJ* **495**:871–890.

- M. Lombardi, et al. (2014). ‘Herschel-Planck dust optical-depth and column-density maps. I. Method description and results for Orion’. *A&A* **566**:A45.
- M. Lombardi, et al. (2008a). ‘2MASS wide field extinction maps. II. The Ophiuchus and the Lupus cloud complexes’. *A&A* **489**:143–156.
- M. Lombardi, et al. (2008b). ‘Hipparcos distance estimates of the Ophiuchus and the Lupus cloud complexes’. *A&A* **480**:785–792.
- M.-M. Mac Low & R. S. Klessen (2004). ‘Control of star formation by supersonic turbulence’. *Reviews of Modern Physics* **76**:125–194.
- A. Maeder & G. Meynet (2012). ‘Rotating massive stars: From first stars to gamma ray bursts’. *Reviews of Modern Physics* **84**:25–63.
- L. Magnani, et al. (1985). ‘Molecular gas at high Galactic latitudes’. *ApJ* **295**:402–421.
- J. G. Mangum & Y. L. Shirley (2015). ‘How to Calculate Molecular Column Density’. *PASP* **127**:266–298.
- J. S. Mathis, et al. (1977). ‘The size distribution of interstellar grains’. *ApJ* **217**:425–433.
- T. Matsumoto, et al. (2015). ‘Star Formation in Turbulent Molecular Clouds with Colliding Flow’. *ApJ* **801**:77.
- T. G. Matthews, et al. (2014). ‘Lupus I Observations from the 2010 Flight of the Balloon-borne Large Aperture Submillimeter Telescope for Polarimetry’. *ApJ* **784**:116.
- N. M. McClure-Griffiths, et al. (2009). ‘Gass: The Parkes Galactic All-Sky Survey. I. Survey Description, Goals, and Initial Data Release’. *ApJS* **181**:398–412.
- C. F. McKee & E. C. Ostriker (2007). ‘Theory of Star Formation’. *ARA&A* **45**:565–687.
- C. F. McKee & J. P. Ostriker (1977). ‘A theory of the interstellar medium - Three components regulated by supernova explosions in an inhomogeneous substrate’. *ApJ* **218**:148–169.
- A. Mellinger (2008). *Handbook of Star Forming Regions, Volume I*, p. 1. ed. B. Reipurth, ASP Monograph Publications.
- B. Merín, et al. (2008). ‘The Spitzer c2d Survey of Large, Nearby, Interstellar Clouds. XI. Lupus Observed with IRAC and MIPS’. *ApJS* **177**:551–583.
- S. Molinari, et al. (2014). ‘The Milky Way as a Star Formation Engine’. *Protostars and Planets VI* pp. 125–148.
- H. S. P. Müller, et al. (2005). ‘The Cologne Database for Molecular Spectroscopy, CDMS: A Tool for Astrochemists and Astrophysicists’. In *IAU Symposium*, vol. 235 of *IAU Symposium*, p. 62P.

- H. S. P. Müller, et al. (2001). ‘The Cologne Database for Molecular Spectroscopy, CDMS’. *A&A* **370**:L49–L52.
- P. C. Myers (1983). ‘Dense cores in dark clouds. III - Subsonic turbulence’. *ApJ* **270**:105–118.
- P. C. Myers, et al. (1983). ‘Dense cores in dark clouds. I - CO observations and column densities of high-extinction regions’. *ApJ* **264**:517–537.
- F. Nakamura & Z.-Y. Li (2008). ‘Magnetically Regulated Star Formation in Three Dimensions: The Case of the Taurus Molecular Cloud Complex’. *ApJ* **687**:354–375.
- S. S. R. Offner, et al. (2014). ‘The Origin and Universality of the Stellar Initial Mass Function’. *Protostars and Planets VI* pp. 53–75.
- T. Oka, et al. (2001). ‘Statistical Properties of Molecular Clouds in the Galactic Center’. *ApJ* **562**:348–362.
- V. Ossenkopf & T. Henning (1994). ‘Dust opacities for protostellar cores’. *A&A* **291**:943–959.
- D. E. Osterbrock & G. J. Ferland (2006). *Astrophysics of gaseous nebulae and active galactic nuclei*. University Science Books.
- J. P. Ostriker & C. F. McKee (1988). ‘Astrophysical blastwaves’. *Reviews of Modern Physics* **60**:1–68.
- S. Ott (2010). ‘The Herschel Data Processing System HIPE and Pipelines Up and Running Since the Start of the Mission’. In Y. Mizumoto, K.-I. Morita, & M. Ohishi (ed.), *Astronomical Data Analysis Software and Systems XIX*, vol. 434 of *Astronomical Society of the Pacific Conference Series*, p. 139.
- Y. Oya, et al. (2014). ‘A Substellar-mass Protostar and its Outflow of IRAS 15398–3359 Revealed by Subarcsecond-resolution Observations of H₂CO and CCH’. *ApJ* **795**:152.
- P. Padoan, et al. (2001). ‘The Turbulent Shock Origin of Proto-Stellar Cores’. *ApJ* **553**:227–234.
- P. Padoan & Å. Nordlund (2002). ‘The Stellar Initial Mass Function from Turbulent Fragmentation’. *ApJ* **576**:870–879.
- P. Palmeirim, et al. (2013). ‘Herschel view of the Taurus B211/3 filament and striations: evidence of filamentary growth?’. *A&A* **550**:A38.
- T. G. Phillips, et al. (1979). ‘Observations of CO/J = 2-1/ emission from molecular clouds’. *ApJ* **231**:720–731.

- H. M. Pickett, et al. (1998). ‘Submillimeter, millimeter and microwave spectral line catalog.’. *Journal of Quantitative Spectroscopy and Radiative Transfer* **60**:883–890.
- G. L. Pilbratt, et al. (2010). ‘Herschel Space Observatory. An ESA facility for far-infrared and submillimetre astronomy’. *A&A* **518**:L1.
- Planck Collaboration, et al. (2014). ‘Planck 2013 results. XI. All-sky model of thermal dust emission’. *A&A* **571**:A11.
- Planck Collaboration, et al. (2011). ‘Planck early results. XIX. All-sky temperature and dust optical depth from Planck and IRAS. Constraints on the ”dark gas” in our Galaxy’. *A&A* **536**:A19.
- A. Poglitsch, et al. (2010). ‘The Photodetector Array Camera and Spectrometer (PACS) on the Herschel Space Observatory’. *A&A* **518**:L2.
- T. Preibisch, et al. (2002). ‘Exploring the Full Stellar Population of the Upper Scorpius OB Association’. *AJ* **124**:404–416.
- T. Preibisch, et al. (1998). ‘A lithium-survey for pre-main sequence stars in the Upper Scorpius OB association’. *A&A* **333**:619–628.
- T. Preibisch & E. Mamajek (2008). *Handbook of Star Forming Regions, Volume II*, p. 235. ed. B. Reipurth, ASP Monograph Publications.
- T. Preibisch & H. Zinnecker (2007). ‘Sequentially triggered star formation in OB associations’. In B. G. Elmegreen & J. Palous (ed.), *IAU Symposium*, vol. 237 of *IAU Symposium*, pp. 270–277.
- R. J. Reynolds (1991). ‘Ionized disk/halo gas - Insight from optical emission lines and pulsar dispersion measures’. In H. Bloemen (ed.), *The Interstellar Disk-Halo Connection in Galaxies*, vol. 144 of *IAU Symposium*, pp. 67–76.
- V. Roccoatagliata, et al. (2015). ‘A network of filaments detected by Herschel in the Serpens Core: A laboratory to test simulations of low-mass star formation’. *ArXiv e-prints* **1509.06216**.
- H. Roussel (2013). ‘Scanamorphos: A Map-making Software for Herschel and Similar Scanning Bolometer Arrays’. *PASP* **125**:1126–1163.
- N. Roy, et al. (2013). ‘The temperature of the diffuse H I in the Milky Way - II. Gaussian decomposition of the H I-21 cm absorption spectra’. *MNRAS* **436**:2366–2385.
- K. L. J. Rygl, et al. (2013). ‘Recent star formation in the Lupus clouds as seen by Herschel’. *A&A* **549**:L1.
- E. E. Salpeter (1955). ‘The Luminosity Function and Stellar Evolution.’. *ApJ* **121**:161.

- E. E. Salpeter (1976). ‘Planetary nebulae, supernova remnants, and the interstellar medium /The Henry Norris Russell Lecture/’. *ApJ* **206**:673–678.
- J. Santiago-García, et al. (2009). ‘Shells, jets, and internal working surfaces in the molecular outflow from IRAS 04166+2706’. *A&A* **495**:169–181.
- J. Scalo & B. G. Elmegreen (2004). ‘Interstellar Turbulence II: Implications and Effects’. *ARA&A* **42**:275–316.
- M. Schmidt (1959). ‘The Rate of Star Formation.’. *ApJ* **129**:243.
- N. Schneider, et al. (2013). ‘What Determines the Density Structure of Molecular Clouds? A Case Study of Orion B with Herschel’. *ApJL* **766**:L17.
- N. Schneider, et al. (2012). ‘Cluster-formation in the Rosette molecular cloud at the junctions of filaments’. *A&A* **540**:L11.
- N. Schneider, et al. (2015). ‘Understanding star formation in molecular clouds. I. Effects of line-of-sight contamination on the column density structure’. *A&A* **575**:A79.
- F. Schuller (2012). ‘BoA: a versatile software for bolometer data reduction’. In *Society of Photo-Optical Instrumentation Engineers (SPIE) Conference Series*, vol. 8452 of *Society of Photo-Optical Instrumentation Engineers (SPIE) Conference Series*.
- F. Schuller, et al. (2009). ‘ATLASGAL - The APEX telescope large area survey of the galaxy at 870 μm ’. *A&A* **504**:415–427.
- N. S. Schulz (2005). *From Dust to Stars*. Springer with Praxis Publishing, Chichester, UK.
- N. S. Schulz (2005). *From Dust To Stars Studies of the Formation and Early Evolution of Stars*. Praxis Publishing Ltd.
- N. Z. Scoville & P. M. Solomon (1975). ‘Molecular clouds in the Galaxy’. *ApJL* **199**:L105–L109.
- C. G. Seab (1987). ‘Grain destruction, formation, and evolution’. In D. J. Hollenbach & H. A. Thronson, Jr. (eds.), *Interstellar Processes*, vol. 134 of *Astrophysics and Space Science Library*, pp. 491–512.
- F. H. Shu, et al. (1987). ‘Star formation in molecular clouds - Observation and theory’. *ARA&A* **25**:23–81.
- J. M. Shull & S. Beckwith (1982). ‘Interstellar molecular hydrogen’. *ARA&A* **20**:163–190.
- G. Siringo, et al. (2009). ‘The Large APEX BOlometer CAmera LABOCA’. *A&A* **497**:945–962.

- S.-i. Sirono (2013). ‘Size and Surface Area of Icy Dust Aggregates after a Heating Event at a Protoplanetary Nebula’. *ApJ* **765**:50.
- K. Tachihara, et al. (1996). ‘ ^{13}CO (J= 1–0) Observations of the Lupus Molecular Clouds’. *PASJ* **48**:489–502.
- K. Tachihara, et al. (2001). ‘ ^{12}CO Molecular Cloud Survey and Global Star Formation in Lupus’. *PASJ* **53**:1081–1096.
- J. C. Tan, et al. (2014). ‘Massive Star Formation’. *Protostars and Planets VI* pp. 149–172.
- N. F. H. Tothill, et al. (2009). ‘Large-Scale CO Maps of the Lupus Molecular Cloud Complex’. *ApJS* **185**:98–123.
- P. Tremblin, et al. (2012). ‘Three-dimensional simulations of globule and pillar formation around HII regions: turbulence and shock curvature’. *A&A* **546**:A33.
- P. Tremblin, et al. (2014). ‘Ionization compression impact on dense gas distribution and star formation. Probability density functions around H II regions as seen by Herschel’. *A&A* **564**:A106.
- J. Trümper, et al. (1991). ‘X-ray survey of the Large Magellanic Cloud by ROSAT’. *Nature* **349**:579–583.
- E. F. van Dishoeck (1987). ‘Photodissociation processes of astrophysical molecules’. In M. S. Vardya & S. P. Tarafdar (eds.), *Astrochemistry*, vol. 120 of *IAU Symposium*, pp. 51–63.
- S. Van Loo, et al. (2013). ‘Sputtering in oblique C-type shocks’. *MNRAS* **428**:381–388.
- V. Vassilev, et al. (2008). ‘A Swedish heterodyne facility instrument for the APEX telescope’. *A&A* **490**:1157–1163.
- E. Vázquez-Semadeni (1994). ‘Hierarchical Structure in Nearly Pressureless Flows as a Consequence of Self-similar Statistics’. *ApJ* **423**:681.
- E. Vázquez-Semadeni, et al. (2011). ‘Molecular cloud evolution - IV. Magnetic fields, ambipolar diffusion and the star formation efficiency’. *MNRAS* **414**:2511–2527.
- E. Vázquez-Semadeni, et al. (2007). ‘Molecular Cloud Evolution. II. From Cloud Formation to the Early Stages of Star Formation in Decaying Conditions’. *ApJ* **657**:870–883.
- J. W. S. Vilas-Boas, et al. (2000). ‘Dense Cores of Dark Clouds. XII. ^{13}CO and C^{18}O in Lupus, Corona Australis, Vela, and Scorpius’. *ApJ* **532**:1038–1050.
- N. A. Walton, et al. (2011). ‘VAMDC: The Virtual Atomic and Molecular Data Center’. In I. N. Evans, A. Accomazzi, D. J. Mink, & A. H. Rots (eds.), *Astronomical Data Analysis Software and Systems XX*, vol. 442 of *Astronomical Society of the Pacific Conference Series*, p. 89.

- R. L. Ward, et al. (2014). ‘Evolving molecular cloud structure and the column density probability distribution function’. *MNRAS* **445**:1575–1583.
- J. P. Williams, et al. (1994). ‘Determining structure in molecular clouds’. *ApJ* **428**:693–712.
- R. W. Wilson, et al. (1970). ‘Carbon Monoxide in the Orion Nebula’. *ApJL* **161**:L43.
- T. L. Wilson, et al. (2009). *Tools of Radio Astronomy*. Springer-Verlag.
- T. L. Wilson & R. Rood (1994). ‘Abundances in the Interstellar Medium’. *ARA&A* **32**:191–226.
- C. Winkler, et al. (2003). ‘The INTEGRAL mission’. *A&A* **411**:L1–L6.
- N. J. Woolf & E. P. Ney (1969). ‘Circumstellar Infrared Emission from Cool Stars’. *ApJL* **155**:L181.
- E. M. Xilouris, et al. (2012). ‘Cool and warm dust emission from M 33 (HerM33es)’. *A&A* **543**:A74.
- H. Zinnecker & H. W. Yorke (2007). ‘Toward Understanding Massive Star Formation’. *ARA&A* **45**:481–563.